

Interface Engineering for Highly Efficient Perovskite Solar Cells: Role of Surface Passivation

Jun Peng

April 2018



**Australian
National
University**

A thesis submitted for the degree of
Doctor of Philosophy
of The Australian National University


© Copyright by Jun Peng, 2018

All Rights Reserved


Declaration

I certify that this thesis does not incorporate, without acknowledgement any material previously submitted for a degree or diploma in any university, and that, to the best of my knowledge, it does not contain any material previously published or written by another person except where due reference is made in the text. The work in this thesis is my own, except for the contributions made by others as described in the Acknowledgments. The thesis is a compilation of four manuscripts, all of which I am the first author. The manuscript details are given as below.

Manuscript 1 is presented as Chapter 2 in this thesis.

- Title: Efficient indium-doped TiO_x electron transport layers for high-performance perovskite solar cells and perovskite-silicon tandems
- Authors: Jun Peng, The Duong, Xianzhong Zhou, Heping Shen, Yiliang Wu, Hemant Kumar Mulmudi, Yimao Wan, Dingyong Zhong, Juntao Li, Takuya Tsuzuki, Klaus J. Weber, Kylie R. Catchpole, and Thomas P. White
- Current status: published in *Advanced Energy Materials*. (*Adv. Energy Mater.*, **2017**, 7, 1601768)
- Contributions: J. P. conceived the idea, designed the overall experiments and led the project. T. P. W. supervised the project. T. D. optimized the Cs-mixed halide perovskite absorber materials. J. P. and T. D. conducted the tandem cells experiments. J. P., T. D., T. P. W., K.J. W. and K. R. C. contributed to the tandem cells' characterizations and analysis. J. P., X. Z., D. Z. and J. L. conducted the XPS/UPS measurements and analysis. H. S. and T. D. conducted the XRD and SEM measurements and analysis. Y. W., H. M. and Y. W. conducted the Hall Effect measurements and analysis. J. P. wrote the manuscript. The manuscript was mainly revised by J. P. and T. P. W. All authors contributed to the discussion of the results and commented on the manuscript.
- Declaration signed from a senior author: 


Manuscript 2 is presented as Chapter 3 in this thesis.

- Title: Interface passivation using ultrathin polymer-fullerene films for high-efficiency perovskite solar cells with negligible hysteresis
- Authors: Jun Peng, Yiliang Wu, Wang Ye, Daniel Jacobs, Heping Shen, Xiao Fu, Yimao Wan, The Duong, Nandi Wu, Chog Barugkin, Hieu Nguyen, Dingyong Zhong, Juntao Li, Teng Lu, Yun Liu, Mark N. Lockrey, Klaus J. Weber, Kylie R. Catchpole, Thomas P. White
- Current status: published in *Energy & Environmental Science*. (*Energy Environ. Sci.*, **2017**, 10, 1792-1800)
- Contributions: J. P. conceived the idea, designed the overall experiments and led the project. T. P. W. supervised the project. J. P., Y. W., H. S., T. D., N. W. and D. J. prepared and characterized the perovskite cell devices. Y. W. and N. W. conducted the PL imaging measurements and analysis. W. Y., D. Z. and J. L. conducted the XPS/UPS measurements and analysis. X. F. and H. N. performed the TRPL measurements and analysis. H. S. and T. D. conducted the XRD and SEM measurements and analysis. C. B. conducted the optical transmittance measurements and analysis. T. L. and Y. L. conducted the C-AFM measurements and analysis. M. N. L. conducted the EDX (SEM) measurements and analysis. J. P., D. J., K. J. W., K. R. C. and T. P. W. contributed to the results analysis and interpretation. J. P. wrote the manuscript. The manuscript was mainly revised by J. P. and T. P. W. All authors contributed to the discussion of the results and commented on the manuscript.
- Declaration signed from a senior author: 

Manuscript 3 is presented as Chapter 4 in this thesis.

- Title: A Universal Double-side passivation for high open-circuit voltage in perovskite solar cells: role of carbonyl groups in poly(methyl methacrylate)
- Authors: Jun Peng, Jafar I. Khan, Wenzhu Liu, Esmâ Ugur, The Duong, Yiliang Wu, Heping Shen, Kai Wang, Hoang Dang, Erkan Aydin, Xinbo Yang, Yimao Wan, Klaus J. Weber, Kylie R. Catchpole, Frédéric Laquai, Stefaan De Wolf, Thomas P. White
- Current status: published in *Advanced Energy Materials*. (*Adv. Energy Mater.*, **2018**, 8, 1801208)

- Contributions: J. P. conceived the idea, designed the overall experiments and led the project. T. P. W. supervised the project. J. P., T. D., H. S. and Y. W. prepared and characterized the perovskite cell devices. J. I. K. and E. U. performed the TA and TRPL measurements and data analysis. F. L. supervised the TA and TRPL measurements and analysis. W. L., X. Y. and J. P. conducted the FTIR measurements and analysis. W. L. performed the DFT calculation. T. D., H. S. and Y. W. conducted the PL imaging measurements. H. D. conducted the XRD and SEM measurements. K. W. conducted the NMR measurements and analysis. E. A. conducted the EQE measurements. J. P., J. I. K., K. J. W., K. R. C., F. L., S. D. W. and T. P. W. contributed to the results analysis and interpretation. J. P. wrote the manuscript. The manuscript was mainly revised by J. P. and T. P. W. All authors contributed to the discussion of the results and revision of the manuscript.

- Declaration signed from a senior author: 

Manuscript 4 is presented as Chapter 5 in this thesis.

- Title: Inorganic ZnO/MgF₂ Bi-Layers as a High-Performance Alternative to Fullerene-Based Electron Transport Layers in Inverted Perovskite Solar Cells
- Authors: Jun Peng, Yimao Wan, Xianzhong Zhou, The Duong, Heping Shen, Daniel A. Jacobs, Hieu T. Nguyen, Mark N. Lockrey, Felipe Kremer, Shenyou Zhao, Xinbo Yang, Wenzhu Liu, Dingyong Zhong, Juntao Li, Klaus J. Weber, Kylie R. Catchpole, Stefaan De Wolf, Thomas P. White
- Current status: under submission.
- Contributions: J. P. conceived the idea, designed the overall experiments and led the project. T. P. W. supervised the project. J. P., Y. W., H. S. and T. D. prepared and characterized the perovskite cell devices. X. Z., D. Z. and J. L. performed the XPS/UPS measurements and analysis. H. T. N. performed the steady-state PL and TRPL measurements. H. S. performed the XRD measurements and analysis. M. N. L. performed the SEM and cross-sectional SEM measurements. S. Z. performed the transmission measurements. X. Y. and W. L. conducted the EQE measurements. F. K. performed the TEM measurements. J. P., Y. W., D. J., K. J. W., K. R. C., S. D. W. and T. P. W. contributed to the results analysis and interpretation. J. P. wrote the manuscript. The manuscript was mainly revised by J. P. and T. P. W. All authors contributed to the discussion of the results and revision of the manuscript.

- Declaration signed from a senior author:

A handwritten signature in blue ink, appearing to read "Jun Peng".

All the supporting documents of the four manuscripts are presented in the Appendix of this thesis.

A handwritten signature in black ink, appearing to read "Jun Peng".

Jun Peng

April 2018

Acknowledgements

First of all, I would like to express my deepest gratitude to my supervisor, Assoc. Prof. Thomas White, for his constant guidance, support, and encouragement on my PhD research program, for always contributing his time to share his knowledge and discuss the problems encountered in the experiments, for his motivation, patience and enthusiasm.

I would like to thank my co-supervisor, Prof. Kylie Catchpole and Assoc. Prof. Klaus Weber, for giving me constant support and valuable advice on my PhD research. I would also like to show my gratitude to my co-supervisor Assoc. Prof. Takuya Tsuzuki, for being so generous with his time, knowledge and ideas and for allowing me to carry out my first PhD project (the indium-doped TiO_x project) in his lab.

I would like to thank Assoc. Prof. Stefaan De Wolf for his supports and guidance on my PhD research during my visiting King KAUST Solar Center. I also would like to thank Assoc. Prof. Frédéric Laquai (from KAUST solar center) for his support and valuable advice on my PhD research.

I would like to thank Assoc. Prof. Juntao Li (from Sun Yat-Sen University) for his generous funding support that allows me to carry on the UPS/XPS measurements for my first two PhD projects in Sun Yat-Sen University. I would also like to thank Prof. Dingyong Zhong for his support in UPS/XPS measurements and analysis.

I am grateful to my friends, Dr. Heping Shen, Miss Xiao Fu, Miss Nandi Wu, Mr. Daniel Jacobs, Dr. The Duong, Mr. Yiliang Wu, Dr. Chog Barugkin, Dr. Sachin Surve, Dr. Mark Lockrey, Dr. Felipe Kremer, Dr. Li Li, Dr. Hieu Nguyen, Dr. Hemant Kumar Mulmudi, Mr. Dale Grant and Mr. Shenyou Zhao for their support and help on my research. I also would like to thanks Dr. Yimao Wan, Dr. Jie Cui and Dr. Di Yan for their support and help and for sharing their valuable knowledge on silicon solar cells. In addition, I would like to thank the other people from ANU Solar Center who made the time very enjoyable.

I would like to thank my friends from KAUST Solar Center, Miss Usma Ugur, Dr. Jafar Khan, Dr. Wenzhu Liu, Dr. Xinbo Yang, and Dr. Kai Wang, for their support and help on my research. I also would like to thank my friends from Sun Yat-Sen University, Miss Qiaoling Lin, Dr. Xianzhong Zhou, and Mr. Wang Ye for their support and help.

I would like to thank Dr. Nina De Caritat, Ms Maureen Brauers, Mr. James Cotsel, Mr. Mark Saunders and Mr. Bruce Condon for their constant contribution to keeping the lab safe and running smoothly.

I gratefully acknowledge the University for offering me a full-scholarship that supports me to pursue my PhD degree in Australian National University (ANU). The research was supported by the Australian Research Council (ARC) and Australian Renewable Energy Agency (ARENA). I also thank the ANU Vice-Chancellor's HDR and Australian Nanotechnology Network (ANN) for providing financial assistance for my overseas visiting and conference travel.

Finally, I am deeply grateful to my parents and my family, their support and encouragement allow me to overcome many challenges. Most importantly, I would like to take this opportunity to express my love to my wife Lingling Deng and my son Zhouyi Peng and thank them for their support, encouragement and patience throughout this entire journey.

Abstract

This thesis focuses on developing high-efficiency perovskite solar cells *via* interface engineering; and on understanding the correlation between open-circuit voltage and surface recombination. This work can be divided into four parts: (i) introducing an indium-doped TiO_x electron transport layer; (ii) developing a one-side passivation layer (PMMA:PCBM) to passivate the ETL/perovskite interfaces, where PMMA, PCBM and ETL are poly(methyl methacrylate), phenyl-C61-butyric acid methyl ester and electron transport layer, respectively; (iii) establishing a double-sided passivation design to passivate both ETLs/perovskite and perovskite/HTLs interfaces, where HTL is hole transport layer; (iv) exploiting a set of combination ETLs (ZnO/MgF_2) for substituting the fullerene-based ETLs in inverted perovskite solar cells.

We first show that the extrinsic indium-doping improves both the conductivity of the transport layer and the band alignment at the ETL/perovskite interface compared to pure TiO_2 , boosting the fill-factor and voltage of perovskite cells. Using the optimized transport layers, we demonstrate a high steady-state efficiency of 17.9% for $\text{CH}_3\text{NH}_3\text{PbI}_3$ -based cells and 19.3% for $\text{Cs}_{0.05}(\text{MA}_{0.17}\text{FA}_{0.83})_{0.95}\text{Pb}(\text{I}_{0.83}\text{Br}_{0.17})_3$ -based cells, corresponding to absolute efficiency gains of 4.4% and 1.2% respectively as compared to TiO_2 -based control cells. In addition, we report a steady-state efficiency of 16.6% for a semi-transparent cell and use it to achieve a four-terminal perovskite-silicon tandem cell with a steady-state efficiency of 24.5%.

Second, we demonstrate an ultrathin passivation layer consisting of a PMMA:PCBM mixture that can effectively passivate defects at or near to the perovskite/ TiO_2 interface, significantly suppressing interfacial recombination. The passivation layer increases the open circuit voltage of mixed-cation perovskite cells by as much as 80 mV, with champion cells achieving $V_{oc} \sim 1.18$ V. As a result, we obtain efficient and stable perovskite solar cells with a steady-state PCE of 20.4% and negligible hysteresis over a large range of scan rates. In addition, we show that the passivated cells exhibit very fast current and voltage response times of less than 3 s under cyclic illumination.

Third, we introduce a double-side passivating contact design using ultrathin PMMA films. We demonstrate very high-efficiency ($\sim 20.8\%$) perovskite cells with

some of the highest open circuit voltages (1.22 V) reported for the same 1.6 eV bandgap. Photoluminescence imaging and transient spectroscopic measurements confirm a significant reduction in non-radiative recombination in the passivated cells, consistent with the voltage increase. Analysis of the molecular interactions between perovskite and PMMA reveals that the carbonyl (C=O) groups on the PMMA are responsible for the excellent passivation *via* Lewis-base electronic passivation of Pb^{2+} ions.

At last, we demonstrate a set of effective combination ETLs comprising ZnO (~70 nm)/MgF₂ (~1.5 nm) for the purpose of enhancing the performance of MAPbI₃-based inverted perovskite solar cells. The outstanding work function, conductivity and hole-blocking properties of ZnO nanomaterials along with the extra contribution from the ultrathin insulating MgF₂ layer (diminished the injection barrier of ETLs/Al interfaces, thus reducing the contact resistance), make them ideal for use as excellent ETLs that can replace and outperform the fullerene-based ETLs in inverted perovskite solar cells. Combining the ZnO/MgF₂ ETL with an ultrathin PMMA:PCBM passivation film, a high PCE of 17.5% with a high FF (~0.795) and negligible hysteresis was achieved for the poly(3,4-ethylenedioxythiophene) polystyrene sulfonate (PEDOT:PSS) based inverted perovskite cells.

Contents

Introduction	1
Chapter 1: Perovskite Materials and Perovskite Solar Cells	7
1.1 Perovskite Materials: Property and Application	7
1.2 Perovskite Solar Cells: Device Structure, Working Principle and Deposition Technology.....	9
1.2.1 The Device Structure of Perovskite Solar Cells.....	9
1.2.2 The Working Principle of Perovskite Solar Cells.....	10
1.2.3 The Deposition Technology of Perovskite Solar Cells	11
1.3 Electron Transport Materials for Perovskite Solar Cells	16
1.4 Hole Transport Materials for Perovskite Solar Cells	18
1.5 Defect Passivation for Perovskite Solar Cells.....	19
1.6 High-Efficiency Perovskite Solar Cells: Progress, Design and Challenge	21
1.7 Summary and Outlook	22
Chapter 2: Efficient Indium-Doped TiO_x Electron Transport Layers for High-Performance Perovskite Solar Cells and Perovskite-Silicon Tandems	33
Chapter 3: Interface Passivation Using Ultrathin Polymer-Fullerene Films for High-Efficiency Perovskite Solar Cells with Negligible Hysteresis	45
Chapter 4: A Universal Double-Side Passivation for High Open-Circuit Voltage in Perovskite Solar Cells: Role of Carbonyl Groups in Poly(methyl methacrylate) ...	57
Chapter 5: Inorganic ZnO/MgF₂ Bi-Layers as a High-Performance Alternative to Fullerene-Based Electron Transport Layers in Inverted Perovskite Solar Cells ...	69
Chapter 6: Summary and Future Work	87
6.1 Summary	87
6.1.1 Passivating the Defects/Trap States within TiO ₂ Lattices	87
6.1.2 One-Side Passivation: Passivating the Electron Transport Layer/Perovskite Interfaces	88

6.1.3 Double-Side Passivation: Passivating the Perovskite/Transport Layers Interfaces.....	89
6.1.4 Combination ETLs (ZnO/MgF ₂) for Inverted Perovskite Solar Cells: Substituting the Organic Electron Transport Materials	89
6.2 Future Work	90
6.2.1 Passivating the Perovskite Bulk Defects.....	90
6.2.2 Developing UV-Stable Electron Transport Layers	90
6.2.3 Exploiting Thermal-Stable Hole Transport Layers.....	91
6.2.4 Utilizing Stable Electrodes.....	91
List of Other Publications and Conferences.....	93
Appendix.....	95

Introduction

Thesis Motivation

Energy is a basic requirement for productivity and for life itself. The growth and modernization of the world economy is significantly reliant on the widespread use of fossil energy, such as oil, gas, and coal.^[1-4] All this consumption costs draws on the earth's limited, non-renewable resources. Increased consumption of traditional fossil energy has a direct impact on the earth's environment, causing serious pollution to the atmosphere and water resources, thus resulting in haze, acid rain, greenhouse effect, ozonosphere destruction and similarly catastrophic environmental disasters.^[1-4]

Today, more and more people recognize the growing importance of holistic, coordinated, sustainable development and production. Consequently, there is an urgent demand for green, clean energy. Solar energy (radiant light and heat from the sun) has been regarded as the best solution to substitute the traditional fossil energy.^[2] It is a sustainable energy that can be harnessed using solar heating, solar thermal energy and photovoltaics (PV) technologies.^[5]

Silicon solar cell is a well-developed industrialized PV technology. The silicon PV industry has undergone a blooming growth during the past decades. The cost of the silicon solar cells is now still expensive that makes its price higher than that of fossil energy. It is therefore persuasive to develop new kinds of cost-effective, high-efficiency PV technologies.

Organic/inorganic hybrid perovskite solar cells have attracted tremendous attention and been regarded as one of the most promising candidates for the next generation PV technologies due to their cost-effective advantageous and outstanding optoelectronic properties.^[6,7] Since the first perovskite solar cell reported with a power conversion efficiency (PCE) of ~4.0% in 2009,^[8] much research effort regarding the development of charge transporting materials^[7,9,10] perovskite absorbing materials^[6,11,12] and surface passivation technologies^[7,13] have been reported for perovskite solar cells. To date, the record efficiency of the perovskite solar cells is over 22% (certified),^[11] which is comparable to that of the commercial silicon solar cells,^[14] indicating the great potential for perovskite PV commercialisation.

State-of-the-art perovskite solar cells are based on a sandwich structure of ETLs/Perovskite/HTLs or HTLs/Perovskite/ETLs, where ETLs and HTLs are electron

transport layers and hole transport layers (variously identified as electron and hole selective layers), respectively.^[6,13] For the active layer, the best-performing cells use mixed cation and mixed halide perovskite compositions with a bandgap (E_g) of ~ 1.6 eV.^[6,11] The theoretical (Shockley-Queisser) PCE limit for this bandgap is $>30\%$,^[15] well above the current experimental record.^[6,11]

Despite their significant progress, perovskite ($E_g \sim 1.6$ eV) solar cells still suffer from low open-circuit voltages (V_{oc}) which are well below the theoretical limit ($V_{oc} \sim 1.33$ V).^[15] Defect-induced non-radiative carrier recombination at the perovskite/transport layers interfaces has been identified as a major source of efficiency loss in perovskite solar cells.^[7,16] On a device level, non-radiative recombination via these defects reduces the V_{oc} and overall device performance. Interface recombination has also been linked to current-voltage hysteresis, and may have an impact on long-term stability. It is therefore essential to minimize the sources of recombination in perovskite films and their interfaces to further improve the performance of the perovskite solar cells.

Thesis Outline

This is a thesis by compilation, and the Chapters 2-5 are based on publications.

Chapter 1 briefly introduces the outstanding properties of perovskite materials that enable their application in a variety of optoelectronic devices, especially in photovoltaics. We then summarize the development and progress of perovskite solar cells over the past eight years. Different cell designs, including the various material choices available for the electron and hole transporting layers, are discussed in conjunction with passivation strategies. Finally, we cover the progress, design and future challenges in store for state-of-the-art perovskite solar cells.

In Chapter 2, we demonstrate efficient ETLs for high-performance normal structured perovskite solar cells and tandems based on indium-doped TiO_x electron transport layers. We show that the extrinsic indium ions (with a valency of +3) can effectively passivate/remove the defect or trap state within TiO_2 lattices, thus reducing its sub-bandgap states and raising the conduction band. Therefore, by increasing the cell's built-in voltage and improving the ETL conductivity, indium-doped TiO_x ETLs improve the efficiency of normal structured perovskite cells.

In Chapter 3, we cover the development of one-side passivation technology using ultrathin PMMA:PCBM blend films to address the defect/trap states located at or near to the mesoporous TiO₂/perovskite interfaces, where PMMA and PCBM are poly(methyl methacrylate) and phenyl-C61-butyric acid methyl ester, respectively. We show that the PMMA:PCBM passivation layer can effectively suppress interfacial recombination, thus dramatically boosting the V_{oc} and significantly eliminating current-voltage hysteresis for mixed cations and mixed halides perovskite solar cells.

Chapter 4 presents a two-side passivating contact design using ultrathin PMMA to passivate both the ETL/perovskite and perovskite/HTL interfaces. We demonstrate that the extra PMMA passivation layer between perovskite and the HTL can provide further gains in open-circuit voltage as compared to the one-sided passivation configuration presented in Chapter 3. Detailed analysis of the perovskite-PMMA interactions reveals that the passivation results from the Lewis-base properties of the carbonyl (C=O) group on the PMMA, which can effectively passivate under-coordinated lead atoms (Pb²⁺), which are known to cause non-radiative recombination at perovskite surfaces and grain boundaries. This two-side passivating contact design significantly reduces the surface recombination, thus dramatically boosting the V_{oc} to 1.22 V (theoretical limit, 1.33 V) for ~1.6 eV bandgap perovskite solar cells.

We show in Chapter 5 that the inorganic bi-layer ETLs (ZnO/MgF₂) can serve as efficient ETL in MAPbI₃-based inverted perovskite solar cells. A detailed analysis of ZnO and MgF₂ reveals that the ZnO possesses an outstanding work function, conductivity and hole-blocking property. Meanwhile, the ultrathin insulating MgF₂ layer reduces the aluminum contact resistance and diminishes the injection barrier at the ETL/Al interface. Together these properties make ZnO/MgF₂ bi-layers ideal for use as excellent ETLs, which can substitute for the conventional PCBM and related fullerene derivatives in inverted perovskite solar cells.

Finally, Chapter 6 summarizes the highlights of the main works in this thesis. A research plan is proposed to further enhance the efficiency and stability of perovskite solar cells.

References

- [1] C. Le Quéré, R. J. Andres, T. Boden, T. Conway, R. A. Houghton, J. I. House, *et al.*, "The global carbon budget 1959–2011," *Earth System Science Data Discussions*, vol. 5, pp. 1107-1157, 2012.
- [2] J. L. Sawin, F. Sverrisson, K. Seyboth, R. Adib, H. E. Murdock, C. Lins, *et al.*, "Renewables 2017 Global Status Report," 2013.
- [3] M. Ha-Duong, "Climate change 2014-Mitigation of climate change," 2015.
- [4] T. J. Crowley, "Causes of climate change over the past 1000 years," *Science*, vol. 289, pp. 270-277, 2000.
- [5] https://en.wikipedia.org/wiki/Solar_energy.
- [6] M. Saliba, T. Matsui, K. Domanski, J.-Y. Seo, A. Ummadisingu, S. M. Zakeeruddin, *et al.*, "Incorporation of rubidium cations into perovskite solar cells improves photovoltaic performance," *Science*, vol. 354, pp. 206-209, 2016.
- [7] H. Tan, A. Jain, O. Voznyy, X. Lan, F. P. G. de Arquer, J. Z. Fan, *et al.*, "Efficient and stable solution-processed planar perovskite solar cells via contact passivation," *Science*, vol. 355, pp. 722-726, 2017.
- [8] A. Kojima, K. Teshima, Y. Shirai, and T. Miyasaka, "Organometal Halide Perovskites as Visible-Light Sensitizers for Photovoltaic Cells," *Journal of the American Chemical Society*, vol. 131, pp. 6050-6051, 2009.
- [9] Z. Yu and L. C. Sun, "Recent Progress on Hole-Transporting Materials for Emerging Organometal Halide Perovskite Solar Cells," *Advanced Energy Materials*, vol. 5, pp. 1500213, 2015.
- [10] H. Zhou, Q. Chen, G. Li, S. Luo, T.-b. Song, H.-S. Duan, *et al.*, "Interface engineering of highly efficient perovskite solar cells," *Science*, vol. 345, pp. 542-546, 2014.
- [11] W. S. Yang, B.-W. Park, E. H. Jung, N. J. Jeon, Y. C. Kim, D. U. Lee, *et al.*, "Iodide management in formamidinium-lead-halide-based perovskite layers for efficient solar cells," *Science*, vol. 356, pp. 1376-1379, 2017.
- [12] M. Saliba, T. Matsui, J.-Y. Seo, K. Domanski, J.-P. Correa-Baena, M. K. Nazeeruddin, *et al.*, "Cesium-containing triple cation perovskite solar cells: improved stability, reproducibility and high efficiency," *Energy & Environmental Science*, vol. 9, pp. 1989-1997, 2016.
- [13] F. Giordano, A. Abate, J. P. Correa Baena, M. Saliba, T. Matsui, S. H. Im, *et al.*, "Enhanced electronic properties in mesoporous TiO₂ via lithium doping for

high-efficiency perovskite solar cells," *Nature Communication*, vol. 7, pp. 10379, 2016.

- [14] <https://www.nrel.gov/pv/assets/images/efficiency-chart.png>. (Accessed on 16/04/2018)
- [15] W. Tress, "Perovskite Solar Cells on the Way to Their Radiative Efficiency Limit—Insights Into a Success Story of High Open-Circuit Voltage and Low Recombination," *Advanced Energy Materials*, vol. 7, pp. 1602358, 2017.
- [16] S. D. Stranks, "Nonradiative losses in metal halide perovskites," *ACS Energy Letters*, vol. 2, pp. 1515-1525, 2017.

Chapter 1: Perovskite Materials and Perovskite Solar Cells

Since the first perovskite solar cell (efficiency~4.0%) was reported in 2009,^[1] perovskite solar cells have rapidly risen to the forefront of emerging photovoltaic technologies.^[2-15] To date, the champion efficiency of the perovskite solar cells is 22.7% (certified),^[16] rivalling commercial silicon solar cells, indicating its great potential for commercialization.^[16]

In this chapter, we first provide an overview of perovskite materials, and briefly introduce the enabling physico-chemical properties of perovskites and their applications. Then, we discuss the device structure, working principles and deposition technologies relevant to the current generation of perovskite solar cells. Furthermore, we review the development of electron and hole transport materials as well as defect passivation technology used in the state-of-the-art perovskite solar cells of the past eight years. Subsequently, we discuss the progress, design and future challenges of high-efficiency perovskite solar cells. A summary and outlook is provided at the chapter's close.

1.1 Perovskite Materials: Property and Application

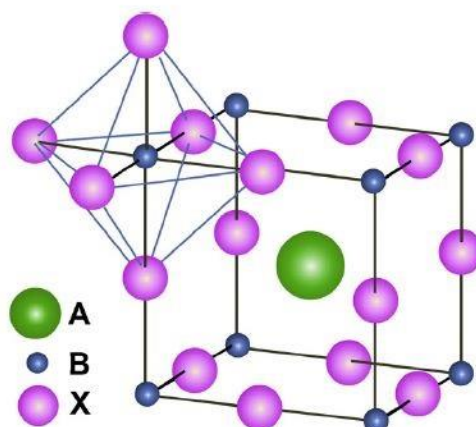


Figure 1.1 The schematic diagram of perovskite crystal structure ABX_3 , where A is monovalent cation, B is a divalent metal cation and X is an anion. Adapted from Ref [18].

Perovskite generally refers to a class of crystal materials with chemical formula ABX_3 , where A is a monovalent cation, B is a divalent metal cation and X is an anion (see **Figure 1.1**). Technically speaking, to maintain high symmetry cubic structure, the Goldschmidt tolerance factor t (defined by the equation: $t = (R_A + R_X)/\{\sqrt{2}(R_B + R_X)\}$) should be close to 1, where R_A , R_B and R_X represent the ionic radii of A, B and X, respectively.^[17] It is noted that for the ideal symmetry cubic structure, the ionic radii of A should be much larger than that of B.^[17]

It is known that perovskite structured materials are widespread in nature as naturally-occurring minerals. There are two dominant kinds of perovskite materials: oxide perovskites and halide perovskites. Oxide perovskites have been extensively investigated over the past century, due to their sought-after physical properties such as magneto-resistance, ferroelectricity and superconductivity.^[19] Recently, halide perovskites, $CH_3NH_3PbX_3$ (X= Cl, Br, I) being the prime example, have drawn substantial attention and interest in the fields of material and photovoltaic research.^[1]

Organic/inorganic hybrid perovskite are characterized by the inclusion of organic components (such as CH_3NH_3 (methylammonium or MA), $NH_2(CH)NH_2$ (formamidinium or FA)) into the halide perovskite structure.^[3,4,7,20] The organic molecular functional groups are connected with the inorganic framework through hydrogen bonds, forming long-range ordered crystals with alternating organic and inorganic components. In the organic/inorganic hybrid perovskite, the organic composition and inorganic framework have a strict stoichiometric ratio, making it a real molecular composite material. In particular, the superior properties (such as structural variability, mechanical plasticity, large polarity and processability) of the organic components in organic-inorganic hybrid perovskite can enable its large area production.^[21-23]

Numerous perovskite compositions have been developed for organic/inorganic hybrid perovskite solar cells.^[3,4,7,24-28] $MAPbI_3$ was the first material to kickstart perovskite photovoltaics, and is still widely used as an absorber in perovskite cells due to its outstanding optoelectronic property and controllable, easy deposition processing.^[2] However, it suffers from quite poor stability.^[26] Fortunately, FA can be used as an effective cation to replace the MA or incorporate with MA to respectively form $FAPbI_3$ or $FAMAPbI_3$, strengthening the stability of the perovskite materials.^[26] In addition, Cl, Br anions have also been proven to be good options to form mixed cations (FA^+ , MA^+) and mixed halides (Cl^- , I^- , Br^-) perovskite absorbers, furthering the stability of the organic/inorganic hybrid perovskite solar cells.^[29-31] Alternatively, The incorporation of

Cs^+ ,^[4] Rb^+ ^[8] and the like alkyl cations^[32] can effectively control the quality of the triple cations, quadruple cations or multiple cations (more than 5 cations) perovskite films, significantly boosting the overall device performance of the perovskite solar cells. Other kinds of metal elements (such as In ,^[33] Sn ^[34] and the like^[35-39]) doping have been reported to enhance the performance of their perovskite cells as well.

In addition to the above-mentioned multi-crystal perovskite materials, 2D,^[40] 2D/3D hybrid perovskite materials^[41] and inorganic halide perovskite^[42-44] have also been demonstrated to further improve the device performance in perovskite devices.

The outstanding optoelectronic properties of the halide perovskite, such as tuneable bandgap, low exciton binding energy, high charge mobility, high extinction coefficient and long carrier diffusion lengths are important factors explaining perovskite solar cells' rapid rise to the forefront of thin-film photovoltaics.^[1,4,8,45-47]

1.2 Perovskite Solar Cells: Device Structure, Working Principle and Deposition Technology

1.2.1 The Device Structure of Perovskite Solar Cells

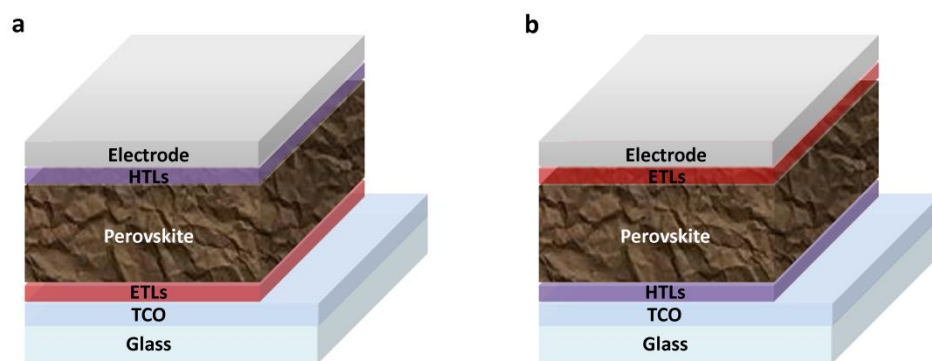


Figure 1.2 (a) The schematic diagram of the normal structured (n-i-p) perovskite solar cells. (b) The schematic diagram of the inverted (p-i-n) perovskite solar cells.

There are two kinds of device structure for the perovskite solar cells: normal structured (n-i-p) perovskite solar cells and inverted (p-i-n) perovskite solar cells as shown in **Figure 1.2**. Generally, transparent conducting oxides (TCOs) such as fluorine-doped tin oxide (FTO) and indium-doped tin oxide (ITO) are used as transparent

conducting substrates; while metals (gold, silver and aluminium) are used as top electrodes deposited by evaporation or sputtering.

For normal structured perovskite solar cells (see **Figure 1.2a**), the device structure is Glass/TCO/ETL/Perovskite/HTL/Electrode. A further division can be made into mesoporous and planar structured perovskite solar cells as seen in **Figure 1.3**. The biggest difference between mesoporous and planar perovskite solar cells is that mesoporous metal oxide (such as TiO_2 ,^[8,22] Al_2O_3 ^[48]) scaffolds facilitate the extraction of electrons from the perovskite, and can improve film quality by reducing pinhole formation. The normal structured, mesoporous perovskite solar cells using mixed cation perovskite have been demonstrated with a champion efficiency of over 22% (certified).^[7] In addition to the normal structured perovskite solar cells, inverted perovskite solar cells also have been developed, where the device configuration is of Glass/TCO/HTL/Perovskite/ETL/Electrode (see **Figure 1.2b**). To date, the record certified efficiency of the inverted perovskite solar cells is close to 21 %, ^[12] which is comparable to that of the normal structured perovskite solar cells.^[7]

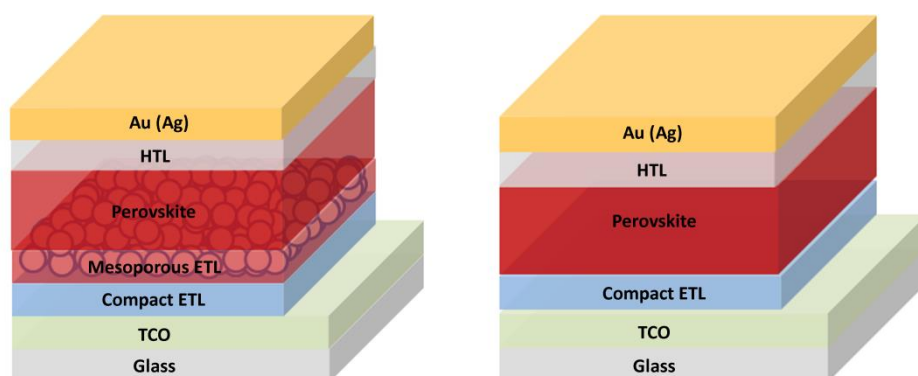


Figure 1.3 The schematic diagram of the mesoporous structured normal perovskite solar cells (left image); and the planar structured normal perovskite solar cells (right image).

1.2.2 The Working Principle of Perovskite Solar Cells

As depicted in **Figure 1.4a**, TiO_2 and 2,2',7,7'-tetrakis(N,N-di-p-methoxyphenylamine)-9,9'-spirobifluorene (Spiro-OMeTAD) are commonly employed as ETLs and HTLs respectively in normal structured (n-i-p) perovskite solar cells. In an ideal model, the vacuum energy levels of different layers in the n-i-p perovskite solar cell are illustrated in **Figure 1.4b**, assuming the perovskite is intrinsic. When the perovskite solar cell is under illumination, the quasi Fermi-levels of carriers in the

perovskite will be split and will be correspondingly relocated according to the Fermi-level of the TiO_2 and Spiro-OMeTAD. The achievable open-circuit voltage under illumination is therefore largely decided by the difference between the ETL and HTL work functions (the built-in voltage).

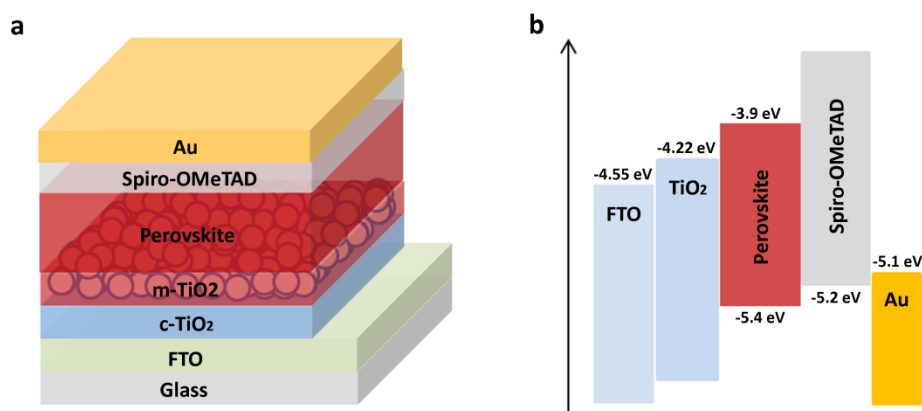


Figure 1.4 (a) The schematic diagram of the mesoporous structured normal perovskite solar cells (Glass/FTO/c- TiO_2 /m- TiO_2 /Perovskite/Spiro-OMeTAD/Au). (b) Diagram showing the energy levels of different materials.

Under working conditions, the photo-generated electrons and holes within perovskite active layers will drift and diffuse towards to the selective contacts. These principles apply similarly to both normal structure and inverted cells.

1.2.3 The Deposition Technology of Perovskite Solar Cells

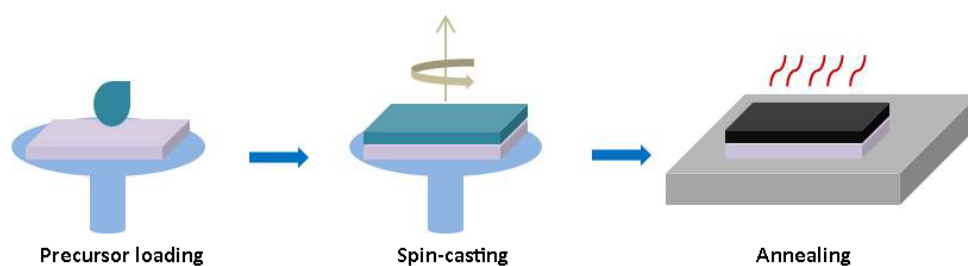


Figure 1.5 The Schematic illustration of the one-step solution processed deposition technology.

Following the pioneering perovskite solar cells established by Miyasaka in 2009,^[1] substantial research effort has dramatically boosted the PCE of perovskite solar cells from ~4.0% to 22.7% (certified).^[16] In addition to high quality electron and hole transport layers (discussed in the following two sections **1.3** and **1.4**), the other key parameter is to have a good crystallinity and uniformity of the perovskite film.

Numerous efforts regarding the deposition technologies of perovskite active layers have been systematically investigated for the enhanced performance perovskite solar cells over the past eight years.

For solution-processed perovskite solar cells, the very first fabrication technology to be developed was the one-step deposition method.^[31,49,50] In this process, as shown in **Figure 1.5**, the pre-prepared perovskite precursor solution will be loaded on the top of TCO substrate, where the TCO substrate is seated on the spinner. The pre-programmed spinner is then initiated to cast the perovskite precursor thin film. This sample is subsequently annealed on a hot-plate (set temperature~100 °C) to improve the film crystallinity. Although straightforward, it has proven difficult to obtain homogeneous, pinhole-free perovskite films using the one-step spin-coating method, which explains the relatively low performance of perovskite solar cells at the very earliest stage development.

To improve on the shortcomings of the one step method, two-step deposition was developed and led to improved film quality.^[51] As demonstrated in **Figure 1.6**, the steps in the two-step method are: (1) spin-casting the pure PbI_2 precursor film on the TCO substrate; (2) annealing the PbI_2 sample at 100 °C for 30 ~ 60 min; (3) spin coating the MAI solution on the top of PbI_2 sample or dip coating the PbI_2 sample into MAI solution; (4) annealing the perovskite sample again.

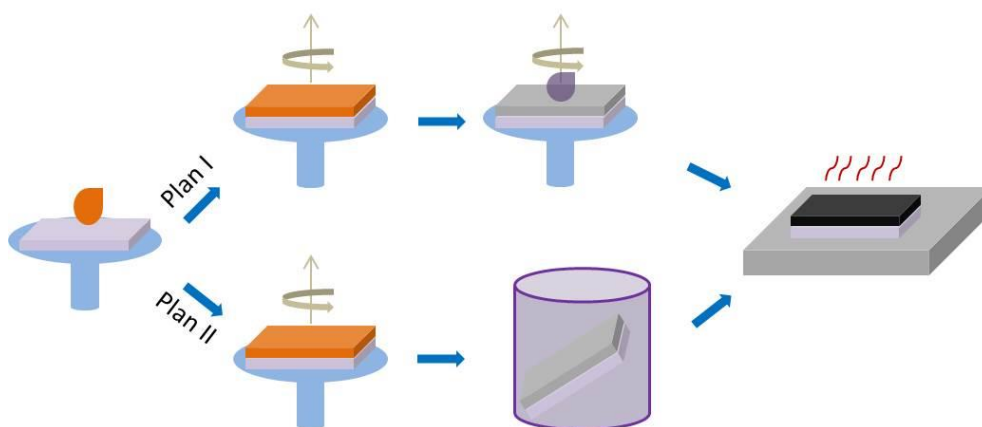


Figure 1.6 The Schematic diagram of the two-step solution processed deposition technology.

A modified two-step (also called three-step) deposition^[52] was further developed to improve the coverage of the perovskite film and eliminate pinholes. Details of the deposition procedures are shown in **Figure 1.7a**. It is evident that the quality of the perovskite film prepared by the modified two-step deposition is much better than the perovskite film fabricated by the two-step deposition (see **Figures 1.7b** and **1.7c**).

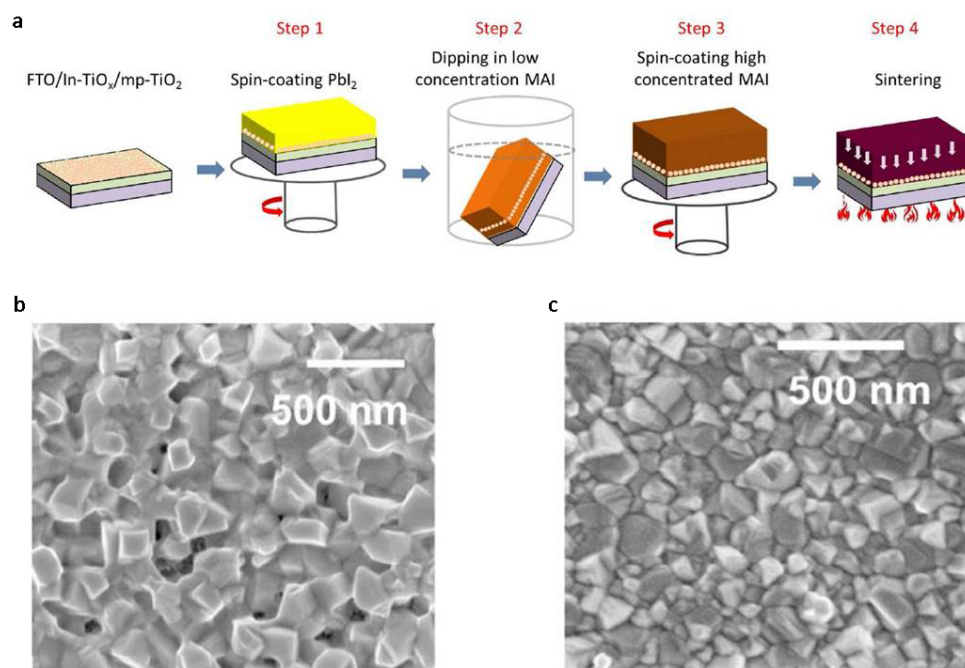


Figure 1.7 (a) The schematic diagram of the modified two-step solution process deposition technology. (b) Surface morphology SEM of the perovskite fabricated by the two-step deposition technology. (c) Surface morphology SEM of the perovskite fabricated by the modified two-step deposition technology. Adapted from our previous work Ref [52].

However, based on the one-step, two-step and modified two-step deposition technologies, we found that it is still a challenge to control the growth of the perovskite crystals. To further improve the crystallization of the perovskite films, Xiao *et al.*^[53] proposed a fast deposition crystallization technology (also named anti-solvent deposition technology). The schematic illustration of the procedures of the anti-solvent deposition is provided in **Figure 1.8**. As shown in **Figures 1.8a to 1.8f**, it demonstrates that the anti-solvent deposition technology significantly improved the crystallinity and uniformity of the perovskite film.

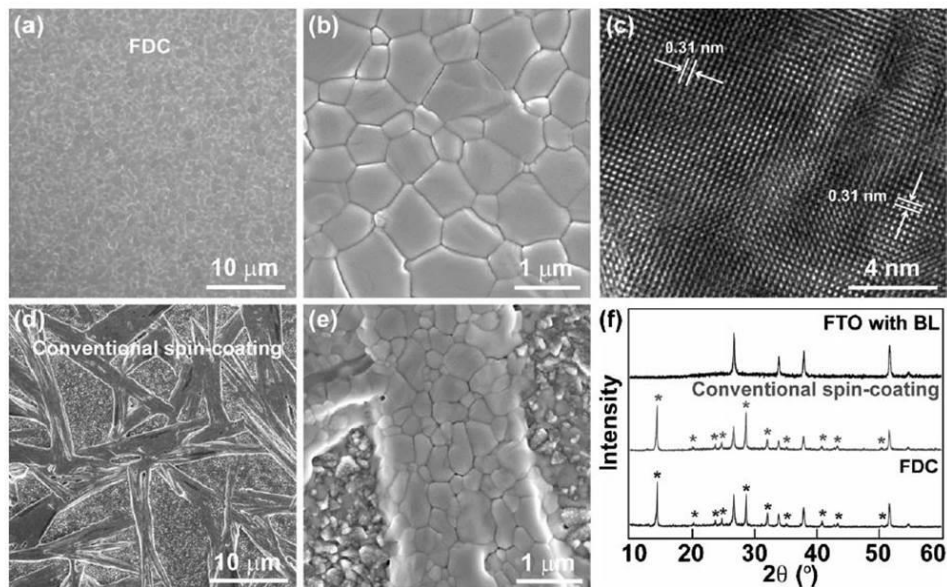
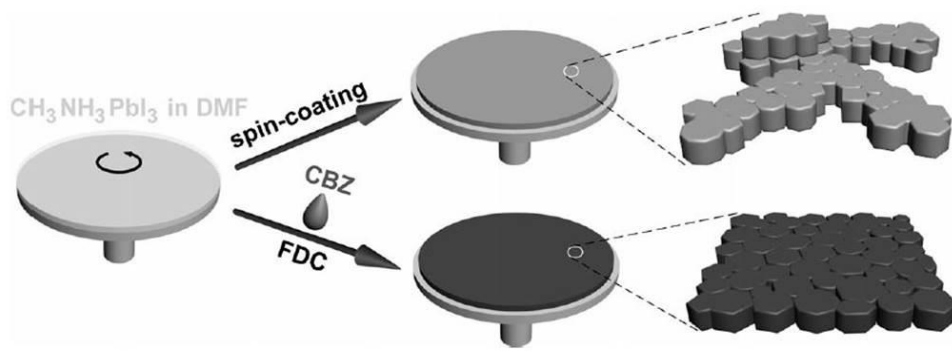


Figure 1.8 The schematic illustration of the anti-solvent solution process (also called fast deposition-crystallization, FDC) deposition technology (top panel). In the bottom panel, (a) and (b) Low- and high-resolution surface SEM images of the MAPbI_3 deposited by FDC with the anti-solvent of chlorobenzene. (c) TEM image of a MAPbI_3 grain from the film deposited by FDC with the anti-solvent of chlorobenzene. (d) and (e) Low- and high-resolution surface SEM images of the MAPbI_3 deposited by conventional one-step deposition technology. (f) XRD patterns of the films prepared by FDC and one-step deposition technologies. Adapted from Ref [53].

In addition to the anti-solvent deposition technology, vacuum-flash assisted deposition technology^[22] has also been demonstrated for improving/controlling the crystallization and uniformity of the solution-processed perovskite films (see **Figure 1.9**).

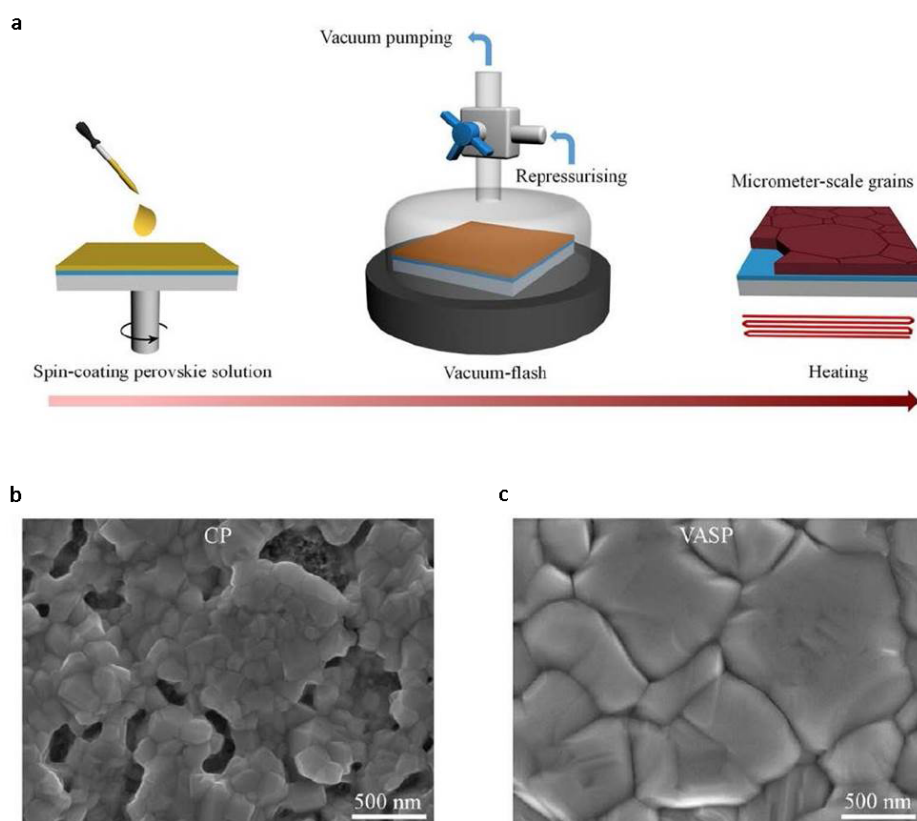


Figure 1.9 (a) The schematic diagram of vacuum-flash assisted deposition technology (top panel). (b) Surface morphology SEM image of the perovskite film deposition by the conventional process (CP). (c) Surface morphology SEM image of the perovskite film deposition by the vacuum-assisted solution process (VASP). Adapted from Ref [22].

According to the literature to date, most high-efficiency perovskite solar cells have been reported with an active area less than 0.2 cm^2 . Although obtaining larger areas would be desirable for demonstrating commercial viability, the above-mentioned deposition technologies are not ideal options to achieve high-quality, large-area perovskite films. To scale up the perovskite film area, one of the most promising deposition technologies is thermal evaporation. The setup of the thermal evaporation is illustrated in **Figure 1.10a**. Liu *et al.*^[54] demonstrated that the coverage and uniformity of the perovskite film prepared by thermal deposition is much better than the perovskite film fabricated by the one-step solution processed deposition technology (see **Figures 1.10b** to **1.10d**), indicating the thermal evaporation technology could satisfy the technical requirements of large-scale perovskite production. Alternatively, vapour-assisted deposition might be another plausible option for fabricating the large-area perovskite thin films.^[55]

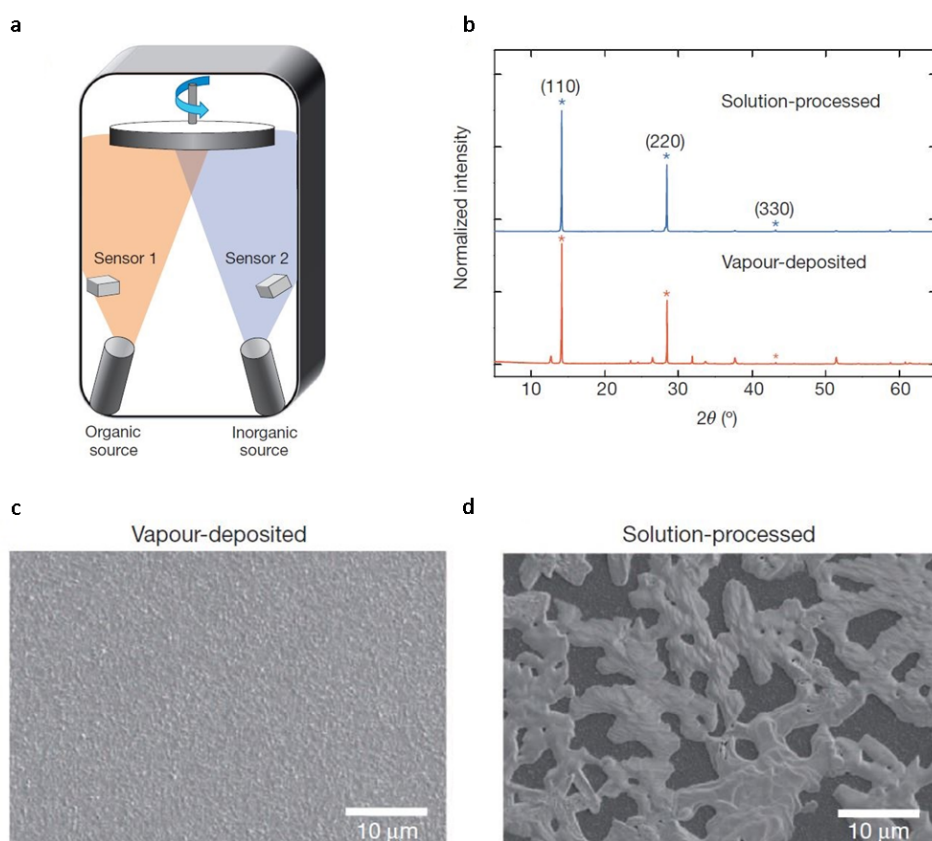


Figure 1.10 (a) The schematic illustration of thermal evaporation deposition technology. (b) XRD patterns of the films prepared by thermal evaporation and one-step solution process deposition technologies (c) Surface morphology SEM image of the perovskite film deposition by the thermal evaporation technology.(d) Surface morphology SEM image of the perovskite film prepared by the one-step solution deposition technology. Adapted from Ref [54].

1.3 Electron Transport Materials for Perovskite Solar Cells

In addition to a high-quality, pinhole-free perovskite absorber, charge transport layers also play critical roles in achieving high-efficiency perovskite solar cells.^[2,56,57] High-temperature sintered titanium dioxide (*ht*-TiO₂) has been widely used as an ETL in perovskite solar cells due to its good chemical resistance, high bandgap, suitable work function and good conductivity.^[8] Most perovskite solar cells based on *ht*-TiO₂ ETLs typically produce a decent short-circuit current density (J_{sc}), but suffer from a low V_{oc} and a poor fill factor (FF), thus limiting their efficiencies.^[2,57,58] In addition, most of them exhibited some current-voltage (J - V) hysteresis.^[9,59]

However, it is challenge to maintain the strict stoichiometry of Ti to O (1:2) for *ht*-TiO₂, causing some defects/traps such as Ti interstitials, non-stoichiometry oxygen or

oxygen vacancies) within TiO_2 lattices.^[57,60] Indeed, some non-stoichiometry is essential for obtaining the n-type property of TiO_2 (often designated as TiO_x). However, defects at the perovskite/ TiO_2 interface may act as recombination centers, whereas traps can reduce the conductivity of the bulk material, thus impacting the performance of finished cells.^[57,60]

To overcome the drawback of the *ht*- TiO_2 , low-temperature TiO_x (*lt*- TiO_2)^[58] nanomaterials were developed as alternatives. It demonstrated that with a small amount of TiAcAc additives, the *lt*- TiO_2 films exhibited much lower sub-bandgap states than the *ht*- TiO_2 films, resulting in the increased conductivity of the *lt*- TiO_2 films. The use of *lt*- TiO_2 ETLs hence resulted in improved FF and efficiency for perovskite cells as compared to the *ht*- TiO_2 ETLs.

Moreover, doped TiO_x were also demonstrated as efficient ETLs to further the efficiency of perovskite solar cells.^[2,23,57,61] For example, Zhou *et al.*, in Yttrium-doped TiO_2 (Y- TiO_2) study, demonstrated that the Yttrium dopants can effectively tailor the work function of the TiO_2 ,^[2] providing a better energy level alignment between Y- TiO_2 and perovskite (indicating the realization of a higher V_{oc} in perovskite cells). Additionally, the improved conductivity of Y- TiO_2 allows for balancing the carrier transport, leading to the reduction of the non-ideal space charge distribution. Thus, the use of the Y- TiO_2 ETLs in MAPbI_3 -based perovskite solar cells yielded a high PCE of 19.3% with a high V_{oc} of 1.13 V and a FF of 0.75.

Another example is lithium-doped TiO_2 (Li- TiO_2),^[57] Giordano *et al.* reported that the incorporation of lithium doping can remove the electronic defects/traps originated from the oxygen vacancies, thus reducing the concentration of the sub-bandgap states within the TiO_2 lattice. As a result, a high PCE of over 19% with negligible *J-V* hysteresis behavior using Li-doped meso- TiO_2 as an efficient scaffold was achieved for their champion MAPbI_3 -based perovskite solar cells.

The third option is to exploit alternative n-type materials, such as SnO_2 ,^[6,62-64] ZnO ,^[65-67] ZnSnO_4 ^[68] and C_{60} .^[56] For example, Jiang *et al.*^[6] demonstrated that the SnO_2 nanomaterials with a deep conduction band and a high electron mobility enables the enhancement of charge transfer from perovskite to electron transport layers, thus reducing charge accumulation at the interface. Consequently, an enhanced efficiency of ~20.5% was reported for their $(\text{FAPbI}_3)_{0.97}(\text{MAPbBr}_3)_{0.03}$ -based perovskite solar cells.

Besides, more complex bilayer-structure ETLs consisting of metal oxides and organic materials such as TiO_x/PCBM ,^[69] $\text{SnO}_2/\text{C}_{60}$ ^[64] and the like^[70,71] have also been developed. Many of these bilayer-structure ETLs have been shown to increase either the

FF or V_{oc} of perovskite solar cells through improved conductivity or improved band alignment respectively.

Hence, further improvement in the overall device performance for perovskite solar cells can be gained by tailoring the work function and conductivity of the ETLs as well as minimizing the density of defects or traps within the electron transport materials.

1.4 Hole Transport Materials for Perovskite Solar Cells

Spiro-OMeTAD^[8,10] and PTAA^[26,72] are widely used as HTLs in the state-of-the-art perovskite solar cells due to their outstanding conductivity and suitable work function properties, where PTAA stand for poly(triaryl amine). In general, these two hole transport materials need Li-TFSI doping-assisted oxidation to enhance their conductivity, where Li-TFSI is bis(trifluoromethane)sulfonimide lithium salt.^[8,72]

One big disadvantage of Spiro-OMeTAD and PTAA is that the lithium doping (from Li-TFSI) can easily diffuse into the perovskite layer and act as defects/traps, ruining the performance and stability of the perovskite solar cells during the long-term operation.^[73]

Dopant-free organic HTLs were developed to substitute the Spiro-OMeTAD and PTAA.^[74-76] For example, Rakstys *et al.*^[74] reported that the highly ordered characteristic face-on organization of the star-shaped D- π -A type **KR321** for use as efficient dopant-free HTLs in perovskite solar cells, yielding an equivalent device efficiency as compared to cells with Spiro-OMeTAD. Among those organic HTLs reported, **RCP**^[75] and **DORDTS-TFBT**^[76] were also proven for use as effective HTLs.

Inorganic HTLs such as NiO_x,^[77] Ta-WO_x,^[46] and CuSCN^[73] were also investigated to further enhance the stability of the perovskite cells. Yi *et al.*,^[46] in 2017, reported the combination of inorganic material Ta-WO_x and conjugated polymer **PDCBT** for use as efficient HTLs in improved efficiency perovskite solar cells. They showed that the insertion of Ta-WO_x formed quasi-ohmic contacts to **PDCBT**, bridging the Schottky-type barrier contact between **PDCBT** and Au. With the improved Ta-WO_x doped HTLs interface, they obtained a very high efficiency of 21.2%. In addition, an enhanced stability (T_{95} ~1000 hours) was also demonstrated for their champion perovskite device.

Further improvement in the thermal stability of perovskite solar cells was also reported by Arora *et al* in 2017.^[73] Inorganic CuSCN was employed as a HTL, which was demonstrated to have an outstanding conductivity of $\sim 1.2 \times 10^{-3} \text{ cm}^2 \text{ v}^{-1} \text{ s}^{-1}$,

promoting the efficient transportation of the electrons to the external circuit. Benefiting from the excellent physico-chemical property of the CuSCN and reduced graphene oxide, their champion device exhibited a stabilized efficiency of 20.5% and retained >95% of its initial efficiency after aging at a maximum power point for 1000 hours at 60 °C.

Although numerous efforts regarding the hole transport materials' design have yielded promising results, there still remains a large space for furthering the efficiency and thermal stability (85 °C standard test) of perovskite solar cells by engineering dedicated hole transport materials.

1.5 Defect Passivation for Perovskite Solar Cells

Defects-induced non-radiative recombination within the perovskite devices has been identified as a major source of efficiency loss, and it may also impact long-term stability.^[78,79] The extent of non-radiative recombination has also been shown to contribute to the degree of J - V hysteresis in perovskite cells.^[6,8,10,57,69,78-88]

J - V Hysteresis is a very common issue in perovskite solar cells.^[78-88] It normally occurs between forward scan and reverse scan when the perovskite cells are tested under different scan rates, while the cells also have slow V_{oc} and J_{sc} transient behaviour.^[80-84] A plausible origin of the J - V hysteresis is through a combination of mobile ions and defect-induced interface recombination.^[80-84] It is therefore critical to passivate/remove the defects/traps to further improve both the overall device performance and reduce hysteresis.^[10,79]

According to the literature, there are four main approaches for reducing the impact of defects-induced non-radiative recombination in perovskite solar cells, outlined below.

The first is to reduce the host materials' defect density by adding dopants. For example, Giordano *et al.*^[57] demonstrated that Li-doping induced a partial reduction of Ti^{+4} to Ti^{+3} can effectively passivate the defects/traps in titania, reducing the density of sub bandgap states within the TiO_2 lattice, thus resulting in the increased V_{oc} from 1.04 V to 1.14 V. Subsequently, Saliba *et al.* reported a perovskite solar cell with a stabilized PCE of 21.6% and an impressive V_{oc} of 1.18 V by incorporating the Li-doped *meso*- TiO_2 scaffold and Rb-containing perovskite.^[8] In addition, inclusion of a small amount of extrinsic dopant with valency +3 (Al-doped TiO_2 ^[60]) was also reported as an efficient way to passivate the traps within TiO_2 lattice.

The second approach is to use alternative transport layer materials that have lower defect densities and/or form better quality interfaces to perovskite.^[6,81] For example, Jiang *et al.*^[6] demonstrated that the deep conduction band and high electron mobility of SnO₂ enables the enhancement of charge transfer from perovskite to electron transport layers, reduces charge accumulation at the interface, and thus achieves an enhanced efficiency of 20.5% with negligible hysteresis. Correa Baena *et al.*^[81] showed that reducing the doping concentration of the Spiro-OMeTAD can suppress interfacial recombination, producing a stabilized PCE of approx. 20% with V_{oc} =1.17 V.

The third approach to reduce interfacial recombination is to introduce a very thin passivation layer between the perovskite and transport layers.^[10,69,82-84] For example, Zhang *et al.*^[82] showed that a very thin fullerene derivative (α -bis-PCBM) layer between the perovskite and the Spiro-OMeTAD HTL can passivate defects located at the perovskite/HTL interface, yielding a PCE of 20.8%, and V_{oc} = 1.13 V. Similarly, Koushik *et al.*^[83] and Wang *et al.*^[84] used ultrathin layers of Al₂O₃ and PMMA respectively to passivate the perovskite/Spiro-OMeTAD interface, resulting in improved V_{oc} (1.08V and 1.06V respectively) and reduced hysteresis. Tao *et al.*^[69] introduced the PCBM to passivate the TiO_x/perovskite interfaces and achieved a stabilized efficiency of 17.6% perovskite cell. Recently, Tan *et al.*^[10] reported that chlorine-capped TiO₂ colloidal nanocrystal ETLs can mitigate interfacial recombination and improve interface binding, resulting in a high V_{oc} of 1.189 V, a certified PCE of 20.1%, and negligible hysteresis.

The fourth approach is to passivate the perovskite crystal grain boundaries and bulk materials.^[85-88] For example, Chiang *et al.*^[85] reported that the incorporation of the PCBM into the PCBM-perovskite blend films can improve the quality of the perovskite film as well as effectively passivate the perovskite crystal grain boundaries, thus resulting in an enhanced efficiency with high fill factor of 0.82. Similarly, Li *et al.*^[86] demonstrated that the alkylphosphonic acid ω -ammonium chlorides additives can effectively passivate the perovskite surface defects, through strong hydrogen bonding of the -PO(OH)₂ and -NH₃⁺ terminal groups to the perovskite surface, thus improving the perovskite solar cells performance. Other passivation materials such as thiophene/pyridine,^[87] and polystyrene^[88] also demonstrated the capability of passivating the localized defects/traps at perovskite/transport layers interfaces, and also in perovskite films.

While these examples show that reducing interface recombination is essential for improving V_{oc} and cell efficiency, most perovskite solar cells reported so far still suffer

from low V_{oc} (less than 1.20 V), well below the theoretical limit (1.33 V).^[78] Hence, there is a clear need to develop new interface passivation approaches to realize the full potential of perovskite photovoltaics.

1.6 High-Efficiency Perovskite Solar Cells: Progress, Design and Challenge

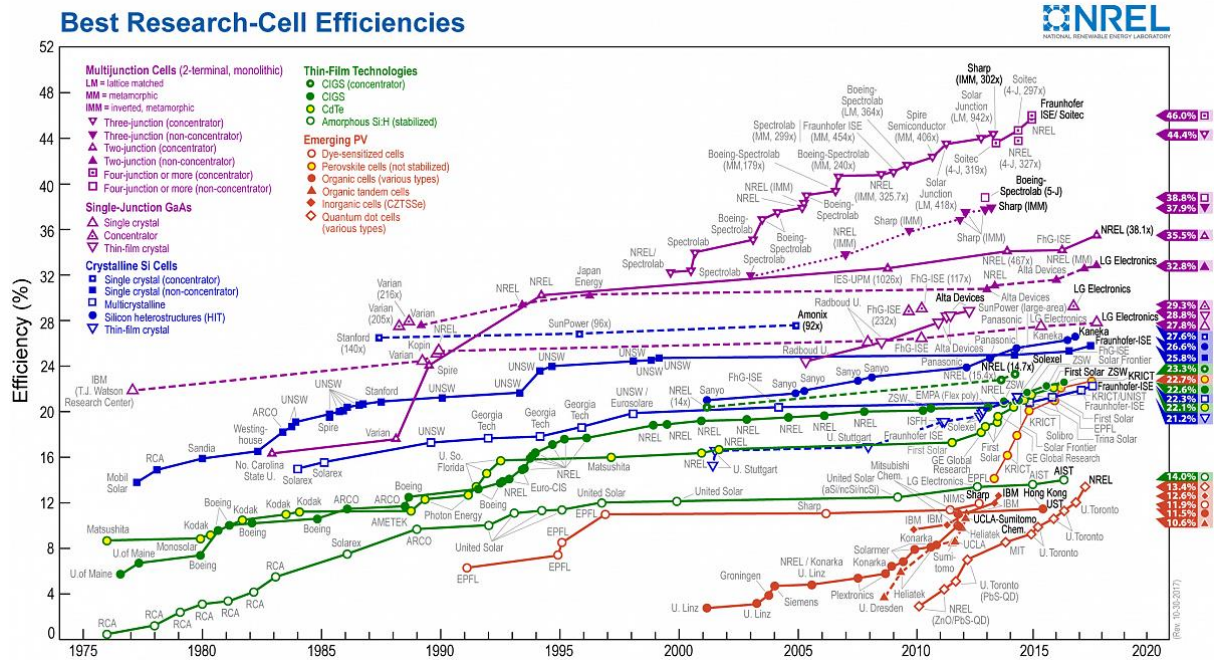


Figure 1.11 The historic progress of the efficiencies of different PV technologies. Adapted from Ref [16].

Since the first perovskite solar cell reported in 2009, tremendous research efforts regarding perovskite composition, electron- and hole transport materials design as well as the passivation technologies design have been made, with impressive results.^[3,10,46,57,73] Improvements in each of these research areas have led to the current PCE record of 22.7% (certified).^[16] Moreover, the stability of perovskite solar cells is also increasing, with reports of cells maintaining high-efficiency (>20%) under prolonged (~1000 hours) one-sun illumination and at elevated operating temperatures (60 °C).^[73] This rapid progress is encouraging for the future commercialization of perovskite PV technology. The historic progress of the efficiencies for perovskite solar cells is presented in **Figure 1.11**.^[16] It is astonishing that the perovskite PV technology only took 8 years to achieve the milestone of over 22% efficiency, rivalling commercial silicon solar cells.^[16]

To further boost the efficiency and stability of perovskite solar cells, future works are required to address the following four aspects:

- 1) Developing UV-stable, thermal-stable charge transport layers with high carrier mobility, good charge blocking property and suitable work function.
- 2) Developing defect-less, stable perovskite absorbers.
- 3) Exploiting new passivation materials to passivate the defects/traps in perovskite film and perovskite/transport layers interfaces.
- 4) Utilizing stable electrodes.

1.7 Summary and Outlook

In this chapter, we briefly introduced the properties and applications of perovskite materials. We then reviewed and discussed the development of the electron- and hole transport materials, as well as the development of the defect passivation technologies for high-efficiency perovskite solar cells.

To date, the current record efficiency of perovskite ($E_g \sim 1.6$ eV) solar cells is 22.7% (certified), but still well below the theoretical (Shockley-Queisser) power conversion efficiency limit ($>30\%$). In addition, the challenges of scale-up and stability will be the biggest obstacles to meet the requirements of commercialization. Much more future effort is demanded for furthering the overall performance of the perovskite solar cells.

This thesis mainly focuses on developing novel ETLs with tailored work function and excellent electron-selective (hole-blocking) property to improve the performance of perovskite solar cells; and on exploiting new passivation materials to passivate the defects/traps located at or near perovskite/transport layers interfaces to boost the perovskite cells' efficiency as well as to mitigate the J - V hysteresis behaviour.

In the following four chapters, we will sequentially discuss the indium-doped TiO_x ETLs; one-side passivation (passivate the ETLs/perovskite interfaces); two-side passivation (passivate both the ETLs/perovskite and perovskite/HTLs interfaces); and alternative ETLs design (ZnO/MgF_2) to substitute the PCBM and other fullerene derivatives.

References

- [1] A. Kojima, K. Teshima, Y. Shirai, and T. Miyasaka, "Organometal Halide Perovskites as Visible-Light Sensitizers for Photovoltaic Cells," *Journal of the American Chemical Society*, vol. 131, pp. 6050-6051, 2009.
- [2] H. Zhou, Q. Chen, G. Li, S. Luo, T.-b. Song, H.-S. Duan, *et al.*, "Interface engineering of highly efficient perovskite solar cells," *Science*, vol. 345, pp. 542-546, 2014.
- [3] W. S. Yang, J. H. Noh, N. J. Jeon, Y. C. Kim, S. Ryu, J. Seo, *et al.*, "High-performance photovoltaic perovskite layers fabricated through intramolecular exchange," *Science*, vol. 348, pp. 1234-1237, 2015.
- [4] M. Saliba, T. Matsui, J.-Y. Seo, K. Domanski, J.-P. Correa-Baena, M. K. Nazeeruddin, *et al.*, "Cesium-containing triple cation perovskite solar cells: improved stability, reproducibility and high efficiency," *Energy & Environmental Science*, vol. 9, pp. 1989-1997, 2016.
- [5] D. Bi, C. Yi, J. Luo, J.-D. Décoppet, F. Zhang, S. M. Zakeeruddin, *et al.*, "Polymer-templated nucleation and crystal growth of perovskite films for solar cells with efficiency greater than 21%," *Nature Energy*, vol. 1, pp. 16142, 2016.
- [6] Q. Jiang, L. Zhang, H. Wang, X. Yang, J. Meng, H. Liu, *et al.*, "Enhanced electron extraction using SnO₂ for high-efficiency planar-structure HC(NH₂)₂PbI₃-based perovskite solar cells," *Nature Energy*, vol. 2, pp. 16177, 2016.
- [7] W. S. Yang, B.-W. Park, E. H. Jung, N. J. Jeon, Y. C. Kim, D. U. Lee, *et al.*, "Iodide management in formamidinium-lead-halide-based perovskite layers for efficient solar cells," *Science*, vol. 356, pp. 1376-1379, 2017.
- [8] M. Saliba, T. Matsui, K. Domanski, J.-Y. Seo, A. Ummadisingu, S. M. Zakeeruddin, *et al.*, "Incorporation of rubidium cations into perovskite solar cells improves photovoltaic performance," *Science*, vol. 354, pp. 206-209, 2016.
- [9] S. S. Shin, E. J. Yeom, W. S. Yang, S. Hur, M. G. Kim, J. Im, *et al.*, "Colloidally prepared La-doped BaSnO₃ electrodes for efficient, photostable perovskite solar cells," *Science*, vol. 356, pp. 167-171, 2017.
- [10] H. Tan, A. Jain, O. Voznyy, X. Lan, F. P. G. de Arquer, J. Z. Fan, *et al.*, "Efficient and stable solution-processed planar perovskite solar cells via contact passivation," *Science*, vol. 355, pp. 722-726, 2017.

- [11] T. Ye, S. Ma, X. Jiang, L. Wei, C. Vijila, and S. Ramakrishna, "Performance Enhancement of Tri-Cation and Dual-Anion Mixed Perovskite Solar Cells by Au@SiO₂ Nanoparticles," *Advanced Functional Materials*, vol.27, pp. 1606545, 2017.
- [12] X. Zheng, B. Chen, J. Dai, Y. Fang, Y. Bai, Y. Lin, *et al.*, "Defect passivation in hybrid perovskite solar cells using quaternary ammonium halide anions and cations," *Nature Energy*, vol. 2, pp. 17102, 2017.
- [13] C.-H. Chiang, M. K. Nazeeruddin, M. Grätzel, and C.-G. Wu, "The synergistic effect of H₂O and DMF towards stable and 20% efficiency inverted perovskite solar cells," *Energy & Environmental Science*, vol. 10, pp. 808-817, 2017.
- [14] D. Luo, L. Zhao, J. Wu, Q. Hu, Y. Zhang, Z. Xu, *et al.*, "Dual-Source Precursor Approach for Highly Efficient Inverted Planar Heterojunction Perovskite Solar Cells," *Advanced Materials*, vol. 29, pp. 1604758, 2017.
- [15] M. Stolterfoht, C. M. Wolff, Y. Amir, A. Paulke, L. Perdigón-Toro, P. Caprioglio, *et al.*, "Approaching the fill factor Shockley–Queisser limit in stable, dopant-free triple cation perovskite solar cells," *Energy & Environmental Science*, vol. 10, pp. 1530-1539, 2017.
- [16] <https://www.nrel.gov/pv/assets/images/efficiency-chart.png>. (Accessed on 16/04/2018)
- [17] W.-J. Yin, J.-H. Yang, J. Kang, Y. Yan, and S.-H. Wei, "Halide perovskite materials for solar cells: a theoretical review," *Journal of Materials Chemistry A*, vol. 3, pp. 8926-8942, 2015.
- [18] N.-G. Park, "Perovskite solar cells: an emerging photovoltaic technology," *Materials Today*, vol. 18, pp. 65-72, 2015.
- [19] L. G. Tejuca and J. L. Fierro, *Properties and applications of perovskite-type oxides*: CRC Press, 1992.
- [20] D. Bi, W. Tress, M. I. Dar, P. Gao, J. Luo, C. Renevier, *et al.*, "Efficient luminescent solar cells based on tailored mixed-cation perovskites," *Science Advances*, vol. 2, pp. e1501170, 2016.
- [21] W. Chen, Y. Wu, Y. Yue, J. Liu, W. Zhang, X. Yang, *et al.*, "Efficient and stable large-area perovskite solar cells with inorganic charge extraction layers," *Science*, vol. 350, pp. 944-948, 2015.
- [22] X. Li, D. Bi, C. Yi, J. D. Decoppet, J. Luo, S. M. Zakeeruddin, *et al.*, "A vacuum flash-assisted solution process for high-efficiency large-area perovskite solar cells," *Science*, vol. 353, pp. 58-62, 2016.

- [23] S. S. Shin, W. S. Yang, J. H. Noh, J. H. Suk, N. J. Jeon, J. H. Park, *et al.*, "High-performance flexible perovskite solar cells exploiting Zn₂SnO₄ prepared in solution below 100 degrees C," *Nature Communication*, vol. 6, pp. 7410, 2015.
- [24] J. W. Lee, D. J. Seol, A. N. Cho, and N. G. Park, "High-efficiency perovskite solar cells based on the black polymorph of HC(NH₂)₂ PbI₃," *Advanced Materials*, vol. 26, pp. 4991-8, 2014.
- [25] W. Ke, C. Xiao, C. Wang, B. Saparov, H. S. Duan, D. Zhao, *et al.*, "Employing Lead Thiocyanate Additive to Reduce the Hysteresis and Boost the Fill Factor of Planar Perovskite Solar Cells," *Advanced Materilas*, vol. 28, pp. 5214-21, 2016.
- [26] N. J. Jeon, J. H. Noh, Y. C. Kim, W. S. Yang, S. Ryu, and S. I. Seok, "Solvent engineering for high-performance inorganic–organic hybrid perovskite solar cells," *Nature Materials*, vol. 13, pp. 897-903, 2014.
- [27] D. P. McMeekin, G. Sadoughi, W. Rehman, G. E. Eperon, M. Saliba, M. T. Hörantner, *et al.*, "A mixed-cation lead mixed-halide perovskite absorber for tandem solar cells," *Science*, vol. 351, pp. 151-155, 2016.
- [28] N. J. Jeon, J. H. Noh, W. S. Yang, Y. C. Kim, S. Ryu, J. Seo, *et al.*, "Compositional engineering of perovskite materials for high-performance solar cells," *Nature*, vol. 517, pp. 476-80, 2015.
- [29] L. Hu, J. Peng, W. Wang, Z. Xia, J. Yuan, J. Lu, *et al.*, "Sequential deposition of CH₃NH₃PbI₃ on planar NiO film for efficient planar perovskite solar cells," *ACS Photonics*, vol. 1, pp. 547-553, 2014.
- [30] L. Hu, W. Wang, H. Liu, J. Peng, H. Cao, G. Shao, *et al.*, "PbS colloidal quantum dots as an effective hole transporter for planar heterojunction perovskite solar cells," *Journal of Materials Chemistry A*, vol. 3, pp. 515-518, 2015.
- [31] Z. Wu, S. Bai, J. Xiang, Z. Yuan, Y. Yang, W. Cui, *et al.*, "Efficient planar heterojunction perovskite solar cells employing graphene oxide as hole conductor," *Nanoscale*, vol. 6, pp. 10505-10510, 2014.
- [32] J. K. Nam, S. U. Chai, W. Cha, Y. J. Choi, W. Kim, M. S. Jung, *et al.*, "Potassium incorporation for enhanced performance and stability of fully inorganic cesium lead halide perovskite solar cells," *Nano Letters*, vol. 17, pp. 2028-2033, 2017.
- [33] Z. K. Wang, M. Li, Y. G. Yang, Y. Hu, H. Ma, X. Y. Gao, *et al.*, "High Efficiency Pb-In Binary Metal Perovskite Solar Cells," *Advanced Materials*, vol. 28, pp. 6695-703, 2016.

- [34] D. Ju, Y. Dang, Z. Zhu, H. Liu, C.-C. Chueh, X. Li, *et al.*, "Tunable Band Gap and Long Carrier Recombination Lifetime of Stable Mixed $\text{CH}_3\text{NH}_3\text{Pb}_x\text{Sn}_{1-x}\text{Br}_3$ Single Crystals," *Chemistry of Materials*, vol. 30, pp. 1556-1565, 2018.
- [35] M. H. Kumar, S. Dharani, W. L. Leong, P. P. Boix, R. R. Prabhakar, T. Baikie, *et al.*, "Lead-free halide perovskite solar cells with high photocurrents realized through vacancy modulation," *Advanced Materials*, vol. 26, pp. 7122-7127, 2014.
- [36] H. Zhang, H. Wang, S. T. Williams, D. Xiong, W. Zhang, C. C. Chueh, *et al.*, "SrCl₂ Derived Perovskite Facilitating a High Efficiency of 16% in Hole-Conductor-Free Fully Printable Mesoscopic Perovskite Solar Cells," *Advanced Materials*, vol. 29, pp. 1606608, 2017.
- [37] P. V. Kamat, J. Bisquert, and J. Buriak, "Lead-free perovskite solar cells," *ACS Energy Letters*, vol. 2, pp. 904-905, 2017.
- [38] F. Hao, C. C. Stoumpos, D. H. Cao, R. P. Chang, and M. G. Kanatzidis, "Lead-free solid-state organic-inorganic halide perovskite solar cells," *Nature Photonics*, vol. 8, pp. 489, 2014.
- [39] N. K. Noel, S. D. Stranks, A. Abate, C. Wehrenfennig, S. Guarnera, A.-A. Haghighirad, *et al.*, "Lead-free organic-inorganic tin halide perovskites for photovoltaic applications," *Energy & Environmental Science*, vol. 7, pp. 3061-3068, 2014.
- [40] H. Tsai, W. Nie, J.-C. Blancon, C. C. Stoumpos, R. Asadpour, B. Harutyunyan, *et al.*, "High-efficiency two-dimensional Ruddlesden-Popper perovskite solar cells," *Nature*, vol. 536, pp. 312, 2016.
- [41] Z. Wang, Q. Lin, F. P. Chmiel, N. Sakai, L. M. Herz, and H. J. Snaith, "Efficient ambient-air-stable solar cells with 2D-3D heterostructured butylammonium-caesium-formamidinium lead halide perovskites," *Nature Energy*, vol. 2, pp. 17135, 2017.
- [42] P. Luo, W. Xia, S. Zhou, L. Sun, J. Cheng, C. Xu, *et al.*, "Solvent engineering for ambient-air-processed, phase-stable CsPbI₃ in perovskite solar cells," *The Journal of Physical Chemistry Letters*, vol. 7, pp. 3603-3608, 2016.
- [43] T. Zhang, M. I. Dar, G. Li, F. Xu, N. Guo, M. Grätzel, *et al.*, "Bication lead iodide 2D perovskite component to stabilize inorganic α -CsPbI₃ perovskite phase for high-efficiency solar cells," *Science Advances*, vol. 3, pp. e1700841, 2017.

- [44] A. Swarnkar, A. R. Marshall, E. M. Sanehira, B. D. Chernomordik, D. T. Moore, J. A. Christians, *et al.*, "Quantum dot-induced phase stabilization of α -CsPbI₃ perovskite for high-efficiency photovoltaics," *Science*, vol. 354, pp. 92-95, 2016.
- [45] S. D. Stranks, G. E. Eperon, G. Grancini, C. Menelaou, M. J. Alcocer, T. Leijtens, *et al.*, "Electron-hole diffusion lengths exceeding 1 micrometer in an organometal trihalide perovskite absorber," *Science*, vol. 342, pp. 341-344, 2013.
- [46] Y. Hou, X. Du, S. Scheiner, D. P. McMeekin, Z. Wang, N. Li, *et al.*, "A generic interface to reduce the efficiency-stability-cost gap of perovskite solar cells," *Science*, vol. 358, pp. 1192-1197, 2017.
- [47] G. Xing, N. Mathews, S. Sun, S. S. Lim, Y. M. Lam, M. Grätzel, *et al.*, "Long-range balanced electron-and hole-transport lengths in organic-inorganic CH₃NH₃PbI₃," *Science*, vol. 342, pp. 344-347, 2013.
- [48] J. M. Ball, M. M. Lee, A. Hey, and H. J. Snaith, "Low-temperature processed meso-superstructured to thin-film perovskite solar cells," *Energy & Environmental Science*, vol. 6, pp. 1739, 2013.
- [49] S. Bai, Z. Wu, X. Wu, Y. Jin, N. Zhao, Z. Chen, *et al.*, "High-performance planar heterojunction perovskite solar cells: Preserving long charge carrier diffusion lengths and interfacial engineering," *Nano Research*, vol. 7, pp. 1749-1758, 2014.
- [50] M. M. Lee, J. Teuscher, T. Miyasaka, T. N. Murakami, and H. J. Snaith, "Efficient Hybrid Solar Cells Based on Meso-Superstructured Organometal Halide Perovskites," *Science*, vol. 338, pp. 643-647, 2012.
- [51] J. Burschka, N. Pellet, S. J. Moon, R. Humphry-Baker, P. Gao, M. K. Nazeeruddin, *et al.*, "Sequential deposition as a route to high-performance perovskite-sensitized solar cells," *Nature*, vol. 499, pp. 316-9, 2013.
- [52] H. Shen, Y. Wu, J. Peng, T. Duong, X. Fu, C. Barugkin, *et al.*, "Improved reproducibility for Perovskite solar cells with 1 cm² active area by a modified two-step process," *ACS Appl Mater Interfaces*, vol. 9, pp. 5974-5981, 2017.
- [53] M. Xiao, F. Huang, W. Huang, Y. Dkhissi, Y. Zhu, J. Etheridge, *et al.*, "A fast deposition-crystallization procedure for highly efficient lead iodide perovskite thin-film solar cells," *Angew Chem Int Ed Engl*, vol. 53, pp. 9898-903, 2014.
- [54] M. Liu, M. B. Johnston, and H. J. Snaith, "Efficient planar heterojunction perovskite solar cells by vapour deposition," *Nature*, vol. 501, pp. 395-8, 2013.

- [55] Q. Chen, H. Zhou, Z. Hong, S. Luo, H. S. Duan, H. H. Wang, *et al.*, "Planar heterojunction perovskite solar cells via vapor-assisted solution process," *Journal of American Chemical Society*, vol. 136, pp. 622-5, 2014.
- [56] H. Yoon, S. M. Kang, J.-K. Lee, and M. Choi, "Hysteresis-free low-temperature-processed planar perovskite solar cells with 19.1% efficiency," *Energy & Environmental Science*, vol. 9, pp. 2262-2266, 2016.
- [57] F. Giordano, A. Abate, J. P. Correa Baena, M. Saliba, T. Matsui, S. H. Im, *et al.*, "Enhanced electronic properties in mesoporous TiO₂ via lithium doping for high-efficiency perovskite solar cells," *Nature Communication*, vol. 7, pp. 10379, 2016.
- [58] K. Wojciechowski, M. Saliba, T. Leijtens, A. Abate, and H. J. Snaith, "Sub-150 °C processed meso-superstructured perovskite solar cells with enhanced efficiency," *Energy Environmental. Science*, vol. 7, pp. 1142-1147, 2014.
- [59] G. Richardson, S. E. O'Kane, R. G. Niemann, T. A. Peltola, J. M. Foster, P. J. Cameron, *et al.*, "Can slow-moving ions explain hysteresis in the current-voltage curves of perovskite solar cells?," *Energy & Environmental Science*, vol. 9, pp. 1476-1485, 2016.
- [60] S. K. Pathak, A. Abate, P. Ruckdeschel, B. Roose, K. C. Gödel, Y. Vaynzof, *et al.*, "Performance and Stability Enhancement of Dye-Sensitized and Perovskite Solar Cells by Al Doping of TiO₂," *Advanced Functional Materials*, vol. 24, pp. 6046-6055, 2014.
- [61] M. Lv, W. Lv, X. Fang, P. Sun, B. Lin, S. Zhang, *et al.*, "Performance enhancement of perovskite solar cells with a modified TiO₂ electron transport layer using Zn-based additives," *RSC Advances*, vol. 6, pp. 35044-35050, 2016.
- [62] E. H. Anaraki, A. Kermanpur, L. Steier, K. Domanski, T. Matsui, W. Tress, *et al.*, "Highly efficient and stable planar perovskite solar cells by solution-processed tin oxide," *Energy & Environmental Science*, vol. 9, pp. 3128-3134, 2016.
- [63] J. P. Correa Baena, L. Steier, W. Tress, M. Saliba, S. Neutzner, T. Matsui, *et al.*, "Highly efficient planar perovskite solar cells through band alignment engineering," *Energy & Environmental Science*, vol. 8, pp. 2928-2934, 2015.
- [64] C. L. Wang, D. W. Zhao, C. R. Grice, W. Q. Liao, Y. Yu, A. Cimaroli, *et al.*, "Low-temperature plasma-enhanced atomic layer deposition of tin oxide electron selective layers for highly efficient planar perovskite solar cells," *Journal of Materials Chemistry A*, vol. 4, pp. 12080-12087, 2016.

- [65] L. Zuo, Z. Gu, T. Ye, W. Fu, G. Wu, H. Li, *et al.*, "Enhanced photovoltaic performance of CH₃NH₃PbI₃ perovskite solar cells through interfacial engineering using self-assembling monolayer," *Journal of American Chemical Society*, vol. 137, pp. 2674-9, 2015.
- [66] J. You, L. Meng, T.-B. Song, T.-F. Guo, Y. Yang, W.-H. Chang, *et al.*, "Improved air stability of perovskite solar cells via solution-processed metal oxide transport layers," *Nature Nanotechnology*, vol. 11, pp. 75-81, 2016.
- [67] D. Liu and T. L. Kelly, "Perovskite solar cells with a planar heterojunction structure prepared using room-temperature solution processing techniques," *Nature Photonics*, vol. 8, pp. 133-138, 2014.
- [68] L. S. Oh, D. H. Kim, J. A. Lee, S. S. Shin, J.-W. Lee, I. J. Park, *et al.*, "Zn₂SnO₄-Based Photoelectrodes for Organolead Halide Perovskite Solar Cells," *The Journal of Physical Chemistry C*, vol. 118, pp. 22991-22994, 2014.
- [69] C. Tao, S. Neutzner, L. Colella, S. Marras, A. R. S. Kandada, M. Gandini, *et al.*, "17.6% stabilized efficiency in low-temperature processed planar perovskite solar cells," *Energy & Environmental Science*, vol. 8, pp. 2365-2370, 2015.
- [70] C. Tao, J. Van Der Velden, L. Cabau, N. F. Montcada, S. Neutzner, S. Kandada, *et al.*, "Fully Solution-Processed n-i-p-Like Perovskite Solar Cells with Planar Junction: How the Charge Extracting Layer Determines the Open-Circuit Voltage," *Advanced Materials*, vol. 29, p. 1604493, 2017.
- [71] J. T.-W. Wang, J. M. Ball, E. M. Barea, A. Abate, J. A. Alexander-Webber, J. Huang, *et al.*, "Low-temperature processed electron collection layers of graphene/TiO₂ nanocomposites in thin film perovskite solar cells," *Nano Letters*, vol. 14, pp. 724-730, 2013.
- [72] T. Duong, Y. Wu, H. Shen, J. Peng, X. Fu, D. Jacobs, *et al.*, "Rubidium Multication Perovskite with Optimized Bandgap for Perovskite-Silicon Tandem with over 26% Efficiency," *Advanced Energy Materials*, vol.7, pp.1700228, 2017.
- [73] N. Arora, M. I. Dar, A. Hinderhofer, N. Pellet, F. Schreiber, S. M. Zakeeruddin, *et al.*, "Perovskite solar cells with CuSCN hole extraction layers yield stabilized efficiencies greater than 20%," *Science*, 2017. DOI: 10.1126/science.aam5655.
- [74] K. Rakstys, S. Paek, P. Gao, P. Gratia, T. Marszalek, G. Grancini, *et al.*, "Molecular engineering of face-on oriented dopant-free hole transporting material for perovskite solar cells with 19% PCE," *Journal of Materials Chemistry A*, vol. 5, pp. 7811-7815, 2017.

- [75] G.-W. Kim, G. Kang, J. Kim, G.-Y. Lee, H. I. Kim, L. Pyeon, *et al.*, "Dopant-free polymeric hole transport materials for highly efficient and stable perovskite solar cells," *Energy & Environmental Science*, vol. 9, pp. 2326-2333, 2016.
- [76] Y. Liu, Z. Hong, Q. Chen, H. Chen, W. H. Chang, Y. M. Yang, *et al.*, "Perovskite Solar Cells Employing Dopant-Free Organic Hole Transport Materials with Tunable Energy Levels," *Advanced Materials*, vol. 28, pp. 440-446, 2016.
- [77] W. Chen, Y. Wu, Y. Yue, J. Liu, W. Zhang, X. Yang, *et al.*, "Efficient and stable large-area perovskite solar cells with inorganic charge extraction layers," *Science*, vol. 350, pp. 944-948, 2015.
- [78] W. Tress, "Perovskite Solar Cells on the Way to Their Radiative Efficiency Limit—Insights Into a Success Story of High Open-Circuit Voltage and Low Recombination," *Advanced Energy Materials*, vol. 7, pp. 1602358, 2017.
- [79] S. D. Stranks, "Nonradiative losses in metal halide perovskites," *ACS Energy Letters*, vol. 2, pp. 1515-1525, 2017.
- [80] D. A. Jacobs, Y. Wu, H. Shen, C. Barugkin, F. J. Beck, T. P. White, *et al.*, "Hysteresis phenomena in perovskite solar cells: the many and varied effects of ionic accumulation," *Physical Chemistry Chemical Physics*, vol. 19, pp. 3094-3103, 2017.
- [81] J.-P. Correa-Baena, W. Tress, K. Domanski, E. H. Anaraki, S.-H. Turren-Cruz, B. Roose, *et al.*, "Identifying and suppressing interfacial recombination to achieve high open-circuit voltage in perovskite solar cells," *Energy & Environmental Science*, vol. 10, pp. 1207-1212, 2017.
- [82] F. Zhang, W. Shi, J. Luo, N. Pellet, C. Yi, X. Li, *et al.*, "Isomer-Pure Bis-PCBM-Assisted Crystal Engineering of Perovskite Solar Cells Showing Excellent Efficiency and Stability," *Advanced Materilas*, vol. 29, pp. 1606806, 2017.
- [83] D. Koushik, W. J. H. Verhees, Y. H. Kuang, S. Veenstra, D. Zhang, M. A. Verheijen, *et al.*, "High-efficiency humidity-stable planar perovskite solar cells based on atomic layer architecture," *Energy & Environmental Science*, vol. 10, pp. 91-100, 2017.
- [84] F. Wang, A. Shimazaki, F. Yang, K. Kanahashi, K. Matsuki, Y. Miyauchi, *et al.*, "Highly Efficient and Stable Perovskite Solar Cells by Interfacial Engineering Using Solution-Processed Polymer Layer," *The Journal of Physical Chemistry C*, vol. 121, pp. 1562-1568, 2017.

- [85] C.-H. Chiang and C.-G. Wu, "Bulk heterojunction perovskite–PCBM solar cells with high fill factor," *Nature Photonics*, vol. 10, pp. 196-200, 2016.
- [86] X. Li, M. Ibrahim Dar, C. Yi, J. Luo, M. Tschumi, S. M. Zakeeruddin, *et al.*, "Improved performance and stability of perovskite solar cells by crystal crosslinking with alkylphosphonic acid ω -ammonium chlorides," *Nature Chemistry*, vol. 7, pp. 703-711, 2015.
- [87] N. K. Noel, A. Abate, S. D. Stranks, E. S. Parrott, V. M. Burlakov, A. Goriely, *et al.*, "Enhanced photoluminescence and solar cell performance via Lewis base passivation of organic–inorganic lead halide perovskites," *ACS Nano*, vol. 8, pp. 9815-9821, 2014.
- [88] L. Zuo, H. Guo, S. Jariwala, N. De Marco, S. Dong, R. DeBlock, *et al.*, "Polymer-modified halide perovskite films for efficient and stable planar heterojunction solar cells," *Science Advances*, vol. 3, pp. e1700106, 2017.

Chapter 2: Efficient Indium-Doped TiO_x Electron Transport Layers for High-Performance Perovskite Solar Cells and Perovskite-Silicon Tandems

The use of optimized charge transport layers with suitable work functions, good conductivity and excellent charge selectivity is vital to the task of achieving high-efficiency perovskite solar cells. As discussed in Chapter 1, TiO_2 is a highly selective n-type material suitable for use as an ETL in optoelectronic devices, and has found a natural application in perovskite solar cells.^[1-3]

Anatase TiO_2 , in general, needs high temperature (450 °C to 500 °C) sintering under air or oxygen atmosphere to crystallize out of amorphous TiO_2 .^[1-3] It is therefore challenging to precisely control the stoichiometry of TiO_2 during the fabrication, causing oxygen vacancies, Ti interstitial sites and non-stoichiometric oxygen-induced defects/trap states within the TiO_2 lattice.^[4,5] Those defects/trap states can trap injected electrons, and act as recombination centres at the interface, thus impacting the overall performance of perovskite solar cells.^[4,5]

To overcome this problem, we introduced a small amount of indium ions (In^{3+}) into the TiO_2 bulk material. It is shown that the extrinsic indium dopants can effectively passivate/remove the defects or trap states, reduce the sub-bandgap states and raise the conduction band for TiO_x , as evidenced by our detailed x-ray photoelectron spectroscopy/ultraviolet photoelectron spectroscopy (XPS/UPS) and Hall-Effect measurements.

Consequently, the use of indium-doped TiO_x ETLs enabled us to obtain high efficiencies of 18.9% for $\text{CH}_3\text{NH}_3\text{PbI}_3$ -based solar cells and 20.1% for $\text{Cs}_{0.05}(\text{MA}_{0.17}\text{FA}_{0.83})_{0.95}\text{-Pb}(\text{I}_{0.83}\text{Br}_{0.17})_3$ -based cells. A slight *J-V* hysteresis was still present in the indium-doped TiO_x -based perovskite cells, but these were improved relative to the pure- TiO_2 -based cells. We also applied the optimized indium-doped TiO_x ETLs to semi-transparent perovskite cells, achieving a steady-state efficiency of 16.6%, and used these cells to demonstrate a four-terminal perovskite-silicon tandem cell with an efficiency of 24.5%.

The detailed results and analysis of indium-doped TiO_x ETLs are presented in the following paper.

References

- [1] W. S. Yang, B.-W. Park, E. H. Jung, N. J. Jeon, Y. C. Kim, D. U. Lee, *et al.*, "Iodide management in formamidinium-lead-halide-based perovskite layers for efficient solar cells," *Science*, vol. 356, pp. 1376-1379, 2017.
- [2] M. Saliba, T. Matsui, K. Domanski, J.-Y. Seo, A. Ummadisingu, S. M. Zakeeruddin, *et al.*, "Incorporation of rubidium cations into perovskite solar cells improves photovoltaic performance," *Science*, vol. 354, pp. 206-209, 2016.
- [3] D. Bi, W. Tress, M. I. Dar, P. Gao, J. Luo, C. Renevier, *et al.*, "Efficient luminescent solar cells based on tailored mixed-cation perovskites," *Science Advances*, vol. 2, pp. e1501170, 2016.
- [4] F. Giordano, A. Abate, J. P. Correa Baena, M. Saliba, T. Matsui, S. H. Im, *et al.*, "Enhanced electronic properties in mesoporous TiO₂ via lithium doping for high-efficiency perovskite solar cells," *Nature Communication*, vol. 7, pp. 10379, 2016.
- [5] S. K. Pathak, A. Abate, P. Ruckdeschel, B. Roose, K. C. Gödel, Y. Vaynzof, *et al.*, "Performance and Stability Enhancement of Dye-Sensitized and Perovskite Solar Cells by Al Doping of TiO₂," *Advanced Functional Materials*, vol. 24, pp. 6046-6055, 2014.

Efficient Indium-Doped TiO_x Electron Transport Layers for High-Performance Perovskite Solar Cells and Perovskite-Silicon Tandems

Jun Peng,* The Duong, Xianzhong Zhou, Heping Shen, Yiliang Wu, Hemant Kumar Mulmudi, Yimao Wan, Dingyong Zhong, Juntao Li, Takuya Tsuzuki, Klaus J. Weber, Kylie R. Catchpole, and Thomas P. White*

In addition to a good perovskite light absorbing layer, the hole and electron transport layers play a crucial role in achieving high-efficiency perovskite solar cells. Here, a simple, one-step, solution-based method is introduced for fabricating high quality indium-doped titanium oxide electron transport layers. It is shown that indium-doping improves both the conductivity of the transport layer and the band alignment at the ETL/perovskite interface compared to pure TiO_2 , boosting the fill-factor and voltage of perovskite cells. Using the optimized transport layers, a high steady-state efficiency of 17.9% for $\text{CH}_3\text{NH}_3\text{PbI}_3$ -based cells and 19.3% for $\text{Cs}_{0.05}(\text{MA}_{0.17}\text{FA}_{0.83})_{0.95}\text{Pb}(\text{I}_{0.83}\text{Br}_{0.17})_3$ -based cells is demonstrated, corresponding to absolute efficiency gains of 4.4% and 1.2% respectively compared to TiO_2 -based control cells. In addition, a steady-state efficiency of 16.6% for a semi-transparent cell is reported and it is used to achieve a four-terminal perovskite-silicon tandem cell with a steady-state efficiency of 24.5%.

tunable bandgap of perovskite cells make them promising candidates for tandem devices. Perovskite-silicon tandem cells built on conventional crystalline silicon technology are regarded as a highly promising low-cost solution to push efficiencies toward 30%; well above the efficiency limit of single-junction silicon cells.^[14–21]

Much of the perovskite cell research to date has focused on improving the crystallinity and the formation of high-quality, uniform perovskite thin films, via one step^[2,3] and two-step solution processes,^[22] additives^[23–26] and anti-solvent treatments,^[27,28] thermal evaporation^[29] and other methods.^[30–36] In addition, many different perovskite compositions have been systematically developed and investigated to improve and enhance the PCE and stability of perovskite solar cells.^[4,21,37–41]

1. Introduction

Organometal trihalide perovskite solar cells have recently received tremendous attention as promising candidates for next-generation solar cells due to their low bandgap, high charge mobility, high extinction coefficient, and weak exciton binding energy.^[1–12] Since 2009, significant research effort has dramatically boosted the power conversion efficiency (PCE) of perovskite solar cells from $\approx 4.0\%$ ^[1] to 22.1% (certified).^[13] In addition to stand-alone cells, the high-efficiency, easy-processing, and

Other work has focused on reducing the energy barrier of charge injection in perovskite solar cells by developing new kinds of high-performance hole-transporting materials (HTMs)^[42,43] and exploiting efficient electron-transporting materials with suitable workfunction (WF) and high conductivity.^[9,10,44–59]

To date, most high-efficiency perovskite solar cells have been obtained from devices with a structure of FTO/ETL/Perovskite/HTL/metal contact, where ETL and HTL represent the electron and hole transport layers respectively. The most common HTLs are 2,2',7,7'-Tetrakis-(N,N-di-4-methoxyphenylamino)-9,9'-spirobifluorene (Spiro-OMeTAD) and poly (triaryl amine), which have been proved to be excellent HTMs with high charge mobility and efficient electron-blocking property.^[4,5,9,41] Titanium oxide (TiO_2) is the most common ETL, and has been widely used in perovskite solar cells due to its good chemical resistance, electronic and optical properties, as well as being compatible with a variety of deposition methods.^[2,5,22] Pure TiO_2 -based perovskite solar cells typically produce high short-circuit current density (J_{sc}), but can suffer from lower open circuit voltage (V_{oc}) and fill factor (FF), which limits their PCE. Thus, highly conductive TiO_2 ^[46,59] and its dopants,^[9,45,60–62] ZnO ^[44] and its dopants,^[47,63] SnO_2 ^[55,56] and *n*-type organic materials^[51,53,58,64] have all been investigated as alternative ETLs. For example, Zhou et al.^[9] reported Y-doped TiO_2 used as an efficient ETL for perovskite solar cells, yielding a high PCE of 19.3% with a V_{oc}

J. Peng, T. Duong, Dr. H. Shen, Y. Wu,
Dr. H. K. Mulmudi, Dr. Y. Wan, A/Prof. T. Tsuzuki,
A/Prof. K. J. Weber, A/Prof. K. R. Catchpole,
Dr. T. P. White

Research School of Engineering
The Australian National University
Canberra, ACT 2601, Australia
E-mail: u5686151@anu.edu.au,
pengjun.88.81@gmail.com; thomas.white@anu.edu.au

Dr. X. Zhou, Prof. D. Zhong, A/Prof. J. Li, Dr. T. P. White
State Key Laboratory of Optoelectronic Materials and Technologies
School of Physics
Sun Yat-sen University
Guangzhou 510275, China



DOI: 10.1002/aenm.201601768

of 1.13 V and *FF* of 0.75. In 2016, Giordano et al.^[45] reported a PCE of more than 19% with negligible hysteric behavior using Li-doped meso-TiO₂ as a scaffold for the perovskite active layer. Al-doped TiO₂^[61] and Zn-doped TiO₂^[62] have also been reported, although the PCEs were relatively low. In addition, more complex bilayer-structure ETLs consisting of metal oxides and organic materials, such as TiO₂/PCBM ([6,6]-phenyl-C61-butyric acid methyl ester),^[54] TiO₂/Graphene,^[48] SnO₂/C₆₀,^[49] PEIE (polyethyleneimine ethoxylated)/Y-TiO₂,^[9] and the like^[50,52] have also been developed. Many of these ETL variations have been shown to increase either the *FF* or *V*_{oc} of perovskite solar cells through improved conductivity^[44,48,59] or improved band alignment^[52] respectively, but only a small number has successfully increased both cell parameters simultaneously.^[9,45,54] Hence, there remains a large space for improving both the *FF* and *V*_{oc} in perovskite solar cells by optimizing ETLs to have a suitable WF and good conductivity.

In this work, we demonstrate a solution-processed In-TiO_x as an efficient ETL for perovskite solar cells, where the precursor of In-TiO_x can be easily obtained by mixing the indium precursor with the TiO₂ precursor in the correct proportions. The conductivity of compact In-TiO_x thin films increases due to the indium dopant, thus dramatically improving the *FF* of perovskite solar cells compared to cells with pure TiO₂ ETLs. Furthermore, indium-doping allows us to tune the work function of the ETL to improve the band alignment at the ETL/perovskite interface. Consequently, we obtained high efficiencies of 18.9% for CH₃NH₃PbI₃-based (MAPbI₃) solar cells and 20.1% for Cs_{0.05}(MA_{0.17}FA_{0.83})_{0.95}-Pb(I_{0.83}Br_{0.17})₃-based cells. These cells exhibit impressive *FF* values of 0.771 and 0.791, respectively, which are among the highest values reported for TiO_x-based perovskite solar cells.^[4,9,12,39,41,54] We also apply the optimized ETL to semi-transparent perovskite cells, achieving a steady-state efficiency of 16.6%, and use these cells to demonstrate a four-terminal perovskite-silicon tandem cell with an efficiency of 24.5%.

2. Results and Discussion

In the following sections, we systematically characterize the physical, electrical, and optical properties of In-TiO_x thin films on various substrates using X-ray photoelectron spectroscopy/ultraviolet photoelectron spectroscopy (XPS/UPS), atomic force microscopy (AFM), optical transmittance, impedance spectroscopy, and Hall Effect measurements. We directly compare these properties to undoped compact TiO₂ ETLs as typically used in perovskite cells. These results are further supported by scanning electron microscope (SEM), X-ray diffraction (XRD), and device characterization to further investigate the performance of In-TiO_x and TiO₂-based perovskite solar cells. Detailed information for In-TiO_x processing and device fabrication can be found in the Experimental Section.

2.1. XPS and UPS Analysis

In-TiO_x thin films for XPS/UPS and AFM characterizations were prepared according to our best indium-doping condition

(3%-In-TiO_x). XPS measurements were conducted to elucidate the chemical compositions of TiO₂ and In-TiO_x deposited on fluorine-doped tin oxide (FTO) substrates. Figure 1a,b compares the XPS spectra of the Ti 2p and In 3d peaks respectively for the two films. Figure 1a shows the Ti 2p1 and Ti 2p3 peaks of the TiO₂ film at binding energies of ≈464.3 and ≈458.5 eV, which are consistent with literature values.^[65] For the In-TiO_x films, the Ti 2p3 peak is shifted slightly higher to 458.8 eV. This shift can be explained by the Pauling electronegativity theory; the electronegativity value of Ti is 1.5 and In is 1.7, which

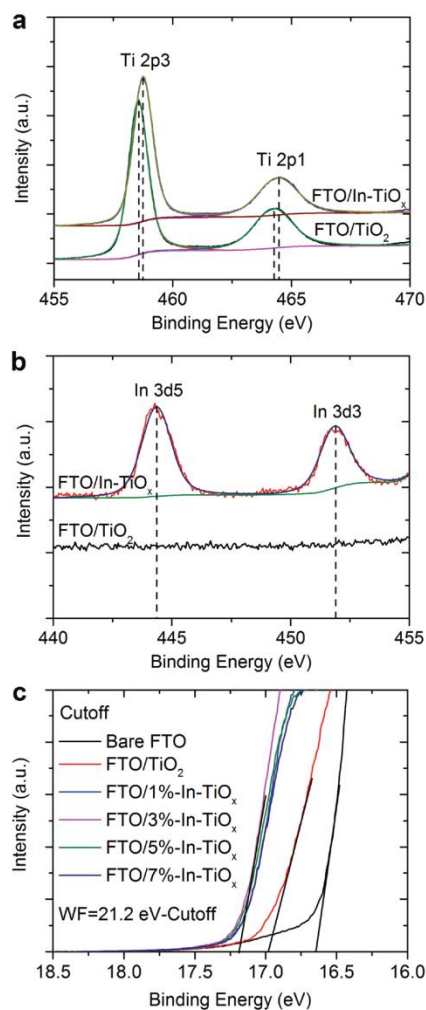


Figure 1. The XPS and UPS spectra of FTO/TiO₂ and FTO/In-TiO_x. a) XPS spectra of Ti 2p peaks, b) XPS spectra of In 3d peaks, c) UPS spectra of bare FTO, FTO/TiO₂, and FTO/In-TiO_x.

indicates negative charge transfer toward indium in the Ti-O-In bond, thereby increasing the Ti 2p core level binding energy.^[65] Figure 1b shows the XPS spectrum of In 3d5 for the In-TiO_x film, with a single peak centered at ≈444.3 eV that can be ascribed to indium oxide.^[65] As expected, the TiO₂ does not have a corresponding peak. The surface stoichiometry of the samples was calculated by comparing the elements' relative peak areas and their corresponding relative sensitivity factors. The atomic ratio of Ti:O for TiO₂ sample is about 1:2, and the atomic ratio of In:Ti for In-TiO_x is 2:98. Detailed analysis of O 1s peaks for In-TiO_x and TiO₂ is also provided in Figure S1a (Supporting Information). Samples prepared on indium tin oxide (ITO) substrates were found to have very similar XPS spectra as shown in Figure S1b-d (Supporting Information).

UPS measurements were also performed to estimate the WF of FTO/TiO₂ and FTO/In-TiO_x samples. Figure 1c shows that the photoemission cutoff of bare FTO is 16.65 eV corresponding to a WF of ≈4.55 eV, while the WF of FTO/TiO₂ is ≈4.22 eV. To better investigate the WF of the FTO/In-TiO_x, we prepared films with four different indium doping concentrations varying from 1% to 7% (v/v), labelled as 1%-In-TiO_x to 7%-In-TiO_x. As depicted in Figure 1c, the WF initially decreases with increasing indium concentration from ≈4.06 eV for 1%-In-TiO_x to ≈4.00 eV for 3%-In-TiO_x. With additional indium content, the WF increases again, to ≈4.02 eV for 5%-In-TiO_x and ≈4.06 eV for 7%-In-TiO_x, which is the same as for 1%-In-TiO_x. For all doping levels, the WF of In-TiO_x is closer

to the conduction band of MAPbI₃ perovskite (≈3.9 eV)^[66] than that of TiO₂ shown in Figure 2a. We show later that this translates into higher V_{oc} values for MAPbI₃-based solar cells with In-TiO_x ETLs compared to those with TiO₂ ETLs. UPS spectra were also obtained for ITO/TiO₂ and ITO/In-TiO_x samples (see Figure S2a, Supporting Information). The WF of ITO/TiO₂ and ITO/In-TiO_x are similar to those of FTO/TiO₂ and FTO/In-TiO_x, further proving the band alignment of In-TiO_x is better than that of pure TiO₂ for MAPbI₃-based device structures.

The role of In as a dopant in TiO_x may be ascribed to the following explanations. From the Ti 2p XPS data of In-TiO_x and TiO₂ in Figure 1a, we observe a Ti 2p core-level shift with indium doping. This shift is caused by a charge transfer effect in the Ti-O-In bond, indicating that the indium ions are incorporated into the TiO₂ lattice.^[61,65] According to Pathak et al.,^[61] Giordano et al.,^[45] and Rourke et al.,^[67] oxygen vacancies, Ti interstitial sites and non-stoichiometric oxygen-induced defects or trap states within the TiO₂ lattice can trap injected electrons, and act as recombination centres. These works reported that a small amount of extrinsic dopants with valency +3 (such as Al³⁺ ions) can effectively passivate/remove the defect or trap states, reduce the sub-bandgap states and raise the conduction band.^[45,61,67] According to our UPS results (Figure 1c) and Hall Effect measurements (Table S1, Supporting Information), the WF of In-TiO_x is lower than that of pure TiO₂, and the carrier density for In-TiO_x is higher than that of pure TiO₂, suggesting that In-doping reduces the density of sub-bandgap states and

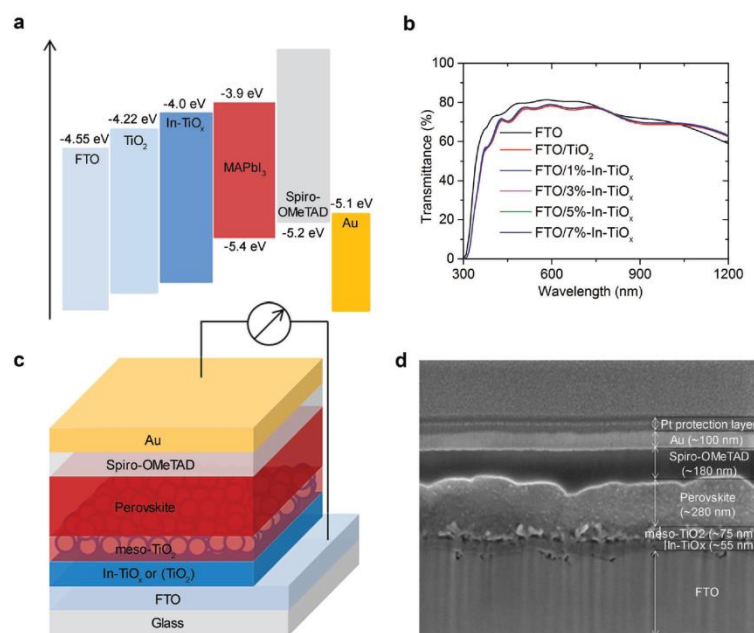


Figure 2. a) Diagram showing the energy levels of different materials. b) Transmittance spectra of bare FTO, FTO/TiO₂, and FTO/In-TiO_x. c) Schematic of the standard device structure studied here. d) SEM cross-sectional image of the device with a structure: FTO/In-TiO_x/meso-TiO₂/MAPbI₃/Spiro-OMeTAD/Au. Note that the Pt protection layer was only used to prepare the focused ion beam (FIB) SEM cross-sectional image.

increases the electron conductivity. Therefore, the In^{3+} doping mechanism might be consistent with that of the Al-doped TiO_2 .^[61] Thus, a low level of In-doping can passivate the electronic defects or trap states caused by non-stoichiometric oxygen-induced defects within the TiO_2 lattice,^[45,61] resulting in improved electron transport properties and band alignment for perovskite solar cells.

2.2. AFM & Transmittance Analysis

AFM was used to probe the surface morphology of the solution-processed ≈ 50 nm TiO_2 and In-TiO_x films deposited on both FTO and ITO substrates (see Figure S3, Supporting Information). Measurements of FTO/In-TiO_x (FTO/TiO_2) samples show a continuous and conformal film with rms roughness of ≈ 17.2 nm (≈ 17.5 nm), compared to ≈ 28.3 nm for the bare FTO. ITO/TiO_2 and ITO/In-TiO_x samples have roughness of 1.31 and 1.29 nm, respectively, compared to 3.8 nm for bare ITO. These results confirm that the In-TiO_x film provides a dense and compact transport layer on multiple substrate types.

In addition to high quality conformal films, it is also essential for the In-TiO_x to have a high transmittance to maximize the current of perovskite solar cells. Figure 2b demonstrates that the transmittance of FTO/In-TiO_x samples is almost identical to that of FTO/TiO_2 . Note that all of the coated samples have lower transmittance than the bare FTO due to increased reflectance resulting from the high refractive index $\text{TiO}_2/\text{In-TiO}_x$ films. Transmittance spectra for ITO-based samples are provided in Figure S2b (Supporting Information) and show similar behavior. We therefore conclude that the indium doping has a negligible effect on the optical properties of the $\text{TiO}_2/\text{In-TiO}_x$ films.

2.3. MAPbI_3 Cell Performance with In-TiO_x ETL

We used a normal device structure, consisting of FTO/In-TiO_x (or TiO_2)/meso- TiO_2 / MAPbI_3 /Spiro-OMeTAD/Au (see Figure 2c), to verify the performance improvement provided by the In-TiO_x ETL compared to cells with a pure TiO_2 ETL. Figure 2d shows a SEM cross-sectional image of a complete cell. The thickness of the In-TiO_x film and mesoporous TiO_2 layers are ≈ 55 and ≈ 75 nm respectively, capped by ≈ 280 nm of MAPbI_3 and 180 nm of Spiro-OMeTAD.

To optimize the performance of In-TiO_x -based cells, we prepared cells on FTO substrates using indium doping concentrations varying from 0% to 7% (v/v), labeled as TiO_2 , 1%- In-TiO_x , 3%- In-TiO_x , 5%- In-TiO_x , and 7%- In-TiO_x . Figure 3 shows the measured values of V_{oc} , J_{sc} , FF , and PCE of 100 different cells as a function of indium concentration. Figure 3a shows that even 1% indium doping

can dramatically improve the V_{oc} from ≈ 1.04 V (the median V_{oc} for TiO_2) to ≈ 1.07 V (median V_{oc} for 1%- In-TiO_x). The V_{oc} reached a maximum median value of 1.09 V for the 3%- In-TiO_x . A slightly decreased V_{oc} (≈ 1.085 V) was observed with the 5% indium doping concentration before the V_{oc} drops back to ≈ 1.07 V for the 7%- In-TiO_x . This trend is consistent with the UPS measurements of the WF of In-TiO_x and TiO_2 discussed in the UPS section.

The statistical distribution of FF for the TiO_2 and In-TiO_x -based cells shows a similar trend to that of V_{oc} (see Figure 3b). A median FF of 0.665 was obtained from TiO_2 -based control cells, whereas the 3%- In-TiO_x -based cells exhibited a median FF of ≈ 0.750 , corresponding to a $\approx 13\%$ improvement. Comparing to the current density versus voltage (J - V) curve of In-TiO_x -based and TiO_2 -based cells shown in Figure 4a, it appears that the improved FF is largely due to a reduced series resistance in the In-TiO_x -based cells. Therefore, Hall Effect measurements were employed to further study the electronic properties of the ETL layer. The results in Table S1 (Supporting Information) show that the conductivity of In-TiO_x is higher than that of TiO_2 , which is possibly caused by the increased carrier density and hall mobility, thus reducing the series resistance in In-TiO_x -based cells.^[9,59] We also note that the conductivity of In-TiO_x shows a similar trend to the WF of In-TiO_x ; initially increasing with indium content up to concentrations of 3%–5%, then decreasing again for higher doping levels.

In Figure 3c, the median J_{sc} for In-TiO_x -based cells shows only a weak variation with indium content, where the median J_{sc} of 22.09 mA cm^{-2} for 3%- In-TiO_x -based cells is slightly

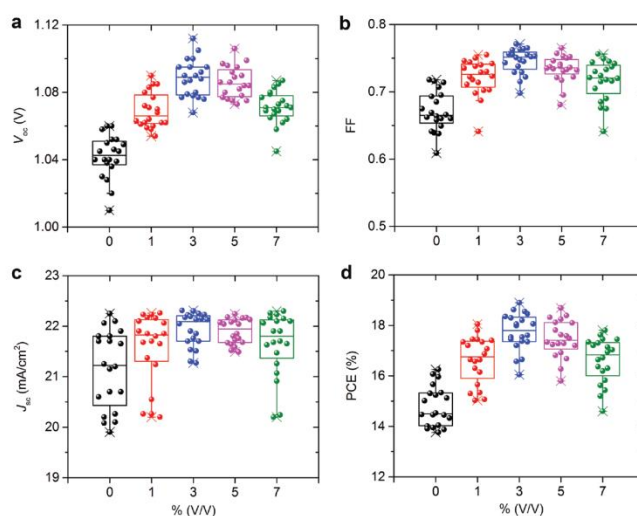


Figure 3. Statistical distribution of the photovoltaic parameters for cells with different indium doping concentrations, with a structure of FTO/In-TiO_x /meso- TiO_2 / MAPbI_3 /Spiro-OMeTAD/Au. a) Distribution of V_{oc} , b) distribution of FF , c) distribution of J_{sc} , d) distribution of PCE. Note that the 0% (v/v) condition is pure TiO_2 . Results are shown for 100 cells (each condition has 20 cells) collected from 12 different batches. All devices were tested at a 50 mV s^{-1} reverse scan rate.

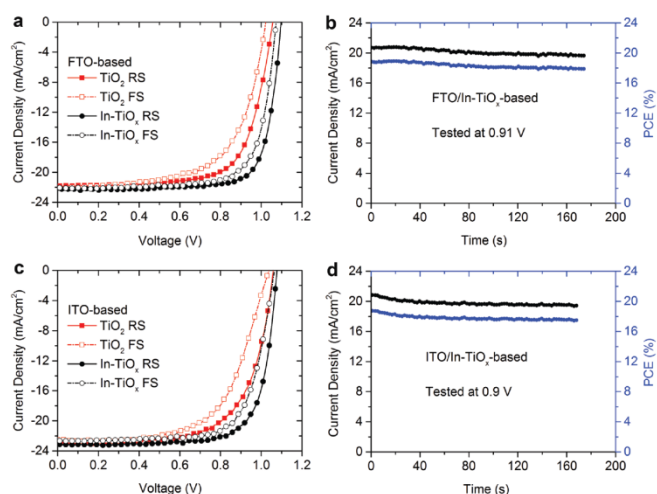


Figure 4. Photovoltaic performance of our champion devices. a) Current density–voltage curves of the FTO/In-TiO_x (or TiO₂)/meso-TiO₂/MAPbI₃/Spiro-OMeTAD/Au cells; and b) steady-state current density and efficiency of the In-TiO_x-based cell tested at 0.91 V. c) Current density–voltage curves of the ITO/In-TiO_x (or TiO₂)/meso-TiO₂/MAPbI₃/Spiro-OMeTAD/Au cells; and d) steady-state current density and efficiency of the In-TiO_x-based cell tested at 0.90 V. Note the legend label RS represents reverse scan (from V_{oc} to J_{sc}), and the FS represents forward scan (from J_{sc} to V_{oc}). All devices were tested at a 50 mV s⁻¹ scan rate.

(≈4%) higher than that of the TiO₂-based control devices (J_{sc} ≈21.3 mA cm⁻²). Indeed, the data of XRD and SEM (Figure S4, Supporting Information) show that MAPbI₃ thin films deposited on Glass, FTO/TiO₂ and FTO/In-TiO_x substrates exhibited similar coverage and crystallinity, so we would not expect significant variation in J_{sc} . The combination of higher V_{oc} and FF , and J_{sc} results in an absolute efficiency increase of more than ≈3.3% for 3%-In-TiO_x-based cells (PCE_{median} ≈ 17.8%) as compared to the TiO₂-based control cells (PCE_{median} ≈ 14.5%) (see Figure 3d).

Furthermore, we used impedance spectroscopy to investigate the series resistance, interfacial and bulk recombination within the In-TiO_x-based and TiO₂-based perovskite cells. As shown in Figure S5 (Supporting Information), the series resistance extracted from the In-TiO_x-based perovskite cell is significantly lower than that of TiO₂-based perovskite cell. In addition, the bulk charge recombination lifetimes for both cells show no significant difference. However, the surface charge recombination lifetime for the In-TiO_x-based perovskite cell is higher than that of the TiO₂-based perovskite cell. This further supports the conclusion that the improved cell performance results from higher conductivity and improved interface properties of the In-TiO_x-based ETL.

J - V curves of MAPbI₃-based cells with In-TiO_x and TiO₂ ETLs are shown in Figure 4a. Our champion In-TiO_x-based cell had a PCE of 18.9% with J_{sc} = 22.3 mA cm⁻², V_{oc} = 1.10 V and FF = 0.771, measured by reverse J - V scan. The best TiO₂-based control device, exhibited a PCE of 16.3%, with V_{oc} = 1.06 V, J_{sc} = 22.1 mA cm⁻² and FF = 0.706. Forward scanning and steady-state efficiency measurements were also

performed to verify the cell performance. As shown in Figure 4b, the steady-state efficiency of the In-TiO_x-based cell is 17.9% after holding it at a constant bias voltage of 0.91 V for 170 s. The corresponding efficiency of the TiO₂-based control device was 13.5% at a bias of 0.81 V, also after 170 s of continuous measurement (see Figure S6a, Supporting Information). Since the cells exhibit some hysteresis between forward and reverse scans, the bias voltage for these steady-state measurements was chosen as the average of the maximum power point voltage (V_{mpp}) of the two scan directions. With In-TiO_x-based cells, as shown in Figure 4a, we observed a small reduction in hysteresis compared with the TiO₂-based control devices. This may be attributed to the In-doping passivating the electronic defects or trap states caused by non-stoichiometric oxygen-induced defects within the TiO₂ lattice,^[45,61] thus suppressing the perovskite cell's hysteresis.^[45]

Figure 4c shows the reverse (forward) scanning J - V curves of the best ITO/In-TiO_x-based cell with an efficiency of 18.8% (17.4%) and the ITO/TiO₂-based control cell with an efficiency of 16.1% (14.5%). This further confirms that the

performance of In-TiO_x-based cells is significantly higher than that of control cells with a pure TiO₂ ETL. The corresponding steady-state efficiencies are shown in Figure 4d and Figure S6b (Supporting Information). We also observed a slight (≈3%) increase in J_{sc} for ITO-based cells as compared to FTO-based cells due to the higher transmittance of the ITO substrates, as seen in Figure 2b and Figure S2b (Supporting Information). All photovoltaic parameters of the devices are summarized in **Table 1**. In addition, long time steady-state efficiencies for another batch of FTO/In-TiO_x and ITO/In-TiO_x MAPbI₃-based cells are also provided in Figure S7 (Supporting Information).

2.4. Cs-Mixed Halide-Based Perovskite Cells

Recently, Saliba et al.^[39] reported high efficiency and stable perovskite cells based on a cesium-containing triple cation perovskite absorber material: Cs_{0.05}(MA_{0.17}FA_{0.83})_{0.95}Pb(I_{0.83}Br_{0.17})₃. We also applied the optimized In-TiO_x ETLs in Cs_{0.05}(MA_{0.17}FA_{0.83})_{0.95}Pb(I_{0.83}Br_{0.17})₃-based perovskite cells to study the compatibility of In-TiO_x with different perovskite compositions. By combining the 3%-In-TiO_x ETL (the best indium doping condition) with a Cs_{0.05}(MA_{0.17}FA_{0.83})_{0.95}Pb(I_{0.83}Br_{0.17})₃ perovskite active layer, we obtained a high PCE of 20.1% from the reverse scan and a corresponding PCE of 18.7% from the forward scan, whereas the TiO₂-based control cell exhibited a PCE of 18.8% and 17.6% respectively (see Figure 5a). Detailed results of the best devices are presented in Figure 5a and summarized in **Table 2**. ITO/In-TiO_x and ITO/TiO₂-based

Table 1. Photovoltaic parameters of our champion devices with a structure of FTO/In-TiO_x (or TiO₂)/meso-TiO₂/MAPbI₃/Spiro-OMeTAD/Au.

ETL	Scan direction	V _{oc} [V]	J _{sc} [mA cm ⁻²]	FF [%]	PCE [%]	R _s [Ω cm ²]	R _{sh} [Ω cm ²]	Steady-state efficiency [%]
FTO/In-TiO _x	RS	1.10	22.3	77.1	18.9	4.1	1454	17.9
	FS	1.08	22.1	74.3	17.7	5.5	1309	
FTO/TiO ₂	RS	1.06	21.8	70.6	16.3	6.8	1013	13.5
	FS	1.03	22.1	62.9	14.3	11.0	961	
ITO/In-TiO _x	RS	1.09	23.0	75.0	18.8	4.5	1241	17.5
	FS	1.07	22.6	72.2	17.4	6.3	1026	
ITO/TiO ₂	RS	1.06	22.8	66.7	16.1	8.5	987	14.0
	FS	1.04	22.5	62.1	14.5	11.3	816	

Note that all devices were tested at a 50 mV s⁻¹ scan rate under one sun (100 mW cm⁻², AM 1.5G); RS represents reverse scan (from V_{oc} to J_{sc}); FS represents forward scan (from J_{sc} to V_{oc}). R_s represents series resistance and R_{sh} represents shunt resistance.

Cs_{0.05}(MA_{0.17}FA_{0.83})_{0.95}Pb(I_{0.83}Br_{0.17})₃ perovskite cells were also investigated (see Figure 5c and Table 2). Figure 5b,d shows a steady-state efficiency of 19.3% after 200 s operation at a bias voltage of 0.92 V for the FTO/In-TiO_x-based cell, and 18.4% for the ITO/In-TiO_x-based cell. The control FTO/TiO₂ and ITO/TiO₂-based cells had PCEs of 18.1% (tested at 0.88 V) and 17.4% (tested at 0.87 V) as shown in Figure S8 (Supporting Information). Device performance distributions of the FTO/In-TiO_x-based and ITO/In-TiO_x-based cells are provided in Figure S9 (Supporting Information), demonstrating that the high performance In-TiO_x-based cells are repeatable.

2.5. Four-Terminal Tandem Cells

Encouraged by the high performance of In-TiO_x-based perovskite cells, we have also applied the doped In-TiO_x transport layer in a semi-transparent perovskite cell for use as a top cell in a four-terminal perovskite-silicon tandem cell. In a previous work, we reported a perovskite-silicon tandem with an efficiency of 20.1% by combining a 12.4% efficient semi-transparent CH₃NH₃PbI₃ cell with a 19.6% crystalline Si PERL cell.^[68] Here we take advantage of the excellent performance of the Cs-mixed halide perovskite/In-TiO_x ETL cells from the previous section, combined with a high-efficiency interdigitated back contact (IBC) silicon cell to demonstrate a steady-state tandem efficiency of 24.5%.

While cells on FTO substrates achieved the highest efficiencies, as reported above, we choose ITO substrates for the semi-transparent cells due to their higher optical transmittance in the near infrared region. An SEM cross-sectional image of the semi-transparent perovskite cell is shown in Figure 6a with the structure Glass/ITO/In-TiO_x/meso-TiO₂/Perovskite/Spiro-OMeTAD/MoO₃/ITO/Au, where the perovskite composition is Cs_{0.05}(MA_{0.17}FA_{0.83})_{0.95}Pb(I_{0.83}Br_{0.17})₃, and the Au is a gold-finger contact. The measured thickness of each layer is shown in the same figure. A photo of the completed cell is also shown as an inset to Figure 6c. Figure 6b and Table 3 show the performance characteristics of the best semi-transparent perovskite cell (see the Supporting Information Figure S10a, for the performance distribution of multiple cells). We measure a reverse scan PCE of 17.4% for the semi-transparent cell, with V_{oc} = 1.1 V, J_{sc} = 21.5 mA cm⁻² and FF = 0.735. The corresponding forward scan PCE is 15.3%.

Compared with the opaque cell, the main losses for the semi-transparent cells are in

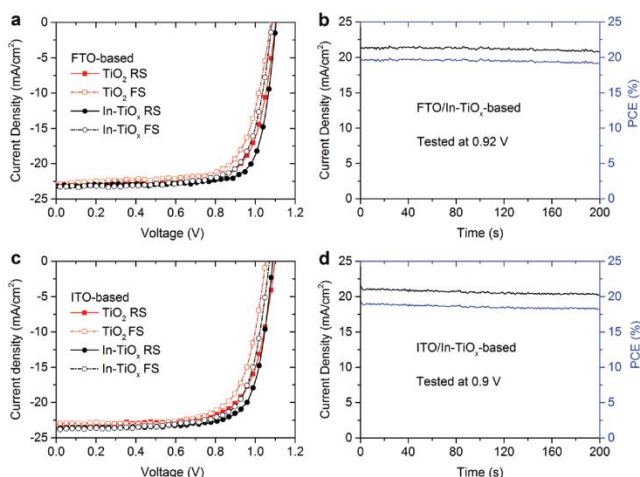


Figure 5. Photovoltaic performance of our champion Cs-mixed halide perovskite devices. a) Current density–voltage curves of the FTO/In-TiO_x (or TiO₂)/meso-TiO₂/Cs-mixed halide perovskite/Spiro-OMeTAD/Au cells and b) steady-state current density and efficiency of the In-TiO_x-based cell tested at 0.92 V. c) Current density–voltage curves of the ITO/In-TiO_x (or TiO₂)/meso-TiO₂/Cs-mixed halide perovskite/Spiro-OMeTAD/Au cells and d) steady-state current density and efficiency of the In-TiO_x-based cell tested at 0.90 V. Note that the Cs-mixed halide is Cs_{0.05}(MA_{0.17}FA_{0.83})_{0.95}Pb(I_{0.83}Br_{0.17})₃. The legend label RS represents reverse scan (from V_{oc} to J_{sc}), and FS represents forward scan (from J_{sc} to V_{oc}). All devices were tested at a 50 mV s⁻¹ scan rate.

Table 2. Photovoltaic parameters of our champion devices, with a structure: FTO/In-TiO_x (or TiO₂)/mesoTiO₂/Cs_{0.05}(MA_{0.17}FA_{0.83})_{0.95}Pb(I_{0.83}Br_{0.17})₃/Spiro-OMeTAD/Au.

ETL	Scan direction	V _{oc} [V]	J _{sc} [mA cm ⁻²]	FF [%]	PCE [%]	R _s [Ω cm ²]	R _{sh} [Ω cm ²]	Steady-state efficiency [%]
FTO/In-TiO _x	RS	1.10	23.1	79.1	20.1	3.4	1647	19.3
	FS	1.09	23.2	74.0	18.7	5.2	1351	
FTO/TiO ₂	RS	1.10	22.9	74.5	18.8	4.7	1264	18.1
	FS	1.08	23.1	70.7	17.6	7.1	1104	
ITO/In-TiO _x	RS	1.09	23.6	76.2	19.6	4.0	1326	18.4
	FS	1.07	23.7	73.1	18.5	5.7	1301	
ITO/TiO ₂	RS	1.10	23.4	71.1	18.3	6.5	1124	17.4
	FS	1.06	23.1	70.2	17.2	6.8	1012	

the J_{sc} and FF. The reduction of the J_{sc} is dominated by reduced absorption in the perovskite cell as a result of removing the reflective rear electrode, and is similar to that reported in our previous work on semi-transparent CH₃NH₃PbI₃ cells.^[68] The lower FF is attributed to increased resistance of the HTM layers and increased recombination at the HTM interfaces caused by the insertion of ≈13 nm MoO₃ and the ≈40 nm sputtered ITO/gold finger contact design. Figure 6c shows a steady-state PCE of 16.6% for the semi-transparent cell after 200 s at 0.82 V, and a PCE of ≈16.4% after 2000 s of continuous testing. Figure 6b also shows the J–V curve of the ≈24.0% IBC silicon cell under full illumination, which reduces to a PCE of 7.9% under illumination of light filtered through a semi-transparent perovskite cell (see Table 3). Thus, we have demonstrated a combined steady state efficiency of ≈24.5% for a four-terminal tandem cell consisting of a mechanically stacked semi-transparent

perovskite cell (top cell) on an IBC silicon cell (bottom cell). Figure 6d shows the measured external quantum efficiency (EQE) of the silicon cell with and without the perovskite cell filter. The measured transmittance of the filter and the predicted EQE (calculated as the product of the filter's transmittance and the measured silicon cell EQE without a filter) of the silicon cell are also plotted, showing excellent agreement. The integrated current densities of the silicon cell with and without the filter are in close agreement with the J–V data shown in Table 3. Measured EQE and absorption spectra of a semi-transparent cell are shown in Figure S11b (Supporting Information). In addition, the EQE of an equivalent ITO/In-TiO_x/Cs-mixed halide-based opaque cell is also provided in Figure S11a (Supporting Information). The integrated J_{sc} for the semi-transparent cell and opaque cell from the EQE measurements are within 10% of the corresponding J_{sc} values obtained from J–V scans.

We have also tested the stability of the semi-transparent cells over longer time periods. As shown in Figure S10b (Supporting Information), a cell with an initial PCE of 16.3% only dropped to 15.5% after ≈19000 s of continuous operation at a bias voltage of 0.82 V. This confirms the In-TiO_x-based semi-transparent cell can retain a reasonable PCE under constant light illumination of several hours.^[69] Note that all cells in this work were unencapsulated.

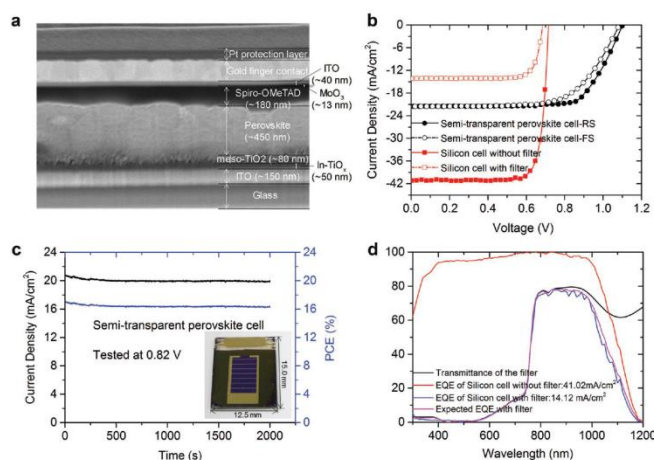


Figure 6. a) SEM cross-sectional image of the semi-transparent cell with a structure of ITO/In-TiO_x/meso-TiO₂/Cs-mixed halide perovskite/Spiro-OMeTAD/MoO₃/ITO/Gold finger contact. Note that the Pt protection layer was only used to prepare the FIB SEM cross-sectional image. b) Current density–voltage curves of the semi-transparent perovskite cell and IBC silicon cell. c) Steady-state current density and efficiency of the semi-transparent cell tested at 0.82 V. d) Transmittance of the semi-transparent cells and EQE of the IBC silicon cell with/without filter.

3. Conclusion

In summary, we have demonstrated a solution-processed In-TiO_x as an efficient ETL for perovskite solar cells, where the precursor of In-TiO_x can be easily prepared by mixing the indium precursor with the TiO₂ precursor in the correct proportions. The indium-doping improves the efficiency of perovskite cells through two separate mechanisms. First, it increases the carrier density and hall mobility, and hence the conductivity of the In-TiO_x ETL compared to the standard TiO₂ ETL, dramatically improving the FF of a range of

Table 3. Photovoltaic parameters of the four-terminal tandem cells.

		V_{oc} [V]	J_{sc} [mA cm ⁻²]	FF [%]	PCE [%]	Steady-state Efficiency [%]
Perovskite (top cell)	RS	1.10	21.5	73.5	17.4	16.6 (after 200 s)
	FS	1.09	21.5	65.4	15.3	
IBC silicon (bottom cell)	Without filter	0.72	41.0	81.3	24.0	24.0
	With filter	0.69	14.2	81.0	7.9	7.9
Four-terminal tandem cell						24.5

cells with different substrate materials and perovskite compositions. Second, the indium-doping allows us to tune the work function of the ETL to improve the band alignment at the ETL/perovskite interface. Using this optimized ETL we obtained a high steady-state efficiency of 17.9% for MAPbI₃-based cells and 19.3% for Cs_{0.05}(MA_{0.17}FA_{0.83})_{0.95}Pb(I_{0.83}Br_{0.17})₃ cells, corresponding to absolute efficiency gains of 4.4% and 1.2% respectively compared to control cells with pure TiO₂ ETLs. In addition, we demonstrated a high steady-state PCE of 16.6% for a semi-transparent cell and used it to achieve a steady-state efficiency of 24.5% for a four-terminal perovskite-silicon tandem cell. This is one of the highest efficiencies reported to date for perovskite-silicon tandem cells.^[14–21]

4. Experimental Section

Precursor Solutions–TiO₂ Precursor Solution: The TiO₂ precursor solution was prepared according to Ref.^[46], which contained 369 μL titanium isopropoxide (Sigma Aldrich, 99.999%) and 35 μL 2 M HCl in 5 mL anhydrous isopropanol.

Precursor Solutions–In-TiO₂ Precursor Solution: First, 90 mg indium acetate (Sigma Aldrich, 99.99%) was degassed in a round-bottom flask for 6 h before adding 6 mL anhydrous Pyridine (Sigma Aldrich). The solution was then held at 40 °C and stirred for 48 h to form a transparent solution, then filtered with a 0.45 μm pore-sized polytetrafluoroethylene (PTFE) filter. Second, the as-prepared indium source precursor solution was added to the TiO₂ precursor solution to achieve the desired indium doping concentration (v/v). Finally, the indium-containing TiO₂ precursor solution was stirred at room temperature for 6 h to form a clear and transparent solution before use. The best 3%-In-TiO₂ precursor solution contains 3% (v/v) indium source precursor solution and 97% (v/v) TiO₂ precursor solution.

Precursor Solutions–Perovskite Precursor Solution: MAPbI₃ precursor solution was prepared by dissolving 1 mol methylamine iodine (MAI) and 1 mol PbI₂ in 1 mL anhydrous dimethyl sulphoxide (DMSO):N,N-dimethylformamide (DMF) (8:2, v/v). The Cs_{0.05}(MA_{0.17}FA_{0.83})_{0.95}Pb(I_{0.83}Br_{0.17})₃ precursor solution was prepared according to the Ref.^[39], which contains CsI (0.065 M), formamidinium iodine (FAI) (1.1 M), PbI₂ (1.2 M), methylamine bromide (MABr) (0.2 M), and PbBr₂ (0.2 M) in anhydrous DMF:DMSO (4:1, v/v).

Precursor Solutions–Spiro-OMeTAD Solution: Spiro-OMeTAD solution was prepared by dissolving 72.5 mg Spiro-OMeTAD, 28.5 μL 4-tert-butylpyridine and 17.5 μL of lithium bis(trifluoromethanesulfonyl) imide solution (520 mg mL⁻¹ in acetonitrile) in 1 mL Chlorobenzene. Note that after spin-coating the Spiro-OMeTAD solution, the substrates are placed in a humidity-control box for 12 h to ensure sufficient oxidation of the Spiro-OMeTAD film prior to electrode/contact layer deposition.

Device Fabrication and J–V Measurement: ≈50 nm In-TiO_x (or TiO₂) compact layers were deposited on the precleaned FTO (≈7 Ω/□, DeySol) and ITO (≈8–12 Ω/□, Sigma Aldrich) substrates via spin coating the In-TiO_x (or TiO₂) precursor solution at 2000 rpm for 30 s. These were then sintered at 500 °C for 30 min, and left to cool down to room temperature. Next, ≈80 nm meso-TiO₂ was deposited on the In-TiO_x (or TiO₂) compact layer via spin coating the meso-TiO₂ paste solution for 30 s at 5000 rpm with a ramp of 5000 rpm s⁻¹, where the meso-TiO₂ paste solution was prepared from 30 nm TiO₂ particle paste (30 NR-D, Dyesol) diluted in anhydrous Ethanol (1:9, w/w). After the spin coating, the samples were annealed at 100 °C for 10 min, then sintered at 500 °C for 30 min under air, and allowed to cool down to room temperature.

Device Fabrication and J–V Measurement–For MAPbI₃-Based Perovskite Cell: MAPbI₃ thin film was deposited by spin coating the MAPbI₃ precursor solution at 3500 rpm with a ramp of 3500 rpm s⁻¹ for 50 s. During this process, around 200 μL Chlorobenzene was poured on the spinning substrates after 10 s. Substrates were then annealed at 100 °C for 10 min. Then, Spiro-OMeTAD thin film was deposited via spin coating at 3000 rpm with a ramp of 3000 rpm s⁻¹ for 40 s. Finally, ≈100 nm gold was deposited through by a mask (cell's effective area, 0.16 cm²). Note that all depositions were conducted in a nitrogen-filled glovebox.

Device Fabrication and J–V Measurement–For Cs_{0.05}(MA_{0.17}FA_{0.83})_{0.95}Pb(I_{0.83}Br_{0.17})₃-Based Perovskite Cell: Cs_{0.05}(MA_{0.17}FA_{0.83})_{0.95}Pb(I_{0.83}Br_{0.17})₃ thin film was deposited by a two-step spin coating program: first at 2000 rpm with a ramp of 200 rpm s⁻¹ for 10 s, and then at 6000 rpm with a ramp of 2000 rpm s⁻¹ for 20 s. During the second step, around 100 μL Chlorobenzene was poured on the spinning substrates 5 s prior to the end of the program. Substrates were then annealed at 100 °C for 10 min. Then, Spiro-OMeTAD thin film was deposited via spin coating at 3000 rpm with a ramp of 3000 rpm s⁻¹ for 40 s. Finally, ≈100 nm gold was deposited through by a mask (cell's effective area, 0.16 cm²). Note that all depositions were conducted in a nitrogen-filled glovebox.

Device Fabrication and J–V Measurement–For Four-Terminal Tandem Cell: The semi-transparent perovskite cell (top cell) was fabricated in the following steps. (1) ≈50 nm In-TiO_x and ≈80 nm meso-TiO₂ were sequentially deposited on ITO substrate as described above. (2) ≈450 nm Cs_{0.05}(MA_{0.17}FA_{0.83})_{0.95}Pb(I_{0.83}Br_{0.17})₃ capping layer was deposited onto ITO/In-TiO_x/meso-TiO₂ substrate as described above. (3) ≈180 nm Spiro-OMeTAD thin film was coated on the top of perovskite thin film. (4) ≈13 nm MoO_x was thermally evaporated on the Spiro-OMeTAD and ≈40 nm ITO was deposited on MoO_x layer via sputtering. (5) ≈180 nm thick gold-finger contacts were deposited on the sputtered ITO through a shadow mask (cell's effective area, 0.36 cm²), where the length and width of gold-finger was 6 mm and 50 μm respectively with a surface coverage of ≈3%. (6) ≈110 nm MgF₂ anti-reflection layer was deposited on the glass side and 180 nm MgF₂ was deposited on the rear side of the semi-transparent cell. A 2.5 cm × 2.5 cm semi-transparent cell used as the filter was also fabricated according to the aforementioned steps; all parameters for the filter are identical to those of the semi-transparent cell. The IBC silicon cell (bottom cell) was fabricated according to Ref. [70].

Device Fabrication and J–V Measurement–J–V Measurement: All devices were tested under 1 sun conditions (100 mW cm⁻², AM 1.5G, 25 °C) in a solar simulator system (model #SS150 from Photo Emission Tech Inc) equipped with a Xenon lamp. The light intensity was calibrated using a certified Fraunhofer CalLab reference cell. For the perovskite solar cells, all cells' J–V curves were tested at a 50 mV s⁻¹ scan rate in a custom-built vacuum measurement jig without aperture mask. Since the cells exhibited some hysteresis between forward and reverse scans, the bias voltage for the steady-state measurements was chosen as the average of the maximum power point voltage (V_{mpp}) of the reverse and forward scan directions. Note that reverse scan is from V_{oc} to J_{sc} (forward bias → short circuit, 1.2 V → -0.1 V), and forward scan is from J_{sc} to V_{oc} (short circuit → forward bias, -0.1 V → 1.2 V). No preconditioning protocol had been used before the characterization.

The light J–V behaviors of IBC silicon cell with/without the filter were measured under standard one sun conditions (100 mW cm⁻², AM 1.5G, 25 °C) with a 2 cm × 2 cm aperture mask.

The EQE spectra of IBC silicon cell with/without the filter were tested under air using a Protoflex Corporation QE measurement AC-Mode system (QE-1400-03).

The EQE spectra of opaque and semi-transparent cells were measured with a modified Protoflex QE1400 system without light bias in direct current (DC) mode using a tungsten light source, two Keithley 2425 sourcemeters, and a reference cell. The EQE response was calibrated using a certified Fraunhofer CalLab reference cell.

All cells in this work were unencapsulated.

Characterization–XPS and UPS: XPS and ultraviolet photoelectron spectroscopy (UPS) measurements were carried out on an XPS machine (Escalab 250 Xi, Thermo Fisher), with a monochromatic Al K_{α} (1486.7 eV) X-ray source for XPS and a He I (21.2 eV) gas discharge lamp for UPS. Note that the XPS samples (FTO/In-TiO₂ and ITO/In-TiO₂) were prepared via spin coating the 3%-In-TiO₂ precursor solution.

Characterization–AFM and SEM: A tapping mode atomic force microscope (Multimode, Bruker) and a FEI Verios SEM were used to investigate the surface morphology of samples. A Helios Nanolab 600 FIB system was used to prepare cross-sectional SEM images of the cells. Note that the FTO/In-TiO₂ and ITO/In-TiO₂ samples were deposited by spin coating the 3%-In-TiO₂ precursor solution.

Characterization–Transmittance: A PerkinElmer Lambda 1050 UV/Vis/NIR spectrophotometer was used to investigate the transmittance of samples.

Characterization–XRD: X-ray diffraction analysis was performed with a Bruker D2 Phaser diffractometer operated at 30 kV, 10 mA at 2θ (Cu K_{α}) 10°–80°, step 0.02° and scan speed 2.3° min⁻¹.

Characterization–Hall Effect Measurement: Hall Effect and resistivity measurements were performed with the four contacts van der Pauw method using Lake Shore 7704A. Note that the structure of sample for Hall Effect measurement was Glass/In-TiO₂ (or TiO₂)/Au, where the thickness of In-TiO₂ (or TiO₂) and gold contact are about 50 and 200 nm, respectively. Current (10 nA) reversal was used to remove the unwanted thermal-electric effects. The magnetic field was kept between 0.1–0.4 T, positive to negative, through the measurement to remove the influence misalignment voltage. All samples were measured in air, under a dark environment, and at room temperature.

Characterization–Impedance Spectroscopy: An Auto-Lab (MEP) workstation was used as a frequency response analyser, and impedance measurements were performed in the 1.7 MHz to 1 Hz frequency range. Impedance data were analyzed using Zview equivalent circuit modelling software.

Supporting Information

Supporting Information is available from the Wiley Online Library or from the author.

Acknowledgements

J.P. and T.D. contributed equally to this paper. This work was supported by the Australian Government through the Australian Renewable Energy Agency (ARENA) and the Australian Research Council. Responsibility for the views, information, or advice expressed herein is not accepted by the Australian Government. X.Z., D.Z., and J.L. acknowledge funding from MSTC (Grant No. 2016YFA0301300), NNSFC (Grant No. 11674402), and GSTP (Grants Nos. 201607010044 and 201607020023). The work was partly conducted at the ACT node of the Australian National Fabrication Facility (ANFF), and the ANU node of the Australian Microscopy and Microanalysis Facility (AMMRF). The authors thank A. Blakers, T. Chong, K. Fong, E. Franklin, T. Kho, K. McIntosh, T. Ratcliff, M. Stocks, E.-C. Wang and S. Zin for providing the IBC silicon cell for the tandem cell measurements.

Received: August 10, 2016

Revised: September 16, 2016

Published online: November 4, 2016

- [1] A. Kojima, K. Teshima, Y. Shirai, T. Miyasaka, *J. Am. Chem. Soc.* **2009**, *131*, 6050.
- [2] M. M. Lee, J. Teuscher, T. Miyasaka, T. N. Murakami, H. J. Snaith, *Science* **2012**, *338*, 643.
- [3] H. S. Kim, C. R. Lee, J. H. Im, K. B. Lee, T. Moehl, A. Marchioro, S. J. Moon, R. Humphry-Baker, J. H. Yum, J. E. Moser, M. Grätzel, N. G. Park, *Sci. Rep.* **2012**, *2*, 591.
- [4] W. S. Yang, J. H. Noh, N. J. Jeon, Y. C. Kim, S. Ryu, J. Seo, S. I. Seok, *Science* **2015**, *348*, 1234.
- [5] X. Li, D. Bi, C. Yi, J. D. Décoppet, J. Luo, S. M. Zakeeruddin, A. Hagfeldt, M. Grätzel, *Science* **2016**, *353*, 58.
- [6] S. D. Stranks, G. E. Eperon, G. Grancini, C. Menelaou, M. J. Alcocer, T. Leijtens, L. M. Herz, A. Petrozza, H. J. Snaith, *Science* **2013**, *342*, 341.
- [7] G. Xing, N. Mathews, S. Sun, S. S. Lim, Y. M. Lam, M. Grätzel, S. Mhaisalkar, T. C. Sum, *Science* **2013**, *342*, 344.
- [8] W. Nie, H. Tsai, R. Asadpour, J. C. Blancon, A. J. Neukirch, G. Gupta, J. J. Crochet, M. Chhowalla, S. Treiaqi, M. A. Alam, *Science* **2015**, *347*, 522.
- [9] H. Zhou, Q. Chen, G. Li, S. Luo, T. B. Song, H. S. Duan, Z. Hong, J. You, Y. Liu, Y. Yang, *Science* **2014**, *345*, 542.
- [10] W. Chen, Y. Wu, Y. Yue, J. Liu, W. Zhang, X. Yang, H. Chen, E. Bi, I. Ashraf, M. Grätzel, L. Han, *Science* **2015**, *350*, 944.
- [11] V. D'Innocenzo, G. Grancini, M. J. Alcocer, A. R. Kandada, S. D. Stranks, M. M. Lee, G. Lanzani, H. J. Snaith, A. Petrozza, *Nat. Commun.* **2014**, *5*, 3586.
- [12] N. Ahn, D. Y. Son, I. H. Jang, S. M. Kang, M. Choi, N. G. Park, *J. Am. Chem. Soc.* **2015**, *137*, 8696.
- [13] NREL chart, www.nrel.gov/ncpv/images/efficiency_chart.jpg, (accessed: May, 2016).
- [14] B. Chen, Y. Bai, Z. Yu, T. Li, X. Zheng, Q. Dong, L. Shen, M. Boccard, A. Gruverman, Z. Holman, J. Huang, *Adv. Energy Mater.* **2016**, *6*, 1601128.
- [15] J. P. Mailoa, C. D. Bailie, E. C. Johlin, E. T. Hoke, A. J. Akey, W. H. Nguyen, M. D. McGehee, T. Buonassisi, *Appl. Phys. Lett.* **2015**, *106*, 121105.
- [16] S. Albrecht, M. Saliba, J. P. Correa Baena, F. Lang, L. Kegelmann, M. Mews, L. Steier, A. Abate, J. Rappich, L. Korte, R. Schlattmann, M. K. Nazeeruddin, A. Hagfeldt, M. Grätzel, B. Rech, *Energy Environ. Sci.* **2016**, *9*, 81.
- [17] C. D. Bailie, M. G. Christoforo, J. P. Mailoa, A. R. Bowring, E. L. Unger, W. H. Nguyen, J. Burschka, N. Pellet, J. Z. Lee, M. Grätzel, R. Noufi, T. Buonassisi, A. Salleo, M. D. McGehee, *Energy Environ. Sci.* **2015**, *8*, 956.
- [18] J. Werner, C. H. Weng, A. Walter, L. Fesquet, J. P. Seif, S. De Wolf, B. Niesen, C. Ballif, *J. Phys. Chem. Lett.* **2016**, *7*, 161.
- [19] F. Fu, T. Feurer, T. Jäger, E. Avancini, B. Bissig, S. Yoon, S. Buecheler, A. N. Tiwari, *Nat. Commun.* **2015**, *6*, 8932.
- [20] J. Werner, G. Dubuis, A. Walter, P. Löper, S. J. Moon, S. Nicolay, M. M. Masis, S. De Wolf, B. Niesen, C. Ballif, *Sol. Energy Mater. Sol. Cells* **2015**, *141*, 407.
- [21] D. P. McMeekin, G. Sadoughi, W. Rehman, G. E. Eperon, M. Saliba, M. T. Hörantner, A. Haghighirad, N. Sakai, L. Korte, B. Rech, M. B. Johnston, L. M. Herz, H. J. Snaith, *Science* **2016**, *351*, 151.
- [22] J. Burschka, N. Pellet, S. J. Moon, R. H. Baker, P. Gao, M. K. Nazeeruddin, M. Grätzel, *Nature* **2013**, *499*, 316.
- [23] W. Ke, C. Xiao, C. Wang, B. Saparov, H. S. Duan, D. Zhao, Z. Xiao, P. Schulz, S. P. Harvey, W. Liao, W. Meng, Y. Yu, A. J. Cimaroli, C. S. Jiang, K. Zhu, M. A. Jassim, G. Fang, D. B. Mitzi, Y. Yan, *Adv. Mater.* **2016**, *28*, 5214.
- [24] P. W. Liang, C. Y. Liao, C. C. Chueh, F. Zuo, S. T. Williams, X. K. Xin, J. Lin, A. K. Jen, *Adv. Mater.* **2014**, *26*, 3748.
- [25] C. G. Wu, C. H. Chiang, Z. L. Tseng, M. K. Nazeeruddin, A. Hagfeldt, M. Grätzel, *Energy Environ. Sci.* **2015**, *8*, 2725.

- [26] X. Li, M. Ibrahim Dar, C. Yi, J. Luo, M. Tschumi, S. M. Zakeeruddin, M. K. Nazeeruddin, H. Han, M. Grätzel, *Nat. Chem.* **2015**, *7*, 703.
- [27] M. Xiao, F. Huang, W. Huang, Y. Dkhissi, Y. Zhu, J. Etheridge, A. G. Weale, U. Bach, Y. B. Cheng, L. Spiccia, *Angew. Chem. Int. Ed.* **2014**, *53*, 9898.
- [28] N. J. Jeon, J. H. Noh, Y. C. Kim, W. S. Yang, S. Ryu, S. I. Seok, *Nat. Mater.* **2014**, *13*, 897.
- [29] M. Liu, M. B. Johnston, H. J. Snaith, *Nature* **2013**, *501*, 395.
- [30] T. Zhang, M. Yang, Y. Zhao, K. Zhu, *Nano Lett.* **2015**, *15*, 3959.
- [31] Q. Chen, H. Zhou, Z. Hong, S. Luo, H. S. Duan, H. H. Wang, Y. Liu, G. Li, Y. Yang, *J. Am. Chem. Soc.* **2014**, *136*, 622.
- [32] Y. Wu, A. Islam, X. Yang, C. Qin, J. Liu, K. Zhang, W. Peng, L. Han, *Energy Environ. Sci.* **2014**, *7*, 2934.
- [33] Q. Dong, Y. Yuan, Y. Shao, Y. Fang, Q. Wang, J. Huang, *Energy Environ. Sci.* **2015**, *8*, 2464.
- [34] J. You, Y. Yang, Z. Hong, T. B. Song, L. Meng, Y. Liu, C. Jiang, H. Zhou, W. H. Chang, G. Li, Y. Yang, *Appl. Phys. Lett.* **2014**, *105*, 183902.
- [35] K. Wang, C. Liu, P. Du, J. Zheng, X. Gong, *Energy Environ. Sci.* **2015**, *8*, 1245.
- [36] C. H. Chiang, C. G. Wu, *Nat. Photon.* **2016**, *10*, 196.
- [37] J. W. Lee, D. J. Seol, A. N. Cho, N. G. Park, *Adv. Mater.* **2014**, *26*, 4991.
- [38] Z. K. Wang, M. Li, Y. G. Yang, Y. Hu, H. Ma, X. Y. Gao, L. S. Liao, *Adv. Mater.* **2016**, *28*, 6695.
- [39] M. Saliba, T. Matsui, J. Y. Seo, K. Domanski, J. P. C. Baena, M. K. Nazeeruddin, S. M. Zakeeruddin, W. Tress, A. Abate, A. Hagfeldt, M. Grätzel, *Energy Environ. Sci.* **2016**, *9*, 1989.
- [40] N. J. Jeon, J. H. Noh, W. S. Yang, Y. C. Kim, S. Ryu, J. Seo, S. I. Seok, *Nature* **2015**, *517*, 476.
- [41] D. Bi, W. Tress, M. I. Dar, P. Gao, J. Luo, C. Renevier, K. Schenk, A. Abate, F. Giordano, J. P. C. Baena, J. D. Decoppet, S. M. Zakeeruddin, M. K. Nazeeruddin, M. Grätzel, *Sci. Adv.* **2016**, *2*, e1501170.
- [42] N. J. Jeon, J. Lee, J. H. Noh, M. K. Nazeeruddin, M. Grätzel, S. I. Seok, *J. Am. Chem. Soc.* **2013**, *135*, 19087.
- [43] Z. Yu, L. Sun, *Adv. Energy Mater.* **2015**, *5*, 1500213.
- [44] D. Liu, T. L. Kelly, *Nat. Photon.* **2014**, *8*, 133.
- [45] F. Giordano, A. Abate, J. P. Correa Baena, M. Saliba, T. Matsui, S. H. Im, S. M. Zakeeruddin, M. K. Nazeeruddin, A. Hagfeldt, M. Grätzel, *Nat. Commun.* **2016**, *7*, 10379.
- [46] P. Docampo, J. M. Ball, M. Darwich, G. E. Eperon, H. J. Snaith, *Nat. Commun.* **2013**, *4*, 2761.
- [47] S. S. Shin, W. S. Yang, J. H. Noh, J. H. Suk, N. J. Jeon, J. H. Park, J. S. Kim, W. M. Seong, S. I. Seok, *Nat. Commun.* **2015**, *6*, 7410.
- [48] J. T. W. Wang, J. M. Ball, E. M. Barea, A. Abate, J. A. A. Webber, J. Huang, M. Saliba, I. N. M. Sero, J. Bisquert, H. J. Snaith, *Nano Lett.* **2013**, *14*, 724.
- [49] C. Wang, D. Zhao, C. R. Grice, W. Liao, Y. Yu, A. Cimaroli, N. Shrestha, P. J. Roland, J. Chen, Z. Yu, P. Liu, N. Cheng, R. J. Ellingson, X. Zhao, Y. Yan, *J. Mater. Chem. A* **2016**, *4*, 12080.
- [50] S. Ryu, J. Seo, S. S. Shin, Y. C. Kim, N. J. Jeon, J. H. Noh, S. I. Seok, *J. Mater. Chem. A* **2015**, *3*, 3271.
- [51] K. Wojciechowski, T. Leijtens, S. Siprova, C. Schlueter, M. T. Horantner, J. T. Wang, C. Z. Li, A. K. Jen, T. L. Lee, H. J. Snaith, *J. Phys. Chem. Lett.* **2015**, *6*, 2399.
- [52] L. Zuo, Z. Gu, T. Ye, W. Fu, G. Wu, H. Li, H. Chen, *J. Am. Chem. Soc.* **2015**, *137*, 2674.
- [53] H. Yoon, S. M. Kang, J. K. Lee, M. Choi, *Energy Environ. Sci.* **2016**, *9*, 2262.
- [54] C. Tao, S. Neutzner, L. Colella, S. Marras, A. R. Srimath Kandada, M. Gandini, M. D. Bastiani, G. Pace, L. Manna, M. Caironi, C. Bertarelli, A. Petrozza, *Energy Environ. Sci.* **2015**, *8*, 2365.
- [55] J. P. Correa Baena, L. Steier, W. Tress, M. Saliba, S. Neutzner, T. Matsui, F. Giordano, T. J. Jacobsson, A. R. Srimath Kandada, S. M. Zakeeruddin, A. Petrozza, A. Abate, M. K. Nazeeruddin, M. Grätzel, A. Hagfeldt, *Energy Environ. Sci.* **2015**, *8*, 2928.
- [56] Q. Liu, M. C. Qin, W. J. Ke, X. L. Zheng, Z. Chen, P. L. Qin, L. B. Xiong, H. W. Lei, J. W. Wan, J. Wen, G. Yang, J. J. Ma, Z. Y. Zhang, G. J. Fang, *Adv. Funct. Mater.* **2016**, *26*, 6069.
- [57] Z. Yuan, Z. Wu, S. Bai, Z. Xia, W. Xu, T. Song, H. Wu, L. Xu, J. Si, Y. Jin, B. Sun, *Adv. Energy Mater.* **2015**, *5*, 1500038.
- [58] J. Y. Jeng, Y. F. Chiang, M. H. Lee, S. R. Peng, T. F. Guo, P. Chen, T. C. Wen, *Adv. Mater.* **2013**, *25*, 3727.
- [59] K. Wojciechowski, M. Saliba, T. Leijtens, A. Abate, H. J. Snaith, *Energy Environ. Sci.* **2014**, *7*, 1142.
- [60] P. Qin, A. L. Domanski, A. K. Chandiran, R. Berger, H. J. Butt, M. I. Dar, T. Moehl, N. Tetreault, P. Gao, S. Ahmad, M. K. Nazeeruddin, M. Grätzel, *Nanoscale* **2014**, *6*, 1508.
- [61] S. K. Pathak, A. Abate, P. Ruckdeschel, B. Roose, K. C. Gödel, Y. Vaynzof, A. Santhala, S. I. Watanabe, D. J. Hollman, N. Noel, A. Sepe, U. Wiesner, R. Friend, H. J. Snaith, U. Steiner, *Adv. Funct. Mater.* **2014**, *24*, 6046.
- [62] M. Lv, W. Lv, X. Fang, P. Sun, B. Lin, S. Zhang, X. Xu, J. Ding, N. Yuan, *RSC Adv.* **2016**, *6*, 35044.
- [63] L. S. Oh, D. H. Kim, J. A. Lee, S. S. Shin, J. W. Lee, I. J. Park, M. J. Ko, N. G. Park, S. G. Pyo, K. S. Hong, J. Y. Kim, *J. Phys. Chem. C* **2014**, *118*, 22991.
- [64] P. W. Liang, C. C. Chueh, S. T. Williams, A. K. Y. Jen, *Adv. Energy Mater.* **2015**, *5*, 1402321.
- [65] B. M. Reddy, B. Chowdhury, P. G. Smirniotis, *Appl. Catal. A: Gen.* **2001**, *219*, 53.
- [66] J. You, L. Meng, T. B. Song, T. F. Guo, Y. Yang, W. H. Chang, Z. Hong, H. Chen, H. Zhou, Q. Chen, Y. Liu, N. De Marco, Y. Yang, *Nat. Nanotechnol.* **2016**, *11*, 75.
- [67] C. O'Rourke, D. R. Bowler, *J. Phys. Chem. C* **2014**, *118*, 7261.
- [68] T. Duong, N. Lal, D. Grant, D. Jacobs, P. Zheng, S. Rahman, H. Shen, M. Stocks, A. Blakers, K. Weber, T. P. White, K. R. Catchpole, *IEEE J. Photovol.* **2016**, *6*, 679.
- [69] K. A. Bush, C. D. Bailie, Y. Chen, A. R. Bowring, W. Wang, W. Ma, T. Leijtens, F. Moghadam, M. D. McGehee, *Adv. Mater.* **2016**, *28*, 3937.
- [70] E. Franklin, K. Fong, K. McIntosh, A. Fell, A. Blakers, T. Kho, D. Walter, D. Wang, N. Zin, M. Stocks, E.-C. Wang, N. Grant, Y. Wan, Y. Yang, X. Zhang, Z. Feng, P. J. Verlinden, *Prog. Photovol.: Res. Appl.* **2016**, *24*, 411.

Chapter 3: Interface Passivation Using Ultrathin Polymer-Fullerene Films for High-Efficiency Perovskite Solar Cells with Negligible Hysteresis

The combination of interface recombination and ion migration have been proven to be the main cause of the V_{oc} loss and the commonly-observed J - V hysteresis in many perovskite solar cells.^[1-8] This implies that the defects/trap-states located at or near to the perovskite-transport layers surface or interface need to be passivated or removed for achieving high-efficiency, hysteresis-free perovskite solar cells.^[1-3]

As we discussed in Chapter 2, extrinsic indium dopants can effectively minimize the density of defects/traps within TiO_x , thus improving the V_{oc} and considerably reducing the J - V hysteresis for perovskite cells. However, the perovskite cells using indium-doped TiO_x ETLs still exhibited an absolute efficiency variation of ~1% - 1.5% for hysteresis and a relative low V_{oc} (~1.10 V).

To further mitigate the J - V hysteresis and boost the voltage, an ultrathin (less than 5 nm) PMMA:PCBM passivation layer was introduced into the interface between the meso- TiO_2 ETL and perovskite active layer. It is evident from our results that the PMMA:PCBM passivation layer can significantly passivate the localized defects/traps at the meso- TiO_2 /perovskite interface, as demonstrated by photoluminescence (PL) imaging and time-resolved PL analysis. The reduced non-radiative recombination allows a significant increment in V_{oc} of as much as 80 mV, leading to a champion voltage of 1.18 V and a high efficiency of 20.4% for mixed cation perovskite cells. In addition, negligible hysteresis in J - V behavior was also observed in the passivated cells, resulting in very fast V_{oc} and J_{sc} response times of less than 3 seconds under changes in illumination.

Detailed results and discussion are provided in the attached paper.

References

- [1] Y. Yang, M. Yang, D. T. Moore, Y. Yan, E. M. Miller, K. Zhu, *et al.*, "Top and bottom surfaces limit carrier lifetime in lead iodide perovskite films," *Nature Energy*, vol. 2, pp. 16207, 2017.
- [2] H. Tan, A. Jain, O. Voznyy, X. Lan, F. P. G. de Arquer, J. Z. Fan, *et al.*, "Efficient and stable solution-processed planar perovskite solar cells via contact passivation," *Science*, vol. 355, pp. 722-726, 2017.
- [3] J.-P. Correa-Baena, W. Tress, K. Domanski, E. H. Anaraki, S.-H. Turren-Cruz, B. Roose, *et al.*, "Identifying and suppressing interfacial recombination to achieve high open-circuit voltage in perovskite solar cells," *Energy & Environmental Science*, vol. 10, pp. 1207-1212, 2017.
- [4] Q. Wang, Q. Dong, T. Li, A. Gruverman, and J. Huang, "Thin Insulating Tunneling Contacts for Efficient and Water-Resistant Perovskite Solar Cells," *Advanced Materials*, vol. 28, pp. 6734-6739, 2016.
- [5] Y. Hou, W. Chen, D. Baran, T. Stubhan, N. A. Luechinger, B. Hartmeier, *et al.*, "Overcoming the Interface Losses in Planar Heterojunction Perovskite-Based Solar Cells," *Advanced Materials*, vol. 28, pp. 5112-5120, 2016.
- [6] G. Richardson, S. E. O'Kane, R. G. Niemann, T. A. Peltola, J. M. Foster, P. J. Cameron, *et al.*, "Can slow-moving ions explain hysteresis in the current-voltage curves of perovskite solar cells?," *Energy & Environmental Science*, vol. 9, pp. 1476-1485, 2016.
- [7] I. Zarazua, G. Han, P. P. Boix, S. Mhaisalkar, F. Fabregat-Santiago, I. Mora-Seró, *et al.*, "Surface Recombination and Collection Efficiency in Perovskite Solar Cells from Impedance Analysis," *The Journal of Physical Chemistry Letter*, vol. 7, pp. 5105-5113, 2016.
- [8] D. A. Jacobs, Y. Wu, H. Shen, C. Barugkin, F. J. Beck, T. P. White, *et al.*, "Hysteresis phenomena in perovskite solar cells: the many and varied effects of ionic accumulation," *Physical Chemistry Chemical Physics*, vol. 19, pp. 3094-3103, 2017.

Cite this: *Energy Environ. Sci.*,
2017, 10, 1792

Interface passivation using ultrathin polymer–fullerene films for high-efficiency perovskite solar cells with negligible hysteresis†

Jun Peng,¹ Yiliang Wu,¹ Wang Ye,² Daniel A. Jacobs,³ Heping Shen,¹
Xiao Fu,¹ Yimao Wan,¹ The Duong,¹ Nandi Wu,¹ Chog Barugkin,¹
Hieu T. Nguyen,¹ Dingyong Zhong,² Juntao Li,² Teng Lu,³ Yun Liu,³
Mark N. Lockrey,⁴ Klaus J. Weber,¹ Kylie R. Catchpole¹ and Thomas P. White^{1*}

Interfacial carrier recombination is one of the dominant loss mechanisms in high efficiency perovskite solar cells, and has also been linked to hysteresis and slow transient responses in these cells. Here we demonstrate an ultrathin passivation layer consisting of a PMMA:PCBM mixture that can effectively passivate defects at or near to the perovskite/TiO₂ interface, significantly suppressing interfacial recombination. The passivation layer increases the open circuit voltage of mixed-cation perovskite cells by as much as 80 mV, with champion cells achieving $V_{oc} \sim 1.18$ V. As a result, we obtain efficient and stable perovskite solar cells with a steady-state PCE of 20.4% and negligible hysteresis over a large range of scan rates. In addition, we show that the passivated cells exhibit very fast current and voltage response times of less than 3 s under cyclic illumination. This new passivation approach addresses one of the key limitations of current perovskite cells, and paves the way to further efficiency gains through interface engineering.

Received 23rd April 2017,
Accepted 20th June 2017
DOI: 10.1039/c7ee01096f

rsc.li/ees

Broader context

Metal halide perovskite solar cells have attracted tremendous attention and rapidly risen to the forefront of the emerging photovoltaic technologies in the past five years. However, most perovskite solar cells reported so far still suffer from low open-circuit voltage well below the theoretical limit (~ 1.33 V). Several recent studies have identified carrier recombination at the perovskite/transport layer interfaces as being the dominant loss mechanism in high-efficiency perovskite cells, resulting from localized defects/trap states at the interfaces. Interface recombination and trapping also contributes to the commonly-observed hysteresis and slow transient responses of many perovskite cells. Therefore, rational interface passivation techniques are critical for further boosting the performance of perovskite solar cells. In this work, we demonstrate the use of ultrathin polymer–fullerene blend films as passivation layers to effectively suppress interface recombination at the perovskite/electron transport layer interface. This approach successfully addresses one of the key limitations of the perovskite solar cells, and paves the way to boost its efficiencies beyond 22%.

Introduction

Solution-processed hybrid organic/inorganic perovskite solar cells have achieved certified power conversion efficiency (PCE)

of over 22%¹ within seven years' development, and are regarded as promising candidates for next-generation thin-film solar cells.^{2–8} State-of-the-art perovskite solar cells use mixed-cation perovskite compositions with a sandwich structure of ETL/perovskite/HTL, where ETL and HTL are the electron transport layer and hole transport layer, respectively.^{3–5} To date numerous organic and inorganic HTLs and ETLs with suitable work functions and high charge mobility have been developed to improve the energy level alignment and to facilitate charge extraction, with the ultimate aim of enhancing the PCE of perovskite solar cells.^{9–14} However, most perovskite solar cells reported so far suffer from a relatively low open-circuit voltage (V_{oc}) (well below the theoretical limit of ~ 1.33 V),^{2,13,15,16} and current–voltage (J – V) hysteresis. Recent studies suggest that both of these major issues are related to the presence of defects and trap

¹ Research School of Engineering, The Australian National University, Canberra, ACT, 2601, Australia. E-mail: u5686151@anu.edu.au, pengjun.88.81@gmail.com, thomas.white@anu.edu.au

² State Key Laboratory of Optoelectronic Materials and Technologies, School of Physics, Sun Yat-sen University, Guangzhou 510275, China

³ Research School of Chemistry, The Australian National University, Canberra, ACT, 2601, Australia

⁴ Australian National Fabrication Facility, Department of Electronic Materials Engineering, Research School of Physics & Engineering, The Australian National University, Canberra, ACT, 2601, Australia

† Electronic supplementary information (ESI) available. See DOI: 10.1039/c7ee01096f

states at the perovskite/ETL and/or perovskite/HTL interfaces.^{3,9,17–19} Interfacial carrier recombination impacts perovskite photovoltaic performance, leading to reduced carrier lifetimes, and voltage loss.^{3,17} Furthermore, the combination of ion migration in the perovskite film, and interfacial recombination is thought to be responsible for many of the observed hysteresis behaviours.^{20–22} Consequently, rational interface passivation techniques are critical for further improving the performance of perovskite solar cells.^{3,23,24}

There are three main approaches for reducing the impact of interfacial recombination in perovskite solar cells. The first is to reduce the host materials' defect density by adding dopants.^{4,9,13,15,25–27} For example, Giordano *et al.*⁹ demonstrated lithium doping of TiO₂ ETLs as a way to passivate trap states within the TiO₂ lattice, increasing V_{oc} from 1.04 V to 1.114 V, and producing cells with negligible hysteresis. Saliba *et al.*⁴ reported a perovskite solar cell with a stabilized PCE of 21.6% and an impressive V_{oc} of 1.18 V by incorporating the Li-doped meso-TiO₂ scaffold and Rb-containing perovskite. The second approach is to use alternative transport layer materials that have lower defect densities and/or form better quality interfaces to perovskite.^{10,11,17,28–33} For example, Correa Baena *et al.*²⁹ and Wang *et al.*³⁰ replaced the commonly-used TiO₂ ETL with SnO₂ and achieved reduced hysteresis and V_{oc} values of 1.14 V and 1.12 V, respectively. Correa Baena *et al.*¹⁷ also showed that reducing the doping concentration of the Spiro-OMeTAD (2,2',7,7'-tetraakis-(*N,N*-di-4-methoxyphenylamino)-9,9'-spirobifluorene) HTL can suppress interfacial recombination, producing a stabilized PCE of approx. 20% with V_{oc} = 1.17 V.

The third approach to reduce interfacial recombination is to introduce a very thin passivation layer between the perovskite and transport layers.^{18,19,34–39} For example, Zhang *et al.*³⁵ showed that a very thin fullerene derivative (α -bis-PCBM) layer between the perovskite and the Spiro-OMeTAD HTL can reduce cell degradation and passivate defects at the perovskite/HTL interface, yielding a PCE of 20.8%, and V_{oc} = 1.13 V. Similarly, Koushik *et al.*³⁷ and Wang *et al.*³⁹ used ultrathin layers of Al₂O₃ and poly(methyl methacrylate) (PMMA) respectively to passivate the perovskite/Spiro-OMeTAD interface, resulting in improved V_{oc} (1.08 V and 1.06 V respectively) and reduced hysteresis. Recently, Tan *et al.*³ reported that chlorine-capped TiO₂ colloidal nanocrystal ETLs can mitigate interfacial recombination and improve interface binding, resulting in a high V_{oc} of 1.189 V, a certified PCE of 20.1%, and negligible hysteresis. While these examples show that reducing interface recombination is crucial for improving V_{oc} and cell efficiency, only a very small number of interfacial passivation methods reported so far have produced cells with V_{oc} > 1.15 V,^{3,4,17,28} and even the best perovskite cells still have voltages well below the theoretical limit.^{2–7,15,25,40,41} Hence, there is a clear need to develop new interface passivation approaches to realize the full potential of perovskite photovoltaics.

In this work, we use very thin layers of PMMA:PCBM mixtures to suppress interfacial recombination at the perovskite/mesoporous-TiO₂ interface of high-efficiency mixed-cation perovskite cells. We show that PMMA provides exceptional passivation, increasing V_{oc} by up to 80 mV, but at the expense

of conductivity (and hence fill factor (FF)). However, the addition of PCBM to the film allows us to tune the passivation/conductivity (V_{oc} /FF) trade-off to maximize efficiency, resulting in a cell with a steady-state PCE of 20.4%, V_{oc} = 1.16 V and negligible hysteresis. We further show that the passivated cells have some of the fastest transient responses reported to date; reaching steady-state conditions less than 3 s after illumination, compared to more than 40 s for control cells.

Results and discussion

To evaluate the passivation performance of ultrathin PMMA:PCBM (less than 5 nm, estimated from the profile atomic force microscopy (AFM) measurement, see Fig. S1, ESI[†]) films at the perovskite/ETL interface, we prepared cells with six different conditions: a control cell (no passivation layer), and cells with PMMA:PCBM ratios (w/w) of 1:0 (pure PMMA), 1:1, 1:3, 1:5 and 0:1 (pure PCBM). All other cell fabrication steps were kept the same and more than 20 cells were prepared for each condition. The final device structure was FTO/c-In-TiO_x (~70 nm)/m-TiO₂ (~110 nm)/passivation layer/perovskite (capping layer ~480 nm)/Spiro-OMeTAD (~160 nm)/Au (Fig. 1a and b), where c-In-TiO_x and m-TiO₂ represent compact indium-doped TiO_x layer²⁷ and mesoporous TiO₂ layer, respectively; and perovskite stands for Cs_{0.07}Rb_{0.03}FA_{0.765}MA_{0.135}PbI_{2.55}Br_{0.45}.

To ensure that the composition and quality of the perovskite film is not influenced by the underlying passivation layer, we investigated the deposited perovskite films using X-ray diffraction (XRD) and scanning electron microscopy (SEM). The XRD spectra show no systematic variations with substrates, and no obvious PbI₂ or other non-perovskite phases, as well as no significant variation in crystallite size (see Fig. S2, ESI[†]). We also observe no significant differences in the top-morphology of the pinhole-free and uniform perovskite films on different substrates in SEM images (see Fig. S3, ESI[†]). In addition, the evidence from backscattered electron (BSE) imaging measurements and energy dispersive X-ray (EDX) analysis further support our XRD and SEM results (see Fig. S4 and S5, ESI[†]). From these results we conclude that the bulk quality of the perovskite films is unaffected by the passivation layer, and will be the same in all of the control and passivated cells.

The performance characteristics and distribution of results for each cell condition are plotted in Fig. 1c–f. Fig. 1c shows a dramatic increase in V_{oc} from 1.08 V (mean V_{oc}) for the control cells to ~1.16 V (mean V_{oc}) for the cells with a pure PMMA passivation layer at the m-TiO₂/perovskite interface. The highest V_{oc} for these cells was ~1.18 V. We attribute this significant improvement to the excellent passivation properties of the PMMA, which has previously been used to passivate the perovskite/HTL interface,³⁹ and has also been shown to passivate surface trap states and suppress hysteresis in ZnO field-effect transistors and quantum-dot light-emitting devices.^{42,43} Although the exact passivation mechanism in our cells is unclear, previous work suggests that the PMMA could serve a double-passivation role, reducing defects on both the perovskite and TiO₂ surfaces.

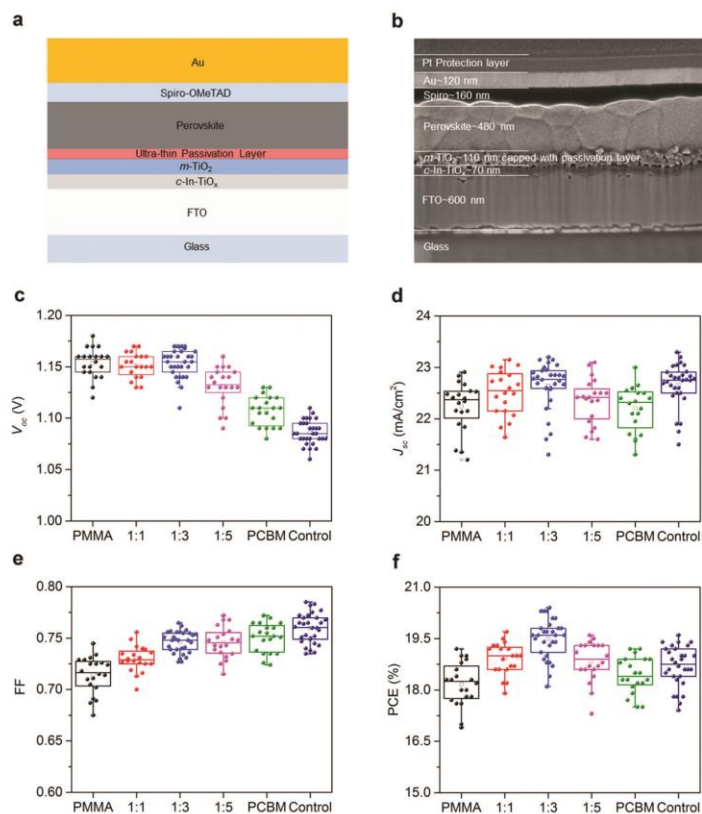


Fig. 1 (a) Schematic of the standard device structure. (b) SEM cross-section of a perovskite solar cell with the structure FTO/c-In-TiO_x/meso-TiO₂/passivation layer/perovskite/Spiro/Au. The perovskite composition is Cs_{0.07}Rb_{0.03}FA_{0.765}MA_{0.135}PbI_{2.55}Br_{0.45}. (c–f) Statistical distribution of the photovoltaic parameters for cells with/without PMMA, PMMA:PCBM, and PCBM passivation layer: (c) distribution of V_{oc} ; (d) distribution of J_{sc} ; (e) distribution of FF; (f) distribution of PCE. Note that the Pt protection layer seen in (b) was only used to prepare the focused ion beam (FIB) SEM cross-sectional image. Results are shown for 140 cells (30 cells for the control and 1:3, and 20 cells for the others) collected from 4 different batches. All devices were tested at a 50 mV s⁻¹ reverse scan rate.

On the ETL side, the cross-linked PMMA film protects the TiO₂ surface from oxygen adsorption which can cause depletion of surface electrons and increased recombination.^{39,43} At the same time, the PMMA may also passivate defects/deep trap centres caused by the dangling bonds (under-coordinated lead ions or iodine terminations) localized at the perovskite surface, as has been suggested by Kong *et al.*⁴⁴ This latter passivation mechanism is similar to that already reported for PCBM¹⁸ and thiophene/pyridine.⁴⁵

As expected, the mean value of FF for the pure PMMA cells was lower than that of the control cells, due to the increased series resistance of the non-conducting PMMA (Fig. 1e). Accordingly, we mixed PCBM, an n-type organic material with a good electron mobility,⁴⁶ into the PMMA to form PMMA:PCBM blend films in an attempt to reduce the series resistance. The role of the PCBM

as an additive in increasing the conductivity of PMMA:PCBM blend films was confirmed by conductive atomic force microscopy (C-AFM) measurements (see Fig. S6, ESI†). As can be seen in Fig. 1c, The mean V_{oc} values (~1.16 V) for the cells with PMMA:PCBM ratios of 1:1 and 1:3 show negligible difference compared to the cells passivated with pure PMMA. However, a decreased V_{oc} (mean ~1.13 V) was observed for a PMMA:PCBM ratio of 1:5. Fig. 1e shows that the FF increases with PCBM content, as expected from an increase in the passivation layer's conductivity. The cell with the pure PCBM passivation layer also showed an increased V_{oc} (~1.11 V) relative to the control cell, consistent with previous reports that PCBM can passivate perovskite grain boundaries and reduce defects/trap states at or near perovskite interfaces.^{18,19,47} The voltage improvement, however is significantly lower than for the optimum PMMA:PCBM

blend, indicating the superior passivation properties of PMMA in this situation.

We next consider the short-circuit current density (J_{sc}), which also shows some dependence on the passivation layer, although much less significant than for the V_{oc} and FF. Since the perovskite and HTL layers in each cell should be identical, one possible origin of J_{sc} differences is the optical properties of the passivation layer. Therefore, we measured the transmittance of the substrates prepared with the different passivation layers (see Fig. S7, ESI†). As expected, the transmittance of the sample with the pure PMMA film is almost identical to the control sample due to the large optical bandgap of the PMMA. The pure PCBM sample had the lowest transmittance, with the highest losses at visible wavelengths where PCBM is known to be absorbing and is widely used as an acceptor in organic solar cells.⁴⁸ As expected, the transmittance of the PMMA:PCBM samples decreases with increasing PCBM content.

Fig. 1d shows that the measured J_{sc} of the control cell, and the cells passivated with pure PCBM and PMMA:PCBM ratios of 1:3 and 1:5 follow the trends predicted by the transmittance data, with the control cell having the highest mean J_{sc} ($\sim 22.7 \text{ mA cm}^{-2}$), and the PCBM cell having the lowest (22.2 mA cm^{-2}). We note, however, that the J_{sc} reduces slightly again with increasing PMMA ratio; the cell with the 1:1 PMMA:PCBM passivation layer has a lower J_{sc} than the 1:3 ratio cell, and the cell with the pure PMMA film has a J_{sc} similar to the pure PCBM cell. This trend cannot be explained by the

transmittance measurements and most likely results from a slight reduction in carrier collection efficiency, the origin of which is not yet known.

The combined effect of the observed trends in V_{oc} , FF and J_{sc} can be seen in Fig. 1f, which shows the PCE distributions for each cell condition. From this figure it is clear that the optimum ratio of PMMA:PCBM is 1:3, resulting in a mean PCE of 19.5%; corresponding to an absolute efficiency gain of 1.1% compared to that of the control cells (mean PCE 18.4%).

The energy band alignment at the perovskite/ETL interface is another important parameter that can influence open circuit voltage. To investigate this possibility further, we measured the work function of FTO/c-In-TiO_x/m-TiO₂ and FTO/c-In-TiO_x/m-TiO₂/PMMA:PCBM samples with different blend ratios using ultraviolet photoelectron spectroscopy (UPS). As shown in Fig. S8 (ESI†), the WF of FTO/c-In-TiO_x/m-TiO₂/PMMA ($\sim 3.97 \text{ eV}$) shows only a 30 meV shift relative to the control FTO/c-In-TiO_x/m-TiO₂ ($\sim 4.0 \text{ eV}$) sample, while the FTO/c-In-TiO_x/m-TiO₂/PCBM has a 60 meV shift ($\sim 3.94 \text{ eV}$). Predictably, samples with PMMA:PCBM blends show WF shifts of 40–50 meV relative to the control. Given the relatively small changes in WF and the lack of obvious correlation with measured V_{oc} we infer that the shift in WF with the addition of the ultrathin films is not a dominant contribution to the improved cell performance.

To further characterize the passivation performance of the PMMA:PCBM layers, we also investigated the photo-luminescence (PL) intensity of four different complete cells using PL imaging

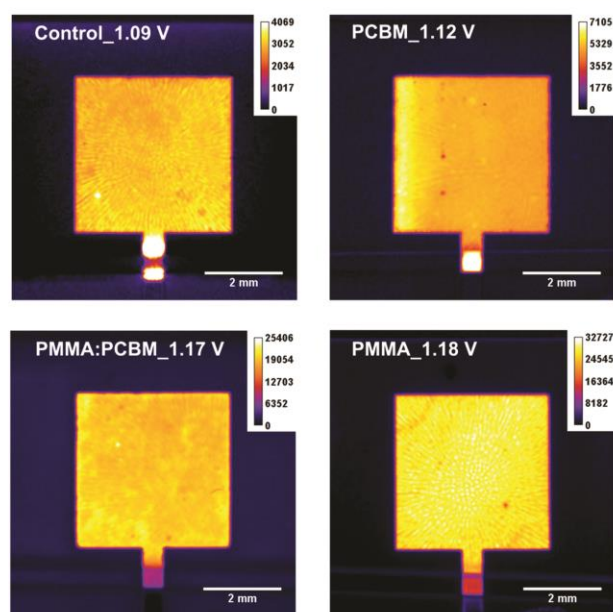


Fig. 2 Photoluminescence (PL) images of a control (no passivation layer) cell and cells with PCBM, PMMA:PCBM (1:3), and PMMA passivation layers.

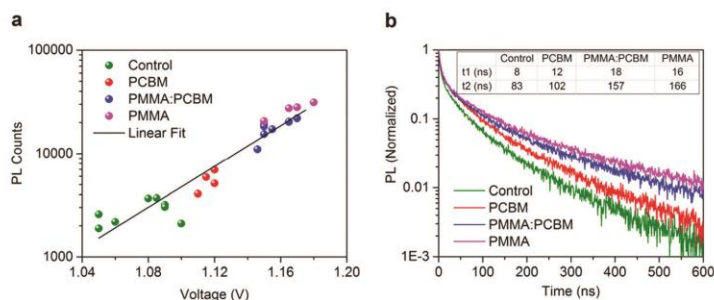


Fig. 3 (a) Logarithmic plot of PL intensity vs. V_{oc} . (b) Time-resolved photoluminescence (TRPL) decay measurements for the perovskite thin films on FTO/c-In-TiO_x/m-TiO₂ substrates with/without PCBM, PMMA:PCBM (1:3) or PMMA passivation layer.

under open-circuit condition (see Fig. 2). As expected, the cells with the highest V_{oc} have the highest PL intensity. In an ideal cell at $T = 300$ K, the steady-state PL intensity will increase by tenfold if the open circuit voltage increases by ~ 60 mV.^{49–51} A logarithmic plot of PL intensity vs. V_{oc} (Fig. 3a) shows a clear linear relationship for our cells, with a slope of ~ 101 mV per decade. This higher value than the theory may result from a potential barrier at one or both interfaces causing ion accumulation, as has been reported previously.⁵¹ Another possibility is energy level misalignment at the perovskite/ETL and/or perovskite/HTL interfaces contributing to V_{oc} loss, especially in the samples with higher interfacial recombination. Nevertheless, the clear logarithmic relationship between PL intensity and V_{oc} across multiple cells is notable given that few papers have shown this trend before for perovskite cells.

Defect related recombination can normally be divided into bulk and interface defects. The bulk defects within perovskite absorber are not expected to change with the addition of the passivation layers given the XRD and SEM observations discussed earlier. Therefore, the more than six-fold increase in PL intensity for our best passivated cells suggest that the surface recombination at or near to the perovskite/ETL interfaces is significantly suppressed by the addition of the thin PMMA:PCBM film.

The steady-state PL results are supported by time-resolved photoluminescence (TRPL) decay measurements. Transient PL curves for perovskite thin films on FTO/c-In-TiO_x/m-TiO₂ substrates with/without PCBM, PMMA:PCBM (1:3) or PMMA passivation layer are plotted in Fig. 3b, showing a much slower PL decay for the passivated samples compared to the unpassivated control. A bi-exponential model in the decay analysis software was used to fit the PL decay data and extract the lifetimes shown in the table inserted in the Fig. 3b. The control sample has a fast decay lifetime $\tau_1 = 8$ ns and a slow decay lifetime $\tau_2 = 83$ ns. In contrast, the perovskite thin films with the PMMA:PCBM (or PMMA) passivation layers have a $\tau_1 = 18$ ns (16 ns) and $\tau_2 = 157$ ns (166 ns), respectively. The lifetimes of the pure PCBM coated samples lie between these samples and the control. We therefore find that both the fast and slow PL lifetime components increase as a result of the passivation. These observations further support our conclusions from the

full cell results and steady-state PL measurements that the ultra-thin PMMA:PCBM film effectively reduces non-radiative recombination at the perovskite/ETL interface by reducing the density of defects and trap states, resulting in the dramatic increase in open-circuit voltage. In addition, the evidence from space charge limited current (SCLC) measurements for our passivated and non-passivated cells may further support our findings obtained from the steady-state PL and transient PL measurements (see Fig. S9, ESI†).

Fig. 4 shows the performance of our champion control and passivated cells. The control cell, without a passivation layer, has a PCE of 19.6%, $V_{oc} = 1.09$ V, $J_{sc} = 23.2$ mA cm⁻² and FF = 0.775 obtained from a reverse J - V scan at 50 mV s⁻¹ scan rate (see Fig. 4a). However, due to some hysteresis, the efficiency is $\sim 0.9\%$ lower when measured by a forward scan at the same rate. In contrast, the cell with the PMMA:PCBM (1:3) passivation layer shows negligible hysteresis between reverse and forward J - V scans at 50 mV s⁻¹ scan rate, achieving a PCE of 20.4%, $V_{oc} = 1.16$ V, $J_{sc} = 23.1$ mA cm⁻² and FF = 0.762 (see Fig. 4b). Integrated current densities from the measured external quantum efficiency (EQE) spectra of both control and passivated cells are within 6% of the J_{sc} values extracted from the J - V curves (see Fig. S10, ESI†). Note when comparing the transmission data (Fig. S7, ESI†) and EQE data (Fig. S10, ESI†) that the reflection of FTO/c-In-TiO_x/m-TiO₂/mixed-cation perovskite/Spiro-OMeTAD/Au is lower than that of FTO/c-In-TiO_x/m-TiO₂, due to the more gradual change of refractive index of the layers within the structure, as well as the absorption within the perovskite for wavelengths below 750 nm.

Steady-state efficiencies measured at the maximum power point voltage (V_{mpp}) for both control and passivated cells are also provided in Fig. S11 (ESI†). The steady-state efficiency of 18.5% for the control cell is 1.1% lower than the value obtained from the J - V scan due to hysteresis effects. For the passivated cell, however, the steady-state PCE (20.4%, tested at 0.97 V) matches exactly the PCE measured from both the reverse and forward J - V scans.

To further demonstrate the very low hysteresis of our passivated cells, we measured the cells at different scan rates varying from fast (500 mV s⁻¹) to very slow (1 mV s⁻¹). As shown

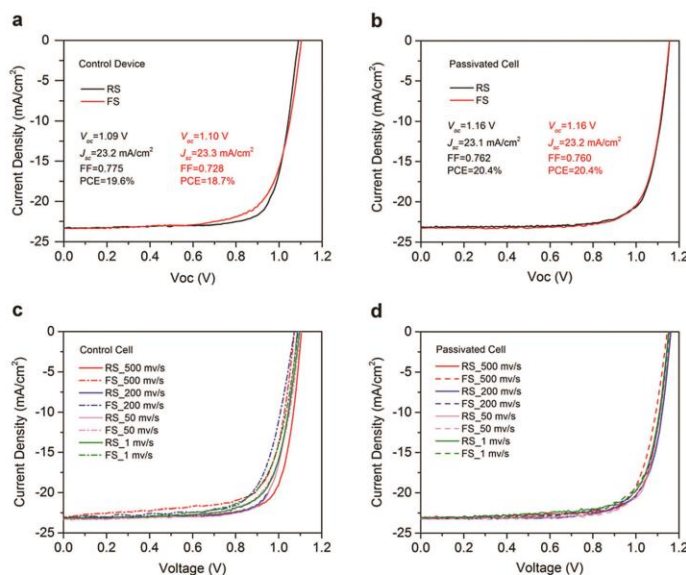


Fig. 4 Photovoltaic parameters of champion control and passivated cells. (a) Current density–voltage curves of the control cell. (b) Current density–voltage curves of the passivated cell with PMMA:PCBM (1:3) passivation layer. (c) Current density–voltage curves of the control cell measured at different scan rates. (d) Current density–voltage curves of the passivated cell measured at different scan rates. Note that the legend label RS represents reverse scan (from V_{oc} to J_{sc}), and the FS represents forward scan (from J_{sc} to V_{oc}).

in Fig. 4c and d, we found that the hysteresis of the control cell gets worse when tested at fast scan rates of 200 mV s^{-1} and 500 mV s^{-1} , or very slow scan rates of 1 mV s^{-1} . On the other hand, the passivated cell shows negligible hysteresis between reverse and forward scans under different scan rates. The detailed performance parameters of the control cell and passivated cell are also provided in Table S1 (ESI[†]) and Table S2 (ESI[†]). We also summarize in Table S3 (ESI[†]) the performance parameters of the best n–i–p perovskite cells reported in the literature so far with efficiencies above 20%.

The low hysteresis in the passivated cells is a direct consequence of the very rapid response times of these cells, as seen in transient V_{oc} and J_{sc} measurements under light/dark cycling (Fig. 5). This data was obtained in the following way: first, fresh cells were kept in the dark with no pre-conditioning, until the V_{oc} (or J_{sc}) was stable ($V_{oc} \sim 0$, or $J_{sc} \sim 0$) for 100 s; next, the light (solar simulator, one sun intensity) was switched on and the V_{oc} (or J_{sc}) was tracked over time until it reached a steady value (maximum V_{oc} or J_{sc}); finally the light was switched off and the V_{oc} (or J_{sc}) was tracked for another 300 s. This was repeated four more times (Fig. 5).

As shown in Fig. 5, the passivated cell exhibits a much faster response than the control cell. Zooming on the first dark/light transition (Fig. 5a and c) reveals that the V_{oc} of the passivated cell reaches a steady-state maximum in less than 3 s. In contrast, the control cell took around 40 s for the V_{oc} to stabilize. There is also a significant difference in response

when the light is switched off: while the V_{oc} of the passivated cell rapidly drops back to 0 V, the V_{oc} of the control cell initially drops rapidly to 0.2 V, and then decreases much more slowly to ~ 0.1 V after 300 s. As a consequence of this slow voltage decay, the response of the control cell to the first illumination cycle is different to the second and subsequent cycles, whereas the response of the passivated cell is the same on each cycle.

There are a number of possible explanations for the difference in transient behaviour of the control and passivated cells, two of which are the slow release of trapped ions or charge carriers. Several sources have suggested that ion trapping at the TiO_2 interface may contribute to the slow response time of cells prepared on TiO_2 substrates.^{52,53} The availability of ionic traps would be greatly reduced by the passivation layers, so that fewer ions are trapped and released, resulting in a much faster response. Alternatively, the voltage transient at the end of the illumination cycle may be due to injection of carriers into the perovskite⁵⁴ from interfacial defects that become filled with carriers (electrons or holes) during illumination. When illumination is turned off, these carriers may de-trap over timescales of seconds leading to a transient voltage.⁵⁴ Again, passivation of the interface would reduce the trapped carrier concentration, leading to a faster transient response. We stress, however, that there are several other possible mechanisms responsible for the transient voltage decay, and further work would be required to establish the exact cause.

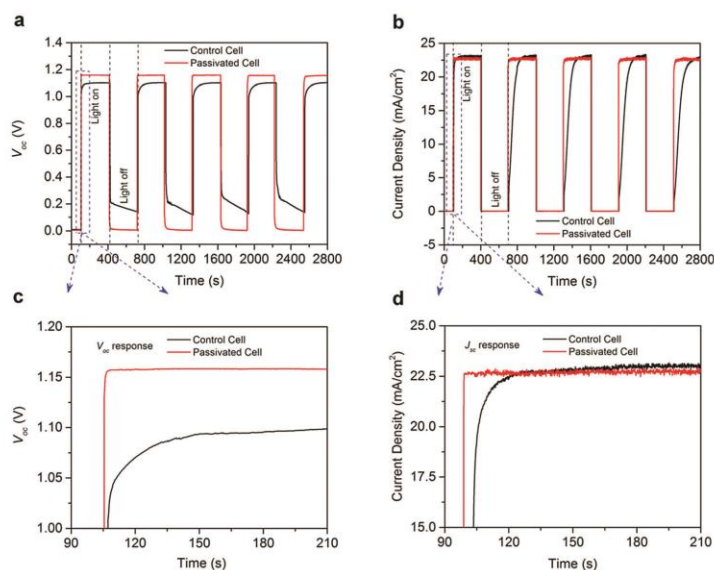


Fig. 5 V_{oc} and J_{sc} response tests for control and passivated cells under cyclic illumination. (a and c) V_{oc} response; (b and d) J_{sc} response. Note that (c and d) are zoomed-in versions of (a and b), respectively.

The dark/light J_{sc} response for the cells with/without PMMA:PCBM passivation layer are also provided in Fig. 5b and d. Similarly to the V_{oc} , the J_{sc} response of the passivated cell shows a much smaller delay than the control cell. These very rapid V_{oc} and J_{sc} response rates are some of the fastest ever reported for perovskite cells.^{4,17,25,28}

We have also conducted 12 h light/dark cycling to simulate day/night operation of the cells as shown in Fig. 6. In these tests the cells were held at the V_{mpp} during the light part of the cycle, and open circuit during the dark part of the cycle. Impressively, the steady-state PCE of the passivated cell exhibits an excellent stability (the steady-state PCE \sim 19.4%) under continuous

operation at V_{mpp} after four cycles of the 12-hour-light/dark test compared to the control cell which dropped in efficiency from 18.5% to 16.2%. This suggests that the passivation layer may also protect the cells from degradation associated with repeated light/dark cycling, perhaps by reducing the availability of ion trapping sites.⁵⁵

Conclusions

We have shown that ultrathin PMMA:PCBM blend films can effectively passivate the perovskite/m-TiO₂ interface of high efficiency perovskite cells, leading to a significant reduction in interfacial recombination and a dramatic increase in V_{oc} from 1.1 V (control cell) to 1.18 V (passivated cell). By optimizing the PMMA:PCBM ratio to achieve both high V_{oc} and fill-factor we obtained stable perovskite solar cells with a steady-state PCE of 20.4% and negligible hysteresis. The optimized cells also exhibit an exceptionally rapid current and voltage response when illuminated, reaching steady-state V_{oc} or J_{sc} in less than 3 s. This new passivation approach addresses one of the main limitations of current high-efficiency perovskite solar cells – interface recombination – and demonstrates the potential for ultrathin passivation layers to significantly improve cell performance. Furthermore, our finding that pure PMMA films provided the best passivation, but insufficient conductivity, indicates the potential for further improvements if new n-type polymer materials can be developed with appropriate band alignment and carrier mobility.

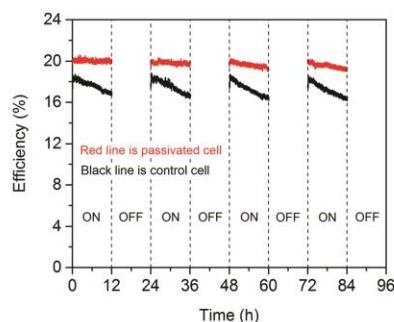


Fig. 6 The stability of the control cell and passivated cell under four cycles of 12 h illumination (on)/12 h dark (off).

Author contribution

J. P. conceived and designed the overall experiments. J. P., Y. W., H. S., T. D., N. W. and D. J. prepared and characterized the perovskite cell devices. Y. W. and N. W. conducted the PL imaging measurements and analysis. W. Y., D. Z. and J. L. conducted the XPS/UPS measurements and analysis. X. F. and H. N. performed the TRPL measurements and analysis. H. S. and T. D. conducted the XRD and SEM measurements and analysis. C. B. conducted the optical transmittance measurements and analysis. T. L. and Y. L. conducted the C-AFM measurements and analysis. M. N. L. conducted the EDX (SEM) measurements and analysis. J. P., D. J., K. J. W., K. R. C. and T. P. W. contributed to the results analysis and interpretation. The manuscript was mainly written and revised by J. P. and T. P. W. All authors contributed to the discussion of the results and commented on the manuscript.

Acknowledgements

This work was supported by the Australian Government through the Australian Renewable Energy Agency (ARENA) and the Australian Research Council. Responsibility for the views, information or advice expressed herein is not accepted by the Australian Government. W. Y., D. Z. and J. L. acknowledge funding from MSTC (Grant No. 2016YFA0301300), NNSFC (Grant No. 11674402) and GSTP (Grant No. 201607010044, 201607020023). The work was partly conducted at the ACT node of the Australian National Fabrication Facility (ANFF), and the ANU node of the Australian Microscopy and Microanalysis Facility (AMMRF). The authors thank X. Z. Zhou and J. Xiang for discussing the UPS measurements.

References

- NREL chart, www.nrel.gov/ncpv/images/efficiency_chart.jpg, accessed: April 2017.
- W. S. Yang, J. H. Noh, N. J. Jeon, Y. C. Kim, S. Ryu, J. Seo and S. I. Seok, *Science*, 2015, **348**, 1234–1237.
- H. Tan, A. Jain, O. Voznyy, X. Lan, F. P. G. de Arquer, J. Z. Fan, R. Quintero-Bermudez, M. Yuan, B. Zhang and Y. Zhao, *Science*, 2017, **355**, 722–726.
- M. Saliba, T. Matsui, K. Domanski, J.-Y. Seo, A. Ummadisingu, S. M. Zakeeruddin, J.-P. Correa-Baena, W. R. Tress, A. Abate and A. Hagfeldt, *Science*, 2016, **354**, 206–209.
- X. Li, D. Bi, C. Yi, J. D. Decoppet, J. Luo, S. M. Zakeeruddin, A. Hagfeldt and M. Grätzel, *Science*, 2016, **353**, 58–62.
- D. Bi, W. Tress, M. I. Dar, P. Gao, J. Luo, C. Renevier, K. Schenk, A. Abate, F. Giordano, J. P. Correa Baena, J. D. Decoppet, S. M. Zakeeruddin, M. K. Nazeeruddin, M. Grätzel and A. Hagfeldt, *Sci. Adv.*, 2016, **2**, e1501170.
- Q. Jiang, L. Zhang, H. Wang, X. Yang, J. Meng, H. Liu, Z. Yin, J. Wu, X. Zhang and J. You, *Nat. Energy*, 2016, **2**, 16177.
- C. Momblona, L. Gil-Escrig, E. Bandiello, E. M. Hutter, M. Sessolo, K. Lederer, J. Blochwitz-Nimoth and H. J. Bolink, *Energy Environ. Sci.*, 2016, **9**, 3456–3463.
- F. Giordano, A. Abate, J. P. Correa Baena, M. Saliba, T. Matsui, S. H. Im, S. M. Zakeeruddin, M. K. Nazeeruddin, A. Hagfeldt and M. Grätzel, *Nat. Commun.*, 2016, **7**, 10379.
- J. You, L. Meng, T.-B. Song, T.-F. Guo, Y. Yang, W.-H. Chang, Z. Hong, H. Chen, H. Zhou, Q. Chen, Y. Liu, N. De Marco and Y. Yang, *Nat. Nanotechnol.*, 2016, **11**, 75–81.
- Z. Yu and L. C. Sun, *Adv. Energy Mater.*, 2015, **5**, 1500213.
- S. S. Shin, W. S. Yang, J. H. Noh, J. H. Suk, N. J. Jeon, J. H. Park, J. S. Kim, W. M. Seong and S. I. Seok, *Nat. Commun.*, 2015, **6**, 7410.
- H. Zhou, Q. Chen, G. Li, S. Luo, T.-b. Song, H.-S. Duan, Z. Hong, J. You, Y. Liu and Y. Yang, *Science*, 2014, **345**, 542–546.
- J. T.-W. Wang, J. M. Ball, E. M. Barea, A. Abate, J. A. Alexander-Webber, J. Huang, M. Saliba, I. n. Mora-Sero, J. Bisquert and H. J. Snaith, *Nano Lett.*, 2013, **14**, 724–730.
- S. S. Shin, E. J. Yeom, W. S. Yang, S. Hur, M. G. Kim, J. Im, J. Seo, J. H. Noh and S. I. Seok, *Science*, 2017, **356**, 167–171.
- W. Tress, *Adv. Energy Mater.*, 2017, 1602358, DOI: 10.1002/aenm.201602358.
- J.-P. Correa-Baena, W. Tress, K. Domanski, E. H. Anaraki, S.-H. Turren-Cruz, B. Roose, P. P. Boix, M. Grätzel, M. Saliba and A. Abate, *Energy Environ. Sci.*, 2017, **10**, 1207–1212.
- Y. Shao, Z. Xiao, C. Bi, Y. Yuan and J. Huang, *Nat. Commun.*, 2014, **5**, 5784.
- C. Tao, S. Neutzner, L. Colella, S. Marras, A. R. S. Kandada, M. Gandini, M. De Bastiani, G. Pace, L. Manna, M. Caironi, C. Bertarelli and A. Petrozza, *Energy Environ. Sci.*, 2015, **8**, 2365–2370.
- D. A. Jacobs, Y. Wu, H. Shen, C. Barugkin, F. J. Beck, T. P. White, K. Weber and K. R. Catchpole, *Phys. Chem. Chem. Phys.*, 2017, **19**, 3094–3103.
- B. Chen, M. Yang, S. Priya and K. Zhu, *J. Phys. Chem. Lett.*, 2016, **7**, 905–917.
- G. Richardson, S. E. O’Kane, R. G. Niemann, T. A. Peltola, J. M. Foster, P. J. Cameron and A. B. Walker, *Energy Environ. Sci.*, 2016, **9**, 1476–1485.
- Y. Yang, M. Yang, D. T. Moore, Y. Yan, E. M. Miller, K. Zhu and M. C. Beard, *Nat. Energy*, 2017, **2**, 16207.
- Y. Hou, W. Chen, D. Baran, T. Stubhan, N. A. Luechinger, B. Hartmeier, M. Richter, J. Min, S. Chen and C. O. R. Quiroz, *Adv. Mater.*, 2016, **28**, 5112–5120.
- M. Saliba, T. Matsui, J.-Y. Seo, K. Domanski, J.-P. Correa-Baena, M. K. Nazeeruddin, S. M. Zakeeruddin, W. Tress, A. Abate, A. Hagfeldt and M. Grätzel, *Energy Environ. Sci.*, 2016, **9**, 1989–1997.
- S. K. Pathak, A. Abate, P. Ruckdeschel, B. Roose, K. C. Gödel, Y. Vaynzof, A. Santhala, S.-I. Watanabe, D. J. Hollman, N. Noel, A. Sepe, U. Wiesner, R. Friend, H. J. Snaith and U. Steiner, *Adv. Funct. Mater.*, 2014, **24**, 6046–6055.
- J. Peng, T. Duong, X. Z. Zhou, H. P. Shen, Y. L. Wu, H. K. Mulmudi, Y. M. Wan, D. Y. Zhong, J. T. Li, T. Tsuzuki, K. J. Weber, K. R. Catchpole and T. P. White, *Adv. Energy Mater.*, 2017, **7**, 1601768.
- E. H. Anaraki, A. Kermanpur, L. Steier, K. Domanski, T. Matsui, W. Tress, M. Saliba, A. Abate, M. Grätzel,

- A. Hagfeldt and J. P. Correa-Baena, *Energy Environ. Sci.*, 2016, **9**, 3128–3134.
- 29 J. P. Correa Baena, L. Steier, W. Tress, M. Saliba, S. Neutzner, T. Matsui, F. Giordano, T. J. Jacobsson, A. R. Srimath Kandada, S. M. Zakeeruddin, A. Petrozza, A. Abate, M. K. Nazeeruddin, M. Gratzel and A. Hagfeldt, *Energy Environ. Sci.*, 2015, **8**, 2928–2934.
- 30 C. L. Wang, D. W. Zhao, C. R. Grice, W. Q. Liao, Y. Yu, A. Cimaroli, N. Shrestha, P. J. Roland, J. Chen, Z. H. Yu, P. Liu, N. Cheng, R. J. Ellingson, X. Z. Zhao and Y. F. Yan, *J. Mater. Chem. A*, 2016, **4**, 12080–12087.
- 31 N. J. Jeon, J. Lee, J. H. Noh, M. K. Nazeeruddin, M. Gratzel and S. I. Seok, *J. Am. Chem. Soc.*, 2013, **135**, 19087–19090.
- 32 Z. Yuan, Z. Wu, S. Bai, Z. Xia, W. Xu, T. Song, H. Wu, L. Xu, J. Si, Y. Jin and B. Sun, *Adv. Energy Mater.*, 2015, **5**, 1500038.
- 33 T. Ye, S. Ma, X. Jiang, L. Wei, C. Vijila and S. Ramakrishna, *Adv. Funct. Mater.*, 2017, 1606545, DOI: 10.1002/adfm.201606545.
- 34 Q. Wang, Q. Dong, T. Li, A. Gruverman and J. Huang, *Adv. Mater.*, 2016, **28**, 6734–6739.
- 35 F. Zhang, W. Shi, J. Luo, N. Pellet, C. Yi, X. Li, X. Zhao, T. J. Dennis, X. Li, S. Wang, Y. Xiao, S. M. Zakeeruddin, D. Bi and M. Gratzel, *Adv. Mater.*, 2017, 1606806, DOI: 10.1002/adma.201606806.
- 36 C. Tao, J. Van Der Velden, L. Cabau, N. F. Montcada, S. Neutzner, S. Kandada, A. Ram, S. Marras, L. Brambilla and M. Tommasini, *Adv. Mater.*, 2017, **29**, 1604493.
- 37 D. Koushik, W. J. H. Verhees, Y. H. Kuang, S. Veenstra, D. Zhang, M. A. Verheijen, M. Creatore and R. E. I. Schropp, *Energy Environ. Sci.*, 2017, **10**, 91–100.
- 38 L. Zuo, Z. Gu, T. Ye, W. Fu, G. Wu, H. Li and H. Chen, *J. Am. Chem. Soc.*, 2015, **137**, 2674–2679.
- 39 F. Wang, A. Shimazaki, F. Yang, K. Kanahashi, K. Matsuki, Y. Miyauchi, T. Takenobu, A. Wakamiya, Y. Murata and K. Matsuda, *J. Phys. Chem. C*, 2017, **121**, 1562–1568.
- 40 D. Bi, C. Yi, J. Luo, J.-D. Décoppet, F. Zhang, S. M. Zakeeruddin, X. Li, A. Hagfeldt and M. Gratzel, *Nat. Energy*, 2016, **1**, 16142.
- 41 D.-Y. Son, J.-W. Lee, Y. J. Choi, I.-H. Jang, S. Lee, P. J. Yoo, H. Shin, N. Ahn, M. Choi and D. Kim, *Nat. Energy*, 2016, **1**, 16081.
- 42 X. Dai, Z. Zhang, Y. Jin, Y. Niu, H. Cao, X. Liang, L. Chen, J. Wang and X. Peng, *Nature*, 2014, **515**, 96–99.
- 43 S. Song, W.-K. Hong, S.-S. Kwon and T. Lee, *Appl. Phys. Lett.*, 2008, **92**, 263109.
- 44 W. Kong, T. Ding, G. Bi and H. Wu, *Phys. Chem. Chem. Phys.*, 2016, **18**, 12626–12632.
- 45 N. K. Noel, A. Abate, S. D. Stranks, E. S. Parrott, V. M. Burlakov, A. Goriely and H. J. Snaith, *ACS Nano*, 2014, **8**, 9815–9821.
- 46 P.-W. Liang, C.-C. Chueh, S. T. Williams and A. K. Y. Jen, *Adv. Energy Mater.*, 2015, **5**, 1402321.
- 47 C. H. Chiang and C. G. Wu, *Nat. Photonics*, 2016, **10**, 196–200.
- 48 C. J. Brabec, S. Gowrisanker, J. J. M. Halls, D. Laird, S. Jia and S. P. Williams, *Adv. Mater.*, 2010, **22**, 3839–3856.
- 49 P. Wurfel, *J. Phys. C: Solid State Phys.*, 1982, **15**, 3967–3985.
- 50 G. Smestad and H. Ries, *Sol. Energy Mater. Sol. Cells*, 1992, **25**, 51–71.
- 51 Y. Wu, H. Shen, D. Walter, D. Jacobs, T. Duong, J. Peng, L. Jiang, Y.-B. Cheng and K. Weber, *Adv. Funct. Mater.*, 2016, **26**, 6807–6813.
- 52 H. Yu, H. P. Lu, F. Y. Xie, S. Zhou and N. Zhao, *Adv. Funct. Mater.*, 2016, **26**, 1411–1419.
- 53 I. Levine, P. K. Nayak, J. T.-W. Wang, N. Sakai, S. Van Reenen, T. M. Brenner, S. Mukhopadhyay, H. J. Snaith, G. Hodes and D. Cahen, *J. Phys. Chem. C*, 2016, **120**, 16399–16411.
- 54 A. Baumann, K. Tvingstedt, M. Heiber, S. Våth, C. Momblona, H. Bolink and V. Dyakonov, *APL Mater.*, 2014, **2**, 081501.
- 55 F. Huang, L. Jiang, A. R. Pascoe, Y. Yan, U. Bach, L. Spiccia and Y.-B. Cheng, *Nano Energy*, 2016, **27**, 509–514.

Chapter 4: A Universal Double-Side Passivation for High Open-Circuit Voltage in Perovskite Solar Cells: Role of Carbonyl Groups in Poly(methyl methacrylate)

According to the Shockley-Queisser theory, the theoretical V_{oc} limit of perovskite ($E_g \sim 1.6$ eV) is ~ 1.33 V,^[1] however, most perovskite solar cells reported so far still have V_{oc} below 1.20 V.^[2-5] Defect-induced non-radiative recombination impedes the realization of high V_{oc} in perovskite solar cells.^[6,7]

The under-coordinated Pb atoms (Pb^{2+}) have been identified as a major source of recombination-active defects/traps, reducing the V_{oc} as well as the overall device performance in perovskite solar cells.^[8,9] It is therefore critical to passivate the Pb^{2+} defects/traps to further efficiency gains.^[8,9]

Inspired by our previous work demonstrated in Chapter 3, we developed a two-sides passivation design using ultrathin polymer PMMA films to passivate both ETLs/perovskite and perovskite/HTLs interfaces. The symmetric passivating contact provided a significant reduction of non-radiative recombination, furthering the V_{oc} up to 1.22 V for normal bandgap (~ 1.6 eV) perovskite composition. Consequently, we successfully obtained a very high efficiency of 20.8% perovskite solar cells without hysteresis.

By studying the molecular interactions between PMMA and perovskite precursors *via* Fourier-transform infrared (FTIR), nuclear magnetic resonance (NMR) spectroscopy measurements and DFT calculations, we found that the functional carbonyl (C=O) groups on the PMMA take the credit for passivating the Pb^{2+} defects/traps.

Details can be found in the following manuscript.

References

- [1] W. Tress, "Perovskite Solar Cells on the Way to Their Radiative Efficiency Limit—Insights Into a Success Story of High Open-Circuit Voltage and Low Recombination," *Advanced Energy Materials*, vol. 7, pp. 1602358, 2017.
- [2] D. Bi, C. Yi, J. Luo, J.-D. Décoppet, F. Zhang, S. M. Zakeeruddin, *et al.*, "Polymer-templated nucleation and crystal growth of perovskite films for solar cells with efficiency greater than 21%," *Nature Energy*, vol. 1, pp. 16142, 2016.
- [3] Q. Jiang, L. Zhang, H. Wang, X. Yang, J. Meng, H. Liu, *et al.*, "Enhanced electron extraction using SnO₂ for high-efficiency planar-structure HC(NH₂)₂PbI₃-based perovskite solar cells," *Nature Energy*, vol. 2, pp. 16177, 2016.
- [4] D. Bi, W. Tress, M. I. Dar, P. Gao, J. Luo, C. Renevier, *et al.*, "Efficient luminescent solar cells based on tailored mixed-cation perovskites," *Science Advances*, vol. 2, pp. e1501170, 2016.
- [5] H. Zhou, Q. Chen, G. Li, S. Luo, T.-b. Song, H.-S. Duan, *et al.*, "Interface engineering of highly efficient perovskite solar cells," *Science*, vol. 345, pp. 542-546, 2014.
- [6] S. D. Stranks, "Nonradiative losses in metal halide perovskites," *ACS Energy Letters*, vol. 2, pp. 1515-1525, 2017.
- [7] H. Tan, A. Jain, O. Voznyy, X. Lan, F. P. G. de Arquer, J. Z. Fan, *et al.*, "Efficient and stable solution-processed planar perovskite solar cells via contact passivation," *Science*, vol. 355, pp. 722-726, 2017.
- [8] N. K. Noel, A. Abate, S. D. Stranks, E. S. Parrott, V. M. Burlakov, A. Goriely, *et al.*, "Enhanced photoluminescence and solar cell performance via Lewis base passivation of organic–inorganic lead halide perovskites," *ACS Nano*, vol. 8, pp. 9815-9821, 2014.
- [9] A. Abate, M. Saliba, D. J. Hollman, S. D. Stranks, K. Wojciechowski, R. Avolio, *et al.*, "Supramolecular halogen bond passivation of organic–inorganic halide perovskite solar cells," *Nano Letters*, vol. 14, pp. 3247-3254, 2014.

A Universal Double-Side Passivation for High Open-Circuit Voltage in Perovskite Solar Cells: Role of Carbonyl Groups in Poly(methyl methacrylate)

Jun Peng, Jafar I. Khan, Wenzhu Liu, Esma Ugur, The Duong, Yiliang Wu, Heping Shen, Kai Wang, Hoang Dang, Erkan Aydin, Xinbo Yang, Yimao Wan, Klaus J. Weber, Kylie R. Catchpole, Frédéric Laquai, Stefaan De Wolf,* and Thomas P. White*


The performance of state-of-the-art perovskite solar cells is currently limited by defect-induced recombination at interfaces between the perovskite and the electron and hole transport layers. These defects, most likely undercoordinated Pb and halide ions, must either be removed or passivated if cell efficiencies are to approach their theoretical limit. In this work, a universal double-side polymer passivation approach is introduced using ultrathin poly(methyl methacrylate) (PMMA) films. Very high-efficiency ($\approx 20.8\%$) perovskite cells with some of the highest open circuit voltages (1.22 V) reported for the same 1.6 eV bandgap are demonstrated. Photoluminescence imaging and transient spectroscopic measurements confirm a significant reduction in nonradiative recombination in the passivated cells, consistent with the voltage increase. Analysis of the molecular interactions between perovskite and PMMA reveals that the carbonyl (C=O) groups on the PMMA are responsible for the excellent passivation via Lewis-base electronic passivation of Pb^{2+} ions. This work provides new insights and a compelling explanation of how PMMA passivation works, and suggests future directions for developing improved passivation layers.

1. Introduction

Perovskite solar cells combine a high absorption coefficient with long carrier diffusion lengths, which are important factors explaining their rapid rise to the forefront of thin-film

J. Peng, Dr. T. Duong, Y. Wu, Dr. H. Shen, Dr. Y. Wan, Dr. K. J. Weber, Prof. K. R. Catchpole, Dr. T. P. White
Research School of Engineering
The Australian National University
Canberra, ACT 2601, Australia
E-mail: thomas.white@anu.edu.au

Dr. J. I. Khan, Dr. W. Liu, E. Ugur, Dr. K. Wang, Dr. H. Dang, Dr. E. Aydin, Dr. X. Yang, Dr. F. Laquai, Dr. S. De Wolf
King Abdullah University of Science and Technology (KAUST)
KAUST Solar Center (KSC)
Physical Sciences and Engineering Division (PSE)
Thuwal 23955-6900, Kingdom of Saudi Arabia
E-mail: stefaan.dewolf@kaust.edu.sa

 The ORCID identification number(s) for the author(s) of this article can be found under <https://doi.org/10.1002/aenm.201801208>.

DOI: 10.1002/aenm.201801208

photovoltaics (PV).^[1–6] Ever since the pioneering work by Miyasaka reporting the first perovskite solar cells with power conversion efficiencies (PCE) of $\approx 3.8\%$ in 2009,^[7] much of the research effort has been focused on controlling the perovskite composition and morphology,^[8–12] and engineering dedicated hole- and electron transport layers (HTLs and ETLs).^[13–16] Combined improvements in each of these areas have led to the current PCE record of $>22\%$.^[17] Perovskite solar cell stability is also increasing, with reports of cells maintaining high-efficiency ($>20\%$) under prolonged (≈ 1000 hours) one-sun illumination and at elevated operating temperatures (60°C).^[18] This rapid progress is encouraging for the future commercialization of perovskite PV technology.

To date, the best-performing cells use active layers consisting of a mixed halide and mixed cation perovskite composition with a bandgap (E_g) of ≈ 1.6 eV. The theoretical (Shockley–Queisser) PCE limit for this bandgap is $>30\%$; well above the current experimental record.^[19,20] A number of recent studies have identified nonradiative carrier recombination via defects (traps) at the perovskite-transport layer interfaces as a major source of efficiency loss in state-of-the-art cells.^[19] Although the exact nature of these is still to be confirmed, both theoretical and experimental evidence points to undercoordinated Pb (Pb^{2+}) and/or halide (I^-) ions as the dominant recombination-active defects at interfaces of as-deposited films, at grain boundaries, and also in the bulk.^[21–25] On a device level, nonradiative recombination via these defects reduces the open circuit voltage (V_{oc}) and overall device performance. Interface defects have also been linked to hysteresis in current–voltage characteristics,^[26,27] and may also impact long-term stability.^[28] To bridge the gap between the radiative efficiency limit and experimental PCE values, it is therefore imperative to minimize the sources of recombination in perovskite films and their interfaces.^[19,20]

Several recent studies suggest that interface passivation can significantly mitigate nonradiative recombination in cells, yielding both improved V_{oc} and device stability.^[29–38] Many of these passivation schemes target the positively charged Pb^{2+}

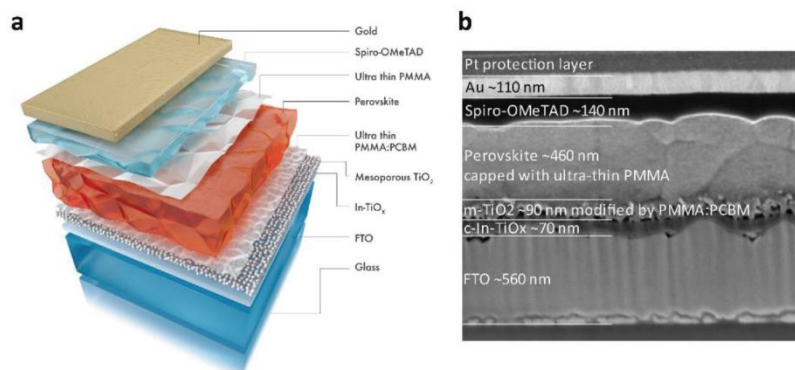


Figure 1. Schematic of the device structure and corresponding SEM cross-sectional image. a) Schematic of the device structure. b) SEM cross-sectional image of the perovskite cell. Note that the Pt protection layer seen in (b) was only used to prepare the focused ion beam (FIB) SEM cross-sectional image. “Perovskite” refers here to the composition $\text{Cs}_{0.07}\text{Rb}_{0.03}\text{FA}_{0.765}\text{MA}_{0.135}\text{PbI}_{2.55}\text{Br}_{0.45}$.

defect using electron donor materials, or Lewis-bases. This general electron-passivation approach was first identified by Noel et al., in ref. [21] where perovskite films and cells treated with the Lewis bases thiophene and pyridine were shown to display significantly increased carrier lifetimes and open-circuit voltages. Since then, various other Lewis-base passivation materials have been identified, including the polymers poly(4-vinylpyridine) (PVP),^[29] and PCDTBT,^[30] which can be applied either as an ultrathin interface layer or blended with the perovskite precursor solution.

Other organic passivation materials include fullerenes and their derivatives (e.g., C60,^[31] phenyl-C61-butyric acid methyl ester (PCBM)^[32–34]), graphene,^[35] and poly(methyl methacrylate) (PMMA).^[36–38] PCBM has been reported to passivate under-coordinated I atoms (I^-) at the surface and grain boundaries of perovskite films,^[34] but the passivation mechanism of PMMA is not well understood. PMMA has been shown by a number of groups to effectively reduce trap density and improve cell performance when inserted as an ultrathin layer either before or after the perovskite film deposition.^[36–38] This has been variously attributed to improved perovskite microstructure and surface morphology,^[36,37] filling of pinholes, and unspecified passivation of surface traps.^[38] PMMA has also been used as an additive during perovskite film deposition to control crystal growth and morphology, but its passivation properties in this case were not explicitly considered.^[36,37]

Here, we fabricate double-side passivated perovskite cells by inserting ultrathin PMMA films at both the perovskite/ETL and perovskite/HTL interfaces. This symmetric passivating-contact structure significantly reduces interface recombination, as evidenced by improved operating voltages, and corroborated by photoluminescence (PL) imaging, time-resolved photoluminescence (TRPL), and transient absorption (TA) measurements. Double-side passivated cells have been fabricated with an efficiency of 20.8% and a remarkable V_{oc} of ≈ 1.22 V with negligible hysteresis. This yields one of the lowest $E_{\text{g}} - qV_{\text{oc}}$ values reported to date (q is the elementary charge).^[39–41] The passivation mechanism is investigated using a combination of Fourier-transform infrared (FTIR) and nuclear magnetic

resonance (NMR) spectroscopy measurements, supported by density functional theory (DFT) calculations. We find strong evidence that the excellent passivation provided by the PMMA films is associated with the Lewis-base nature of the oxygen atoms in the carbonyl (C=O) groups of PMMA. We thus conclude that PMMA is similar to other Lewis-base polymer passivation layers, where donor electrons can reduce the charge state of Pb^{2+} defect ions at the perovskite/ETL and perovskite/HTL interfaces, effectively reducing nonradiative recombination. This work not only demonstrates a universal, simple and effective interface passivation treatment to boost the performance of state-of-the-art perovskite solar cells, but also provides new physical insights into passivation mechanisms that could lead to further improvements in device performance.

2. Results and Discussion

To realize a perovskite solar cell with high operating voltage and negligible hysteresis, we introduce interface passivation on both the ETL and HTL sides in multi-cation perovskite cells. Our device structure is FTO/c-In-TiO_x/m-TiO₂/PMMA:PCBM/perovskite/PMMA/Spiro-OMeTAD/Au (see Figure 1a,b), where the c-In-TiO_x,^[42] m-TiO₂, Perovskite and Spiro-OMeTAD represent compact indium-doped TiO_x, mesoporous TiO₂, $\text{Cs}_{0.07}\text{Rb}_{0.03}\text{FA}_{0.765}\text{MA}_{0.135}\text{PbI}_{2.55}\text{Br}_{0.45}$, and (2,2',7,7'-tetrakis-(*N,N*-di-4-methoxyphenylamino)-9,9'-spiro-bifluorene), respectively. The thickness of each layer is shown in the cross-sectional scanning electron microscope (SEM) image in Figure 1b. We use the perovskite solar cell devoid of any passivation layer as a control device, where the architecture is FTO/c-In-TiO_x/m-TiO₂/Perovskite/Spiro-OMeTAD/Au.

As seen in Figure 2a, the control device yielded a PCE of 19.5% from a reverse current–voltage scan, with $V_{\text{oc}} = 1.110$ V, short-circuit current density $J_{\text{sc}} = 22.85$ mA/cm² and fill-factor FF = 0.770. A small amount of hysteresis is also observed, with a forward scan yielding PCE = 18.5%. Details of the scan rate and J – V measurement procedure are provided in the Supporting Information. After inserting an ultrathin PMMA:PCBM

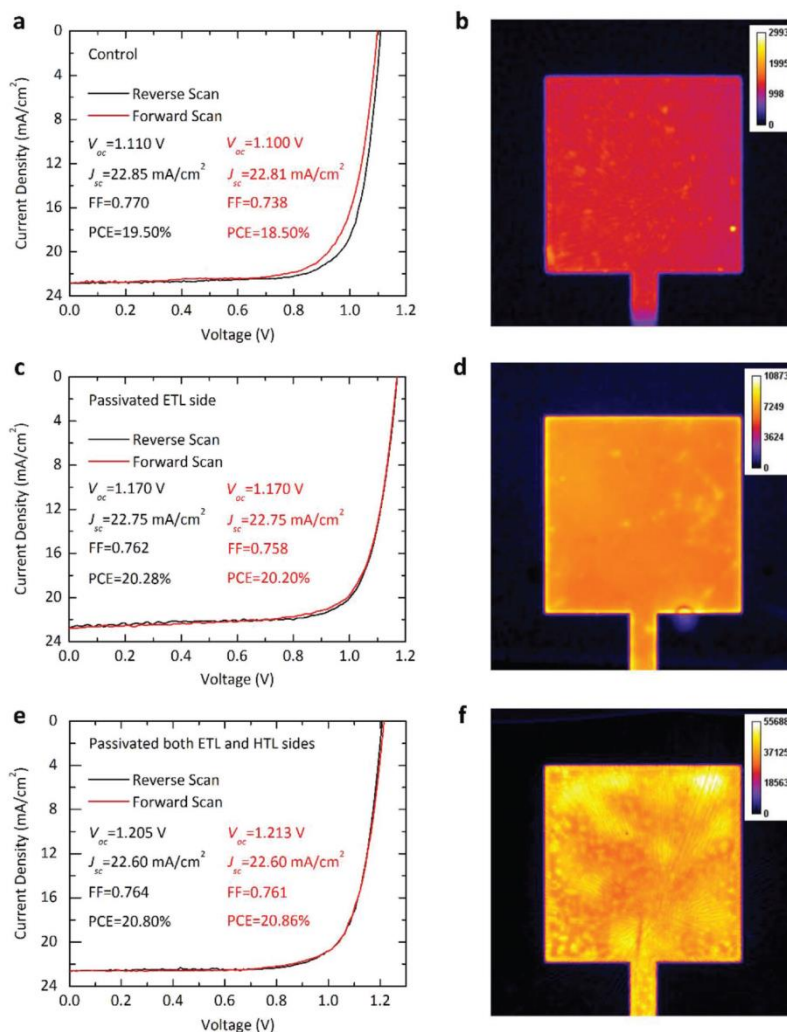


Figure 2. Device performance and PL imaging. a,b) Forward- and reverse-scan J - V curves of the control cell with a structure of FTO/c-In-TiO₂/m-TiO₂/Perovskite/Spiro-OMeTAD/Au, and its corresponding photoluminescence (PL) image. c,d) J - V curves of the passivated ETL side cell with a structure of FTO/c-In-TiO₂/m-TiO₂/PMMA:PCBM/Perovskite/Spiro-OMeTAD/Au, and its corresponding PL image. e) and f) J - V curves of the double-side passivated cell with a structure of FTO/c-In-TiO₂/m-TiO₂/PMMA:PCBM/Perovskite/PMMA/Spiro-OMeTAD/Au, and its corresponding PL image. "Perovskite" refers to the composition Cs_{0.07}Rb_{0.03}FA_{0.765}MA_{0.135}PbI_{2.55}Br_{0.45}.

passivation layer at the m-TiO₂/perovskite interface (labeled as passivated ETL side), the V_{oc} increased to 1.170 V, yielding a PCE of $\approx 20.3\%$ (see Figure 2c), which is consistent with our previous work.^[43] Inspired by this finding, we also inserted an ultrathin pure PMMA film (details in the Supporting Information) at the HTL/perovskite interface. Encouragingly, this double-side passivation significantly boosted the V_{oc} to 1.213 V, resulting in a champion cell with a PCE of $\approx 20.8\%$ and negligible hysteresis as seen in Figure 2e. Consistent with the reduced hysteresis, we also find that the transient V_{oc} response

of the double-side passivated cells is much shorter than that of the control cells, taking less than 3 s to reach their steady-state value after exposure to light (see Figure S1 in the Supporting Information).

Device performance was further characterized with steady-state efficiency and external quantum efficiency (EQE) measurements. Figure S2 (Supporting Information) shows the steady-state PCE of the control cell to be 18.7%, tested at its V_{mpp} (maximum power point voltage) of 0.93 V for 600 s. Notably, the steady-state PCE of the passivated cells was much

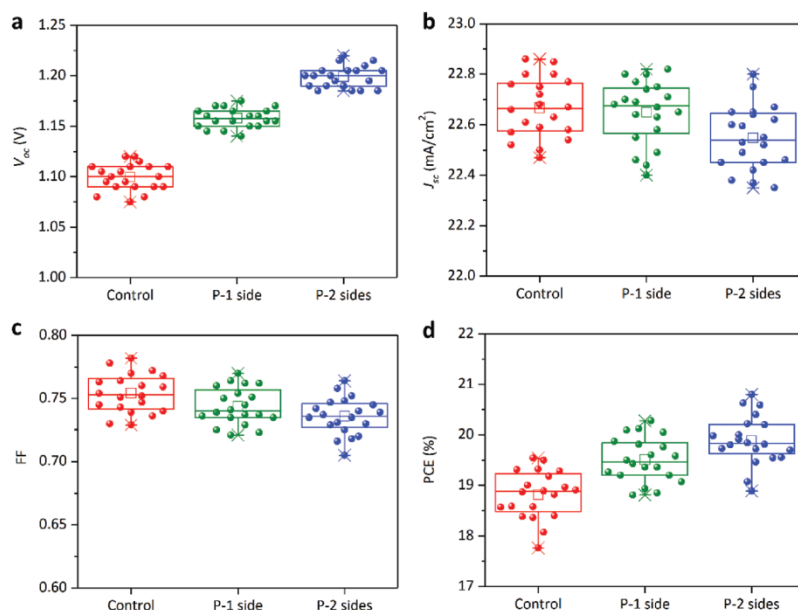


Figure 3. Statistical distribution of the photovoltaic parameters for control and passivated cells with/without PMMA:PCBM and PMMA passivation layer. a) Distribution of V_{oc} . b) Distribution of J_{sc} . c) Distribution of FF. d) Distribution of PCE. Note that “control” represents the control cells with a structure of FTO/c-In-TiO₂/m-TiO₂/Perovskite/Spiro-OMeTAD/Au; “P-1 side” represents the passivated ETL side cells with a structure of FTO/c-In-TiO₂/m-TiO₂/PMMA:PCBM/Perovskite/Spiro-OMeTAD/Au; the “P-2 side” represents the double-side passivated cells with a structure of FTO/c-In-TiO₂/m-TiO₂/PMMA:PCBM/Perovskite/PMMA/Spiro-OMeTAD/Au. “Perovskite” represents Cs_{0.07}Rb_{0.03}FA_{0.765}MA_{0.133}PbI_{2.53}Br_{0.45}. Results are shown for 60 cells (20 cells for each condition) collected from 2 different batches. All devices were tested at a 50 mV s⁻¹ reverse scan rate.

improved with respect to the control device, resulting in a stabilized PCE of 20.1% (tested at $V_{mpp} = 0.97$ V) and 20.7% (tested at $V_{mpp} = 1.0$ V) for the ETL-side passivated cell and the double-side passivated cells, respectively. We also performed a much longer (≈ 10 h) steady-state efficiency measurement (see Figure S2d in the Supporting Information), which showed that the PMMA passivation treatment effectively improves the light-soaking stability of cells. EQE measurements on the control and passivated cells show no significant variation with the addition of the passivation layers (Figure S3, Supporting Information) and the integrated current from EQE spectra are within 3% of the values obtained from current–voltage measurements.

In order to quantify more accurately the impact of the passivation layers, we fabricated and measured twenty cells for each condition (control, ETL-side passivation, double-side passivation) in two separate batches. **Figure 3** shows the detailed distribution of the performance parameters extracted from reverse-scan measurements. It is clear that the most significant impact of the passivation is to increase the V_{oc} . The average V_{oc} of the control cells is 1.10 ± 0.01 V. This increases to 1.16 ± 0.01 V with ETL-side passivation, and 1.20 ± 0.01 V for the double-side passivated cells, respectively corresponding to a relative increase of 5.4% and 9.1% compared to that of control cells. At the same time, the FF and J_{sc} for the double-side passivated cells are both reduced slightly (by 2.4% and 0.5% relative, respectively), which we attribute to a small reduction in the carrier-extraction efficiency and increased series resistance

resulting from the insulating PMMA film. Nevertheless, the small penalty in these parameters is more than compensated by the increased voltage. As a result, the average cell efficiency increases from $18.8 \pm 0.5\%$ for the control cells to $19.9 \pm 0.5\%$ for the double-side passivated cells. We also note that the best double-side passivated cell yielded a remarkable $V_{oc} = 1.22$ V (see also Figure S4 in the Supporting Information), which is amongst the highest reported values for ≈ 1.6 eV bandgap perovskite.^[39–41]

To verify that the improved device performance is a result of interface passivation, and not due to a change in bulk properties or film morphology we investigated the deposited films using X-ray diffraction (XRD) and SEM. XRD spectra reveal no systematic variations due to the passivation treatment. No obvious PbI₂ or other nonperovskite phases are observed; nor is there a significant variation in crystallite size, as shown in Figure S5 (Supporting Information). From SEM inspection there is no significant difference in the top-morphology of perovskite films in control and passivated perovskite (see Figure S6 in the Supporting Information).

Subsequently, we performed PL imaging on the control and passivated cells under open-circuit conditions (see Figures 2b,d,f). The PL intensity of the best ETL-side passivated perovskite cell and double-side passivated cell increased more than 5-fold and 34-fold, respectively compared to the control cell. From this, it is evident that the nonradiative recombination was significantly reduced by the PMMA:PCBM and PMMA

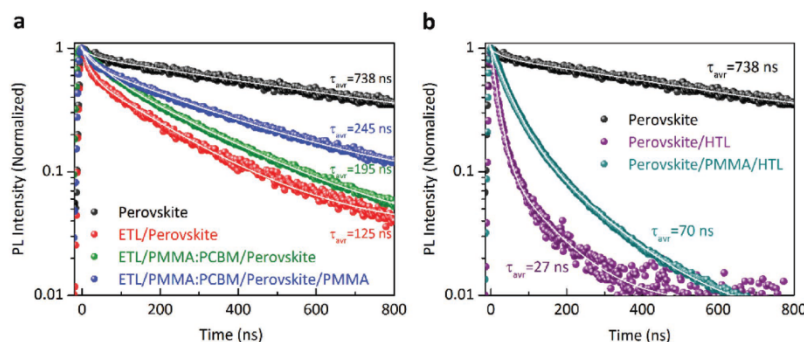


Figure 4. Photoluminescence dynamics from time-resolved (TR-PL) measurements. a) ETL only samples (illuminated from the ETL side): perovskite, ETL/perovskite, ETL/PMMA:PCBM/Perovskite and ETL/PMMA:PCBM/Perovskite/PMMA. b) HTL only samples (illuminated from the HTL side): perovskite, perovskite/HTL and perovskite/PMMA/HTL. Note that all samples were fabricated on high-grade optical quartz substrates. ETL, HTL, and perovskite represent $\text{c-In-TiO}_2/\text{m-TiO}_2$, Spiro-OMeTAD, and $\text{Cs}_{0.07}\text{Rb}_{0.03}\text{FA}_{0.765}\text{MA}_{0.135}\text{PbI}_{2.55}\text{Br}_{0.45}$, respectively.

passivation. Reduced nonradiative recombination increases the excess charge carrier density in the active layer under steady-state open circuit conditions, increasing the quasi Fermi level splitting and thus increasing the V_{oc} of the cells.^[44] This further confirms the origin of the improved V_{oc} in the passivated perovskite cells. The PL images also show good passivation uniformity over the whole device area.

A reduction in recombination rate with the introduction of the PMMA layers is also observed in time-resolved PL measurements shown in **Figure 4**. Two sets of samples were prepared to investigate separately the impact of passivating the ETL and HTL interfaces. Time-resolved PL spectra were measured from the relevant transport layer side using a 650 nm wavelength pulsed laser as the excitation source. The spectral evolution is shown in Figure S7 (Supporting Information); the perovskite layer shows the characteristic PL peak at 770 nm without any additional spectral feature. **Figure 4a** shows PL transients measured at the peak emission wavelength for representative samples with and without a passivation layer between the perovskite and the ETL (no HTL was included in these samples). To measure the impact of the extraction layer and effect of passivation on the PL dynamics, the PL transients were fitted with a sum of two exponential functions and the weighted-average lifetimes were calculated. We note that this is merely a parameterization of the PL dynamics, which lacks physical meaning. In fact, it has been shown that the photogenerated minority carrier lifetime of perovskites is dominated by a combination of first, second, and third order recombination processes. These are respectively equivalent to trap-assisted nonradiative (Shockley–Read–Hall), band-to-band radiative (bimolecular, two-particle), and Auger (three-particle) recombination, which requires fluence-dependent experiments to separate the different processes.^[45–48] However, this is beyond the scope of the present work and thus a parameterization of the decays was chosen instead. Using this parameterization of the transients, we find for the reference ETL/perovskite sample an average PL lifetime of 125 ns, while the one-side and two-side passivated samples exhibit longer average PL lifetimes of 195 and 245 ns, respectively. As reference, we also measured the pristine perovskite sample without any passivation or

interface to a charge extraction layer and found a PL lifetime of 738 ns. The PL average lifetime quenching observed upon addition of the ETL is attributed to a combined effect of carrier extraction (by the ETL) and interface recombination.^[25,49] The significant lifetime recovery observed with the addition of the ultrathin PMMA passivation layer indicates reduced interface recombination and efficient passivation of trap states and recombination centers.

Figure 4b shows PL transients for perovskite/HTL samples with and without the PMMA passivation layer (without using ETL in this configuration). Interestingly, the average PL lifetime is comparably shorter than for the ETL/perovskite samples, specifically 27 ns for the perovskite/HTL sample compared to 125 ns for the ETL/perovskite and 738 ns for the neat perovskite film, implying very fast extraction and/or introduction of significant surface recombination. However, inserting a PMMA passivation layer at the perovskite/HTL interface results in a significant increase in the PL lifetime from 27 to 70 ns.

Recombination dynamics were also investigated with transient absorption (TA) spectroscopy in the nano-to-microsecond time window using a 532 nm pulsed laser excitation source (see Supporting Information for details). Similar to the transient PL measurements, separate samples were prepared to study the ETL/perovskite and perovskite/HTL interfaces with and without a passivation layer. TA measurements were performed with the pump and probe light incident from the side closest to the interface of interest. As with the PL measurements, adding charge extraction layers leads to faster dynamics compared to neat perovskite films, while the passivated samples exhibited slower decay dynamics compared to the nonpassivated samples (see **Figure S8** in the Supporting Information).

The results presented so far show that inserting ultrathin PMMA films at the ETL/perovskite and HTL/perovskite interfaces can dramatically increase the open-circuit voltage of our cells without significant impact on the short-circuit current or fill-factor. This is accompanied by both increased PL intensity and increased carrier lifetime in the perovskite active layer, indicating a strong reduction in nonradiative carrier recombination. We thus conclude that the PMMA films can effectively passivate interface traps/defects on both sides of the perovskite

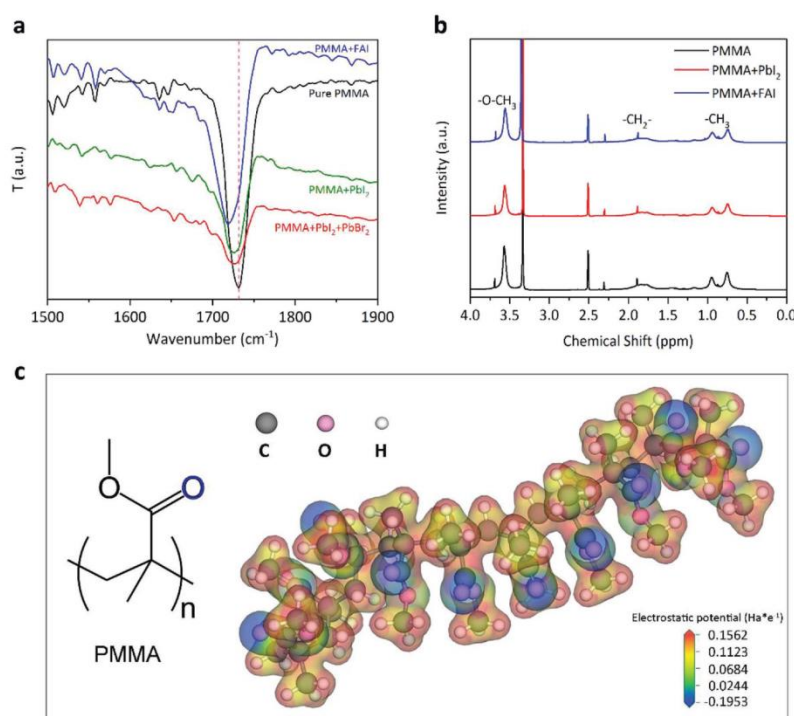


Figure 5. FTIR, NMR measurements, and DFT calculation. a) FTIR spectra of pure PMMA, PMMA + PbI₂, PMMA + PbI₂ + PbBr₂, and PMMA + FAI thin film samples. b) ¹H NMR spectra of pure PMMA, PMMA + PbI₂ and PMMA + FAI. c) Schematic diagram of the first-principle DFT calculation of the electrostatic potential for all functional groups on the PMMA chain. Details of the sample preparation are provided in the Supporting Information.

active layer while still allowing efficient carrier extraction into the charge transport layers.

We next investigate the physical origin of the passivation mechanism and the nature of the interface traps/defects being passivated. To do this, we use Fourier transform infrared (FTIR) and nuclear magnetic resonance (NMR) spectroscopy, combined with numerical simulations to identify the molecular-level interactions at the perovskite–PMMA interface.

In a previous study of polymer-templated perovskite films, Bi et al.^[36] used FTIR to study films of PMMA and PMMA + PbI₂. The spectral feature associated with the stretching vibration of the C=O covalent bond in the PMMA was found to red-shift with the addition of the Lewis acid PbI₂. This was attributed to the formation of an intermediate PMMA-PbI₂ adduct that influenced film crystallization. In a related study, Masi et al.^[37] proposed electrostatic interactions between the same C=O (carbonyl) group and positively charged MA⁺ precursor ions as playing a key role in film morphology.

Here we first use FTIR to probe the stretching vibration of the C=O bond in thin films of pure PMMA, PMMA + PbI₂, PMMA + PbI₂ + PbBr₂, and PMMA + formamidinium iodide (FAI). As can be seen in **Figure 5a**, the C=O spectral feature associated with this bond in pure PMMA film appears at 1732 cm⁻¹, but shifts to 1724 and 1725 cm⁻¹ with the addition of PbI₂ and mixed PbI₂ + PbBr₂, respectively. This indicates a weakening of

the C=O bond similar to the results of Bi et al.^[36] Interestingly, a larger spectral shift (to 1720 cm⁻¹) is measured for the PMMA + FAI thin film, which is consistent with the electrostatic interaction proposed by Masi et al., but involving FA⁺ ions rather than MA⁺. To confirm that the dominant interaction between PMMA and perovskite is via the C=O group (and not one of the other functional groups), we also measured ¹H NMR spectra of PMMA, PMMA + PbI₂ and PMMA + FAI in DMSO-d₆ solution. **Figure 5b** shows that excess PbI₂ or FAI does not affect the chemical shift of protons on PMMA, indicating that there is no significant interaction between PbI₂ or FAI with the saturated C atom or H atom on the PMMA chain. Thus, we have strong evidence that the PMMA carbonyl group can interact with multiple perovskite precursor species, the most likely in this case being positively charged Pb²⁺ and FA⁺ ions.

The oxygen atom in a carbonyl group is a Lewis base (electron donor) site due to the electron pair associated with the C=O double bond.^[50] This is clearly observed as local negative electrical charge (blue) surrounding the oxygen atoms in **Figure 5c**, which plots the electrostatic potential of a PMMA chain calculated using DFT. The interaction between this local negative charge and the Pb²⁺ and FA⁺ ions explains the red-shift observed in the FTIR spectra (**Figure 5a**). The role of Pb²⁺ defects as recombination centers on the surface and grain boundaries of solid perovskite films is widely accepted,

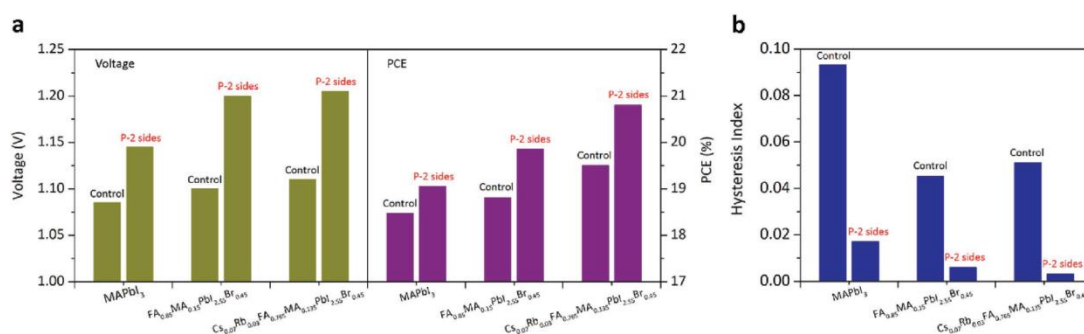


Figure 6. a) V_{oc} and PCE distribution of perovskite solar cells with different perovskite compositions. b) Hysteresis index comparison of perovskite solar cells with and without passivation. Note that “P-2 sides” represents double-side passivation; and all devices were tested at a scan rate of 50 mV s^{-1} . The hysteresis index is defined as: $|(PCE_{reverse} - PCE_{forward})|/PCE_{reverse}$.^[51]

as is the ability of Lewis base materials to passivate these defects.^[21] Therefore we conclude that the improved carrier lifetime and higher photoluminescence of films and cells shown in Figures 2 and 4 are a direct consequence of PMMA passivating undercoordinated Pb atoms at the perovskite/ETL and perovskite/HTL interfaces. This leads to the outstanding open circuit voltages and improved cell efficiencies of double-side passivated cells demonstrated in Figure 2.

To further confirm the universality of our double-side passivation approach, we tested two more sets of different types of perovskite solar cells using PMMA passivation layers. As demonstrated in the Figure 6a, all cells with double-side passivation exhibit much higher V_{oc} than the corresponding nonpassivated (control) cells, boosting their performance. The double-side passivation also significantly suppressed the $J-V$ hysteresis behavior of all cells (see Figure 6b). The detailed $J-V$ curves and $J-V$ parameters are also provided in Figure S9 and Table S1 (Supporting Information).

3. Conclusion

In summary, we demonstrated a universal double-side passivation method that passivates perovskite solar cells incorporating ultrathin PMMA-films at the perovskite-ETL and perovskite-HTL interfaces. The outstanding passivation properties of the PMMA enabled open circuit voltages up to $\approx 1.22 \text{ V}$, which is one of the highest reported for $\approx 1.6 \text{ eV}$ bandgap perovskite. A high PCE of 20.8% with negligible hysteresis was achieved for the champion passivated cells. Analysis of perovskite-PMMA interactions reveals that the passivation results from the Lewis-base properties of the carbonyl (C=O) group on the PMMA, which can effectively passivate under-coordinated lead atoms (Pb^{2+}), which are thought to cause nonradiative recombination at perovskite surfaces and grain boundaries. This finding sheds new light on previous work involving PMMA passivation layers, and may provide additional explanation for the improved performance of PMMA-templated perovskite films.^[36,37]

Although it provides excellent interface passivation, PMMA is an insulating polymer so the passivated cells did have a slightly reduced fill-factor as a result of increased series resistance. This

was mitigated on the ETL side by using a PMMA:PCBM blend, as reported previously,^[43] but future development of novel conducting polymers with C=O groups may lead to even further efficiency gains.

4. Experimental Section

Experimental details are provided in the Supporting Information.

Supporting Information

Supporting Information is available from the Wiley Online Library or from the author.

Acknowledgements

This work was supported by the Australian Government through the Australian Renewable Energy Agency (ARENA) and the Australian Research Council. Responsibility for the views, information or advice expressed herein is not accepted by the Australian Government. J.P. acknowledges the funding support from Australian Nanotechnology Network (ANN) and Department of Innovation, Industry, Science and Research (DIISR). The research reported in this publication was supported by funding from King Abdullah University of Science and Technology (KAUST). The authors thank Xavier Pita, scientific illustrator at King Abdullah University of Science and Technology (KAUST), for producing Figure 1a in this paper. J.P. conceived the idea, designed the overall experiments, and led the project. J.P., T.D., H.S., and Y.W. prepared and characterized the perovskite cell devices. J.I.K. and E.U. performed the TA and TRPL measurements and data analysis. F.L. supervised the TA and TRPL measurements and analysis. W.L., X.Y., and J. P. conducted the FTIR measurements and analysis. W.L. performed the DFT calculation. T.D., H.S., and Y.W. conducted the PL imaging measurements. H.D. conducted the XRD and SEM measurements. K.W. conducted the NMR measurements and analysis. E.A. conducted the EQE measurements. J.P., J.I.K., K.J.W., K.R.C., F.L., S.D.W., and T.P.W. contributed to the results analysis and interpretation. T.P.W. and S.D.W. supervised the project. J.P. wrote the manuscript. All authors contributed to the discussion of the results and revision of the manuscript.

Conflict of Interest

The authors declare no conflict of interest.

Keywords

carbonyl group, nonradiative recombination, passivation, perovskite solar cells, undercoordinated Pb atoms

Received: April 22, 2018

Revised: August 22, 2018

Published online:

- [1] S. D. Stranks, G. E. Eperon, G. Grancini, C. Menelaou, M. J. Alcocer, T. Leijtens, L. M. Herz, A. Petrozza, H. J. Snaith, *Science* **2013**, *342*, 341.
- [2] G. Xing, N. Mathews, S. Sun, S. S. Lim, Y. M. Lam, M. Grätzel, S. Mhaisalkar, T. C. Sum, *Science* **2013**, *342*, 344.
- [3] M. M. Lee, J. Teuscher, T. Miyasaka, T. N. Murakami, H. J. Snaith, *Science* **2012**, *338*, 643.
- [4] W. Nie, H. Tsai, R. Asadpour, J.-C. Blancon, A. J. Neukirch, G. Gupta, J. J. Crochet, M. Chhowalla, S. Tretiak, M. A. Alam, H.-L. Wang, A. D. Mohite, *Science* **2015**, *347*, 522.
- [5] H. Zhou, Q. Chen, G. Li, S. Luo, T.-B. Song, H.-S. Duan, Z. Hong, J. You, Y. Liu, Y. Yang, *Science* **2014**, *345*, 542.
- [6] V. D'Innocenzo, G. Grancini, M. J. Alcocer, A. R. S. Kandada, S. D. Stranks, M. M. Lee, G. Lanzani, H. J. Snaith, A. Petrozza, *Nat. Commun.* **2014**, *5*, 3586.
- [7] A. Kojima, K. Teshima, Y. Shirai, T. Miyasaka, *J. Am. Chem. Soc.* **2009**, *131*, 6050.
- [8] J. Burschka, N. Pellet, S.-J. Moon, R. Humphry-Baker, P. Gao, M. K. Nazeeruddin, M. Grätzel, *Nature* **2013**, *499*, 316.
- [9] J. W. Lee, D. J. Seol, A. N. Cho, N. G. Park, *Adv. Mater.* **2014**, *26*, 4991.
- [10] N. J. Jeon, J. H. Noh, W. S. Yang, Y. C. Kim, S. Ryu, J. Seo, S. I. Seok, *Nature* **2015**, *517*, 476.
- [11] Z. Wang, Q. Lin, F. P. Chmiel, N. Sakai, L. M. Herz, H. J. Snaith, *Nat. Energy* **2017**, *2*, 17135.
- [12] A. D. Jodkowski, C. Roldán-Carmona, G. Grancini, M. Salado, M. Ralaifarisoa, S. Ahmad, N. Koch, L. Camacho, G. De Miguel, M. K. Nazeeruddin, *Nat. Energy* **2017**, *2*, 972.
- [13] J. A. Christians, P. Schulz, J. S. Tinkham, T. H. Schloemer, S. P. Harvey, B. J. T. de Villers, A. Sellinger, J. J. Berry, J. M. Luther, *Nat. Energy* **2018**, *3*, 68.
- [14] M. Li, Z. K. Wang, Y. G. Yang, Y. Hu, S. L. Feng, J. M. Wang, X. Y. Gao, L. S. Liao, *Adv. Energy Mater.* **2016**, *6*, 1601156.
- [15] W. Chen, Y. Wu, Y. Yue, J. Liu, W. Zhang, X. Yang, H. Chen, E. Bi, I. Ashraf, M. Grätzel, *Science* **2015**, *350*, 944.
- [16] Y. Hou, X. Du, S. Scheiner, D. P. McMeekin, Z. Wang, N. Li, M. S. Killian, H. Chen, M. Richter, I. Levchuk, N. Schrenker, E. Spiecker, T. Stubhan, N. A. Luechinger, A. Hirsch, P. Schmuki, H.-P. Steinruck, R. H. Fink, M. Halik, H. J. Snaith, C. J. Brabec, *Science* **2017**, *358*, 1192.
- [17] W. S. Yang, B. W. Park, E. H. Jung, N. J. Jeon, Y. C. Kim, D. U. Lee, S. S. Shin, J. Seo, E. K. Kim, J. H. Noh, S. I. Seok, *Science* **2017**, *356*, 1376.
- [18] N. Arora, M. I. Dar, A. Hinderhofer, N. Pellet, F. Schreiber, S. M. Zakeeruddin, M. Grätzel, *Science* **2017**, *358*, 768.
- [19] a) P. Schulz, *ACS Energy Lett.* **2018**, *3*, 1287; b) S. D. Stranks, *ACS Energy Lett.* **2017**, *2*, 1515; c) J.-P. Correa-Baena, W. Tress, K. Domanski, E. H. Anaraki, S.-H. Turren-Cruz, B. Roose, P. P. Boix, M. Grätzel, M. Saliba, A. Abate, A. Hagfeldt, *Energy Environ. Sci.* **2017**, *10*, 1207; d) K. K. Wong, A. Fakharuddin, P. Ehrenreich, T. Deckert, M. Abdi-Jalebi, R. H. Friend, L. Schmidt-Mende, *J. Phys. Chem. C* **2018**, *122*, 10691; e) M. Stolterfoht, C. M. Wolff, J. A. Marquez, S. Zhang, C. J. Hages, D. Rothhardt, S. Albrecht, P. L. Burn, P. Meredith, T. Unold, D. Neher, *Nat. Energy* **2018**, <https://doi.org/10.1038/s41560-018-0219-8>.
- [20] W. Tress, *Adv. Energy Mater.* **2017**, *7*, 1602358.
- [21] N. K. Noel, A. Abate, S. D. Stranks, E. S. Parrott, V. M. Burlakov, A. Goriely, H. J. Snaith, *ACS Nano* **2014**, *8*, 9815.
- [22] I. A. Shkrob, T. W. Marin, *J. Phys. Chem. Lett.* **2014**, *5*, 1066.
- [23] W.-J. Yin, T. Shi, Y. Yan, *Appl. Phys. Lett.* **2014**, *104*, 063903.
- [24] a) Z. Xiao, Y. Yuan, Y. Shao, Q. Wang, Q. Dong, C. Bi, P. Sharma, A. Gruverman, J. Huang, *Nat. Mater.* **2015**, *14*, 193; b) H. Uratani, K. Yamashita, *J. Phys. Chem. Lett.* **2017**, *8*, 742.
- [25] A. Abate, M. Saliba, D. J. Hollman, S. D. Stranks, K. Wojciechowski, R. Avolio, G. Grancini, A. Petrozza, H. J. Snaith, *Nano Lett.* **2014**, *14*, 3247.
- [26] B. Chen, M. Yang, S. Priya, K. Zhu, *J. Phys. Chem. Lett.* **2016**, *7*, 905.
- [27] W. Tress, N. Marinova, T. Moehl, S. M. Zakeeruddin, M. K. Nazeeruddin, M. Grätzel, *Energy Environ. Sci.* **2015**, *8*, 995.
- [28] F. Huang, L. Jiang, A. R. Pascoe, Y. Yan, U. Bach, L. Spiccia, Y.-B. Cheng, *Nano Energy* **2016**, *27*, 509.
- [29] a) B. Chaudhary, A. Kulkarni, A. K. Jena, M. Ikegami, Y. Udagawa, H. Kunugita, K. Ema, T. Miyasaka, *ChemSusChem* **2017**, *10*, 2473; b) L. Zuo, H. Guo, S. Jariwala, N. De Marco, S. Dong, R. DeBlock, D. S. Ginger, B. Dunn, M. Wang, Y. Yang, *Sci. Adv.* **2017**, *3*, e1700106.
- [30] C.-C. Zhang, M. Li, Z.-K. Wang, Y.-R. Jiang, H.-R. Liu, Y.-G. Yang, X.-Y. Gao, H. Ma, *J. Mater. Chem. A* **2017**, *5*, 2572.
- [31] H. Yoon, S. M. Kang, J.-K. Lee, M. Choi, *Energy Environ. Sci.* **2016**, *9*, 2262.
- [32] Y. Shao, Z. Xiao, C. Bi, Y. Yuan, J. Huang, *Nat. Commun.* **2014**, *5*, 5784.
- [33] C. Tao, S. Neutzner, L. Colella, S. Marras, A. R. S. Kandada, M. Gandini, M. De Bastiani, G. Pace, L. Manna, M. Caironi, C. Nertarelli, A. Petrozza, *Energy Environ. Sci.* **2015**, *8*, 2365.
- [34] Y. Zhao, W. Zhou, W. Ma, S. Meng, H. Li, J. Wei, R. Fu, K. Liu, D. Yu, Q. Zhao, *ACS Energy Lett.* **2016**, *1*, 266.
- [35] A. Agresti, S. Pescetelli, B. Taheri, A. E. Del Rio Castillo, L. Cina, F. Bonaccorso, A. Di Carlo, *ChemSusChem* **2016**, *9*, 2609.
- [36] D. Bi, C. Yi, J. Luo, J.-D. Décoppet, F. Zhang, S. M. Zakeeruddin, X. Li, A. Hagfeldt, M. Grätzel, *Nat. Energy* **2016**, *1*, 16142.
- [37] S. Masi, A. Rizzo, F. Aiello, F. Balzano, G. Uccello-Barretta, A. Listorti, G. Gigli, S. Colella, *Nanoscale* **2015**, *7*, 18956.
- [38] F. Wang, A. Shimazaki, F. Yang, K. Kanahashi, K. Matsuki, Y. Miyauchi, T. Takenobu, A. Wakamiya, Y. Murata, K. Matsuda, *J. Phys. Chem. C* **2017**, *121*, 1562.
- [39] H. Tan, A. Jain, O. Voznyy, X. Lan, F. P. G. de Arquer, J. Z. Fan, R. Quintero-Bermudez, M. Yuan, B. Zhang, Y. Zhao, F. Fan, P. Li, L. Quan, Y. Zhao, Z.-H. Lu, Z. Yang, S. Hoogland, E. H. Sargent, *Science* **2017**, *355*, 722.
- [40] M. Saliba, T. Matsui, K. Domanski, J.-Y. Seo, A. Ummadisingu, S. M. Zakeeruddin, J.-P. Correa-Baena, W. R. Tress, A. Abate, A. Hagfeldt, M. Grätzel, *Science* **2016**, *354*, 206.
- [41] E. H. Anaraki, A. Kermanpur, L. Steier, K. Domanski, T. Matsui, W. Tress, M. Saliba, A. Abate, A. Abate, M. Grätzel, A. Hagfeldt, J.-P. Correa-Baena, *Energy Environ. Sci.* **2016**, *9*, 3128.
- [42] J. Peng, T. Duong, X. Zhou, H. Shen, Y. Wu, H. K. Mulmudi, Y. Wan, D. Zhong, J. Li, T. Tsuzuki, K. J. Weber, K. R. Catchpole, T. P. White, *Adv. Energy Mater.* **2017**, *7*, 1601768.
- [43] J. Peng, Y. Wu, W. Ye, D. A. Jacobs, H. Shen, X. Fu, Y. Wan, T. Duong, N. Wu, C. Barugkin, H. T. Nguyen, D. Zhong, J. Li, T. Lu, Y. Liu, M. N. Lockrey, K. J. Weber, K. R. Catchpole, T. P. White, *Energy Environ. Sci.* **2017**, *10*, 1792.
- [44] M. I. Dar, M. Frankevičius, N. Arora, K. Redekas, M. Vengris, V. Gulbinas, S. M. Zakeeruddin, M. Grätzel, *Chem. Phys. Lett.* **2017**, *683*, 211.

- [45] J. M. Richter, M. Abdi-Jalebi, A. Sadhanala, M. Tabachnyk, J. P. Rivett, L. M. Pazos-Outón, K. C. Gödel, M. Price, F. Deschler, R. H. Friend, *Nat. Commun.* **2016**, *7*, 13941.
- [46] J. M. Ball, A. Petrozza, *Nat. Energy* **2016**, *1*, 16149.
- [47] L. M. Herz, *Annu. Rev. Phys. Chem.* **2016**, *67*, 65.
- [48] C. L. Davies, M. R. Filip, J. B. Patel, T. W. Crothers, C. Verdi, A. D. Wright, R. L. Milot, F. Giustino, M. B. Johnston, L. M. Herz, *Nat. Commun.* **2018**, *9*, 293.
- [49] Y. Yang, M. Yang, D. T. Moore, Y. Yan, E. M. Miller, K. Zhu, M. C. Beard, *Nat. Energy* **2017**, *2*, 16207.
- [50] A. T. Hubbard, *Encyclopaedia of Surface, Colloid Science P.77*, Vol. 1, Marcel Dekker, New York **2002**.
- [51] T. Duong, Y. Wu, H. Shen, J. Peng, X. Fu, D. Jacobs, E-C. Wang, T. C. Kho, K. C. Fong, M. Stocks, E. Franklin, A. Blakers, N. Zin, K. McIntosh, W. Li, Y.-B. Cheng, T. P. White, K. Weber, K. Catchpole, *Adv. Energy Mater.* **2017**, *7*, 1700228.

Chapter 5: Inorganic ZnO/MgF₂ Bi-Layers as a High-Performance Alternative to Fullerene-Based Electron Transport Layers in Inverted Perovskite Solar Cells

In addition to the normal structured perovskite solar cells, the concept of an inverted perovskite cell also has been developed with a structure of Glass/TCO/HTL/Perovskite/ETL/Electrode.^[1-9] To date, the current record efficiency for inverted perovskite solar cells is 21.5%,^[1] which is comparable to that of normal perovskite solar cells.^[6]

In general, high temperature annealing is essential to prepare TiO₂, a widely used electron transport layer in normal perovskite cells.^[6] Inverted perovskite cells in general do not require a high temperature sintering process, which makes them potentially more cost-effective for future industrialization.^[1]

In inverted perovskite solar cells, PCBM,^[1-3] C₆₀^[2,7] and other fullerene derivatives^[3,8,9] are commonly used as ETLs although these n-type materials have relatively poor hole-blocking properties and inferior energy level alignment. In addition, PCBM and related fullerene derivatives (widely used as acceptors in organic solar cells),^[8,9] cause considerable optical loss over the whole UV-infrared wavelength range. This prohibits the use of PCBM and other fullerene derivatives in highly efficient perovskite-silicon tandem solar cells.

In order to overcome these challenges, we designed a set of inorganic combination layers (ZnO/MgF₂) that can perfectly substitute the aforementioned n-type materials for use as efficient ETLs in inverted perovskite solar cells. Together with an ultrathin (less than 5 nm) PMMA:PCBM passivation layer demonstrated in Chapter 3, the use of ZnO/MgF₂ ETLs yielded a high PCE of 17.5% with a high FF of 0.795 for MAPbI₃-based inverted perovskite solar cells. In addition to the superior physical and electronic properties of the ZnO/MgF₂, the optical property of the ZnO is much better than that of PCBM, indicating that ZnO/MgF₂ can be a good candidate for use as an ETL in high-performance perovskite-silicon tandems.

Further results and discussion are presented in the following manuscript.

References

- [1] D. Luo, W. Yang, Z. Wang, A. Sadhanala, Q. Hu, R. Su, *et al.*, "Enhanced photovoltage for inverted planar heterojunction perovskite solar cells," *Science*, vol. 360, pp. 1442, 2018.
- [2] D. Luo, L. Zhao, J. Wu, Q. Hu, Y. Zhang, Z. Xu, *et al.*, "Dual-Source Precursor Approach for Highly Efficient Inverted Planar Heterojunction Perovskite Solar Cells," *Advanced Materials*, vol. 29, pp. 1604758, 2017.
- [3] C.-H. Chiang, M. K. Nazeeruddin, M. Grätzel, and C.-G. Wu, "The synergistic effect of H₂O and DMF towards stable and 20% efficiency inverted perovskite solar cells," *Energy & Environmental Science*, vol. 10, pp. 808-817, 2017.
- [4] M. Stolterfoht, C. M. Wolff, Y. Amir, A. Paulke, L. Perdigón-Toro, P. Caprioglio, *et al.*, "Approaching the fill factor Shockley–Queisser limit in stable, dopant-free triple cation perovskite solar cells," *Energy & Environmental Science*, vol. 10, pp. 1530-1539, 2017.
- [5] W. Nie, H. Tsai, R. Asadpour, J.-C. Blancon, A. J. Neukirch, G. Gupta, *et al.*, "High-efficiency solution-processed perovskite solar cells with millimeter-scale grains," *Science*, vol. 347, pp. 522-525, 2015.
- [6] W. S. Yang, B.-W. Park, E. H. Jung, N. J. Jeon, Y. C. Kim, D. U. Lee, *et al.*, "Iodide management in formamidinium-lead-halide-based perovskite layers for efficient solar cells," *Science*, vol. 356, pp. 1376-1379, 2017.
- [7] Z. Zhu, Y. Bai, X. Liu, C. C. Chueh, S. Yang, and A. K. Y. Jen, "Enhanced Efficiency and Stability of Inverted Perovskite Solar Cells Using Highly Crystalline SnO₂ Nanocrystals as the Robust Electron-Transporting Layer," *Advanced Materials*, vol. 28, pp. 6478-6484, 2016.
- [8] J. Y. Jeng, Y. F. Chiang, M. H. Lee, S. R. Peng, T. F. Guo, P. Chen, *et al.*, "CH₃NH₃PbI₃ perovskite/fullerene planar-heterojunction hybrid solar cells," *Advanced Materials*, vol. 25, pp. 3727-32, 2013.
- [9] P. W. Liang, C. C. Chueh, S. T. Williams, and A. K. Y. Jen, "Roles of Fullerene-Based Interlayers in Enhancing the Performance of Organometal Perovskite Thin-Film Solar Cells," *Advanced Energy Materials*, vol. 5, p. 1402321, 2015.

Inorganic ZnO/MgF₂ Bi-Layers as a High-Performance Alternative to Fullerene-Based Electron Transport Layers in Inverted Perovskite Solar Cells

Jun Peng^{1,2*}, Yimao Wan¹, Xianzhong Zhou³, The Duong¹, Heping Shen¹, Daniel A. Jacobs¹, Hieu T. Nguyen¹, Mark N. Lockrey⁴, Felipe Kremer⁵, Shenyong Zhao¹, Nandi Wu¹, Yiliang Wu¹, Xinbo Yang², Wenzhu Liu², Dingyong Zhong³, Juntao Li³, Klaus J. Weber¹, Kylie R. Catchpole¹, Stefaan De Wolf^{2*}, Thomas P. White^{1*}

¹Research School of Engineering, The Australian National University, Canberra, ACT 2601, Australia

²King Abdullah University of Science and Technology (KAUST), KAUST Solar Center (KSC), Physical Sciences and Engineering Division (PSE), Thuwal 23955-6900, Kingdom of Saudi Arabia

³State Key Laboratory of Optoelectronic Materials and Technologies, School of Physics, Sun Yat-sen University, Guangzhou 510275, China

⁴Australian National Fabrication Facility, Department of Electronic Materials Engineering, Research School of Physics & Engineering, The Australian National University, Canberra, ACT, 2601, Australia

⁵Centre for Advanced Microscopy, The Australian National University, Canberra, ACT, 2601, Australia

E-mail: jun.peng@anu.edu.au or pengjun.88.81@gmail.com;
stefaan.dewolf@kaust.edu.sa;
thomas.white@anu.edu.au

Keywords: electron transport layers, ZnO, MgF₂, interface passivation, inverted perovskite solar cells

Abstract

Charge transport layers play a critical role in achieving high-performance perovskite solar cells. In inverted perovskite solar cells, PCBM and other fullerene derivatives are commonly used as electron transport layers (ETLs), but these materials are non-ideal for several reasons. First, as a single-layer ETL they are not sufficiently carrier selective to achieve very high efficiencies. Second, they have poor energy level

alignment to common electrode materials such as Ag and Al. Third, they have relatively strong optical absorption at visible wavelengths, and low refractive indices, which make them particularly unsuitable for perovskite-based tandem applications. Here, we demonstrate bi-layer inorganic ZnO/MgF₂ ETLs as effective substitutes for PCBM and organic ETL materials. The bi-layer structure takes advantage of the suitable work function, good conductivity and excellent hole-blocking properties of ZnO, and pairs this with an ultrathin MgF₂ layer to provide low contact resistance between the ZnO and Al electrode. When this bi-layer ETL is combined with an ultrathin polymer passivation layer at the perovskite/ZnO interface we achieve a champion cell with 17.5% efficiency, a fill-factor of 79.5% and negligible hysteresis. This is one of the highest efficiencies reported for an inverted cell using PEDOT:PSS as the hole transport layer. Moreover, the ZnO/MgF₂ ETL is significantly more transparent and has a higher refractive index than the organic layers it replaces, making it a promising option for use in monolithic perovskite-silicon tandems.

Introduction

Organic-inorganic hybrid perovskite solar cells have attracted significant research attention in the past eight years and are regarded as a promising candidate for next-generation photovoltaic technology.^[1-12] Following the first perovskite solar cells reported in 2009 with a power conversion efficiency (PCE) of ~4%,^[1] optimization of the perovskite composition, the electron and hole transport layers and the interfaces between these layers has dramatically boosted their efficiency to more than 22 %.^[10] The highest-performing cells ('normal' or n-i-p structure) have a layer structure of Glass/TCO/ETL/Perovskite/HTL/Metal electrode, where TCO, ETL and HTL are the transparent conductive oxide, electron transport layer and hole transport layer respectively.^[2, 10] 'Inverted' perovskite cells, where the order of the ETL and HTL layers is reversed, have also achieved efficiencies above 20%.^[13-16]

There are many suitable organic and inorganic materials for the bottom (HTL) transport layer in inverted cells, including poly(2,3-dihydrothieno-1,4-dioxin)-poly(styrenesulfonate) (PEDOT:PSS),^[17-20] NiO_x,^[21-24] CuO_x,^[25, 26] CuSCN,^[27] PTAA^[13, 16] and others.^[28-32] There are far fewer options, however, for the top (ETL) transport layer due to the strict deposition compatibility and thermal processing constraints imposed by the underlying perovskite and HTL materials. The most widely-used and best-performing ETLs for inverted cells are [6,6]-Phenyl C₆₁ butyric acid methyl ester

(PCBM),^[19, 20, 29, 33] C₆₀^[16, 23, 25] and other fullerene derivatives^[15, 34, 35]). While these materials have allowed impressive efficiencies in a small number of cases, inverted perovskite solar cells typically exhibit lower performance (especially in open circuit voltage) than ‘normal’ structured cells. This largely due to the relatively poor hole-blocking property and non-ideal energy level alignment of the fullerene layers.^[13, 16, 25, 29, 33]

To address the limitations of fullerene-based ETLs, there have been many attempts to modify these layers by combining or replacing them with other high bandgap n-type materials such as ZnO,^[24, 29, 33] TiO_x,^[28, 36] SnO_x,^[23, 37] and BCP(bathocuproine)^[13, 16, 26, 30]. For example, bi-layer ETLs consisting of PCBM/Ti(Nb)O_x and PCBM/ZnMgO ETLs were used in inverted cells with efficiencies >18% in Refs[28] and [38] respectively. The highest efficiency inverted perovskite solar cells reported to date combined a C₆₀/BCP bi-layer ETL with choline chloride interface passivation to achieve a certified efficiency of 20.6%,^[13] approaching the performance of the best normal structured perovskite solar cells.^[10]

Inverted perovskite cells are also playing an important role in the development of monolithic, two-terminal perovskite-silicon tandem cells. The record certified efficiency (23.6%) for such a tandem cell was achieved with a planar inverted perovskite top cell incorporating an ETL structure of LiF/PCBM/SnO₂/Zn-doped SnO_x.^[39] While relatively effective, this ETL stack is complex, and the PCBM film contributes to the parasitic optical absorption at short wavelengths. Hence, the development of electrically and optically optimized non-fullerene ETLs for inverted cells would be especially beneficial for tandem applications.

It is known that n-type inorganic metal oxides such as ZnO,^[24, 29, 33] TiO_x,^[28, 36] and SnO_x^[23, 37] demonstrate higher electron mobility (good conductivity), better WF (suitable Fermi-level) , larger bandgap (excellent hole-blocking property) and better optical properties (transmittance and refractive index) than the above-mentioned organic materials. This makes the n-type inorganic metal oxides promising candidates for high-performance inverted perovskite solar cells and monolithic tandems. However, it is challenging to adopt these n-type inorganic metal oxides in inverted perovskite solar cells due to the incompatibility of many deposition processes (solvents and temperature) with the underlying cell materials. Fortunately, metal oxide nanomaterials can provide a way around this issue.

In this work, we first demonstrate a new combination ETL design integrating a highly conductive zinc oxide (ZnO) nanoparticle layer with an ultrathin MgF₂

tunnelling layer. We show that this structure can successfully substitute PCBM and other fullerene derivatives for high-performance inverted perovskite solar cells. In addition, we introduce an ultrathin poly(methyl methacrylate): PCBM (PMMA:PCBM) passivation layer to effectively suppress interfacial recombination induced by defects/trap-states perovskite/ETL interface, as demonstrated previously for normal-structured cells.^[40] We show that the ZnO nanomaterial layer can provide efficient electron extraction from the perovskite absorber, while simultaneously blocking holes, thus mitigating non-radiative recombination at the ETL/electrode side. The insertion of the ultrathin insulating MgF₂ tunneling layer decreases the Schottky barrier between ZnO and the aluminium electrode, thus reducing the contact resistance. The combined properties of the ZnO/MgF₂ bi-layer ETL together with the ultrathin polymer passivation layer result in a PCE of 17.5% with a high fill factor (FF) of 0.795. This is one of the highest efficiencies reported for inverted perovskite solar cells using PEDOT:PSS as the HTL.^[15, 17, 18]

Results and Discussions

The ZnO nanomaterials were synthesized according to Ref [41]. Detailed experimental information for the synthesis routes and raw materials are provided in experimental section. To verify the quality and physical properties of the synthesized material, we first characterized the nanoparticle diameter, chemical stoichiometry, WF, optical bandgap and valance band maximum (VBM) using transmission electron microscopy (TEM) and EDS (energy dispersive spectroscopy, TEM), x-ray photoelectron spectroscopy/ultraviolet photoelectron spectroscopy (XPS/UPS), optical transmittance and scanning electron microscope (SEM) measurements.

The TEM image in **Figure 1a** shows the size of the as-synthesized ZnO nanoparticles is ~10 nm. XPS measurements were conducted to further elucidate the chemical composition of nanoparticle films deposited on an ITO substrate. Figure 1c shows the Zn 2p₁ and Zn 2p₃ peaks (with a corresponding single symmetric component fitting, respectively) of the ZnO film at binding energies of ~1044.7 eV and ~ 1021.7 eV, which are consistent with literature values.^[24, 42] The XPS spectra of O 1s in Figure 1d exhibits a degree of asymmetry in its shape, where it can be deconvoluted with two different oxygen species. The binding energy of O 1s peak centred at ~530.2 eV can be ascribed to O atoms in the ZnO crystal^[24, 42] while the second peak binding energy (531.5 eV) is attributed to the presence of an oxygen-deficient component (such as zinc hydroxide)^[24, 42] or hydroxyl adsorbed onto the surface (due to surface contamination

from the samples being exposed to air before the XPS measurements).^[42] Additionally, the surface stoichiometry of the samples was also calculated by comparing the elements' relative peak areas and their corresponding relative sensitivity factors. The atomic ratio of Zn:O for the ZnO nanoparticles is about 1:1.

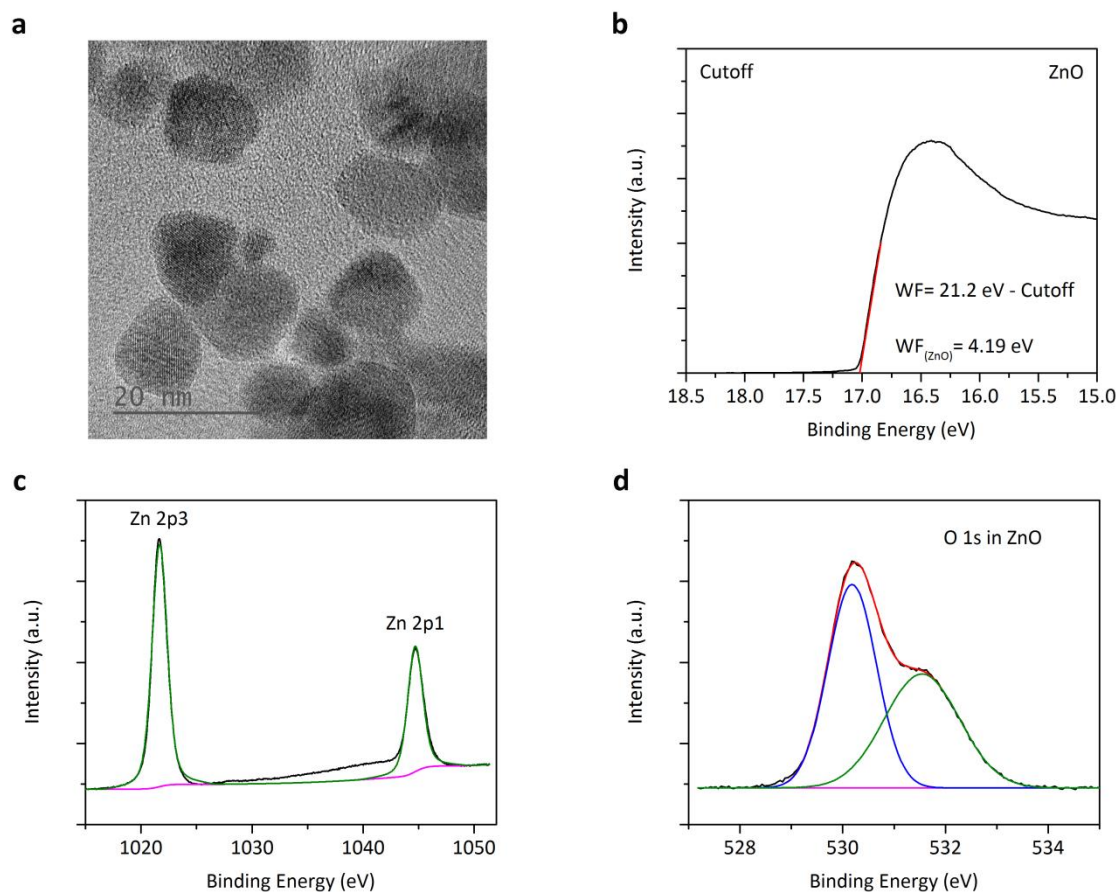


Figure 1. a) TEM image of the synthesized ZnO nanoparticles. b) UPS spectra of a ZnO nanoparticle thin film deposited on a Glass/ITO substrate. c) XPS spectra of Zn 2p peaks for the ZnO film. d) XPS spectra of O1s peaks for ZnO film.

UPS measurements were also performed to estimate the ZnO work function (WF) and valance band maximum (VBM). The UPS cut-off spectra in Figure 1b shows the WF of ZnO is of 4.19 eV, which is similar to literature values.^[24] As shown in Figure S1a (Supporting Information), the VBM of ZnO is about 3.21 eV. Based on the calculated WF and VBM values, the valance band energy of ZnO is 7.4 eV. Considering the optical bandgap of ZnO ($E_g \sim 3.3$ eV, Figure S1b, Supporting Information), the calculated conduction band energy is therefore ~ 4.1 eV, indicating the ZnO nanomaterials are heavily doped (which contributes to the high fill-factor of the ZnO-based perovskite cells presented later). The ~ 4.1 eV conduction band energy is also close to that of the MAPbI₃ (~ 3.9 eV),^[24] thus demonstrating that the synthesized ZnO

particles are suitable for use as ETLs in MAPbI_3 -based perovskite solar cells (see **Figures 2a,b**). In addition, the transmittance of the ZnO film is much higher than that of the PCBM film (a common ETL in inverted perovskite solar cells) as seen in the Figure S1c (Supporting Information).

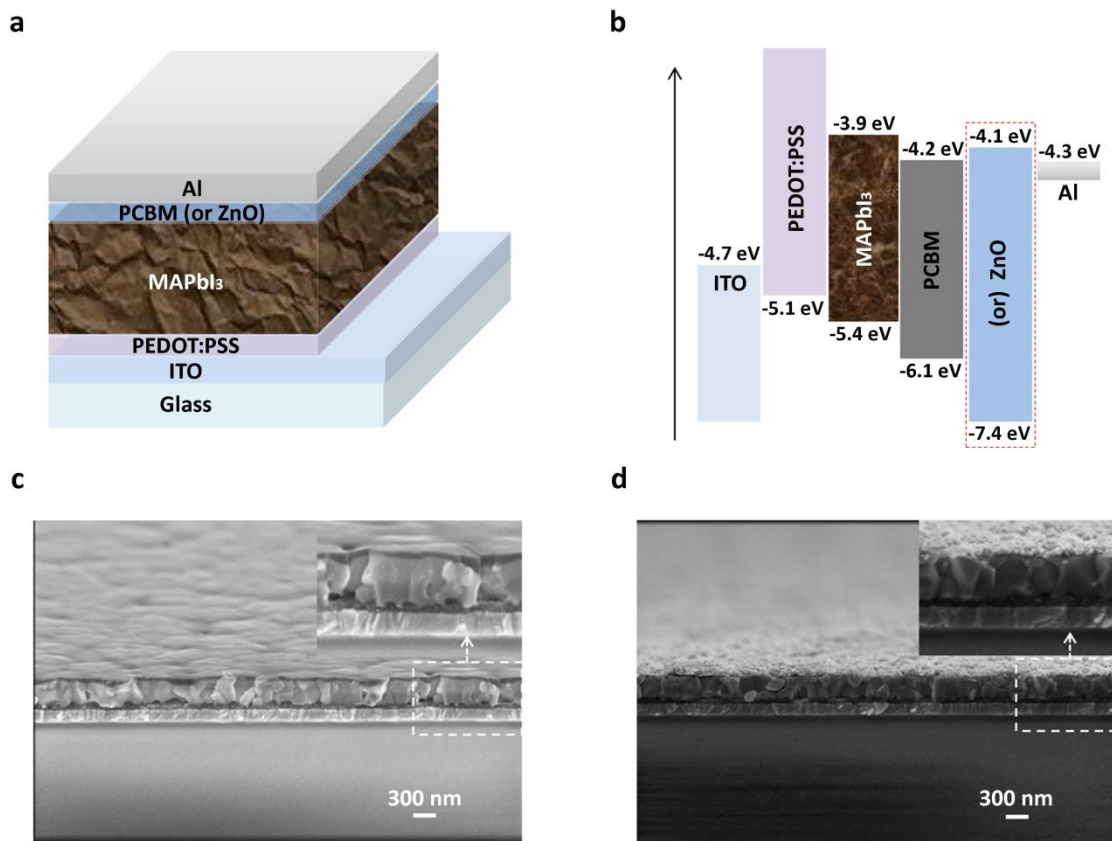


Figure 2. a) Schematic of the MAPbI_3 -based inverted perovskite cell structure studied here. b) Diagram showing the energy levels of the different cell materials. c) SEM cross-sectional image of the Control 1 dummy device with a structure of Glass/ITO/PEDOT:PSS/ MAPbI_3 /PCBM. d) SEM cross-sectional image of the Device 1 dummy device with a structure of Glass/ITO/PEDOT:PSS/ MAPbI_3 /ZnO.

We next fabricated inverted perovskite cells with the structure ITO/PEDOT:PSS/ MAPbI_3 /PCBM (or ZnO)/Al (see Figure 2a), to directly compare cells with ZnO ETLs to control cells using a standard PCBM ETL. Figures 2c,d show SEM cross-section images of two cells without the rear aluminum electrode. The estimated thickness of the ITO, PEDOT:PSS, MAPbI_3 , PCBM and ZnO layers are around 150 nm, 60 nm, 300 nm, 50 nm and 70 nm, respectively. Standard SEM and XRD measurements were also carried out to probe the formation of MAPbI_3 crystal thin films on ITO/PEDOT:PSS substrates. Figure S2a (Supporting Information), shows an SEM image of a typical

pinhole-free and uniform perovskite film. The corresponding XRD (Figure S2b, Supporting Information) shows no obvious PbI_2 or other non-perovskite phases, further confirming the film quality.

As shown in **Figure 3a**, the PCBM-based cell (labeled Control 1) had a PCE of 11.52% with a current density $J_{sc} = 21.16 \text{ mA/cm}^2$, $V_{oc} = 0.830 \text{ V}$ and $\text{FF} = 0.656$, measured by reverse J - V scan. The forward scan data is also shown in the figure, indicating only minor hysteresis, leading to an absolute PCE difference of 0.3%. The ZnO-based device (Device 1, Figure 3b), has a PCE of 13.13%, with $V_{oc} = 0.900 \text{ V}$, $J_{sc} = 21.3 \text{ mA/cm}^2$ and $\text{FF} = 0.685$, and a 0.8% absolute efficiency variation between reverse scan and forward scan. Steady-state efficiency measurements were also performed to verify the Control 1 and Device 1 performance shown in Figures S3a,b (Supporting Information), resulting in similar efficiency values.

It is observed that the Control 1 (PCBM/Al) exhibits a lower V_{oc} ($\sim 0.830 \text{ V}$) than the Device 2 (ZnO/MgF₂/Al) ($V_{oc} \sim 0.900 \text{ V}$). Given that PCBM is known to passivate the perovskite surface,^[19,20] it seems unlikely that the lower voltage of Control 1 is due to a higher density of surface defects. An alternative explanation may be an inferior built-in voltage in Control 1. The built-in voltage is determined by the work-function difference between the HTL and ETL contact layers, corrected for any surface dipole contributions at the two perovskite interfaces.^[8] In the absence of knowledge about these surface dipoles, the built-in voltage can be estimated by the difference in vacuum work functions. This may account for the difference between Device 1 and Control 1 in terms of V_{oc} : while ZnO has a vacuum WF of 4.19 eV (determined by UPS measurement), the conduction band for PCBM films have been reported in the range of 4.2 - 4.3 eV,^[43-45] and should therefore yield a lower built-in voltage (see Figure 2b).

To further reduce the Al contact resistance, a common strategy is to introduce an ultra-thin tunneling layer like LiF^[46] or low WF metal (e.g. Ca^[15, 17]) between ETL and Al electrode. Here we use a tunneling layer of the insulating material MgF₂. As shown in Figure 3c, adding an ultrathin MgF₂ layer between the ZnO and Al provided a modest increase in both V_{oc} and FF for the ZnO/MgF₂-based device (Device 2) as compared to Device 1. This improvement increased the PCE to 14.26% with a FF of 0.732, although we note that the cell still suffered a small amount of current-voltage hysteresis with different scan directions. The improved V_{oc} and FF can be attributed to the fact that MgF₂ can react with Al to form an Al-Mg-F alloy during Al evaporation as suggested by previous reports.^[47] This alloyed interface decreases the Schottky barrier between the ZnO ETL and the Al electrode, thus reducing the contact resistance.^[47] We also found

the same phenomenon that MgF_2 can bridging the injection barrier between the PCBM and Al electrode as demonstrated in the Control 2 device (ITO/PEDOT:PSS/MAPbI₃/PCBM/MgF₂/Al) (See Figure S4a, Supporting Information).

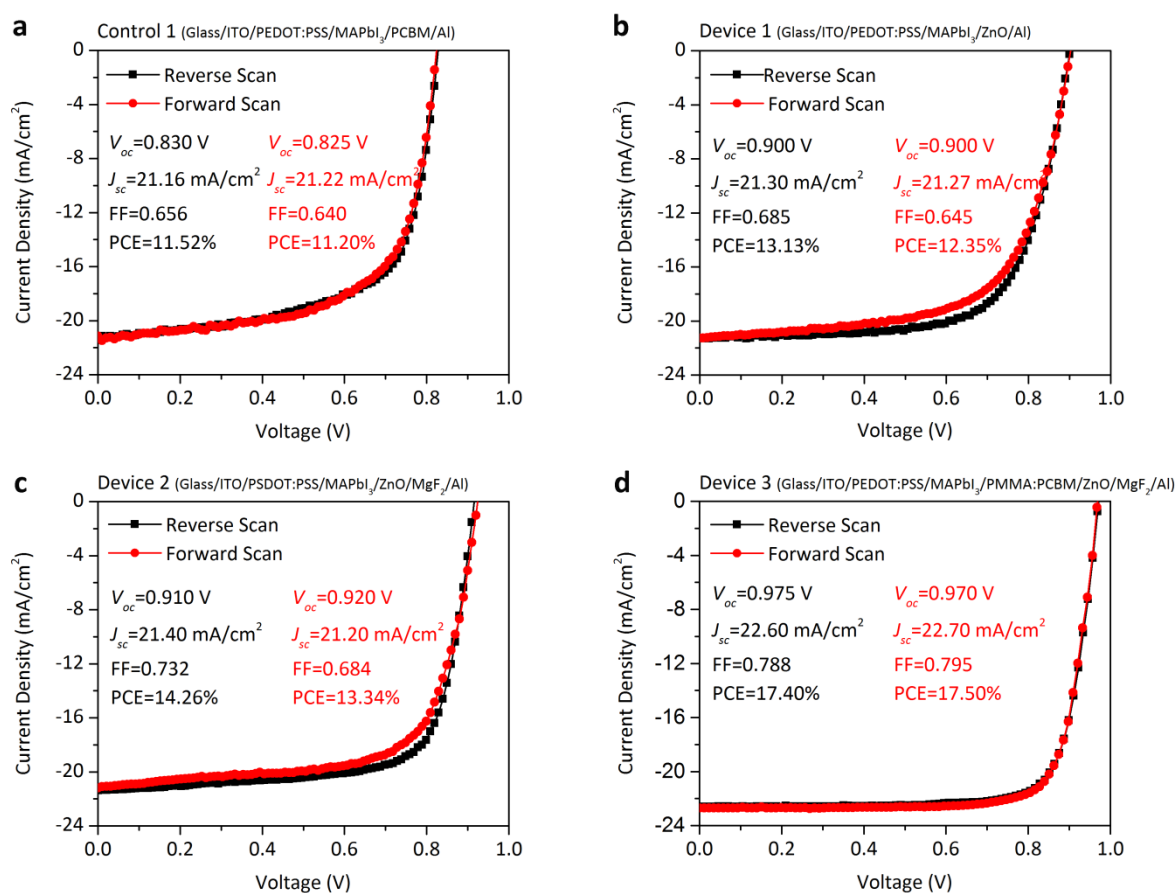


Figure 3. Photovoltaic parameters and current density – voltage curves of the different inverted perovskite cells. a) Control 1 (Glass/ITO/PEDOT:PSS/MAPbI₃/PCBM/Al). b) Device 1 (Glass/ITO/PEDOT:PSS/MAPbI₃/ZnO/Al). c) Device 2 (Glass/ITO/PEDOT:PS-S/MAPbI₃/ZnO/MgF₂/Al). d) Device 3 (Glass/ITO/PEDOT:PSS/MAPbI₃/PMMA:PCBM/Zn-O/MgF₂/Al). Note that all devices were tested at a 50 mV/s scan rate.

The combination of ion migration in the perovskite film and carrier recombination at perovskite/ETL and perovskite/HTL interfaces is thought to be responsible for the observed hysteresis in many perovskite cells.^[40, 48, 49] Interface recombination has also been identified as the major source of voltage loss in high-efficiency cells. Therefore, inspired by our previous work,^[40] we introduced an ultra-thin PMMA:PCBM passivation layer between the perovskite and ZnO ETL (labeled as Device 3). As seen in Figure 3d, the champion cell with this structure exhibited a PCE of 17.5%, with V_{oc} = 0.970 V, J_{sc} = 22.7 and FF = 0.795. The performance distribution of 25 Device 3 cells is

also plotted in Figure S5 (Supporting Information), showing an average PCE of $16.8 \pm 0.35\%$. Steady-state efficiency measurements for Device 2 (ZnO/MgF₂/Al), Device 3 (PMMA:PCBM/ZnO/MgF₂/Al), and Control 2 (PCBM/MgF₂/Al) are also plotted in Figure S6 (Supporting Information).

External quantum efficiency (EQE) measurements were also made on Control 1 and Device 3 cells to confirm the current densities obtained from the current-voltage scans (see Figure S7). The integrated current densities from the EQE spectra of both cells are within 4% of the J_{sc} values extracted from the J - V curves. We also observe that the EQE response of Device 3 is significantly higher than that of the Control 1 due to the superior properties of the combination ETL (ZnO/MgF₂) as discussed above.

We note that after the insertion of an ultrathin PMMA:PCBM passivation layer, the optimized Device 3 (PMMA:PCBM/ZnO/MgF₂/Al) cells show an ~ 70 mV increase in V_{oc} compared to Device 1 (ZnO/Al) cells. To investigate this further, we conducted steady-state photoluminescence (PL) and time-resolved PL (TRPL) on thin film samples of bare perovskite (labeled as perovskite), perovskite/PCBM (control 1), perovskite/ZnO (device 1), perovskite/ZnO/MgF₂ (device 2) and perovskite/PMMA:PCBM/ZnO/MgF₂ (device 3). As depicted in **Figure 4a**, perovskite films capped with ETLs exhibit much lower PL intensity than that of bare perovskite film. This is commonly observed and may be attributed to some combination of increased recombination at the perovskite/ETL interface^[40] and/or improved charge extraction.^[16] Interestingly, the perovskite/PCBM sample (control 1) shows a higher PL intensity than both the perovskite/ZnO (device 1) and perovskite/ZnO/MgF₂ (device 2), whereas Control 1 cells exhibit a lower V_{oc} (~ 0.830 V) than both Device 1 (~ 0.900 V) and Device 2 (~ 0.910 V) cells (see Figure 3). There is also no significant difference in the PL intensity of device 1 and device 2 samples, despite a ~ 10 mV difference in V_{oc} . In contrast, the passivated Device 3 sample (perovskite/PMMA:PCBM/ZnO/MgF₂) has a much higher PL intensity than the control 1 (perovskite/PCBM) sample.

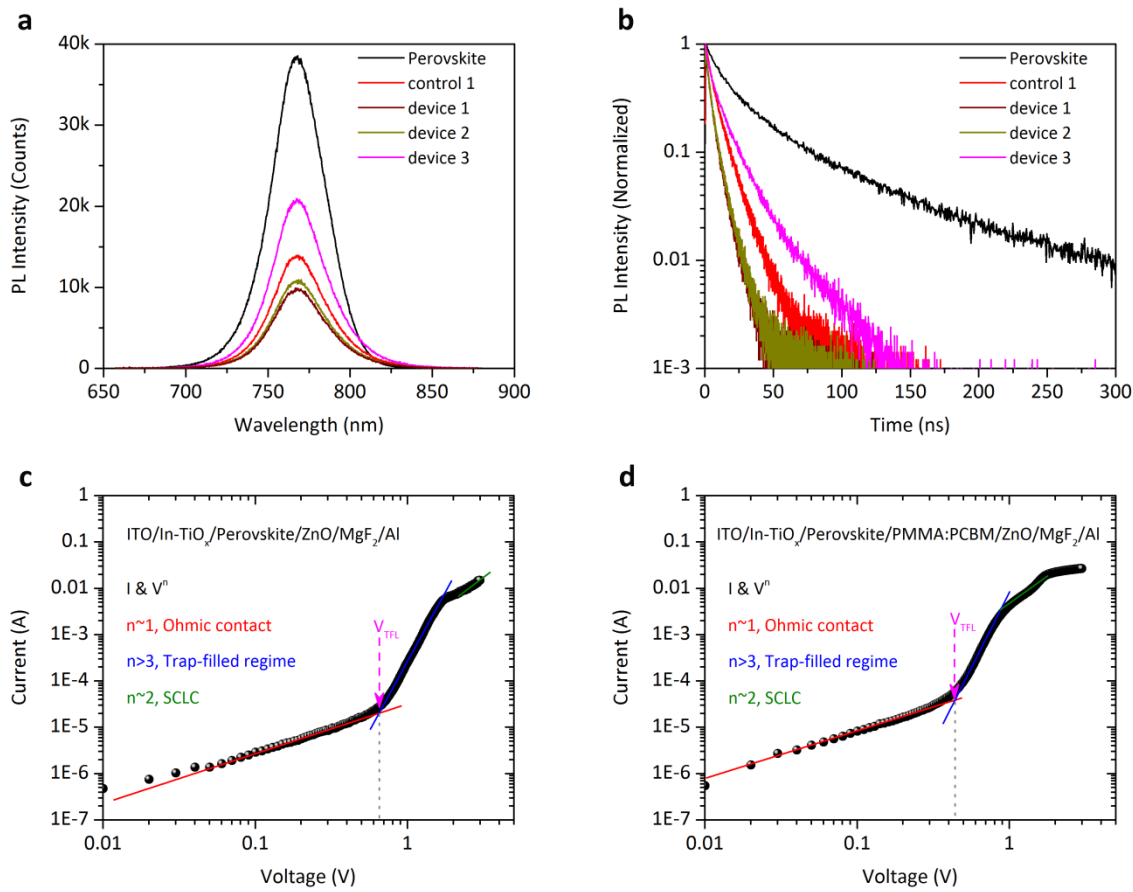


Figure 4. a) Steady-state PL intensity for thin film samples of bare perovskite, perovskite/PCBM (control 1), perovskite/ZnO (device 1), perovskite/ZnO/MgF₂ (device 2) and perovskite/PMMA:PCBM/ZnO/MgF₂ (device 3) deposited on quartz substrates. b) Time-resolved PL measurements for the same samples as in (a). c) SCLC measurement for a non-passivated electron-dominated device with a structure of ITO/In-TiO_x/ /Perovskite/ZnO/MgF₂/Al. d) SCLC measurement for a passivated electron-dominated device with a structure of ITO/In-TiO_x/Perovskite/PMMA:PCBM/ZnO/MgF₂/Al. Here ‘perovskite’ refers to MAPbI₃.

A similar trend can be observed in the PL transient spectra in Figure 4b for the same set of thin film samples. A sum of two exponential functions was applied to fit the PL transients, where the detailed extracted parameters (lifetimes and weight) are listed in Table S1 (Supporting Information). The bare perovskite film has a fast decay lifetime $\tau_1 = 1.8$ ns and a slow decay lifetime $\tau_2 = 87.6$ ns. In contrast, the perovskite/ZnO (device 1) and perovskite/ZnO/MgF₂ (device 2) samples exhibit equivalent lifetimes of $\tau_1 = 2$ ns (2 ns) and $\tau_2 = 6.8$ ns (7.1 ns), respectively. The perovskite/PCBM (Control 1) sample shows a slightly higher lifetime ($\tau_1 = 3.8$ ns, $\tau_2 = 11.0$ ns) as the PCBM is known to passivate the perovskite surface defects.^[19, 20] The observed PL quenching

(steady-state and time-resolved) in the perovskite/ZnO and perovskite/ZnO/MgF₂ samples is consistent with an increase in interface recombination, in contrast to the improved voltage observed in cells with these ETL layers. This provides further indirect evidence to support the aforementioned explanation of why Device 1 yields a higher V_{oc} (0.900 V) than Control 1 (V_{oc} ~0.830 V) ie: V_{oc} is strongly influenced by the WF-induced built-in voltage in these cells.

The second longest transient PL lifetimes ($\tau_1 = 5.3$ ns and $\tau_2 = 19.4$ ns) are measured for the perovskite/PMMA:PCBM/ZnO/MgF₂ sample (Device 3). This further supports our conclusions from the full cell results and steady-state PL measurements that the ultra-thin PMMA:PCBM film effectively reduces non-radiative recombination at the perovskite/ZnO interface by reducing the density of defects and trap states, resulting in a ~75 mV increase in V_{oc} for Device 3 cells compared to Device 1 cells.

Additional evidence for reduced surface defects is presented in Figures 4c,d in the form of space charge limited current (SCLC) measurements. These were conducted on two electron-dominated devices designed to replicate the ETL sides of Devices 2 and 3 with structures ITO/In-TiO_x/MAPbI₃/ZnO/MgF₂/Al and ITO/In-TiO_x/MAPbI₃/PMMA:PCBM/Zn-O/MgF₂/Al respectively. Current-voltage measurements on both samples (plotted on a log-log scale in Figures 4c,d) show three distinct operating regimes (ohmic contact regime, trap-filled regime and SCLC regime) as expected.^[16] Generally, in the SCLC model, the density of the defects/trap states can be estimated from the equation $V_{TFL}=(e*n_t*d^2)/(2*\epsilon*\epsilon_0)$, where V_{TFL} is the trap-filled limit (when all available defects/trap states are filled by injected carriers), and e , n_t , d , ϵ and ϵ_0 are electronic charge, trap density, device thickness, perovskite dielectric constant and permittivity of free space, respectively.^[16] Figures 4c,d, show that the V_{TFL} of the ITO/In-TiO_x/MAPbI₃/ZnO/MgF₂/Al sample is ~0.65 V, compared to ~0.44 V for the passivated ITO/In-TiO_x/MAPbI₃/PMMA:PCBM/ZnO/MgF₂/Al sample. Referring to the equation above, this is indicative of the passivated sample having a significantly lower trap density than the unpassivated sample, consistent with the cell performance and photoluminescence measurements.

Conclusion

In summary, we have demonstrated an inorganic bi-layer ETL (ZnO (~70 nm)/MgF₂ (~1.5 nm)) that can directly replace and out-perform widely-used PCBM in MAPbI₃-based inverted perovskite solar cells. The good work function alignment, high

conductivity and excellent hole-blocking properties of ZnO nanomaterials, combined with the ultrathin MgF₂ layer to improve contact resistance to the Al electrode, make them ideal for use as ETL in inverted perovskite solar cells. Combining this ETL structure with an ultrathin (<5nm) PMMA:PCBM passivation layer at the perovskite/ETL interface, enabled a champion cell with a PCE of 17.5%, a high fill factor (~0.795) and negligible hysteresis. Analysis of the ZnO nanomaterial and MgF₂ tunneling layers reveals the critical role of charge transport layers in controlling recombination, minimizing recombination losses and maximizing carrier extraction in order to achieve high solar cell efficiencies.

It is noteworthy that the cells fabricated in this work are all based on MAPbI₃, and use a standard PEDOT:PSS HTL, which has not been modified or optimized in any way. Thus, although our cell efficiencies are not the highest reported for inverted perovskite cells, they are some of the highest reported for PEDOT:PSS cells, which rarely achieve open circuit voltages above 1V.^[15, 17, 18] Thus, it is quite likely that the performance of our champion passivated cells is currently limited by the HTL side. We expect that higher cell efficiencies could be achieved by replacing the PEDOT:PSS HTL with a superior hole transport material, and incorporating with a suitable mixed cation perovskite absorber. Finally, we observe that the refractive index and transparency of the ZnO/MgF₂ ETLs make them better suited to monolithic perovskite-silicon tandem cells than low-index, low-bandgap organics such as PCBM, potentially providing a further boost to this high-efficiency technology.

Experimental Section

Detailed experimental information is provided in Supporting Information.

Supporting Information

Supporting Information is available from the Wiley Online Library or from the author.

Acknowledgments

This work was supported by the Australian Government through the Australian Renewable Energy Agency (ARENA) and the Australian Research Council. Responsibility for the views, information or advice expressed herein is not accepted by the Australian Government. J. P. acknowledges the funding support from Australian Nanotechnology Network (ANN) and Department of Innovation, Industry, Science and Research (DIISR). The research reported in this publication was supported by funding from King Abdullah University of Science and Technology (KAUST). X. Z, D. Z. and J. L. acknowledge funding from MSTC (Grant No. 2016YFA0301300), NNSFC (Grant No. 11674402) and GSTP (Grant Nos. 201607010044, 201607020023). The work was

partly conducted at the ACT node of the Australian National Fabrication Facility (ANFF), and the ANU node of the Australian Microscopy and Microanalysis Research Facility (AMMRF), and the ANU Centre for Advanced Microscopy (CAM).

Author Contributions

J. P. conceived the idea and designed the overall experiments. J. P. synthesized the ZnO nanoparticles. J. P., Y. W., H. S. and T. D. prepared and characterized the perovskite cell devices. X. Z., D. Z. and J. L. performed the XPS/UPS measurements and analysis. H. T. N. performed the steady-state PL and TRPL measurements. H. S. performed the XRD measurements and analysis. M. N. L. performed the SEM and cross-sectional SEM measurements. F. K. performed the TEM measurements. S. Z. performed the transmission measurements. X. Y. and W. L. conducted the EQE measurements. J. P., Y. W., D. J., K. J. W., K. R. C., S. D. W. and T. P. W. contributed to the results analysis and interpretation. T. P. W. and S. D. W. supervised the project. J. P. wrote the manuscript. All authors contributed to the discussion of the results and revision of the manuscript.

Conflict of Interest

The authors declare no conflict of interest.

Reference

- [1] A. Kojima, K. Teshima, Y. Shirai, T. Miyasaka, *J. Am. Chem. Soc.* **2009**, *131*, 6050.
- [2] M. Saliba, T. Matsui, K. Domanski, J.-Y. Seo, A. Ummadisingu, S. M. Zakeeruddin, J.-P. Correa-Baena, W. R. Tress, A. Abate, A. Hagfeldt, *Science* **2016**, *354*, 206.
- [3] D. Bi, W. Tress, M. I. Dar, P. Gao, J. Luo, C. Renevier, K. Schenk, A. Abate, F. Giordano, J. P. Correa Baena, J. D. Decoppet, S. M. Zakeeruddin, M. K. Nazeeruddin, M. Gratzel, A. Hagfeldt, *Sci. Adv.* **2016**, *2*, e1501170.
- [4] X. Li, D. Bi, C. Yi, J. D. Decoppet, J. Luo, S. M. Zakeeruddin, A. Hagfeldt, M. Gratzel, *Science* **2016**, *353*, 58.
- [5] S. S. Shin, E. J. Yeom, W. S. Yang, S. Hur, M. G. Kim, J. Im, J. Seo, J. H. Noh, S. I. Seok, *Science* **2017**, *356*, 167.
- [6] W. S. Yang, J. H. Noh, N. J. Jeon, Y. C. Kim, S. Ryu, J. Seo, S. I. Seok, *Science* **2015**, *348*, 1234.
- [7] Q. Jiang, L. Zhang, H. Wang, X. Yang, J. Meng, H. Liu, Z. Yin, J. Wu, X. Zhang, J. You, *Nat. Energy* **2016**, *2*, 16177.
- [8] H. Zhou, Q. Chen, G. Li, S. Luo, T.-b. Song, H.-S. Duan, Z. Hong, J. You, Y. Liu, Y. Yang, *Science* **2014**, *345*, 542.
- [9] Y. Hou, X. Du, S. Scheiner, D. P. McMeekin, Z. Wang, N. Li, M. S. Killian, H. Chen, M. Richter, I. Levchuk, *Science* **2017**, *358*, 1192.
- [10] W. S. Yang, B.-W. Park, E. H. Jung, N. J. Jeon, Y. C. Kim, D. U. Lee, S. S. Shin, J. Seo, E. K. Kim, J. H. Noh, *Science* **2017**, *356*, 1376.
- [11] T. Duong, Y. Wu, H. Shen, J. Peng, X. Fu, D. Jacobs, E.-C. Wang, T. C. Kho, K. C. Fong, M. Stocks, E. Franklin, A. Blakers, N. Zin, K. McIntosh, W. Li, Y.-B.

- Cheng, T. P. White, K. Weber, K. Catchpole, *Adv. Energy Mater.* **2017**, 1700228.
- [12] Y. Wu, D. Yan, J. Peng, Y. Wan, S. P. Phang, H. Shen, N. Wu, C. Barugkin, X. Fu, S. Surve, D. Grant, D. Walter, T. P. White, K. R. Catchpole, K. J. Weber, *Energy Environ.Sci.* **2017**, *10*, 2472.
- [13] X. Zheng, B. Chen, J. Dai, Y. Fang, Y. Bai, Y. Lin, H. Wei, X. C. Zeng, J. Huang, *Nat. Energy* **2017**, *2*, 17102.
- [14] M. Stolterfoht, C. M. Wolff, Y. Amir, A. Paulke, L. Perdigon-Toro, P. Caprioglio, D. Neher, *Energy Environ. Sci.* **2017**, *10*, 1530.
- [15] C.-H. Chiang, M. K. Nazeeruddin, M. Grätzel, C.-G. Wu, *Energy Environ. Sci.* **2017**, *10*, 808.
- [16] D. Luo, L. Zhao, J. Wu, Q. Hu, Y. Zhang, Z. Xu, Y. Liu, T. Liu, K. Chen, W. Yang, *Adv.Mater.* **2017**, *29*, 1604758.
- [17] C.-G. Wu, C.-H. Chiang, Z.-L. Tseng, M. K. Nazeeruddin, A. Hagfeldt, M. Grätzel, *Energy Environ. Sci.* **2015**, *8*, 2725.
- [18] W. Nie, H. Tsai, R. Asadpour, J.-C. Blancon, A. J. Neukirch, G. Gupta, J. J. Crochet, M. Chhowalla, S. Tretiak, M. A. Alam, *Science* **2015**, *347*, 522.
- [19] C. H. Chiang, C. G. Wu, *Nat. Photon.* **2016**, *10*, 196.
- [20] Y. Shao, Z. Xiao, C. Bi, Y. Yuan, J. Huang, *Nat. Commun.* **2014**, *5*, 5784.
- [21] L. Hu, J. Peng, W. Wang, Z. Xia, J. Yuan, J. Lu, X. Huang, W. Ma, H. Song, W. Chen, *Acs Photonics* **2014**, *1*, 547.
- [22] W. Nie, H. Tsai, J. C. Blancon, F. Liu, C. C. Stoumpos, B. Traore, M. Kepenekian, O. Durand, C. Katan, S. Tretiak, *Adv. Mater.* **2018**, *30*, 1703879.
- [23] Z. Zhu, Y. Bai, X. Liu, C. C. Chueh, S. Yang, A. K. Y. Jen, *Adv. Mater.* **2016**, *28*, 6478.
- [24] J. You, L. Meng, T.-B. Song, T.-F. Guo, Y. M. Yang, W.-H. Chang, Z. Hong, H. Chen, H. Zhou, Q. Chen, *Nat. Nanotech.* **2016**, *11*, 75.
- [25] H. Rao, S. Ye, W. Sun, W. Yan, Y. Li, H. Peng, Z. Liu, Z. Bian, Y. Li, C. Huang, *Nano Energy* **2016**, *27*, 51.
- [26] W. Sun, Y. Li, S. Ye, H. Rao, W. Yan, H. Peng, Y. Li, Z. Liu, S. Wang, Z. Chen, *Nanoscale* **2016**, *8*, 10806.
- [27] S. Ye, W. Sun, Y. Li, W. Yan, H. Peng, Z. Bian, Z. Liu, C. Huang, *Nano Lett.* **2015**, *15*, 3723.
- [28] W. Chen, Y. Wu, Y. Yue, J. Liu, W. Zhang, X. Yang, H. Chen, E. Bi, I. Ashraful, M. Grätzel, *Science* **2015**, *350*, 944.
- [29] Z. Wu, S. Bai, J. Xiang, Z. Yuan, Y. Yang, W. Cui, X. Gao, Z. Liu, Y. Jin, B. Sun, *Nanoscale* **2014**, *6*, 10505.
- [30] H. Zhang, H. Wang, H. Zhu, C. C. Chueh, W. Chen, S. Yang, A. K. Y. Jen, *Adv. Energy Mater.* **2018**, 1702762
- [31] Q. Xue, G. Chen, M. Liu, J. Xiao, Z. Chen, Z. Hu, X. F. Jiang, B. Zhang, F. Huang, W. Yang, *Adv. Energy Mater.* **2016**, *6*, 1502021.
- [32] L. Hu, W. Wang, H. Liu, J. Peng, H. Cao, G. Shao, Z. Xia, W. Ma, J. Tang, *J. Mater.Chem. A* **2015**, *3*, 515.
- [33] S. Bai, Z. Wu, X. Wu, Y. Jin, N. Zhao, Z. Chen, Q. Mei, X. Wang, Z. Ye, T. Song, *Nano Research* **2014**, *7*, 1749.
- [34] J. Y. Jeng, Y. F. Chiang, M. H. Lee, S. R. Peng, T. F. Guo, P. Chen, T. C. Wen, *Adv. Mater.* **2013**, *25*, 3727.
- [35] P. W. Liang, C. C. Chueh, S. T. Williams, A. K. Y. Jen, *Adv. Energy Mater.* **2015**, *5*, 1402321.
- [36] P. Docampo, J. M. Ball, M. Darwich, G. E. Eperon, H. J. Snaith, *Nat. Commun.* **2013**, *4*, 2761.

- [37] K. Brinkmann, J. Zhao, N. Pourdavoud, T. Becker, T. Hu, S. Olthof, K. Meerholz, L. Hoffmann, T. Gahlmann, R. Heiderhoff, *Nat. Commun.* **2017**, *8*, 13938.
- [38] G. Li, Y. Jiang, S. Deng, A. Tam, P. Xu, M. Wong, H. S. Kwok, *Adv. Sci.* **2017**, *4*, 1700463.
- [39] K. A. Bush, A. F. Palmstrom, J. Y. Zhengshan, M. Boccard, R. Cheacharoen, J. P. Mailoa, D. P. McMeekin, R. L. Hoye, C. D. Bailie, T. Leijtens, *Nat. Energy* **2017**, *2*, 17009.
- [40] J. Peng, Y. Wu, W. Ye, D. A. Jacobs, H. Shen, X. Fu, Y. Wan, N. Wu, C. Barugkin, H. T. Nguyen, *Energy Environ. Sci.* **2017**, *10*, 1792.
- [41] D. A. Schwartz, N. S. Norberg, Q. P. Nguyen, J. M. Parker, D. R. Gamelin, *J. Am. Chem.Soc.* **2003**, *125*, 13205.
- [42] Y. Sun, J. H. Seo, C. J. Takacs, J. Seifert, A. J. Heeger, *Adv.Mater.* **2011**, *23*, 1679.
- [43] H. Choi, C.-K. Mai, H.-B. Kim, J. Jeong, S. Song, G. C. Bazan, J. Y. Kim, A. J. Heeger, *Nature communications* 2015, *6*, 7348.
- [44] H. Dong, Z. Wu, B. Xia, J. Xi, F. Yuan, S. Ning, L. Xiao, X. Hou, *Chemical Communications* **2015**, *51*, 8986.
- [45] W. Chen, Y. Wu, J. Liu, C. Qin, X. Yang, A. Islam, Y.-B. Cheng, L. Han, *Energy Environ.Sci.* **2015**, *8*, 629.
- [46] X. Liu, H. Yu, L. Yan, Q. Dong, Q. Wan, Y. Zhou, B. Song, Y. Li, *ACS Appl. Mater. Interfaces* **2015**, *7*, 6230.
- [47] Y. Wan, C. Samundsett, J. Bullock, T. Allen, M. Hettick, D. Yan, P. Zheng, X. Zhang, J. Cui, J. McKeon, *ACS Appl. Mater. Interfaces* **2016**, *8*, 14671.
- [48] Y. Yang, M. Yang, D. T. Moore, Y. Yan, E. M. Miller, K. Zhu, M. C. Beard, *Nat. Energy* **2017**, *2*, 16207.
- [49] D. A. Jacobs, Y. Wu, H. Shen, C. Barugkin, F. J. Beck, T. P. White, K. Weber, K. R. Catchpole, *Phys. Chem. Chem.Phys.* **2017**, *19*, 3094.

Chapter 6: Summary and Future Work

6.1 Summary

In summary, this thesis demonstrates the development of highly efficient, hysteresis-free perovskite solar cells enabled by electron transport materials with well-matched work functions and high-conductivity, as well as through passivation of the perovskite/contact layer interfaces. We demonstrated that indium-doped TiO_x is better than intrinsic TiO_2 for use as an ETL in normal-structured perovskite solar cells; enhanced steady-state efficiencies of 19.3% and 24.5% were obtained for standalone perovskite cells and perovskite-silicon 4-terminal tandems, respectively. Second, a one-side passivation strategy was introduced to improve the open-circuit voltage ($V_{oc} \sim 1.18$ V) and efficiency (PCE \sim 20.4%) of normal-structure perovskite solar cells. Furthermore, a remarkably high V_{oc} of 1.22 V and a high efficiency of 20.8% were achieved using two-sided passivation in a normal-structured cell. Finally, the performance of inverted perovskite cells was improved through the use of combination (ZnO/MgF_2) ETLs in place of the standard fullerene derivatives, resulting in higher efficiencies and fill factors (PCE \sim 17.5% with a high FF of 0.795).

6.1.1 Passivating the Defects/Trap States within TiO_2 Lattices

TiO_2 is widely used as an ETL in optoelectronic devices due to its advantageous properties: a suitable work function, good electron mobility and high bandgap (~ 3.3 eV). Inevitably, it is challenging to control the stoichiometric ratio of Ti to O during the fabrication of TiO_2 , resulting in the formation of many lattice defects.

We introduced indium-doped TiO_x to overcome this challenge, using a precursor In- TiO_x which can be easily prepared by straightforwardly mixing the indium and titania precursors in the correct proportion. Based on the analysis of XPS and UPS, we have shown that a small amount of valency +3 indium ions can effectively passivate defects, reduce the sub-bandgap states and raise the conduction band.

The indium-doping improves the efficiency of perovskite cells through two separate mechanisms. First, it increases the carrier density and hall mobility, and hence the conductivity of the In- TiO_x ETL compared to the standard TiO_2 ETL, dramatically improving the FF of completed cells. Second, the indium-doping allows us to tune the

work function of the ETL to improve the band alignment at the ETL/perovskite interface, thus enhancing the V_{oc} . As a result, a high steady-state efficiency of 17.9% for MAPbI₃-based cells and 19.3% for Cs_{0.05}(MA_{0.17}FA_{0.83})_{0.95}Pb(I_{0.83}Br_{0.17})₃ was achieved using the optimized In-TiO_x ETLs, corresponding to absolute efficiency gains of 4.4% and 1.2% respectively relative to pure TiO₂ controls. Furthermore, we demonstrated a high steady-state PCE of 16.6% for a semi-transparent cell and used it to achieve a steady-state efficiency of 24.5% in a four-terminal tandem arrangement with a silicon bottom cell. This represented a record efficiency for perovskite-Si tandems at the time of publication.

Although the use of In-TiO_x ETLs demonstrates an avenue for improving the performance of perovskite solar cells, TiO_x materials are not UV-stable, making them less than ideal as an ultimate solution.

6.1.2 One-Side Passivation: Passivating the Electron Transport Layer/Perovskite Interfaces

Defect-induced interface recombination and ion migration have been thought to be responsible for the V_{oc} loss and the current-voltage hysteresis in many perovskite solar cells.

We show that ultrathin PMMA:PCBM blend films can effectively passivate the perovskite/meso-TiO₂ interface, leading to a significant reduction in interfacial recombination and a dramatic increase in V_{oc} from 1.1 V (control cell) to 1.18 V (passivated cell). Photoluminescence imaging and time-resolved photoluminescence studies reveal that a better perovskite solar cell should yield more radiative luminescence. Indeed, our passivated cells exhibit a considerably higher photoluminescence signal than unpassivated cells by a factor of six.

By optimizing the PMMA:PCBM ratio to achieve both high V_{oc} and fill-factor we obtained stable perovskite solar cells with a steady-state PCE of 20.4% and negligible hysteresis. The optimized cells also exhibit an exceptionally rapid current and voltage response when illuminated, reaching steady-state V_{oc} or J_{sc} in less than 3s. This new passivation approach addresses one of the main limitations of current high-efficiency perovskite solar cells - interface recombination - and demonstrates the potential for ultrathin passivation layers to significantly improve cell performance.

Furthermore, our finding that pure PMMA films provided the best passivation, but insufficient conductivity, indicates the potential for further improvements if new n-type

polymer materials can be developed with appropriate band alignment and carrier mobility.

6.1.3 Double-Side Passivation: Passivating the Perovskite/Transport Layers Interfaces

Inspired and encouraged by our one-side passivation design, we then demonstrated double-side passivated perovskite solar cells incorporating ultrathin PMMA-films at the perovskite-ETL and perovskite-HTL interfaces. The outstanding passivation properties of the PMMA enabled V_{oc} values of up to ~ 1.22 V, which is one of the highest reported for ~ 1.6 eV bandgap perovskites. A high PCE of 20.8% with negligible hysteresis was achieved for the champion passivated cells. Analysis of perovskite-PMMA interactions reveals that the passivation results from the Lewis-base properties of the carbonyl (C=O) group on the PMMA, which can effectively passivate under-coordinated lead atoms (Pb^{2+}), known to cause non-radiative recombination at perovskite surfaces and grain boundaries.

Although it provides excellent interface passivation, PMMA is an insulating polymer so the passivated cells did have a slightly reduced fill-factor as a result of increased series resistance. This was mitigated on the ETL side by using a PMMA:PCBM blend, as demonstrated in Chapter 3, but future development of novel conducting polymers with C=O groups may lead to even further efficiency gains.

6.1.4 Combination ETLs (ZnO/MgF_2) for Inverted Perovskite Solar Cells: Substituting the Organic Electron Transport Materials

It is known that the charge transport layers play critical roles in achieving high-performance perovskite solar cells. In inverted perovskite solar cells, PCBM, C_{60} and other fullerene derivatives are commonly used as ETLs although the PCBM, C_{60} and other fullerene derivatives are not ideal ETLs due to their poor hole-blocking property, mismatched energy level alignment issue and considerable optical absorption.

To substitute the aforementioned n-type organic materials, we demonstrated a set of combination ETLs (ZnO (~ 70 nm)/ MgF_2 (~ 1.5 nm)) for enhanced performance MAPbI_3 -based inverted perovskite solar cells. The outstanding work function, conductivity and hole-blocking properties of ZnO nanomaterials, along with the additional effect of the ultrathin insulating MgF_2 layer (which reduces the aluminium

contact resistance and diminishes the injection barrier at the ETL/Al interface), makes the bi-layer combination ideal for use as an excellent ETL for inverted perovskite solar cells. Together with ultrathin (less than 5 nm) PMMA:PCBM passivation layers, a high PCE of 17.5% with a high FF (~0.795) and negligible hysteresis was achieved for our champion inverted perovskite cells.

A further increase in PCE for inverted perovskite cells can be obtained by substituting the PEDOT:PSS with other superior hole transport materials and using mixed cation perovskite absorbers as well. In addition, this finding may provide an efficient combination ETL to further develop the performance of perovskite-silicon 2-terminal tandems.

6.2 Future Work

We consider four aspects as being essential to further improvements of perovskite cell efficiency and stability: passivation of defects within perovskite bulk material; developing UV-stable electron transport layers; exploiting thermally-stable hole transport layers; and utilizing stable electrodes. These are discussed in further detail below.

6.2.1 Passivating the Perovskite Bulk Defects

It is known that thermal annealing is critical to the proper growth of perovskite crystals, but this step never result in perfect crystals. Crystallographic defects and impurities may act as recombination centers that degrade the overall efficiency.^[1,2] It is therefore clearly desirable to develop passivation strategies that address the presence of bulk defects, in complement to the interfacial strategies presented here. A more drastic strategy would be to pursue 2D, and combined 2D/3D perovskite materials as plausible options to further the overall device performance of perovskite solar cells.

6.2.2 Developing UV-Stable Electron Transport Layers

TiO₂ is a photocatalyst that is very sensitive to the UV light. Under UV illumination, the electrons of the TiO₂ will be excited from valence band to conduction band, the electrons and holes will migrate to the surface of the TiO₂ to form electron-hole pairs. The electrons will induce the reduction of Ti⁺⁴ to Ti⁺³,^[3,4] and the holes will

react with the surface bridging oxygen ion to form oxygen vacancies.^[3-4] The Ti^{+3} sites and oxygen vacancies are defects that will induce the perovskite degradation during long-term operation.^[5,6] That makes the TiO_2 less than ideal as an electron transport layer for perovskite solar cells, although a stop-gap solution might be to include UV-filters in the cell design. Thus, UV-stable electron transport layers with suitable work function, good conductivity and excellent hole blocking properties are critical to further enhance the stability of perovskite solar cells. Deep energy level metal oxide materials such SnO_x might be good candidates for addressing this challenge.

6.2.3 Exploiting Thermal-Stable Hole Transport Layers

Spiro-OMeTAD and PTAA have been widely used as hole transporting layers, but normally need Li-TFSI additives and oxidation to enhance their conductivity.^[6,7] Problematically, the lithium ions from Li-TFSI source can easily diffuse into the perovskite layer, potentially acting as recombination centres or mobile ions which will affect the performance and stability during long-term operation.^[6,8,9] The tolerance of the Spiro-OMeTAD and PTAA HTLs becomes even worse when these are tested under elevated-temperatures.^[6,8,9] It is therefore strongly desirable to develop thermally-stable substitutes for Spiro-OMeTAD and PTAA. One plausible solution is to develop inorganic metal oxides (such as NiO_x ,^[10] CuSCN ^[9]) as these have been shown to yield high hole mobilities, suitable work-functions, excellent electron-blocking properties and outstanding thermal stability.

6.2.4 Utilizing Stable Electrodes

Gold, silver and aluminium are common metal electrodes for perovskite solar cells. Unfortunately, it has been discovered that silver and aluminium can easily penetrate and diffuse into the perovskite through the organic transport layers, where they can react with the perovskite components triggering decomposition of the perovskite crystals. Even for the gold materials, penetration and diffusion seems to be inevitable and induces defect-mediated recombination. Consequently, physically and chemically stable electrodes materials are urgently needed to address the stability of perovskite solar cells.

References

- [1] S. D. Stranks, "Nonradiative losses in metal halide perovskites," *ACS Energy Letters*, vol. 2, pp. 1515-1525, 2017.
- [2] W. Tress, "Perovskite Solar Cells on the Way to Their Radiative Efficiency Limit—Insights Into a Success Story of High Open-Circuit Voltage and Low Recombination," *Advanced Energy Materials*, vol. 7, pp. 1602358, 2017.
- [3] M. Muruganandham and M. Swaminathan, "Photocatalytic decolourisation and degradation of Reactive Orange 4 by TiO₂-UV process," *Dyes and Pigments*, vol. 68, pp. 133-142, 2006.
- [4] K. Hashimoto, H. Irie, and A. Fujishima, "TiO₂ photocatalysis: a historical overview and future prospects," *Japanese Journal of Applied Physics*, vol. 44, p. 8269, 2005.
- [5] S. K. Pathak, A. Abate, P. Ruckdeschel, B. Roose, K. C. Gödel, Y. Vaynzof, *et al.*, "Performance and Stability Enhancement of Dye-Sensitized and Perovskite Solar Cells by Al Doping of TiO₂," *Advanced Functional Materials*, vol. 24, pp. 6046-6055, 2014.
- [6] M. Saliba, T. Matsui, K. Domanski, J.-Y. Seo, A. Ummadisingu, S. M. Zakeeruddin, *et al.*, "Incorporation of rubidium cations into perovskite solar cells improves photovoltaic performance," *Science*, vol. 354, pp. 206-209, 2016.
- [7] J.-P. Correa-Baena, W. Tress, K. Domanski, E. H. Anaraki, S.-H. Turren-Cruz, B. Roose, *et al.*, "Identifying and suppressing interfacial recombination to achieve high open-circuit voltage in perovskite solar cells," *Energy & Environmental Science*, vol. 10, pp. 1207-1212, 2017.
- [8] Y. Hou, X. Du, S. Scheiner, D. P. McMeekin, Z. Wang, N. Li, *et al.*, "A generic interface to reduce the efficiency-stability-cost gap of perovskite solar cells," *Science*, vol. 358, pp. 1192-1197, 2017.
- [9] N. Arora, M. I. Dar, A. Hinderhofer, N. Pellet, F. Schreiber, S. M. Zakeeruddin, *et al.*, "Perovskite solar cells with CuSCN hole extraction layers yield stabilized efficiencies greater than 20%," *Science*, 2017. DOI: 10.1126/science.aam5655.
- [10] W. Chen, Y. Wu, Y. Yue, J. Liu, W. Zhang, X. Yang, *et al.*, "Efficient and stable large-area perovskite solar cells with inorganic charge extraction layers," *Science*, vol. 350, pp. 944-948, 2015.

List of Other Publications and Conferences

Other Peer-Reviewed Papers

1. H. Shen, T. Duong, Y. Wu, **J. Peng**, D. Jacobs, N. Wu, K. Weber, T. White and K. Catchpole, *Science and Technology of Advanced Materials*, 2018, 1-36. DOI: 10.1080/14686996.2017.1422365.
2. H. Shen, T. Duong, **J. Peng**, D. Jacobs, N. Wu, J. Gong, Y. Wu, S. K. Karuturi, X. Fu, K. Weber and X. Xiao, K. Weber, X. Xiao, T. P. White, K. R. Catchpole, *Energy & Environmental Science*, 2018. DOI: 10.1039/C7EE02627G.
3. Y. Wan, S. K. Karuturi, C. Samundsett, J. Bullock, M. Hettick, D. Yan, **J. Peng**, P. R. Narangari, S. Mokkapati and H. H. Tan, C. Jagadish, A. Javey, A. Cuevas, *ACS Energy Letters*, 2017. DOI: 10.1021/acseenergylett.7b0115.
4. Y. Wu, D. Yan, **J. Peng**, Y. Wan, S. P. Phang, H. Shen, N. Wu, C. Barugkin, X. Fu and S. Surve, D. Walter, T. P. White, K. R. Catchpole, K. Weber, *Energy & Environmental Science*, 2017, **10**, 2472-2479.
5. D. Walter, Y. Wu, T. Duong, **J. Peng**, L. Jiang, K. C. Fong and K. Weber, *Advanced Energy Materials*, 2018. DOI: 10.1002/aenm.201701522.
6. T. Duong, H. K. Mulmudi, Y. Wu, X. Fu, H. Shen, **J. Peng**, N. Wu, H. T. Nguyen, D. Macdonald and M. Lockrey, T. P. White, K. Weber, K. R. Catchpole, *ACS Applied Materials & Interfaces*, 2017, **9**, 26859-26866.
7. N. Wu, Y. Wu, H. Shen, D. Walter, T. Duong, D. Grant, C. Barugkin, X. Fu, **J. Peng** and H. Mulmudi, T. P. White, K. R. Catchpole, K. Weber, *Energy Technology*, 2017. DOI: 10.1002/ente.201700374.
8. H. Shen, D. A. Jacobs, Y. Wu, T. Duong, **J. Peng**, X. Wen, X. Fu, S. K. Karuturi, T. P. White and K. Weber, K. R. Catchpole, *The Journal of Physical Chemistry Letters*, 2017, **8**, 2672-2680.
9. T. Duong, Y. Wu, H. Shen, **J. Peng**, X. Fu, D. Jacobs, E. C. Wang, T. C. Kho, K. C. Fong and M. Stocks, E. Franklin, A. Blakers, N. Zin, K. McIntosh, W. Li, Y-B. Cheng, T. P. White, K. Weber, K. R. Catchpole, *Advanced Energy Materials*, 2017. DOI: 10.1002/aenm.201700228.

10. H. Shen, Y. Wu, **J. Peng**, T. Duong, X. Fu, C. Barugkin, T. P. White, K. Weber and K. R. Catchpole, *ACS Applied Materials & Interfaces*, 2017, **9**, 5974-5981.
11. Y. Wan, C. Samundsett, J. Bullock, M. Hettick, T. Allen, D. Yan, **J. Peng**, Y. Wu, J. Cui and A. Javey, A. Cuevas, *Advanced Energy Materials*, 2017. DOI: 10.1002/aenm.201601863.
12. T. Duong, H. K. Mulmudi, H. Shen, Y. Wu, C. Barugkin, Y. O. Mayon, H. T. Nguyen, D. Macdonald, **J. Peng**, M. Lockrey and W. Li, Y-B Cheng, T. P. White, K. Weber, K. R. Catchpole, *Nano Energy*, 2016, **30**, 330-340.
13. Y. Wan, C. Samundsett, D. Yan, T. Allen, **J. Peng**, J. Cui, X. Zhang, J. Bullock and A. Cuevas, *Applied Physics Letters*, 2016, **109**, 113901.
14. Y. Wu, H. Shen, D. Walter, D. Jacobs, T. Duong, **J. Peng**, L. Jiang, Y. B. Cheng and K. Weber, *Advanced Functional Materials*, 2016, **26**, 6807-6813.
15. Q.-J. Sun, † **J. Peng**, † W.-H. Chen, X.-J. She, J. Liu, X. Gao, W.-L. Ma and S.-D. Wang, *Organic Electronics*, 2016, **34**, 118-123. († **contributed equally**)

Conference Presentations

1. **Jun Peng**, S. D. Wolf, K. J. Weber, K. R. Catchpole, T. P. White, High Open-Circuit Voltage Perovskite Solar Cells: Role of Surface Passivation, **2018**, PSCO, Lausanne. (**Oral Presentation**)
2. **Jun Peng**, J. I. Khan, W. Liu, T. Duong, H. Shen, Y. Wu, X. Yang, Y. Wan, K. J. Weber, K. R. Catchpole, S. D. Wolf, T. P. White, High-Efficiency and Stable Perovskite Solar Cells with Negligible Hysteresis via Interface Engineering, **2018**, KAUST Research Conference: Synergistic Approaches in Solar Energy Conversion, Jeddah. (**Oral Presentation**)
3. **Jun Peng**, T. Duong, Y. Wu, H. Shen, Y. Wan, K. J. Weber, K. R. Catchpole, T. P. White, Efficient Indium-Doped TiO_x Electron Transport Layers for High-Performance Perovskite Solar Cells and Perovskite-Silicon Tandems, **2016**, Asia-Pacific Solar Research Conference, Canberra. (**Oral Presentation**)
4. **Jun Peng**, Y. Wu, T. Duong, H. Shen, D. Jacobs, Y. Wan, N. Wu, X. Fu, K. J. Weber, K. R. Catchpole, T. P. White, High-Efficiency and Stable Perovskite Solar Cells with Negligible Hysteresis via Suppressing Interfacial Recombination, **2017**, PSCO, Oxford. (**Poster**)

Appendix

The appendix contains the supporting documents from four manuscripts presented in the body of the thesis.

ADVANCED ENERGY MATERIALS

Supporting Information

for *Adv. Energy Mater.*, DOI: 10.1002/aenm.201601768

Efficient Indium-Doped TiO_x Electron Transport Layers for High-Performance Perovskite Solar Cells and Perovskite-Silicon Tandems

Jun Peng, The Duong, Xianzhong Zhou, Heping Shen, Yiliang Wu, Hemant Kumar Mulmudi, Yimao Wan, Dingyong Zhong, Juntao Li, Takuya Tsuzuki, Klaus J. Weber, Kylie R. Catchpole, and Thomas P. White**

Supporting Information

Efficient Indium-Doped TiO_x Electron Transport Layers for High-Performance Perovskite Solar Cells and Perovskite-Silicon Tandems

Jun Peng, The Duong, Xianzhong Zhou, Heping Shen, Yiliang Wu, Hemant Kumar Mulmudi, Yimao Wan, Dingyong Zhong, Juntao Li, Takuya Tsuzuki, Klaus J. Weber, Kylie R. Catchpole, and Thomas P. White**

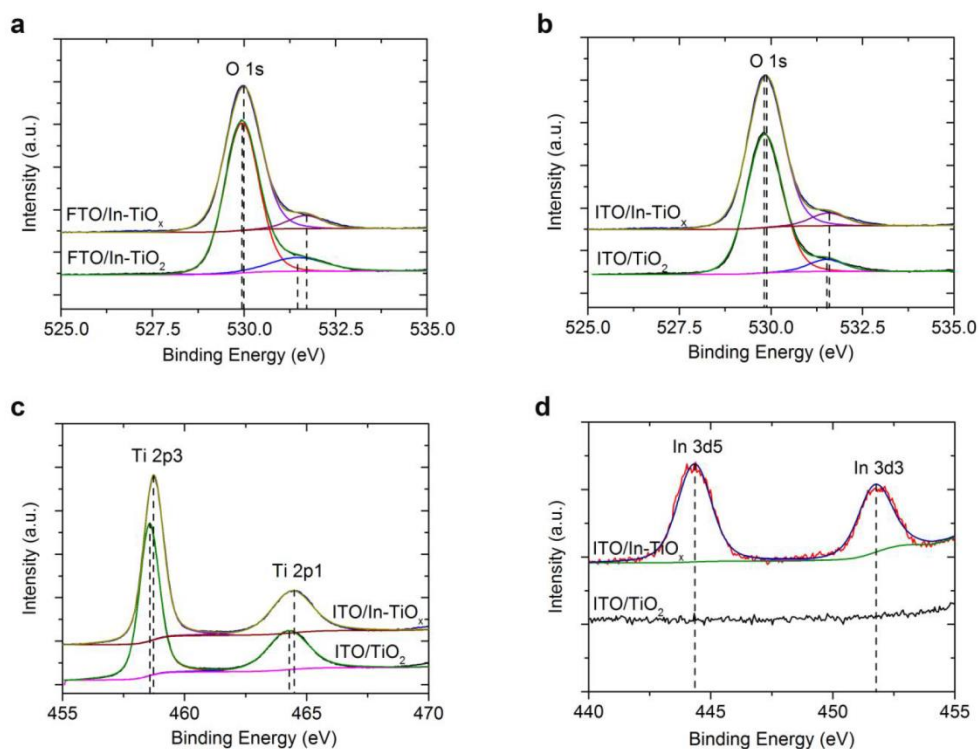


Figure S1. a) XPS spectra of O 1s peaks for FTO/In-TiO_x and FTO/TiO₂ samples. The XPS spectra of ITO/In-TiO_x and ITO/TiO₂; b) XPS spectra of O 1s peaks; c) XPS spectra of Ti 2p peaks; d) XPS spectra of In 3d peaks.

The XPS spectra of O 1s in Figure S1a can be deconvoluted with two different oxygen species. The binding energy of O 1s peak from the FTO/TiO₂ sample centred at ~529.9 eV

can be ascribed to TiO_2 ,^[1] and a slightly higher O 1s binding energy (~ 530.0 eV) from the FTO/In- TiO_x sample can be ascribed to In- TiO_x .^[1] The smaller peak at ~ 531.5 eV and ~ 531.7 eV may be assigned to O_2 , H_2O , hydroxyl (OH^-) and C-O,^[2,3] which corresponds surface contamination resulting from the samples being exposed to air before the XPS measurements.^[2] The O1s spectra for In- TiO_x and TiO_2 films on ITO substrates show similar XPS spectra with that of In- TiO_x and TiO_2 films on FTO substrates (see Figure S1b). Figure S1c shows the Ti2p1 and Ti 2p3 peaks of the TiO_2 film at binding energies of ~ 464.3 eV and ~ 458.5 eV, which are consistent with literature values.^[1] The Ti 2p3 spectrum for In- TiO_x , has a peak centred at 458.7 eV,^[1] which is higher than that of the pure TiO_2 shown in Figure S1c. Figure S1d shows a slightly rough XPS spectrum of In 3d5 for In- TiO_x , with a single peak-fit centred at ~ 444.3 eV that can be ascribed to indium oxide.^[1] The atomic ratio of Ti:O for TiO_2 sample is 1:2 determined by comparing the elements' relative peaks areas and their corresponding relative sensitivity factors, and the ratio of In:Ti for In- TiO_x sample is 2:98.

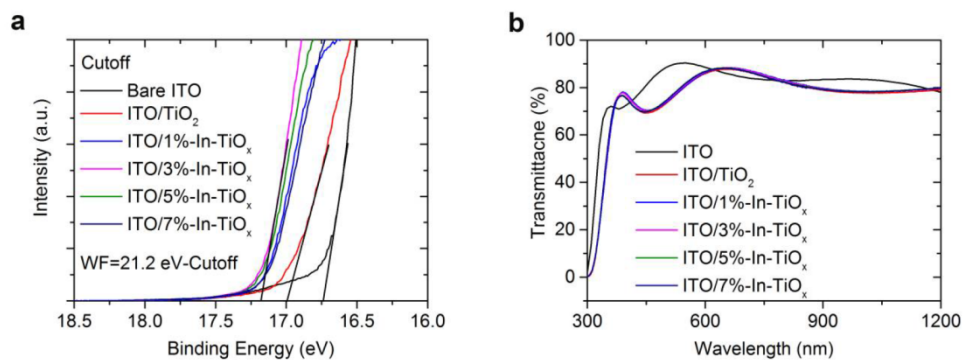


Figure S2. a) UPS spectra of bare ITO, ITO/TiO₂ and ITO/In-TiO_x. b) Transmittance spectra of bare ITO, ITO/TiO₂ and ITO/In-TiO_x.

As shown in Figure S2a, it was found that the WF of bare ITO is about 4.48 eV, the WF of ITO/TiO₂ is ~4.22 eV; for the 1%-In-TiO_x, 3%-In-TiO_x and 5%-In-TiO_x, we measure WFs of ~4.08 eV, ~4.02 eV and ~4.05 eV respectively; and for 7%-In-TiO_x, the WF value goes back to ~4.09 eV. Figure S2b shows that the transmittance of ITO/In-TiO_x samples is almost identical to that of ITO/TiO₂.

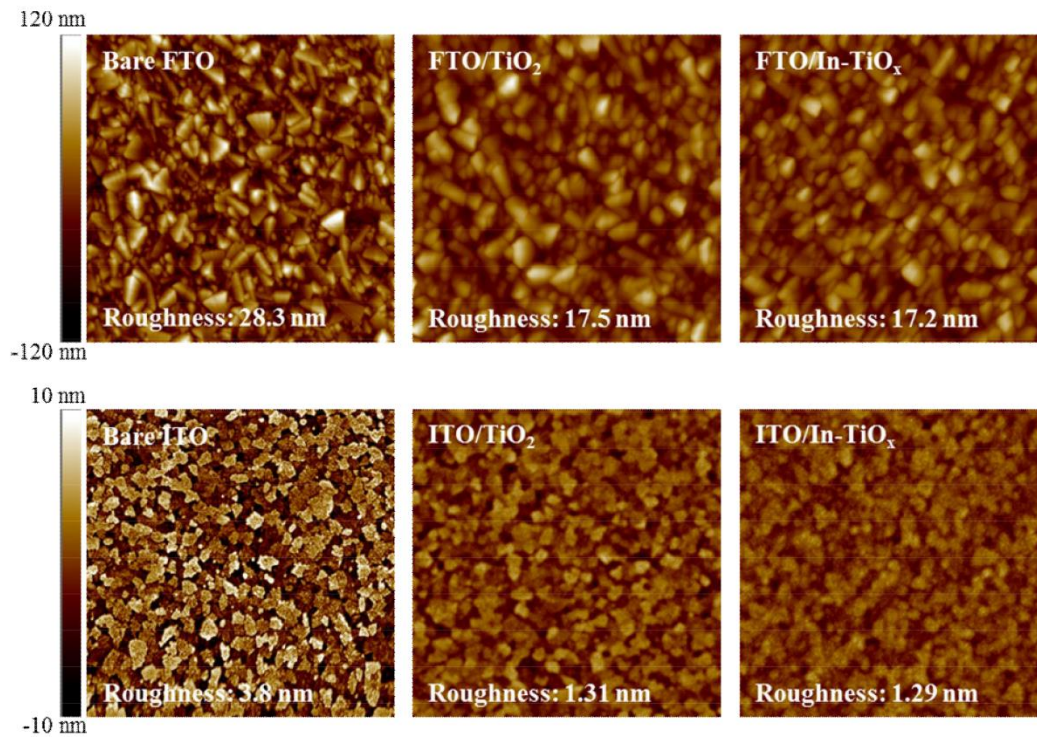


Figure S3. The AFM images of the Bare FTO, FTO/TiO₂, FTO/In-TiO_x, Bare ITO, ITO/TiO₂, ITO/In-TiO_x. Note that all images span 5 μm \times 5 μm . The thickness of TiO₂ and In-TiO_x films deposited on FTO and ITO substrates are about 50 nm.

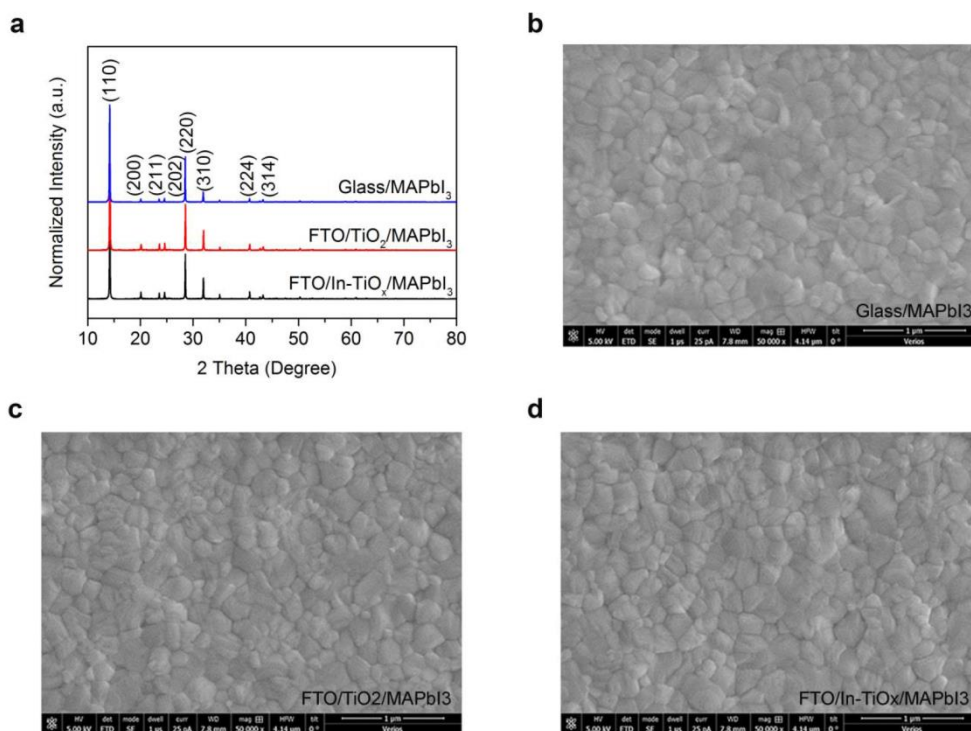


Figure S4. a) XRD patterns of MAPbI₃ thin films deposited on Glass, FTO/TiO₂ and FTO/In-TiO_x substrates. b) SEM of MAPbI₃ thin film deposited on Glass substrate. c) SEM of MAPbI₃ thin film deposited on FTO/TiO₂. d) SEM of MAPbI₃ thin film deposited on FTO/In-TiO_x.

As shown in the Figure S4a, the wide spectra XRD patterns of the pure MAPbI₃ thin films on different substrates exhibited similar crystallinity, and its crystal structure is consistent with the literature.^[4] In Figures S4b-d, the grain sizes of the MAPbI₃ crystals on three different samples show no big variance, and they exhibited continuous and conformal MAPbI₃ thin films with no pinholes.

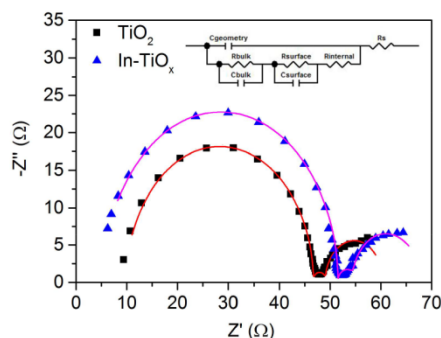


Figure S5. Impedance spectroscopy analysis of the MAPbI₃-based cells, where the device structure is FTO/In-TiO_x (TiO₂) (~50 nm)/meso-TiO₂ (~70 nm)/MAPbI₃/Spiro-OMeTAD/Au tested under one-sun condition with 1 V forward bias voltage. The equivalent circuit used for the parameter extraction is shown in the inset. Note that the effective areas for the MAPbI₃-based cells are 0.36 cm².

As shown in Figure S5, the impedance spectroscopy data were obtained under one-sun condition with 1 V forward bias. The inset of Figure S5 shows the equivalent circuit of our curve fitting model, which has been used previously to investigate interfacial and bulk recombination in perovskite solar cells.^[5,6] The equivalent circuit consists of a resistor in series to measure the overall series resistance, and two resistor-capacitance (RC) element to identify the bulk and interface recombination. It was found that the series resistance extracted from the In-TiO_x-based perovskite cell (5.429 Ω) is significantly smaller than that of TiO₂-based perovskite cell (9.916 Ω). In addition, the R_{bulk} (R_{surf}) and C_{bulk} (C_{surf}) for In-TiO_x-based cells are 13.13 (2.921) and 5.364E-3 (4.404E-4), while the R_{bulk} (R_{surf}) and C_{bulk} (C_{surf}) for TiO₂-based cells are 11.3 (2.35) and 5.23E-3 (2.082E-4). We found that the bulk charge recombination lifetime ($\tau_{\text{bulk}}=R_{\text{bulk}}*C_{\text{bulk}}$) for In-TiO_x and TiO₂-based cells shows no significant difference. However, the surface charge recombination lifetime ($\tau_{\text{surf}}=R_{\text{surf}}*C_{\text{surf}}$) for In-TiO_x-based perovskite cell is ~2.5 times higher than that of for TiO₂-based perovskite cell. This further supports our previous discussion that the improved cell

performance results from higher conductivity and improved interface properties of the In-TiO_x-based ETL.

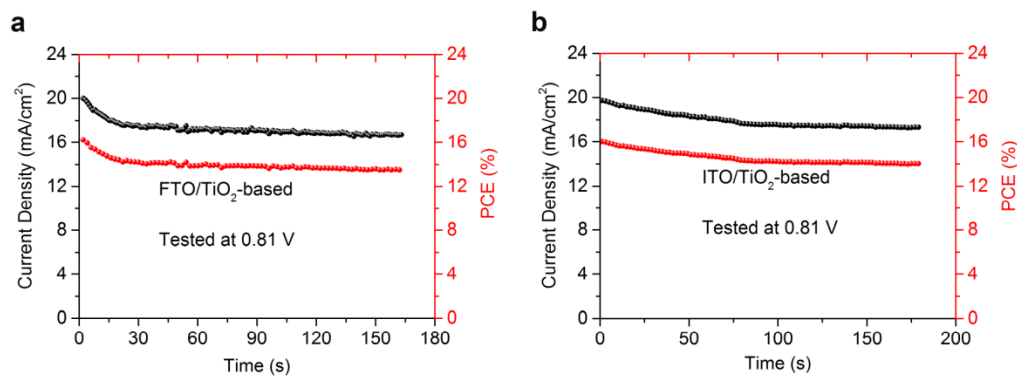


Figure S6. Photovoltaic performance of the MAPbI₃ perovskite and TiO₂ based normal devices. a) The steady-state efficiency of the FTO/TiO₂/meso-TiO₂/MAPbI₃/Spiro-OMeTAD/Au tested at 0.81 V; b) the steady-state efficiency of the ITO/TiO₂/meso-TiO₂/MAPbI₃/Spiro-OMeTAD/Au tested at 0.81 V.

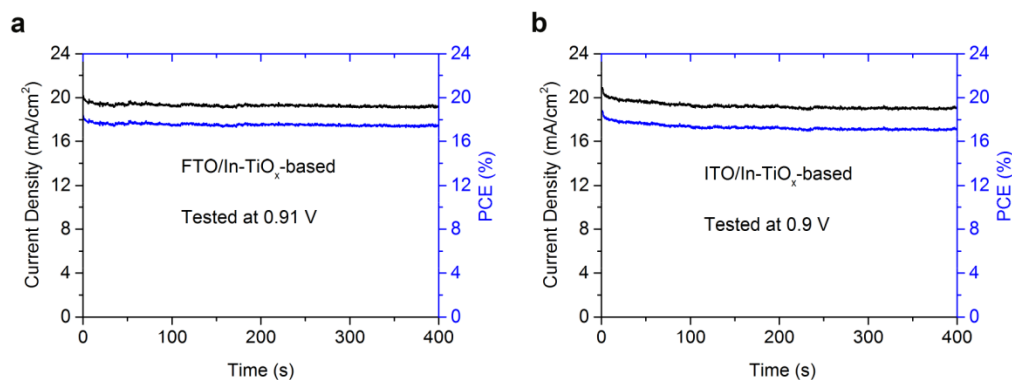


Figure S7. Steady-state measurements for the MAPbI₃-based perovskite cells. a) The steady-state efficiency of the device with a structure of FTO/In-TiO_x/meso-TiO₂/MAPbI₃/Spiro-OMeTAD/Au tested at 0.91 V; b) the steady-state efficiency of the device with a structure of ITO/In-TiO_x/meso-TiO₂/MAPbI₃/Spiro-OMeTAD/Au tested at 0.9V.

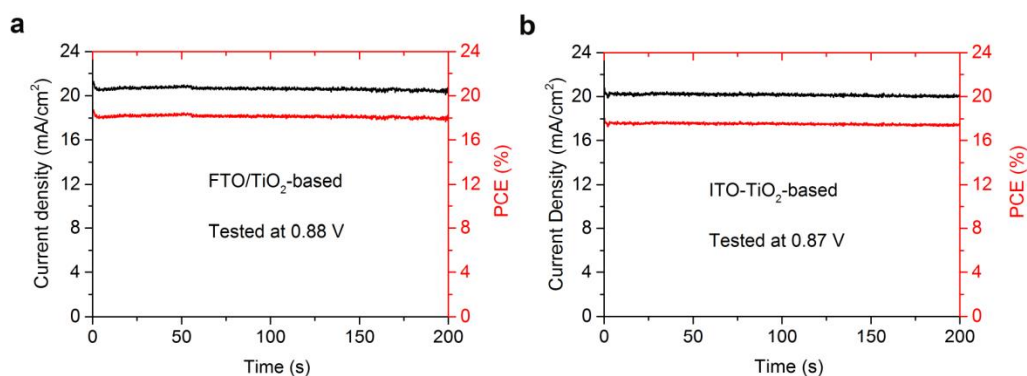


Figure S8. The steady-state measurements for the $\text{Cs}_{0.05}(\text{MA}_{0.17}\text{FA}_{0.83})_{0.95}\text{Pb}(\text{I}_{0.83}\text{Br}_{0.17})_3$ -based perovskite cells. a) The steady-state efficiency of the device with a structure of FTO/TiO₂/meso-TiO₂/ $\text{Cs}_{0.05}(\text{MA}_{0.17}\text{FA}_{0.83})_{0.95}\text{Pb}(\text{I}_{0.83}\text{Br}_{0.17})_3$ /Spiro-OMeTAD/Au tested at 0.88 V; b) the steady-state efficiency of the device with a structure of ITO-TiO₂/meso-TiO₂/ $\text{Cs}_{0.05}(\text{MA}_{0.17}\text{FA}_{0.83})_{0.95}\text{Pb}(\text{I}_{0.83}\text{Br}_{0.17})_3$ /Spiro-OMeTAD/Au tested at 0.87 V.

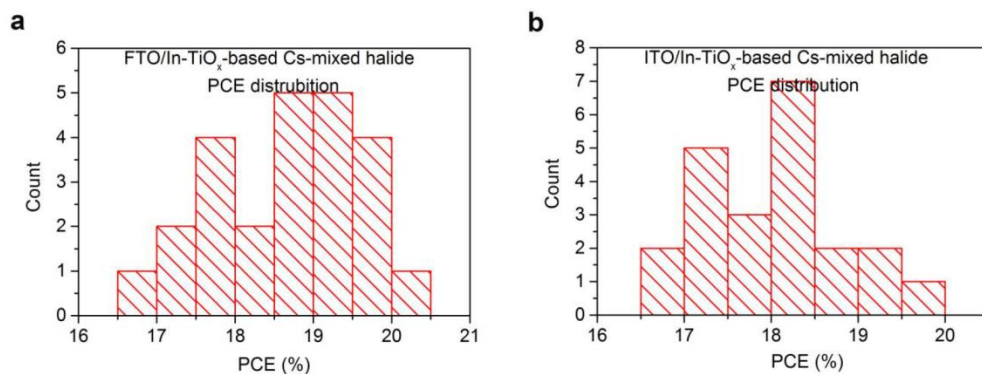


Figure S9. Performance distributions of the Cs-mixed halide perovskite cells. a) The PCE distribution of the device with a structure of FTO/In-TiO_x/meso-TiO₂/Cs-mixed halide perovskite/Spiro-OMeTAD/Au; b) the PCE distribution of the device with a structure of ITO/In-TiO_x/meso-TiO₂/Cs-mixed halide perovskite/Spiro-OMeTAD/Au. Note that the Cs-mixed halide is $\text{Cs}_{0.05}(\text{MA}_{0.17}\text{FA}_{0.83})_{0.95}\text{Pb}(\text{I}_{0.83}\text{Br}_{0.17})_3$.

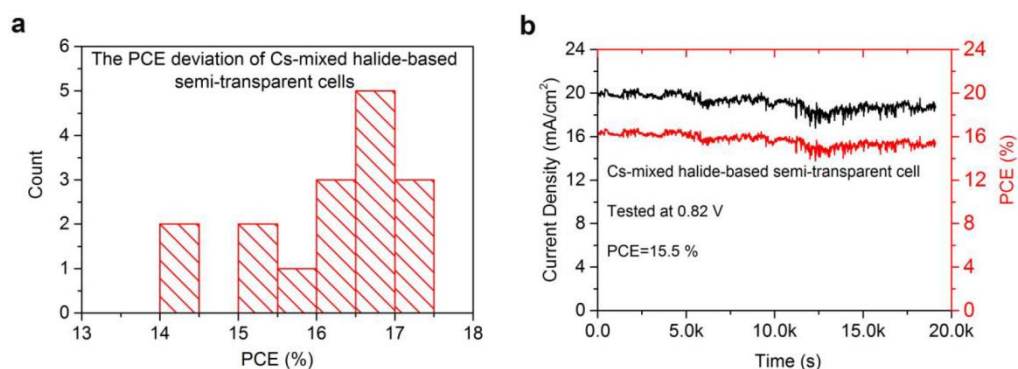


Figure S10. The device performance distribution and steady-state efficiency of Cs-mixed halide-based semi-transparent cell. a) The PCE distribution of semi-transparent cell with a structure of Glass/ITO/In-TiO_x/meso-TiO₂/Cs-mixed halide perovskite/Spiro-OMeTAD/MoO₃/ITO/Au, where Cs-mixed halide is Cs_{0.05}(MA_{0.17}FA_{0.83})_{0.95}Pb(I_{0.83}Br_{0.17})₃. b) An extremely long time steady-state efficiency measurement tested at a bias voltage of 0.82 V under 1 sun conditions (100 mW/cm², AM 1.5G).

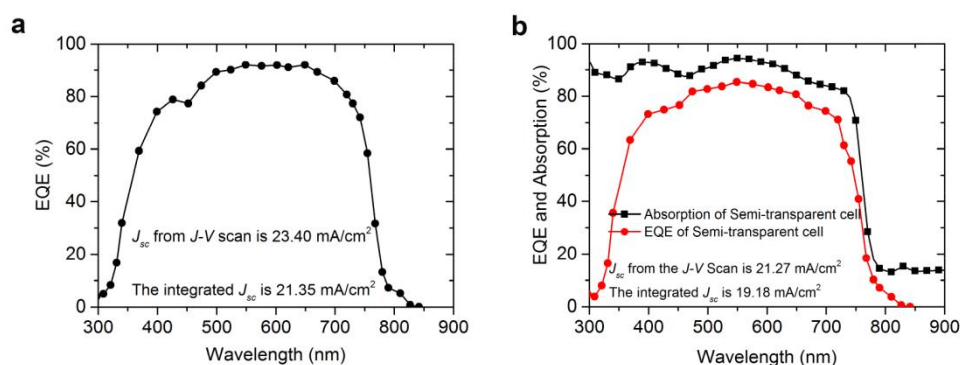


Figure S11. a) EQE spectra of an opaque cell with a structure of Glass/ITO/In-TiO_x/meso-TiO₂/Cs-mixed halide perovskite/Spiro-OMeTAD/Au, where Cs-mixed halide is Cs_{0.05}(MA_{0.17}FA_{0.83})_{0.95}Pb(I_{0.83}Br_{0.17})₃. b) The EQE and absorption spectra of a semi-transparent cell with a structure of Glass/ITO/In-TiO_x/meso-TiO₂/Cs-mixed halide perovskite/Spiro-OMeTAD/MoO₃/ITO/Gold-finger contact, where Cs-mixed halide is Cs_{0.05}(MA_{0.17}FA_{0.83})_{0.95}Pb(I_{0.83}Br_{0.17})₃.

Table S1. The Hall Effect parameters of TiO₂ and In-TiO_x devices, with a structure of Glass/TiO₂ (or In-TiO_x)/Au.

ETL	Type	Carrier Density (1/cm ³)	Hall Mobility (cm V ⁻¹ S ⁻¹)	Resistivity (ohm*cm)	Conductivity (S cm ⁻¹)
TiO ₂	N	2.6E+14	2.4E-1	1.0E+5	1.0E-5
1%-In-TiO _x	N	6.0E+14	3.4E-1	3.4E+4	3.0E-5
3%-In-TiO _x	N	1.8E+15	7.4E-1	3.5E+3	2.9E-4
5%-In-TiO _x	N	1.3E+15	1.4E+0	4.0E+3	2.5E-4
7%-In-TiO _x	N	6.2E+14	8.9E-1	1.0E+4	1.0E-4

- [1] B. M. Reddy, B. Chowdhury, P. G. Smirniotis, *Appl. Catal. A: Gen.* **2001**, *219*, 53.
- [2] P. Babelon, A. S. Dequiedt, H. Mostéfa-Sba, S. Bourgeois, P. Sibillot, M. Sacilotti, *Thin Solid Films* **1998**, *322*, 63.
- [3] J. Peng, Q. Sun, Z. Zhai, J. Yuan, X. Huang, Z. Jin, K. Li, S. Wang, H. Wang, W. Ma, *Nanotechnology* **2013**, *24*, 484010.
- [4] Q. Dong, Y. Yuan, Y. Shao, Y. Fang, Q. Wang, J. Huang, *Energy Environ. Sci.* **2015**, *8*, 2464.
- [5] Y. Shao, Z. Xiao, C. Bi, Y. Yuan, J. Huang, *Nature commun.* **2014**, *5*, 5784.
- [6] A. Guerrero, G. Garcia-Belmonte, I. Mora-Sero, J. Bisquert, Y. S. Kang, T. J. Jacobsson, J.P. Correa-Baena, A. Hagfeldt, *J. Phys. Chem. C* **2016**, *120*, 8023.

Electronic Supplementary Information (ESI) for Energy & Environmental Science.
This journal is © The Royal Society of Chemistry 2017

Supporting Information

Interface passivation using ultrathin polymer-fullerene films for high-efficiency perovskite solar cells with negligible hysteresis

Jun Peng,^{*a} Yiliang Wu,^a Wang Ye,^b Daniel A. Jacobs,^a Heping Shen,^a Xiao Fu,^a Yimao Wan,^a The Duong,^a Nandi Wu,^a Chog Barugkin,^a Hieu T. Nguyen,^a Dingyong Zhong,^b Juntao Li,^b Teng Lu,^c Yun Liu,^c Mark N. Lockrey,^d Klaus J. Weber,^a Kylie R. Catchpole,^a Thomas P. White^{*ab}

^aResearch School of Engineering, The Australian National University, Canberra, ACT, 2601, Australia

^bState Key Laboratory of Optoelectronic Materials and Technologies, School of Physics, Sun Yat-sen University, Guangzhou 510275, China

^cResearch School of Chemistry, The Australian National University, Canberra, ACT, 2601, Australia

^dAustralian National Fabrication Facility, Department of Electronic Materials Engineering, Research School of Physics & Engineering, The Australian National University, Canberra, ACT, 2601, Australia

E-mail: u5686151@anu.edu.au; or pengjun.88.81@gmail.com

thomas.white@anu.edu.au

Experimental Section

Precursor solution preparation

In-TiO_x precursor solution. The In-TiO_x precursor solution was prepared as described in our previous work.¹

PMMA and PCBM precursor solution. PMMA precursor solution was prepared by dissolving 1 mg/mL PMMA (Sigma Aldrich, MW~120,000) in Chlorobenzene. PCBM precursor

solution was prepared by dissolving 5 mg/mL PCBM (Sigma Aldrich, 99.0%) in Chlorobenzene.

PMMA:PCBM precursor solution. PMMA:PCBM (1:1) precursor solution was prepared by dissolving 1 mg PMMA, and 1 mg PCBM into 1 mL Chlorobenzene. PMMA:PCBM (1:3) precursor solution was prepared by dissolving 1 mg PMMA, and 3 mg PCBM into 1 mL Chlorobenzene. PMMA:PCBM (1:5) precursor solution was prepared by dissolving 1 mg PMMA, and 5 mg PCBM into 1 mL Chlorobenzene.

Mixed-cation perovskite precursor solution. The $\text{Cs}_{0.07}\text{Rb}_{0.03}\text{FA}_{0.765}\text{MA}_{0.135}\text{PbI}_{2.55}\text{Br}_{0.45}$ perovskite precursor solution contains 1.2 M lead iodide (PbI_2 , 99%, Sigma Aldrich), 1.1 M formamidinium (FAI, Dyesol), 0.2 M lead bromide (PbBr_2 , 99.999%, Sigma Aldrich), 0.2 M methylamine bromide (MABr, Dyesol), 0.091 M cesium iodide (CsI, 99.999%, Sigma Aldrich), and 0.039 M rubidium iodide (RbI, 99.9%, Sigma Aldrich) in 1 mL anhydrous DMF:DMSO (4:1, v/v, Sigma Aldrich).

Spiro-OMeTAD precursor solution. Spiro-OMeTAD precursor solution was prepared by dissolving 72.5 mg Spiro-OMeTAD, 28.5 μL 4-tert-butylpyridine and 17.5 μL of lithium bis(trifluoromethanesulfonyl)imide solution (520mg/mL in acetonitrile) in 1 mL Chlorobenzene. Note that after spin-coating the Spiro-OMeTAD solution, the substrates are placed in air in a humidity-control box for 12 hours to ensure sufficient oxidation of the Spiro-OMeTAD film prior to electrode/contact layer deposition.

Device fabrication and J - V characterization

Device fabrication. ~ 70 nm In-TiO_x compact layers, and ~ 110 nm mesoporous TiO₂ (30 NR-D, Dyesol) were sequentially deposited on the pre-cleaned FTO ($7\Omega/\square$, Dyesol) substrates according to Ref. [1]. For the ultra-thin passivation layer deposition, 30 μL PMMA, PMMA:PCBM, and PCBM precursor solution were dropped on the top of the FTO/*c*-In-TiO_x/*m*-TiO₂ substrates and separately deposited by spin-coating at 5000 rpm/s with a ramp of 5000 rpm s⁻¹ for 30 s, then annealed at 100 °C for 10 min. Then, $\text{Cs}_{0.07}\text{Rb}_{0.03}\text{FA}_{0.765}\text{MA}_{0.135}\text{PbI}_{2.55}\text{Br}_{0.45}$ thin film was deposited by a two-step spin coating program: first at 2000 rpm with a ramp of 200 rpm s⁻¹ for 10 s, and then at 4000 rpm with a ramp of 1000 rpm s⁻¹ for 20 s. During the second step, around 100 μl Chlorobenzene was poured on the spinning substrates 5 s prior to the end of the program. Substrates were then

annealed at 100 °C for 45 min. Then, Spiro-OMeTAD thin film was deposited via spin coating at 3000 rpm with a ramp of 3000 rpm s⁻¹ for 30 s. Finally, ~100 nm gold was deposited through a shadow mask (cell's effective area, 0.16 cm²). Note that all depositions were conducted in a nitrogen-filled glovebox.

J-V measurement. All devices were tested under 1 sun conditions (100 mW/cm², AM 1.5G, 25 °C) in a solar simulator system (model #SS150 from Photo Emission Tech Inc) equipped with a Xenon lamp. The light intensity was calibrated using a certified Fraunhofer Callab reference cell. For the perovskite solar cells, all cells' *J-V* curves were tested at a 50 mV/s scan rate in a custom-built vacuum measurement jig without aperture mask. Note that reverse scan is from V_{oc} to J_{sc} (forward bias → short circuit, 1.2 V → -0.1V), and forward scan is from J_{sc} to V_{oc} (short circuit → forward bias, -0.1 V → 1.2 V). No preconditioning protocol has been used before the characterization.

EQE measurement. The EQE spectra of our perovskite cells were measured with a modified Protoflex QE1400 system without light bias in DC mode using a tungsten light source, two Keithley 2425 sourcemeters, and a reference cell. The EQE response was calibrated using a certified Fraunhofer Callab reference cell.

Characterization

XPS and UPS. X-ray photoelectron spectroscopy (XPS) and ultraviolet photoelectron spectroscopy (UPS) measurements were carried out on an XPS machine (Escalab 250 Xi, Thermo Fisher), with a monochromatic Al K_α (1486.7 eV) X-ray source for XPS and a He I (21.2 eV) gas discharge lamp for UPS.

SEM. A FEI Verios scanning electron microscope (SEM) was used to investigate the surface morphology of samples. A Helios Nanolab 600 FIB system was used to prepare cross-sectional SEM images of the cells. Energy dispersive X-ray (EDX) (beam conditions: 10 kV, 1.6 nA) and Backscattered electron (BSE) imaging (beam condition: 5 kV, 50 pA) were performed to analyze perovskite materials. Note that ~2 μm Pt used as a protection layer was deposited on sample before preparing the cross-sectional SEM image.

Transmittance. A PerkinElmer Lambda 1050 UV/Vis/NIR spectrophotometer was used to measure the transmittance of the samples.

XRD. X-ray diffraction analysis was performed with a Bruker D2 Phaser diffractometer operated at 30 kV, 10 mA at 2θ (Cu $K\alpha$) $10\text{--}80^\circ$, step 0.02° and scan speed $2.3^\circ \text{ min}^{-1}$.

C-AFM. Conductive atomic force microscopy (C-AFM) measurements were performed on ITO/PMMA and ITO/PMMA:PCBM using Asylum Research Cypher system, where ITO substrates were used as bottom electrodes. Pt/Ir coated conductive tips with spring constant of $\sim 2 \text{ N/m}$ and resonant frequencies of $\sim 70 \text{ kHz}$ (Asylum research AC240TM) were used for both morphology measurement and C-AFM measurement. Voltages (5 V) were applied between the ITO substrate and the conductive probe tip, and the current was traced by internal preamplifier (Asylum ORCA module, 1 nA/V). As some samples were highly conductive, a $500 \text{ M}\Omega$ resistance was added to keep the ORCA amplifier from saturating. Note that the ITO/PMMA sample was prepared by spin-coating 2 mg/mL PMMA in CB on pre-cleaned ITO substrate at 2000 rpm/s for 30 s; and the ITO/PMMA:PCBM sample was prepared by spin-coating 4 mg/mL PMMA:PCBM (1:3, w/w) in CB on the pre-cleaned ITO substrate at 2000 rpm/s for 30 s.

Profile AFM. Profile atomic force microscopy (AFM) measurement was performed on Si/c-In-TiO_x/PMMA:PCBM sample to estimate the thickness of ultrathin PMMA:PCBM film. In order to reduce the uncertainty, the thin PMMA:PCBM film for profile-AFM measurement was deposited by spin-coating 4 mg/mL PMMA:PCBM (1:3, w/w) in CB at 2000 rpm with a ramp of 2000 rpm/s for 30 s on the top of Si/c-In-TiO_x substrate. PMMA and PCBM are organic materials and the blend films are very soft. We therefore used a very sharp blade to create a profile on the top of the Si/c-In-TiO_x/PMMA:PCBM sample by softly and gently cutting the surface. Note that we chose polished silicon wafer as substrate, the compact In-TiO_x layer was deposited from exactly the same deposition procedures as described in device fabrication.

PL imaging. For photoluminescence (PL) imaging, the cells were held in a nitrogen-filled and temperature controlled jig. The jig is mounted in a home-built PL imaging system and uniformly illuminated with two 430 nm royal-blue LED chips, filtered by bandpass filters (451/106 nm). Following illumination (Intensity $\sim 100 \text{ mW/cm}^2$), a Peltier-cooled (-70°C) Si CCD camera (Princeton Instruments Pixis 1024) with a long-pass filter (750 nm) took the image of the luminescence from the perovskite cells with the exposure time of 0.2 second. PL images were taken when cells were under both open circuit and reverse bias (-2 V) conditions. The open circuit images were then subtracted from the reverse bias image to ensure the

luminescence emission was solely from the perovskite absorbers as described in our previous work.²

TRPL. Time-resolved photoluminescence (TRPL) decay measurements were performed using a LabRAM HR Evolution system with a time-correlated single photon counting (TCSPC) system (DeltaPro-DD, Horiba). A 508nm diode laser (DD-510L, Horiba) with pulse duration of 110ps, fluence of $\sim 10 \mu\text{J}/\text{cm}^2/\text{pulse}$, and a repetition rate of 312.5 kHz was used for excitation. The PL signal was extracted at 770 nm. Both the incident light and the reflected light went through a 50x objective lens (LEICA PL FLUOTAR L 50/0.55), which resulted in a spot size of $\sim 2 \mu\text{m}$. The samples were kept in N_2 environment during the measurements. For the analysis of the time-resolved PL decay, a bi-exponential model in the Decay Analysis software was used to fit the experimental result and extract the lifetime.

SCLC. Space charge limited current (SCLC) measurements were performed on electron-dominated devices with a structure of FTO/c-In-TiO_x/m-TiO₂/(with or without PMMA:PCBM passivation layer)/Mixed-cation Perovskite/PCBM ($\sim 50 \text{ nm}$)/Ag ($\sim 100 \text{ nm}$), where the device without PMMA:PCBM layer is the control device (non-passivated cell), and the device with PMMA:PCBM layer is the passivated device. Note that the electron-dominated devices were prepared by the same procedures as described in the aforementioned device fabrication. Then, $\sim 50 \text{ nm}$ PCBM was deposited by spin-coating 20 mg/mL PCBM in CB at 1000 rpm/s for 40 s; and then, $\sim 100 \text{ nm}$ Ag was deposited by thermal evaporation at a deposition rate of 1 $\text{\AA}/\text{s}$. All SCLC tests were carried out at room temperature and under dark.

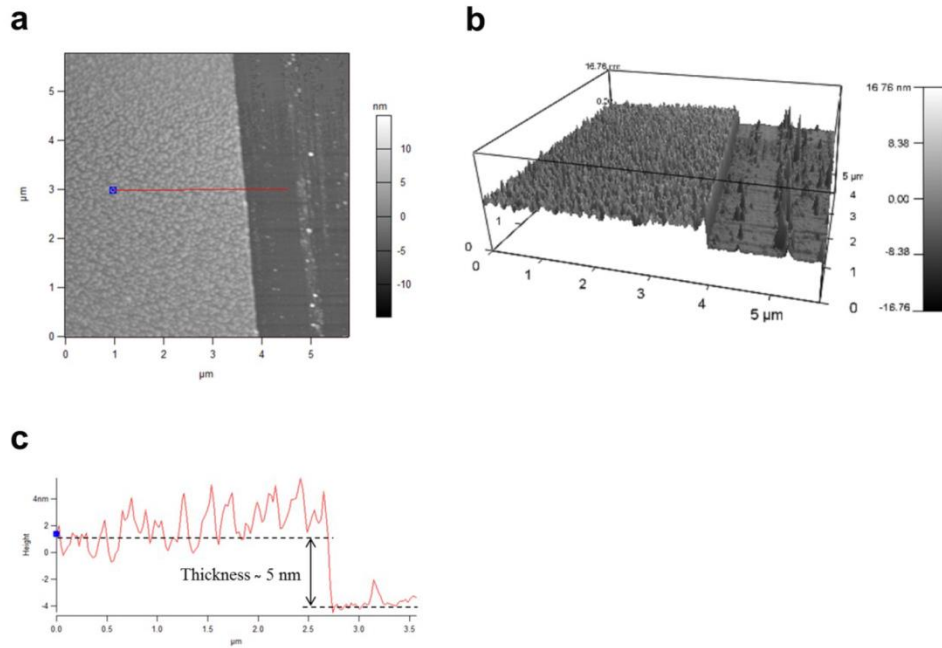


Fig. S1 a) 2-D AFM image of $5\ \mu\text{m} \times 5\ \mu\text{m}$ region of Si/*c*-In-TiO_x/PMMA:PCBM. b) 3-D AFM image of $5\ \mu\text{m} \times 5\ \mu\text{m}$ region of Si/*c*-In-TiO_x/PMMA:PCBM. c) The corresponding line profiling analysis of PMMA:PCBM-coated on Si/*c*-In-TiO_x substrate. Note that the PMMA:PCBM layer for profile-AFM measurement was deposited by spin-coating 4 mg/mL PMMA:PCBM (1:3, w/w) in CB at 2000 rpm with a ramp of 2000 rpm/s for 30 s on the top of Si/*c*-In-TiO_x substrate.

Fig. S1 shows the thickness of PMMA:PCBM film on the Si/*c*-In-TiO_x/PMMA:PCBM sample is around 5 nm. As the thin PMMA:PCBM film used as a passivation layer in our passivated perovskite cell was deposited by spin-coating 4 mg/mL PMMA:PCBM (1:3, w/w) in CB at 5000 rpm with a ramp of 5000 rpm/s for 30 s, the estimated thickness of PMMA:PCBM passivation layer in our passivated cell was less than 5 nm.

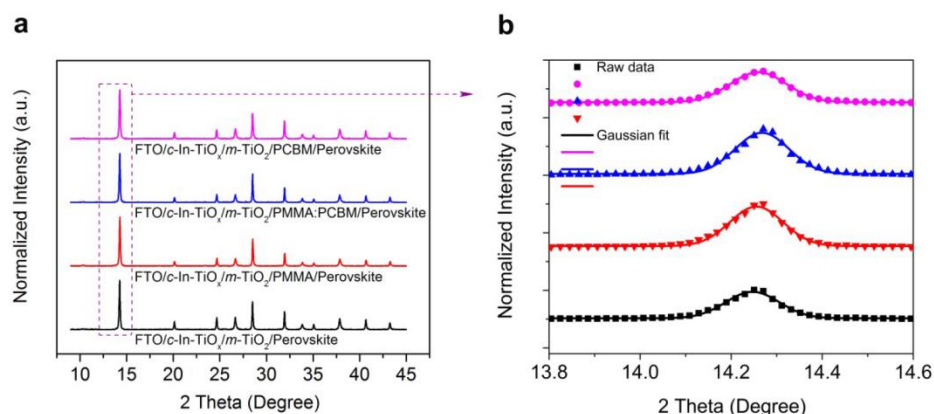


Fig. S2 a) XRD spectra of the perovskite thin films deposited on different FTO/*c*-In-TiO_x/*m*-TiO₂ substrates with/without the PMMA, PMMA:PCBM or PCBM passivation layer. b) The corresponding Gaussian fit of the dominant black perovskite phase for perovskite thin film. Note that the perovskite composition is Cs_{0.07}Rb_{0.03}FA_{0.765}MA_{0.135}PbI_{2.55}Br_{0.45}.

In Fig. S2a, the XRD spectra show no systematic variations with substrates, and no obvious PbI₂ or other non-perovskite phases. To further investigate the crystallite size of perovskite, the dominant black perovskite phase is fitted with a Gaussian distribution to determine the full width at half maximum (FWHM) for each sample. As shown in the Fig. S2b, it reveals that the value of FWHM for FTO/*c*-In-TiO_x/*m*-TiO₂/perovskite sample is 0.13915, while the values of FWHM for the perovskite thin films deposited on different FTO/*c*-In-TiO_x/*m*-TiO₂ substrates with an ultrathin PMMA, PMMA:PCBM or PCBM passivation layer are 0.13788, 0.13931 or 0.1466, respectively. The calculated FWHM shows that there are no significant variations for the crystallite size of perovskite with different substrates.

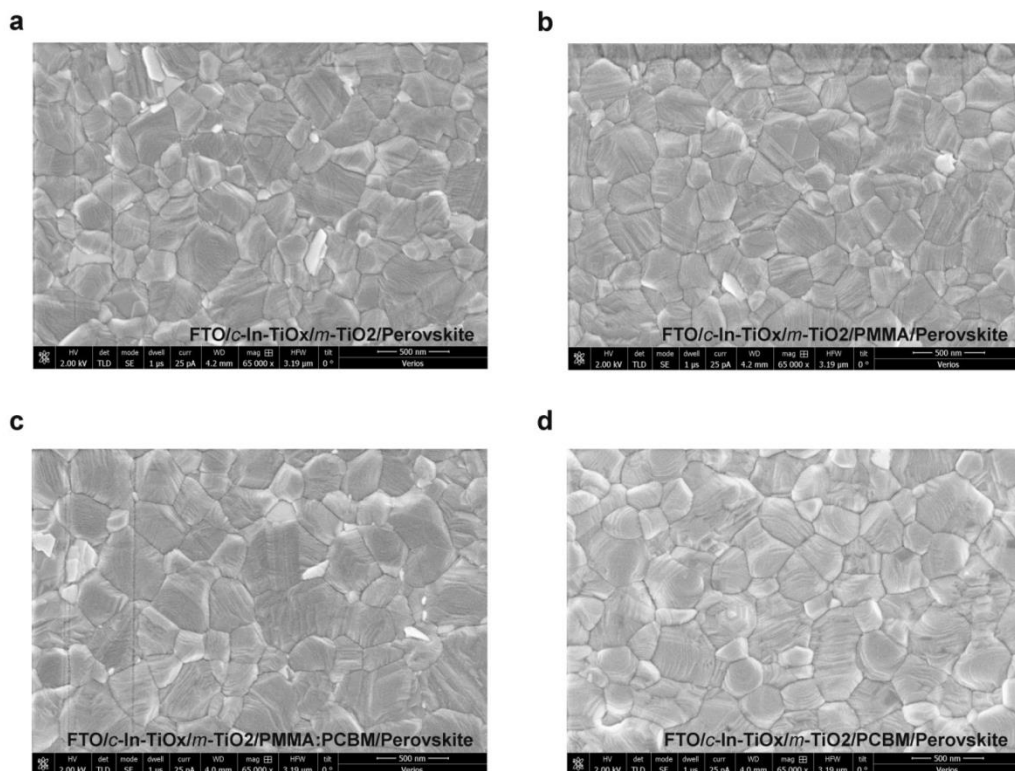


Fig. S3 SEM images of perovskite films deposited on different substrates: a) FTO/*c*-In-TiO_x/*m*-TiO₂. b) FTO/*c*-In-TiO_x/*m*-TiO₂/PMMA. c) FTO/*c*-In-TiO_x/*m*-TiO₂/PMMA:PCBM. d) FTO/*c*-In-TiO_x/*m*-TiO₂/PCBM. Note that the perovskite composition is Cs_{0.07}Rb_{0.03}FA_{0.765}MA_{0.135}PbI_{2.55}Br_{0.45}; the ratio of PMMA:PCBM is 1:3 (w/w).

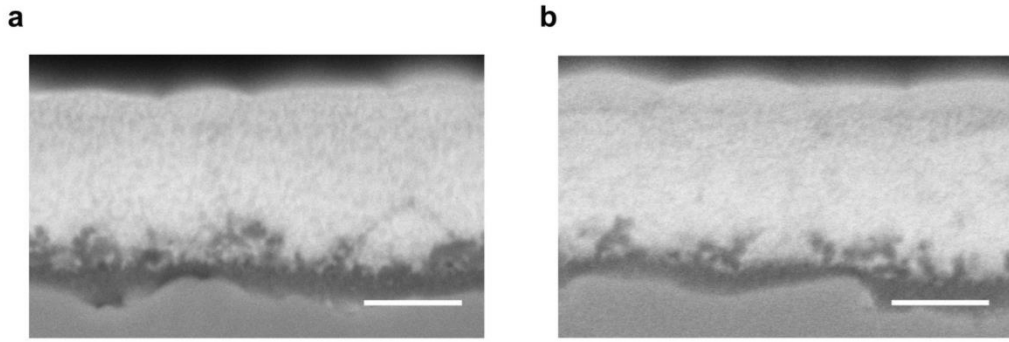


Fig. S4 SEM backscattered electron (BSE) imaging measurements. a) FTO/*c*-In-TiO_x/*m*-TiO₂/Perovskite/Spiro-OMeTAD/Au. b) FTO/*c*-In-TiO_x/*m*-TiO₂/ PMMA:PCBM/Perovskite /Spiro-OMeTAD/Au. Note that the perovskite composition is Cs_{0.07}Rb_{0.03}FA_{0.765}MA_{0.135}PbI_{2.55}Br_{0.45}.

Backscattered electron (BSE) imaging has been used to investigate the penetration of the perovskite into the mesoporous TiO₂ region for cross-sections of both non-passivated and passivated cells (with a PMMA:PCBM passivation layer). The contrast in BSE images is proportional to the average atomic number. This allows for discrimination between areas of different material composition. From the BSE image we can clearly see the difference between the perovskite (bright), *m*-TiO₂ and compact In-TiO_x (dark), and SnO₂ (medium) (see Fig. S4). From Fig. S4 we can see that the mesoporous TiO₂ extends into the perovskite layer and the perovskite fully penetrates into this layer leaving no voids.

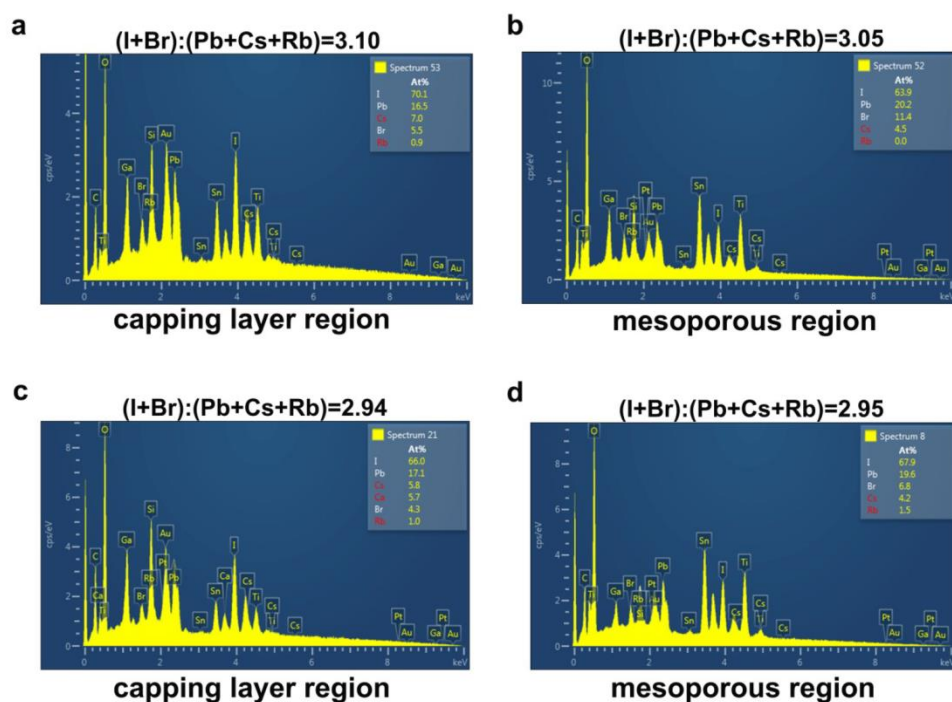


Fig. S5 SEM energy dispersive X-ray detector (EDX) measurements. a) EDX measurement on the perovskite capping layer region and b) EDX measurement on the mesoporous TiO₂ region for FTO/c-In-TiO_x/m-TiO₂/ Perovskite/Spiro-OMeTAD/Au (non-passivated cell); c) EDX measurement on the perovskite capping layer region and d) EDX measurement on the mesoporous TiO₂ region for FTO/c-In-TiO_x/m-TiO₂/PMMA:PCBM/Perovskite/Spiro-OMeTAD/Au (passivated cell). Note that the perovskite composition is Cs_{0.07}Rb_{0.03}FA_{0.765}MA_{0.135}PbI_{2.55}Br_{0.45}.

In addition, SEM energy dispersive X-ray (EDX) analysis was performed on the mesoporous TiO₂ and perovskite capping layer areas for cross-sections of both non-passivated and passivated cells using an electron beam voltage of 10 kV. From the ratio of (I+Br) to (Pb+Cs+Rb), it can be seen that the composition between the mesoporous TiO₂ region-perovskite capping layer region and across the samples remains close to 3:1 (see Fig. S5).

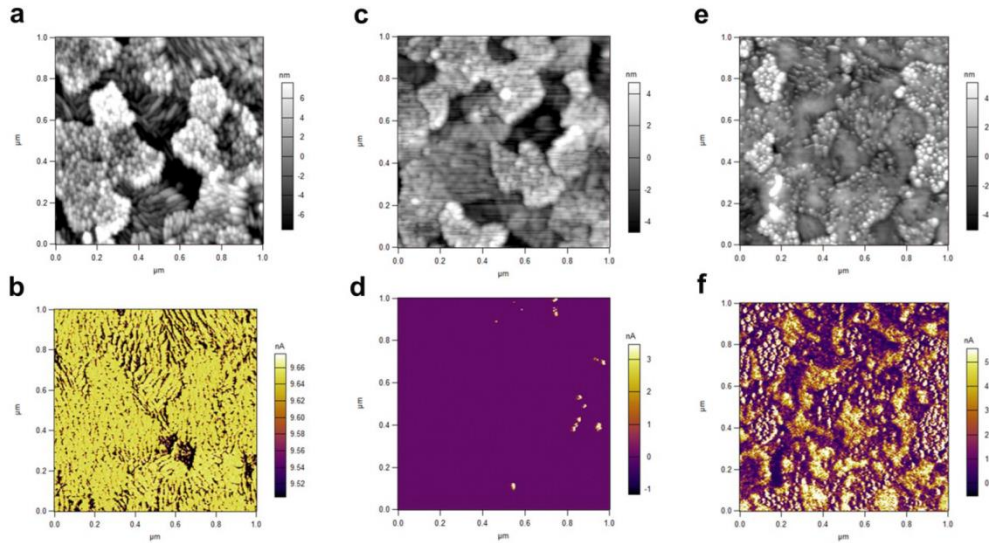


Fig. S6 2-D atomic force microscopy (AFM) images, image scale: $1 \mu\text{m} \times 1 \mu\text{m}$. a) Surface morphology of Glass/ITO. b) Current mapping of Glass/ITO. c) Surface morphology of Glass/ITO/PMMA. d) Current mapping of Glass/ITO/PMMA. e) Surface morphology of Glass/ITO/PMMA:PCBM. f) Current mapping of Glass/ITO/PMMA:PCBM.

Fig. S6a shows the surface morphology for ITO, where the bright and dark contrast suggests the protrusions and depressions and the maximum height difference is around 15 nm. It reveals that the surface of bare ITO substrate is relatively smooth with root mean square roughness of ~ 3.8 nm. Fig. S6b is the current mapping of the same area for the bare ITO substrate. It is evident that the whole region presents relatively homogeneous current around 9.6 nA, consistent with conductivity of ITO. (Note that in order to avoid current saturation, a 500 M Ω resistor was connected in series, and therefore the 5 V bias on the sample will induce a maximum current of around 10 nA). When a PMMA thin film is present on the ITO substrate, it is obvious that the height contrast decreases in comparison with that observed for the bare ITO substrate (see Fig. S6c). The distribution of the current is quite homogeneous and negligible (with most areas ~ 30 pA), indicating the insulating behavior of the PMMA (see Fig. S6d). Although most of the area for Glass/ITO/PMMA sample behaves as insulating, some points exhibit strong currents which possibly results from pinholes in the film. For the PMMA:PCBM composite thin film on an ITO substrate, the surface is more smooth compared to the bare ITO substrate (see Fig. S6e). The current distribution is inhomogeneous, which is different from the conductive ITO and insulating PMMA (see Fig. S6f). The results demonstrate the conductive characteristics of PMMA:PCBM, with some regions with yellow

color (~ 4 nA) presenting good conductive properties, while others with violet color (≤ 1 nA) show higher resistance. This clearly confirms the role of PCBM as an additive increasing the conductivity of PMMA:PCBM blend films.

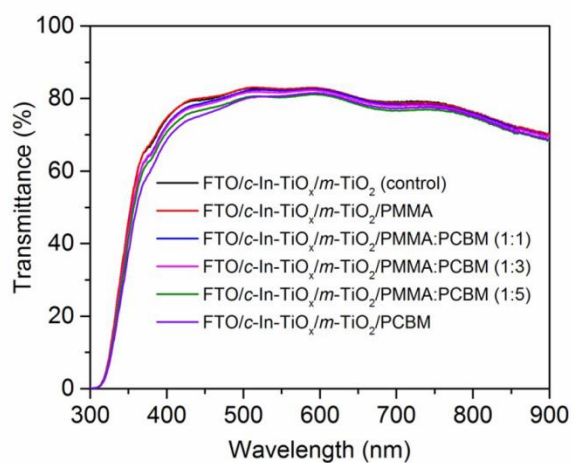


Fig. S7 Transmittance spectra of the FTO/c-In-TiO_x/m-TiO₂ substrates with/without the PMMA, PMMA:PCBM, or PCBM passivation layer.

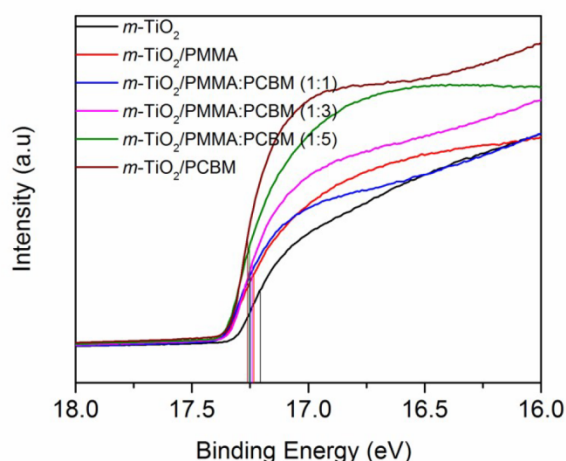


Fig. S8 UPS spectra of FTO/*c*-In-TiO_x/*m*-TiO₂ (labeled as *m*-TiO₂), FTO/*c*-In-TiO_x/*m*-TiO₂/PMMA (labeled as *m*-TiO₂/PMMA), FTO/*c*-In-TiO_x/*m*-TiO₂/PMMA:PCBM (labeled as *m*-TiO₂/PMMA:PCBM) and FTO/*c*-In-TiO_x/*m*-TiO₂/PCBM (labeled as *m*-TiO₂/PCBM). Note that the PMMA:PCBM (1:1) represents the ratio of PMMA:PCBM is 1:1 (w/w); the PMMA:PCBM (1:3) represents the ratio of PMMA:PCBM is 1:3 (w/w); the PMMA:PCBM (1:5) represents the ratio of PMMA:PCBM is 1:5 (w/w).

As shown in Fig. S8, the photoemission cutoff is determined by the UPS measurement,³ the obtained work function (WF) of FTO/*c*-In-TiO_x/*m*-TiO₂ is ~ 4.0 eV. The WF of FTO/*c*-In-TiO_x/*m*-TiO₂/PMMA is ~3.97 eV, which is slightly lower than that of the FTO/*c*-In-TiO_x/*m*-TiO₂. In addition, the WF of FTO/*c*-In-TiO_x/*m*-TiO₂/PMMA:PCBM (1:1) and FTO/*c*-In-TiO_x/*m*-TiO₂/PMMA:PCBM (1:3) are ~3.95 eV and ~3.96 eV, respectively. Similarly, the WF of FTO/*c*-In-TiO_x/*m*-TiO₂/PMMA:PCBM (1:5) is ~3.95 eV. Note that the WF values of these samples with different ratios of the PMMA:PCBM passivation layers show no significant difference. To reveal the effect of the PCBM material, the sample with pure PCBM passivation layer was also investigated and shows that the WF of FTO/*c*-In-TiO_x/*m*-TiO₂/PCBM is ~3.94 eV.

Based on the aforementioned UPS analysis, we found that the WF of FTO/*c*-In-TiO_x/*m*-TiO₂/PMMA (~3.97 eV) shows 30 meV difference as compared to FTO/*c*-In-TiO_x/*m*-TiO₂ (~4.0 eV); the WF of FTO/*c*-In-TiO_x/*m*-TiO₂/PMMA:PCBM with different ratios of PMMA:PCBM show 40 meV - 50 meV variations as compared to FTO/*c*-In-TiO_x/*m*-TiO₂; moreover, the WF of FTO/*c*-In-TiO_x/*m*-TiO₂/PCBM (~3.94 eV) shows 60 meV difference as compared to FTO/*c*-In-TiO_x/*m*-TiO₂ (~4.0 eV).

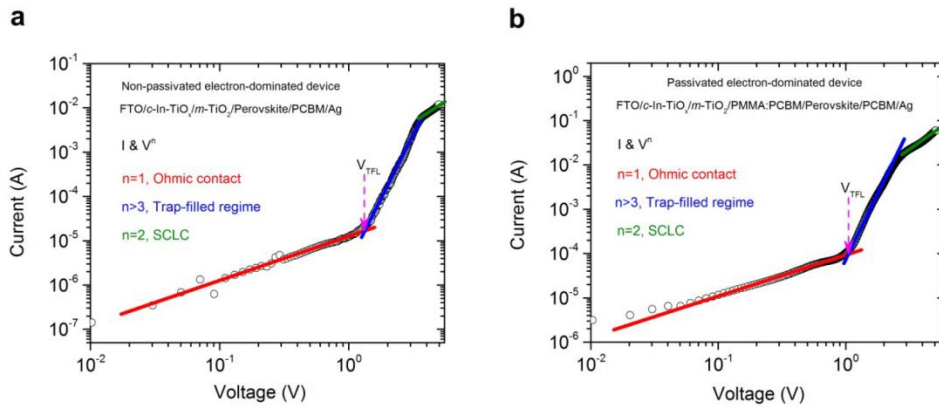


Fig. S9 Space charge limited current (SCLC) measurements. a) Non-passivated electron-dominated device with a structure of FTO/c-In-TiO_x/m-TiO₂/Perovskite/PCBM/Ag. b) Passivated electron-dominated device with a structure of FTO/c-In-TiO_x/m-TiO₂/PMMA:PCBM/Perovskite/PCBM/Ag. Note that the perovskite composition is Cs_{0.07}Rb_{0.03}FA_{0.765}MA_{0.135}PbI_{2.55}Br_{0.45}.

To further investigate the density of defects or trap states within our passivated and non-passivated perovskite cells, space charge limited current (SCLC) measurements were performed on both non-passivated and passivated electron-dominated devices, where the device structure is: FTO/c-In-TiO_x/m-TiO₂/(w/wo PMMA:PCBM)/Perovskite/PCBM/Ag. As shown in the Fig. S9, three regions (ohmic contact regime, trap-filled regime and SCLC regime) were evident in the logarithmic plot of the I - V characteristics of the non-passivated and passivated electron-dominated devices.^{4,5} In the SCLC model, the density of defects or trap states can be simply and roughly estimated by the onset voltage V_{TFL} (trap-filled limit (TFL) a regime in which all available defects or trap states were filled by the injected carriers) based on the equation of $V_{TFL} = (e \cdot n_t \cdot d^2) / (2 \cdot \epsilon \cdot \epsilon_0)$, where e , n_t , d , ϵ and ϵ_0 are electronic charge, trap density, the thickness of device, the dielectric constant of perovskite material and the permittivity of free space, respectively.⁵ For the passivated electron-dominated device, the V_{TFL} was of 1.06 V, while the V_{TFL} for the non-passivated device was 1.32 V shown in the Fig. S9. Based on the V_{TFL} equation, we found that the trap density for our passivated device was lower than that of the non-passivated device. Hence, the evidence from space charge limited current (SCLC) measurements for our passivated and non-passivated cells may further support our findings obtained from the steady-state PL and transient PL measurements.

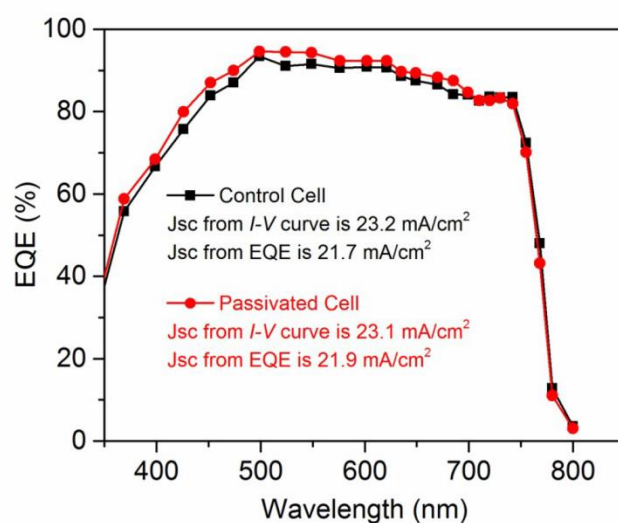


Fig. S10 EQE spectra of the control cell and passivated cell.

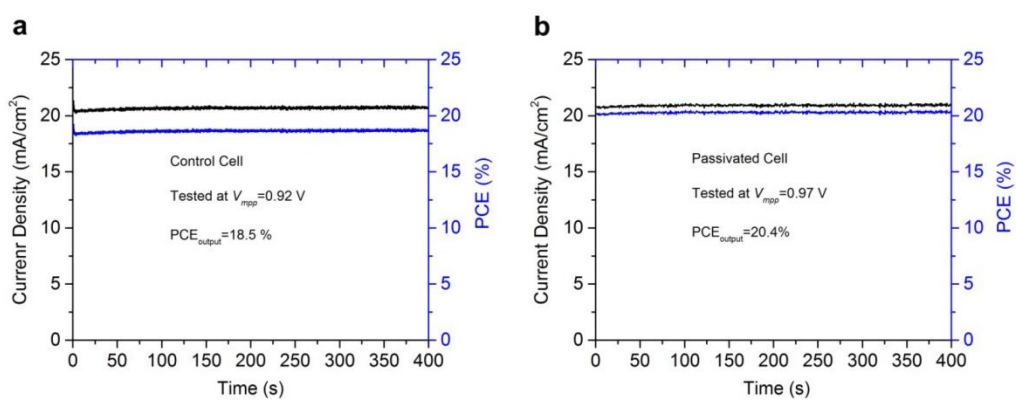


Fig. S11 a) Steady-state PCE of the control cell with a structure of FTO/*c*-In-TiO_x/*m*-TiO₂/Perovskite/Spiro/Au tested at the V_{mpp} of 0.92 V. b) The steady-state PCE of the passivated cell with a structure of FTO/*c*-In-TiO_x/*m*-TiO₂/PMMA:PCBM (1:3)/Perovskite/Spiro/Au tested at the V_{mpp} of 0.97 V.

Table S1 Photovoltaic parameters of the control cell with a structure of FTO/*c*-In-TiO_x/*m*-TiO₂/Perovskite/Spiro/Au.

Scan rates [mV/s]	Scan direction	V_{oc} [V]	J_{sc} [mA/cm ²]	FF [%]	PCE [%]	$\Delta_{(PCE)}=RS_{(PCE)}-FS_{(PCE)}$ [%]
500	RS	1.10	23.12	78.5	19.96	2.15
	FS	1.075	23.01	72.0	17.81	
200	RS	1.09	23.12	77.9	19.62	1.96
	FS	1.07	23.12	71.4	17.66	
50	RS	1.09	23.20	77.5	19.60	0.90
	FS	1.10	23.30	72.8	18.70	
1	RS	1.10	23.15	73.6	18.74	1.00
	FS	1.10	23.20	69.5	17.74	

Note that the perovskite stands for Cs_{0.07}Rb_{0.03}FA_{0.765}MA_{0.135}PbI_{2.55}Br_{0.45}; the legend of RS represents reverse scan (from V_{oc} to J_{sc}), FS represents forward scan (from J_{sc} to V_{oc}).

Table S2 Photovoltaic parameters of the passivated cell with a structure of FTO/*c*-In-TiO_x/*m*-TiO₂/PMMA:PCBM (1:3)/Perovskite/Spiro/Au.

Scan rates [mV/s]	Scan direction	V_{oc} [V]	J_{sc} [mA/cm ²]	FF [%]	PCE [%]	$\Delta_{(PCE)}=RS_{(PCE)}-FS_{(PCE)}$ [%]
500	RS	1.155	23.10	76.8	20.49	0.52
	FS	1.145	23.22	75.1	19.97	
200	RS	1.165	23.09	76.0	20.43	0.32
	FS	1.155	23.15	75.2	20.11	
50	RS	1.160	23.10	76.2	20.40	0
	FS	1.160	23.20	76.0	20.40	
1	RS	1.155	23.05	74.9	19.94	0.36
	FS	1.155	23.15	73.2	19.58	

RS represents reverse scan (from V_{oc} to J_{sc}), FS represents forward scan (from J_{sc} to V_{oc}).

Table S3 Summary of photovoltaic parameters for the n-i-p perovskite solar cells reported with over 20% efficiency.

ETLs	Scan rates [mV/s]	Scan direction	V_{oc} [V]	J_{sc} [mA/cm ²]	FF [%]	PCE [%]	$\Delta_{(PCE)}=RS_{(PCE)}-FS_{(PCE)}$ [%]	Reference
<i>m</i> -TiO ₂ /PMMA:PCBM	50	RS	1.16	23.10	76.2	20.4	0	This work
		FS	1.16	23.20	76.0	20.4		
<i>m</i> -TiO ₂	6	RS	1.117	23.72	77.9	20.6	0.4	6
		FS	1.11	23.67	76.8	20.2		
<i>m</i> -TiO ₂	250	RS	1.06	24.70	77.5	20.2	0	7
		FS	1.06	24.70	77.5	20.2		
Cl-capped TiO ₂	50	RS	1.189	22.30	80.6	21.4	0	8
		FS	1.189	22.30	80.6	21.4		
La-doped BaSnO ₃	250	RS	1.12	23.40	81.3	21.3	n/a	9
		FS	n/a	n/a	n/a	n/a		
Li-doped <i>m</i> -TiO ₂	10	RS	1.18	22.80	81.0	21.8	0.5	10
		FS	1.173	22.80	80.0	21.3		
<i>m</i> -TiO ₂	50	RS	1.141	23.19	75.7	20.38	0.23	11
		FS	1.145	23.28	76.0	20.61		
SnO ₂	n/a	RS	1.09	24.87	74.7	20.27	0.27	12
		FS	1.09	24.88	75.7	20.54		
<i>m</i> -TiO ₂	10	RS	1.167	23.20	73.6	20.0	0.2	13
		FS	1.17	23.3	72.7	19.8		
SnO ₂	10	RS	1.18	22.37	77.0	20.46	n/a	14
		FS	n/a	n/a	n/a	n/a		
<i>m</i> -TiO ₂ /Au@SiO ₂	n/a	RS	1.16	23.8	0.74	20.6	0.3	15
		FS	1.16	23.8	0.73	20.3		
<i>m</i> -TiO ₂	10	RS	1.16	24.6	73.0	20.8	0	16
		FS	1.16	24.6	73.00	20.8		
<i>m</i> -TiO ₂	23.7	RS	1.09	23.43	79.97	20.44	1.93	17
		FS	1.09	23.06	73.78	18.51		
C ₆₀ :PhIm/C ₆₀	n/a	RS	1.141	22.08	80.5	20.3	n/a	18
		FS	n/a	n/a	n/a	n/a		
<i>m</i> -TiO ₂	10	RS	1.13	23.7	77.0	21.3	0.3	19
		FS	1.14	23.7	0.78	21.6		
Li-doped <i>m</i> -TiO ₂	10	RS	1.147	23.5	78.5	21.17	0.85	20
		FS	1.158	23.5	74.6	20.32		

--- continue ---

In-doped TiO _x	50	RS	1.10	23.1	79.1	20.1	1.4	1
		FS	1.09	23.2	74.0	18.7		
TiO ₂ :TOPD/PCBM	n/a	RS	1.1	23.2	80.0	20.3	0.5	21
		FS	1.09	23.2	79.0	19.8		

References

- J. Peng, T. Duong, X. Z. Zhou, H. P. Shen, Y. L. Wu, H. K. Mulmudi, Y. M. Wan, D. Y. Zhong, J. T. Li, T. Tsuzuki, K. J. Weber, K. R. Catchpole and T. P. White, *Adv. Energy Mater.*, 2017, **7**, 1601768.
- Y. Wu, H. Shen, D. Walter, D. Jacobs, T. Duong, J. Peng, L. Jiang, Y.-B. Cheng and K. Weber, *Adv. Funct. Mater.*, 2016, **26**, 6807-6813.
- H. Zhou, Q. Chen, G. Li, S. Luo, T.-b. Song, H.-S. Duan, Z. Hong, J. You, Y. Liu and Y. Yang, *Science*, 2014, **345**, 542-546.
- D. Luo, L. Zhao, J. Wu, Q. Hu, Y. Zhang, Z. Xu, Y. Liu, T. Liu, K. Chen, W. Yang, W. Zhang, R. Zhu and Q. Gong, *Adv. Mater.*, 2017, **29**, 1604758.
- D. Shi, V. Adinolfi, R. Comin, M. Yuan, E. Alarousu, A. Buin, Y. Chen, S. Hoogland, A. Rothenberger and K. Katsiev, *Science*, 2015, **347**, 519-522.
- D.-Y. Son, J.-W. Lee, Y. J. Choi, I.-H. Jang, S. Lee, P. J. Yoo, H. Shin, N. Ahn, M. Choi and D. Kim, *Nature Energy*, 2016, **1**, 16081.
- W. S. Yang, J. H. Noh, N. J. Jeon, Y. C. Kim, S. Ryu, J. Seo and S. I. Seok, *Science*, 2015, **348**, 1234-1237.
- H. Tan, A. Jain, O. Voznyy, X. Lan, F. P. G. de Arquer, J. Z. Fan, R. Quintero-Bermudez, M. Yuan, B. Zhang and Y. Zhao, *Science*, 2017, **355**, 722-726.
- S. S. Shin, E. J. Yeom, W. S. Yang, S. Hur, M. G. Kim, J. Im, J. Seo, J. H. Noh and S. I. Seok, *Science*, 2017, **356**, 167-171.
- M. Saliba, T. Matsui, K. Domanski, J.-Y. Seo, A. Ummadisingu, S. M. Zakeeruddin, J.-P. Correa-Baena, W. R. Tress, A. Abate and A. Hagfeldt, *Science*, 2016, **354**, 206-209.
- X. Li, D. Bi, C. Yi, J. D. Decoppet, J. Luo, S. M. Zakeeruddin, A. Hagfeldt and M. Grätzel, *Science*, 2016, **353**, 58-62.
- Q. Jiang, L. Zhang, H. Wang, X. Yang, J. Meng, H. Liu, Z. Yin, J. Wu, X. Zhang and J. You, *Nature Energy*, 2016, **2**, 16177.
- M. Zhang, J. S. Yun, Q. Ma, J. Zheng, C. F. J. Lau, X. Deng, J. Kim, D. Kim, J. Seidel, M. A. Green, S. Huang and A. W. Y. Ho-Baillie, *ACS Energy Lett.*, 2017, **2**, 438-444.
- E. H. Anaraki, A. Kermanpur, L. Steier, K. Domanski, T. Matsui, W. Tress, M. Saliba, A. Abate, M. Grätzel and A. Hagfeldt, J. P. Correa-Baena, *Energy Environ. Sci.*, 2016, **9**, 3128-3134.
- T. Ye, S. Ma, X. Jiang, L. Wei, C. Vijila and S. Ramakrishna, *Adv. Funct. Mater.*, 2017, 1606545, DOI: 10.1002/adfm.201606545.
- D. Bi, W. Tress, M. I. Dar, P. Gao, J. Luo, C. Renevier, K. Schenk, A. Abate, F. Giordano, J. P. Correa Baena, J. D. Decoppet, S. M. Zakeeruddin, M. K. Nazeeruddin, M. Grätzel and A. Hagfeldt, *Sci. Adv.*, 2016, **2**, e1501170.
- B. Ding, Y. Li, S.-Y. Huang, Q.-Q. Chu, C.-X. Li, C.-J. Li and G.-J. Yang, *J. Mater. Chem. A*, 2017, **5**, 6840-6848.
- C. Momblona, L. Gil-Escrig, E. Bandiello, E. M. Hutter, M. Sessolo, K. Lederer, J. Blochwitz-Nimoth and H. J. Bolink, *Energy Environ. Sci.*, 2016, **9**, 3456-3463.
- D. Bi, C. Yi, J. Luo, J.-D. Decoppet, F. Zhang, S. M. Zakeeruddin, X. Li, A. Hagfeldt and M. Grätzel, *Nature Energy*, 2016, **1**, 16142.
- M. Saliba, T. Matsui, J.-Y. Seo, K. Domanski, J.-P. Correa-Baena, M. K. Nazeeruddin, S. M. Zakeeruddin, W. Tress, A. Abate, A. Hagfeldt and M. Grätzel, *Energy Environ. Sci.*, 2016, **9**, 1989-1997.
- F. Cai, L. Yang, Y. Yan, J. Zhang, F. Qin, D. Liu, Y.-b. Cheng, Y. Zhou and T. Wang, *J. Mater. Chem. A*, 2017, DOI:10.1039/C7TA02317K.

ADVANCED ENERGY MATERIALS

Supporting Information

for *Adv. Energy Mater.*, DOI: 10.1002/aenm.201801208

A Universal Double-Side Passivation for High Open-Circuit Voltage in Perovskite Solar Cells: Role of Carbonyl Groups in Poly(methyl methacrylate)

Jun Peng, Jafar I. Khan, Wenzhu Liu, Esma Ugur, The Duong, Yiliang Wu, Heping Shen, Kai Wang, Hoang Dang, Erkan Aydin, Xinbo Yang, Yimao Wan, Klaus J. Weber, Kylie R. Catchpole, Frédéric Laquai, StefaanDe Wolf, and Thomas P. White**

Supporting Information

A Universal Double-Side Passivation for High Open-Circuit Voltage in Perovskite Solar Cells: Role of Carbonyl Groups in Poly(methyl methacrylate)

Jun Peng, Jafar I. Khan, Wenzhu Liu, Esma Ugur, The Duong, Yiliang Wu, Heping Shen, Kai Wang, Hoang Dang, Erkan Aydin, Xinbo Yang, Yimao Wan, Klaus J. Weber, Kylie R. Catchpole, Frédéric Laquai, Stefaan De Wolf, Thomas P. White**

Jun Peng, Dr. The Duong, Yiliang Wu, Dr. Heping Shen, Dr. Yimao Wan, A/Prof. Klaus J. Weber, Prof. Kylie R. Catchpole and A/Prof. Thomas P. White
Research School of Engineering, The Australian National University, Canberra, ACT 2601, Australia
E-mail: thomas.white@anu.edu.au

Dr. Jafar I. Khan, Dr. Wenzhu Liu, Esam Ugur, Dr. Kai Wang, Dr. Hoang Dang, Dr. Erkan Aydin, Dr. Xinbo Yang, A/Prof. Frédéric Laquai and A/Prof. Stefaan De Wolf
King Abdullah University of Science and Technology (KAUST), KAUST Solar Center (KSC), Physical Sciences and Engineering Division (PSE), Thuwal 23955-6900, Kingdom of Saudi Arabia
E-mail: stefaan.dewolf@kaust.edu.sa

This Supporting Information includes:

Experimental Section

Figures S1 to S8

References

Experimental Section

Perovskite device preparation

(1) FTO/c-In-TiO_x/m-TiO₂ ETLs preparation

FTO substrates ($7\Omega/\square$, Dyesol) were sequentially cleaned by detergent, acetone, isopropanol and ethanol in an ultrasonic bath for 10 min each, followed by UV-O₃ treatment for a further 10 min. Next, ~ 70 nm layers of compact In-TiO₂ were deposited on the pre-cleaned FTO substrates according to the Ref[1]. Mesoporous TiO₂ layers (~ 90 nm thick) were deposited on the FTO/c-In-TiO₂ compact layer via spin casting meso-TiO₂ paste solution for 30 s at 5000 rpm with a ramp of 5000 rpm s⁻¹. The meso-TiO₂ paste solution was prepared from 30 nm TiO₂ particle paste (30 NR-D, Dyesol) diluted in anhydrous Ethanol (1:9, w/w).

(2) PMMA:PCBM passivation layer deposition

The PMMA:PCBM passivation layer was spin coated on the FTO/c-In-TiO_x/m-TiO₂ according to Ref[2], where the PMMA:PCBM blend solution was prepared by dissolving 1 mg PMMA (Mw \sim 120000, Sigma Aldrich) and 3 mg PC₆₁BM (Sigma Aldrich) into 1 mL Chlorobenzene.

(3) Multi-cation perovskite fabrication and PMMA passivation treatment

The multi-cation Cs_{0.07}Rb_{0.03}FA_{0.765}MA_{0.135}PbI_{2.55}Br_{0.45} perovskite precursor was prepared from 1.2 M lead iodide (PbI₂, 99%, Sigma Aldrich), 1.1 M formamidinium (FAI, Dyesol), 0.2 M lead bromide (PbBr₂, 99.999%, Sigma Aldrich), 0.2 M methylamine bromide (MABr, Dyesol), 0.091 M cesium iodide (CsI, 99.999%, Sigma Aldrich), 0.039 M rubidium iodide (RbI, 99.9%, Sigma Aldrich) in 1 mL anhydrous DMF:DMSO (4:1, v/v, Sigma Aldrich) blend solvents.

A two-step spin coating program was used to deposit the perovskite thin films: first at 2000 rpm with a ramp of 200 rpm s⁻¹ for 10 s, and then at 5000 rpm with a ramp of 1000 rpm s⁻¹ for

25 s. During the second step, approximately 200 μl Chlorobenzene was poured on the spinning substrate 8 s prior to the end of the program. This was followed by thermal annealing and PMMA passivation treatment for different perovskite samples as follows:

(i) Perovskite control cell (with a structure of FTO/c-In-TiO_x/m-TiO₂/Perovskite/Spiro-OMeTAD/Au). After the two-step spin coating program, the perovskite sample was immediately annealed on a hotplate at 100 °C for 30 min.

(ii) Passivated ETL side perovskite cell (with a structure of FTO/c-In-TiO₂/m-TiO₂/PMMA:PCBM/Perovskite/Spiro-OMeTAD/Au). After the two-step spin coating program, the perovskite sample was immediately annealed on a hotplate at 100 °C for 30 min.

(iii) Double-side passivated perovskite cell (with a structure of FTO/c-In-TiO_x/m-TiO₂/PMMA:PCBM/Perovskite/PMMA/Spiro-OMeTAD/Au). After the two-step spin coating program, the perovskite sample was immediately annealed on a hotplate at 100 °C for 45 s. The sample was then returned to the spin-coater and immediately cooled down by fast rotation at 5000 rpm with a ramp of 5000 rpm s⁻¹ for 15 s. Next, the PMMA passivation treatment was applied: first, 50 μL PMMA solution (1 mg/ml in Chlorobenzene) was dropped on top of the perovskite sample and left for 2 s; second, the sample was spin-coated for 15 s at 5000 rpm with a ramp of 5000 rpm s⁻¹; finally, the sample was immediately annealed on a hotplate at 100 °C for 30 min.

(4) Spiro-OMeTAD HTL preparation and Gold contact deposition

The Spiro-OMeTAD precursor solution was prepared by dissolving 72.5 mg Spiro-OMeTAD, 28.5 μL 4-tert-butylpyridine and 17.5 μL of lithium bis(trifluoromethanesulfonyl)imide solution (520mg/mL in acetonitrile) in 1 mL Chlorobenzene. Note that after spin-coating (3000 rpm with a ramp of 3000 rpm/s for 30 s) the Spiro-OMeTAD layer, the substrates were placed in air in a humidity-control box for 12 hours to ensure sufficient oxidation of the Spiro-OMeTAD film prior to ~100 nm gold contact layer deposition (thermal evaporation).

The effective area of perovskite cells reported in this work is 4 mm x 4 mm (0.16 cm²) (well-defined by the rear gold contact that was deposited through a shadow mask). Our perovskite cells were fabricated on substrates of dimension 12.5 mm*14.0 mm. Note that we only had one cell on each substrate.

Perovskite device measurements

J-V measurements. All devices were tested under 1 sun conditions (100 mW/cm², AM 1.5G, 25 °C) in a solar simulator system (model #SS150 from Photo Emission Tech Inc) equipped with a Xenon lamp. The light intensity was calibrated using a certified Fraunhofer CalLab reference cell. For the perovskite solar cells, all *J-V* curves were tested at a 50 mV/s scan rate and at room temperature in a custom-built vacuum measurement jig (without an aperture mask) under air. Note that reverse scan is from V_{oc} to J_{sc} (forward bias → short circuit, 1.25 V → -0.1 V), and forward scan is from J_{sc} to V_{oc} (short circuit → forward bias, -0.1 V → 1.25 V). No preconditioning protocol has been applied before the characterization.

External quantum efficiency (EQE) measurements. External quantum efficiency (EQE) were performed on a commercial EQE system (Newport). For our double-side passivated perovskite cell, the estimated spectrum mismatch correction is 98.45 % based on the comparison between the integrated current density calculated from the EQE response and the current density measured under the solar simulator. No preconditioning protocol has been applied before the characterization.

Characterization

Photoluminescence imaging. For photoluminescence (PL) imaging, the cells were held in a nitrogen-filled and temperature-controlled jig. The jig is mounted in a home-built PL imaging system and uniformly illuminated with two 430 nm royal-blue LED chips, filtered by bandpass filters (451/106 nm). Following illumination (Intensity~100 mW/cm²), a Peltier-

cooled (-70 °C) Si CCD camera (Princeton Instruments Pixis 1024) with a long-pass filter (750 nm) was used to image the luminescence from the perovskite cells with an exposure time of 0.08 seconds. PL images were taken when cells were under both open circuit and reverse bias (-2 V) conditions. The open circuit images were then subtracted from the reverse bias image to ensure the luminescence emission was solely from the perovskite absorber layer.

X-ray Diffraction (XRD) measurements. X-ray diffraction analysis was performed with a Bruker D8 Advance diffraction meter operated at 30 kV, 10 mA at 2θ (Cu $K\alpha$) 10–60°, step 0.02° and scan speed 2.3° min⁻¹.

Scanning Electron Microscope (SEM) measurements. A Nova Nano630 scanning electron microscope (SEM) was used to investigate the surface morphology of samples. A Helios Nanolab 600 FIB system was used to prepare cross-sectional SEM images of the cells.

Transient Absorption (TA) Spectroscopy measurements. Ultrafast pump-probe transient absorption (TA) spectroscopy was performed to reveal the charge carrier dynamics of various samples. All measurements were conducted in the time range from 1 nanosecond (ns) to 100 microseconds (μ s). The fundamental output of a titanium:sapphire amplifier, Coherent Legend Duo, operating at 800 nm with a repetition rate of 3 kHz and energy of 4.5 mJ is split into 3 segments (2 mJ, 1 mJ and 1.5 mJ), two of them are used to pump two optical parametric amplifiers (Light conversion TOPAS Prime). One of the TOPAS generates tunable pump pulses, while the second one generates a signal (1300 nm) and idler (2000 nm) only. A fraction of the signal beam of the second TOPAS was focused into a c-cut 3 mm thick CaF₂ window, thereby generating a white-light supercontinuum from 350 to 1000 nm. For long delay TA measurement, the probe white-light supercontinuum was used, the excitation (pump pulse) was provided by an actively Q-switched Nd:YVO₄ laser (InnoLas piccolo AOT)

frequency-doubled to provide pulses at 532 nm, and triggered by an electronic delay generator (Stanford Research Systems DG535), itself triggered by the TTL sync from the Legend DUO, allowing control of the delay between pump and probe with a jitter of roughly 100 ps.

Pump and probe beams were focused to overlap spatially on the sample. The transmitted fraction of the white light was guided to a custom-made prism spectrograph (Entwicklungsbüro Stresing) where it was dispersed by a prism onto a 512 pixel NMOS linear image sensor (Hamamatsu S8381-512). The probe pulse repetition rate was 3 kHz but the excitation was directly generated at 1.5 kHz frequency covering a temporal range from 1 ns to 100 μ s delays, while the detector array was read out at 3 kHz. Adjacent diode readings corresponding to the transmission (T) of the sample after excitation and in the absence of an excitation pulse were used to calculate $\Delta T/T$. Measurements were averaged over several thousand shots to obtain a good signal-to-noise ratio. Finally, the chirp induced by the transmissive optics was corrected with a home-built Matlab code by reevaluating for each wavelength the delay at which pump and probe are simultaneously arriving on the sample as the time of the signal amplitude. All measurements were performed at room temperature in vacuum.

Time-Resolved Photoluminescence (TR-PL) spectroscopy measurements. For TR-PL experiments samples were excited with the wavelength-tunable output of an OPO (Radiantis Inspire HF-100), itself pumped by the fundamental of a Ti:Sa fs-oscillator (Spectra Physics MaiTai eHP) at 820 nm. The repetition rate of the fs pulses was adjusted by a pulse picker (APE Pulse Select) and typical pulse energies were in the range of several nJ. Photoluminescence was collected by an optical telescope (consisting of two plano-convex lenses), focused on the slit of a spectrograph (PI Spectra Pro SP2300) and detected with a Streak Camera (Hamamatsu C10910) system with a temporal resolution of 1.4 ps.

Fourier-Transform Infrared (FTIR) Spectroscopy measurements. FTIR spectroscopy of pure PMMA, PMMA + PbI₂, PMMA + PbI₂ + PbBr₂ and PMMA + FAI thin film samples were performed using a commercial FTIR system (Cary 680, Agilent) in transmission mode. All samples were fabricated by spin-coating their corresponding precursor solutions at 500 rpm for 60 s, then placed in a vacuum chamber to remove the residual solvents. The precursor solution for the pure PMMA sample was prepared by dissolving 50 mg PMMA powder into 1 mL DMSO. The precursor solution for PMMA + PbI₂ sample was prepared by dissolving 25 mg PMMA and 40 mg PbI₂ into 1 mL DMSO. The precursor solution of PMMA + PbI₂ + PbBr₂ sample was prepared by dissolving 25 mg PMMA + 34 mg PbI₂ + 6 mg PbBr₂ into 1 mL DMSO. The precursor solution for the PMMA + FAI sample was prepared by dissolving 25 mg PMMA and 40 mg FAI into 1 mL DMSO.

Nuclear Magnetic Resonance (NMR) Spectroscopy measurements. NMR spectroscopy carried out with a Bruker Avance III Ultrashield Plus instrument using a 400 MHz proton frequency at room temperature. The spectra were measured at DMSO-d₆ with TMS as an internal standard. The PMMA sample was measured at 10 mg/ml; the PMMA + PbI₂ sample was measured at 5 mg/ml for PMMA and 20 mg/ml for PbI₂; the PMMA + FAI sample was measured at 5 mg/ml for PMMA and 20 mg/ml for FAI.

First-Principles Calculations. First-principles calculations: The DFT calculations were performed using the Dmol3 module^[3,4] in Materials Studio 2017 R2 package (Accelrys, SanDiego, CA). The DNP 4.4 basis set was employed to describe electronic charge density and electrostatic potential. The basis set cutoff is 3.3 Å during the geometrical optimization,^[5,6] where the convergence tolerance is 2×10^{-5} Ha for the energy, 0.004 Ha Å⁻¹ for the forces, and 0.005 Å for the displacement. The electronic self-consistence field (SCF)

tolerance is set to 10^{-5} Ha. The exchange correlation adopted the general gradient approximation, Perdew–Burke–Ernzerhof (GGA-PBE) functional.^[7]

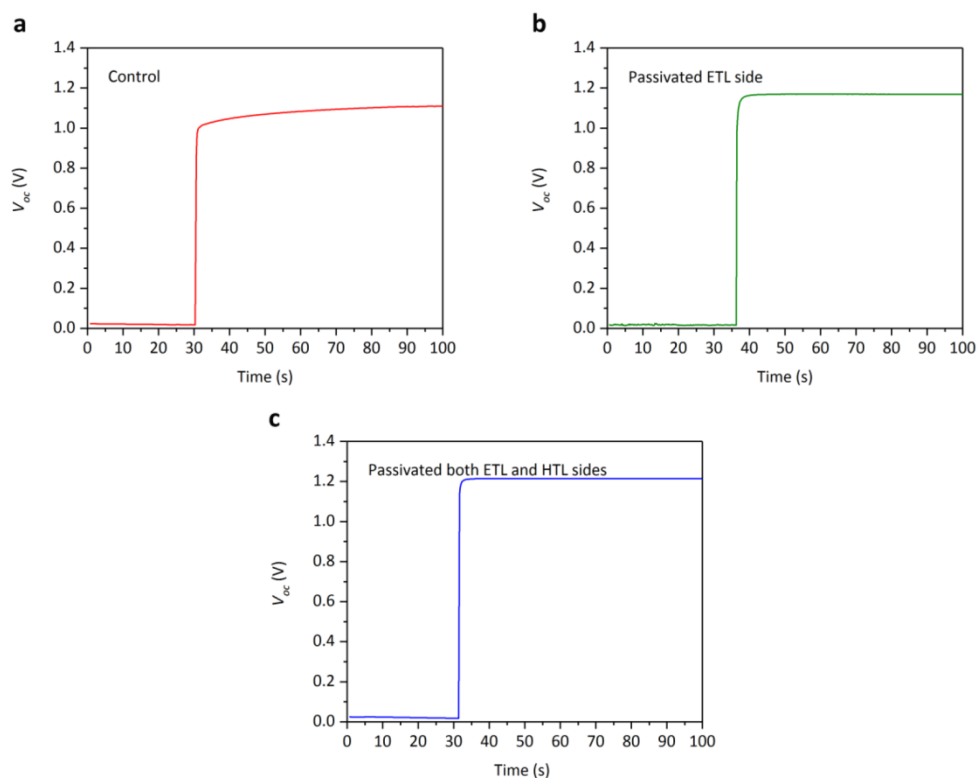


Figure S1. The V_{oc} response of the control and passivated perovskite cells with/without PMMA:PCBM and PMMA passivation layer tested under open circuit condition. a). Control cell, with a structure of FTO/c-In-TiO_x/m-TiO₂/Perovskite/Spiro-OMeTAD/Au. b) Passivated ETL side cell, with a structure of FTO/c-In-TiO_x/m-TiO₂/PMMA:PCBM/Perovskite/Spiro-OMeTAD/Au. c) Double-side passivated cell, with a structure of FTO/c-In-TiO_x/m-TiO₂/PMMA:PCBM/Perovskite/PMMA/Spiro-OMeTAD/Au. Note that ‘perovskite’ represents Cs_{0.07}Rb_{0.03}FA_{0.765}MA_{0.135}PbI_{2.55}Br_{0.45}.

As seen in Figure S1, the V_{oc} of the control cell took around 50 s to reach a steady-state maximum V_{oc} condition, while for the passivated ETL side perovskite cell and the double-side passivated cell the response time was significantly reduced to 2-3 s.

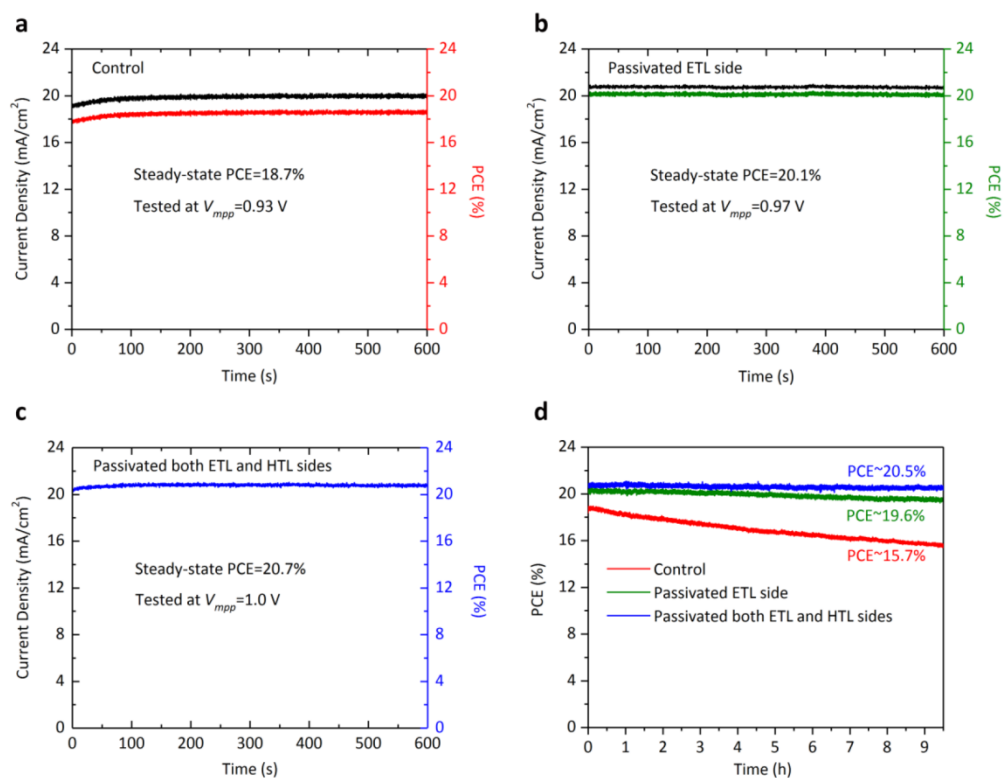


Figure S2. The steady-state PCE of the control and passivated perovskite cells with/without PMMA:PCBM and PMMA passivation layer tested at V_{mpp} . a) Control cell, with a structure of FTO/c-In-TiO_x/m-TiO₂/Perovskite/Spiro-OMeTAD/Au. b) Passivated ETL side cell, with a structure of FTO/c-In-TiO_x/m-TiO₂/PMMA:PCBM/Perovskite/Spiro-OMeTAD/Au. c) Double-side passivated cell, with a structure of FTO/c-In-TiO_x/m-TiO₂/PMMA:PCBM/Perovskite/PMMA/Spiro-OMeTAD/Au. d) Steady-state PCE tests measured over a period of 9.5 hours. Note that 'perovskite' represents $\text{Cs}_{0.07}\text{Rb}_{0.03}\text{FA}_{0.765}\text{MA}_{0.135}\text{PbI}_{2.55}\text{Br}_{0.45}$.

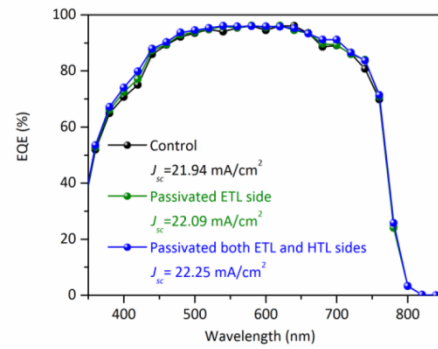


Figure S3. EQE measurements for the control, passivated ETL side and double-side passivated cells. The control cell structure is FTO/c-In-TiO_x/m-TiO₂/Perovskite/Spiro-OMeTAD/Au; passivated ETL side cell structure is FTO/c-In-TiO_x/m-TiO₂/PMMA:PCBM/Perovskite/Spiro-OMeTAD/Au; double-side passivated cell structure is FTO/c-In-TiO_x/m-TiO₂/PMMA:PCBM/Perovskite/PMMA/Spiro-OMeTAD/Au. Note that ‘perovskite’ represents Cs_{0.07}Rb_{0.03}FA_{0.765}MA_{0.135}PbI_{2.55}Br_{0.45}.

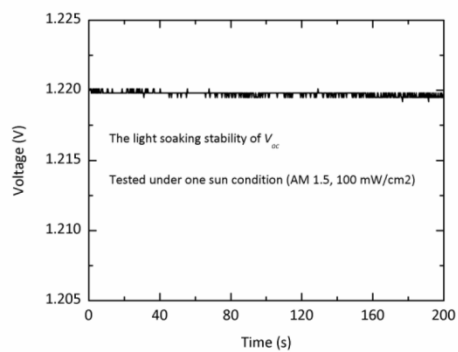


Figure S4. The light soaking stability of the open-circuit voltage (V_{oc}) of our double-side passivated perovskite cell tested under one sun condition (AM 1.5, 100 mW/cm²).

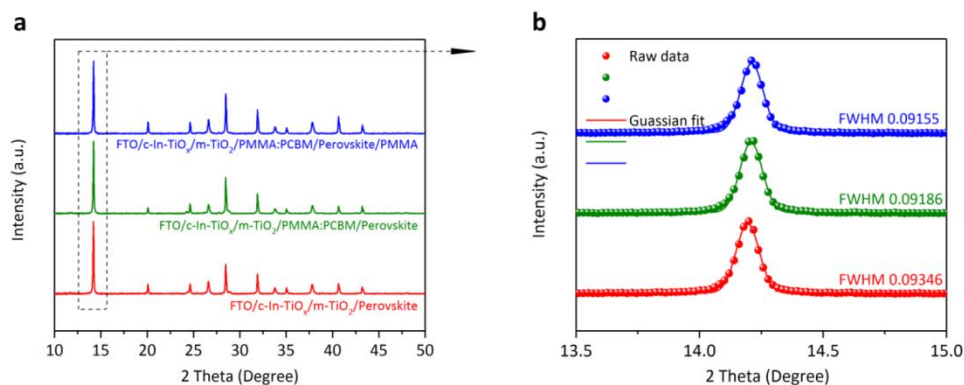


Figure S5. a) XRD spectra of the perovskite thin films deposited on different FTO/c-In-TiO_x/m-TiO₂ substrates with/without the PMMA:PCBM and PMMA passivation layer. b) The corresponding Gaussian fit of the dominant black perovskite phase for perovskite thin film. Note that the perovskite composition is Cs_{0.07}Rb_{0.03}FA_{0.765}MA_{0.135}PbI_{2.55}Br_{0.45}.

In Figure S5a, the XRD spectra show no systematic variations for perovskite samples with/without PMMA:PCBM or PMMA passivation layers, and no obvious PbI₂ or other non-perovskite phases. To further investigate the crystallite size of perovskite, the dominant black perovskite phase is fitted with a Gaussian distribution to determine the full width at half maximum (FWHM) for each sample. As presented in the Figure S5b, it reveals that the value of FWHM for FTO/c-In-TiO_x/m-TiO₂/perovskite sample is 0.09346, while the values of FWHM for FTO/c-In-TiO_x/m-TiO₂/PMMA:PCBM/Perovskite and FTO/c-In-TiO_x/m-TiO₂/PMMA:PCBM/Perovskite/PMMA samples are 0.09186 and 0.09155 respectively. As expected, there are no significant variations for the crystallite size of perovskite deposited on different substrates with/without PMMA:PCBM and PMMA passivation layer based on the calculated FWHM.

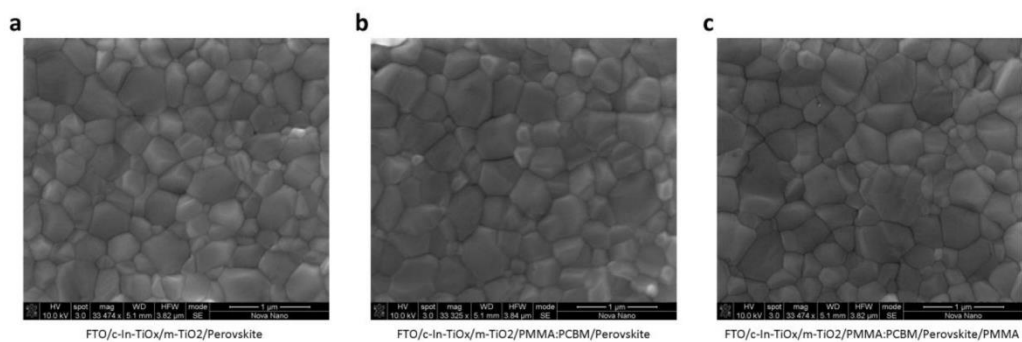


Figure S6. SEM images for different samples: a) FTO/c-In-TiO_x/m-TiO₂/Perovskite; b) FTO/c-In-TiO_x/m-TiO₂/PMMA:PCBM/Perovskite; c) FTO/c-In-TiO_x/m-TiO₂/PMMA:PCBM/Perovskite/PMMA. Note that the perovskite represents Cs_{0.07}Rb_{0.03}FA_{0.765}MA_{0.135}PbI_{2.55}Br_{0.45}.

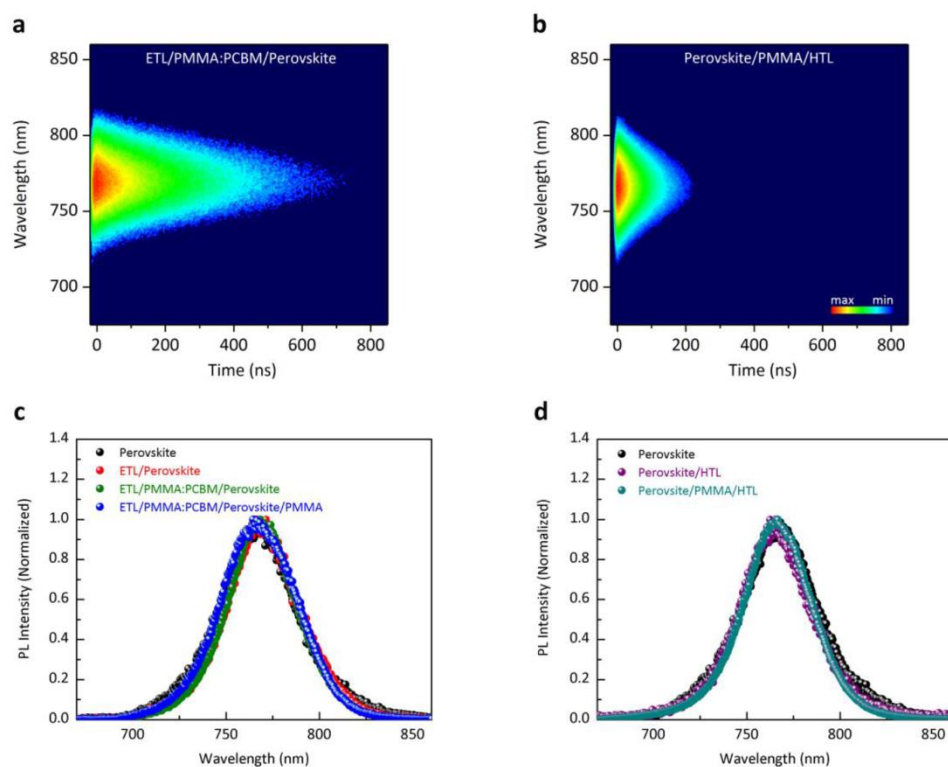


Figure S7. a) TR-PL data for ETL/PMMA:PCBM/Perovskite after excitation at 650 nm. b) TR-PL data for Perovskite/PMMA/HTL samples after excitation at 650 nm. c) The acquired TR-PL spectra of Perovskite, ETL/Perovskite, ETL/PMMA:PCBM/Perovskite and ETL/PMMA:PCBM/Perovskite/PMMA samples with the characteristic peak at 770 nm. d) TR-PL spectra of Perovskite, Perovskite/HTL and Perovskite/PMMA/HTL samples with the characteristic peak at 770 nm. Note that all samples were fabricated on high-grade optical quartz substrates. And the ETL, HTL and Perovskite represent $c\text{-In-TiO}_x/m\text{-TiO}_2$, Spiro-OMeTAD and $\text{Cs}_{0.07}\text{Rb}_{0.03}\text{FA}_{0.765}\text{MA}_{0.135}\text{PbI}_{2.55}\text{Br}_{0.45}$, respectively.

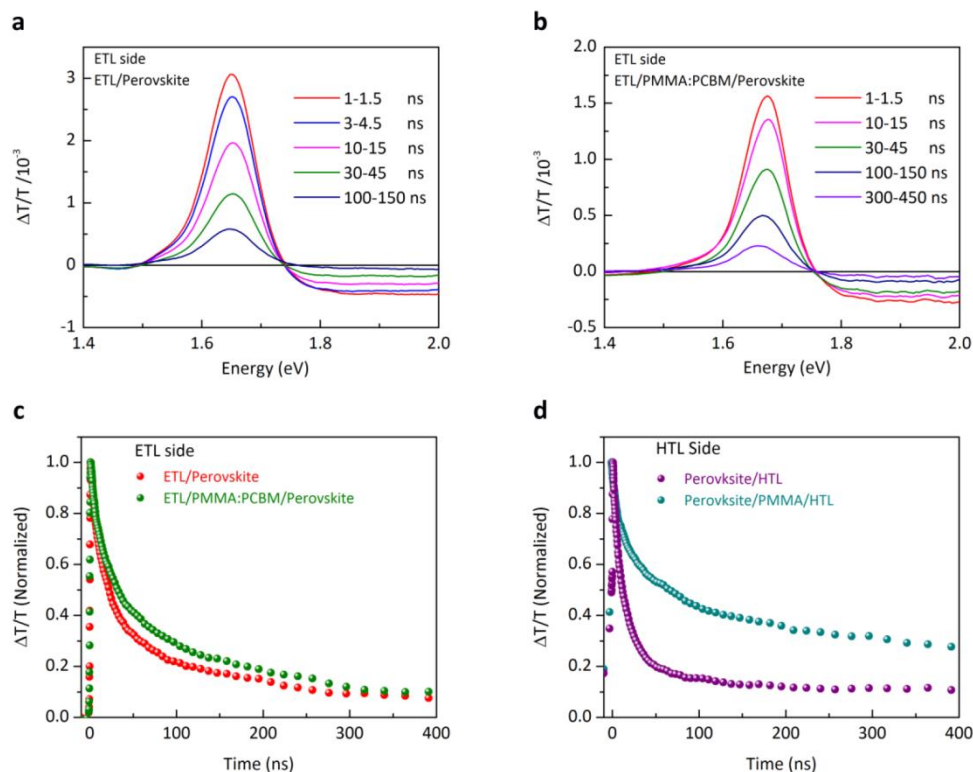


Figure S8. Transient absorption (TA) spectra of: a) ETL only samples (illuminated from the ETL side): ETL/perovskite; b) ETL only samples (illuminated from the ETL side): ETL/PMMA:PCBM/Perovskite. ns- μ s dynamics of TA data monitored at the position of the ground state bleach; c) ETL only samples (illuminated from the ETL side): ETL/perovskite and ETL/PMMA:PCBM/Perovskite; d) HTL only samples (illuminated from the HTL side): perovskite/HTL and perovskite/PMMA/HTL. Note that all samples were fabricated on high-grade optical quartz substrates. ETL, HTL and perovskite represent c-In-TiO_x/m-TiO₂, Spiro-OMeTAD and Cs_{0.07}Rb_{0.03}FA_{0.765}MA_{0.135}PbI_{2.55}Br_{0.45}, respectively.

The recombination dynamics were also determined by transient absorption (TA) spectroscopy in the nano-to-microsecond time range, using a 532 nm laser as excitation source (corresponding to an absorption depth into the perovskite layer of around 100 nm). As the thickness of the perovskite absorber layer is 300 nm, this technique thus will mostly monitor the recombination dynamics close to the excited side of the sample. The spectral evolution is depicted in Figure S8, showing the typical narrow peak at 1.65 eV, which is a convolution of

the ground state bleach (GSB) band of the perovskite and stimulated emission, whereas a broad photo-induced absorption (PIA) band spans the spectral range of 1.75 eV-2.25 eV. The data shows that when illuminating from the ETL-side the signal decays slower for the passivated sample (more than 450 ns), compared to the control sample (about 200 ns). Figure S8c shows the normalized kinetics of the GSB recovery for these samples, underlining again the beneficial effect of passivation. Interestingly, when illuminating from the HTL side (see Figure S8d), the passivated sample clearly exhibits a much slower dynamics with 40 % of the signal still remaining after 200 ns, while only 10 % is left for the case of the reference sample (without passivation). We attribute this to reduced recombination at the HTL/perovskite interface due to the passivation effect of the PMMA layer.

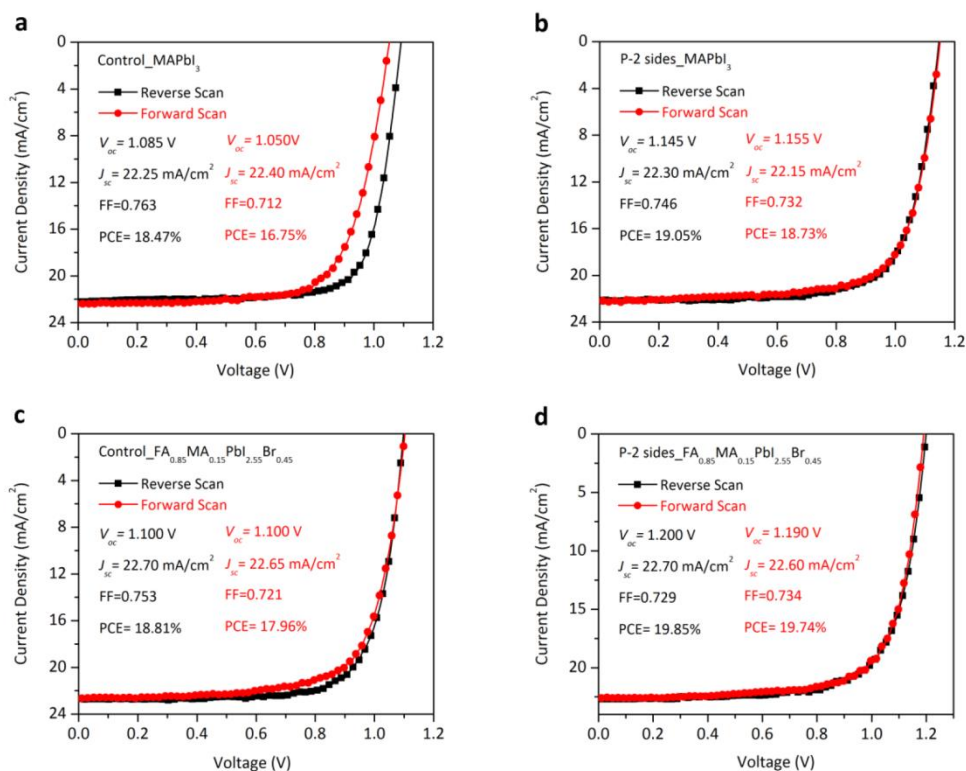


Figure S9. Forward- and reverse-scan J - V curves of different perovskite cells. a) Control_MAPbI₃ with a structure of FTO/c-In-TiO_x/m-TiO₂/MAPbI₃/Spiro-OMeTAD/Au. b) P-2 sides_MAPbI₃ with a structure of FTO/c-In-TiO_x/m-TiO₂/PMMA:PCBM/MAPbI₃/PMMA/Spiro-OMeTAD/Au. c) Control_FA_{0.85}MA_{0.15}PbI_{0.25}Br_{0.45} with a structure of FTO/c-In-TiO_x/m-TiO₂/FA_{0.85}MA_{0.15}PbI_{0.25}Br_{0.45}/Spiro-OMeTAD/Au. d) P-2 sides_FA_{0.85}MA_{0.15}PbI_{0.25}Br_{0.45} with a structure of FTO/c-In-TiO_x/m-TiO₂/PMMA:PCBM/FA_{0.85}MA_{0.15}PbI_{0.25}Br_{0.45}/PMMA/Spiro-OMeTAD/Au. Note that all devices were tested at a scan rate of 50 mV/s.

Table S1. Summary of the detailed photovoltaic parameters of different perovskite cells.

Perovskite	Device Type	Scan Direction	V_{oc} (V)	J_{sc} (mA/cm ²)	FF	PCE (%)
MAPbI ₃	Control	RS	1.085	22.25	0.763	18.47
		FS	1.050	22.40	0.712	16.75
	P-2 sides	RS	1.145	22.30	0.746	19.05
		FS	1.155	22.15	0.732	18.73
FA _{0.85} MA _{0.15} PbI _{2.55} Br _{0.45}	Control	RS	1.100	22.70	0.753	18.81
		FS	1.100	22.65	0.721	17.96
	P-2 sides	RS	1.200	22.70	0.729	19.85
		FS	1.190	22.60	0.734	19.74
CS _{0.07} Rb _{0.03} FA _{0.765} MA _{0.135} PbI _{2.55} Br _{0.45}	Control	RS	1.110	22.85	0.770	19.50
		FS	1.100	22.81	0.738	18.50
	P-2 sides	RS	1.205	22.60	0.764	20.80
		FS	1.213	22.60	0.761	20.86

References

- [1] J. Peng, T. Duong, X. Zhou, H. Shen, Y. Wu, H. K. Mulmudi, Y. Wan, D. Zhong, J. Li and T. Tsuzuki, K. J. Weber, K. R. Catchpole and T. P. White, *Adv. Energy Mater.* **2017**, *7*, 1601768.
- [2] J. Peng, Y. Wu, W. Ye, D. A. Jacobs, H. Shen, X. Fu, Y. Wan, N. Wu, C. Barugkin and H. T. Nguyen, D. Zhong, J. Li, T. Lu, Y. Liu, M. N. Lockrey, K. J. Weber, K. R. Catchpole and T. P. White, *Energy Environ. Sci.* **2017**, *10*, 1792.
- [3] B. Delley, *J. Chem. Phys.* **1990**, *92*, 508.
- [4] B. Delley, *J. Chem. Phys.* **2000**, *113*, 7756.
- [5] J. Baker, A. Kessi and B. Delley, *J. Chem. Phys.* **1996**, *105*, 192.
- [6] J. Andzelm, R. King-Smith and G. Fitzgerald, *Chem. Phys. Lett.* **2001**, *335*, 321.
- [7] J. P. Perdew, K. Burke and M. Ernzerhof, *Phys. Rev. Lett.* **1996**, *77*, 3865.

Supporting Information for

Inorganic ZnO/MgF₂ Bi-Layers as a High-Performance Alternative to Fullerene-Based Electron Transport Layers in Inverted Perovskite Solar Cells

Jun Peng^{1,2*}, Yimao Wan¹, Xianzhong Zhou³, The Duong¹, Heping Shen¹, Daniel A. Jacobs¹, Hieu T. Nguyen¹, Mark N. Lockrey⁴, Felipe Kremer⁵, Shenyou Zhao¹, Nandi Wu¹, Yiliang Wu¹, Xinbo Yang², Wenzhu Liu², Dingyong Zhong³, Juntao Li³, Klaus J. Weber¹, Kylie R. Catchpole¹, Stefaan De Wolf^{2*}, Thomas P. White^{1*}

¹Research School of Engineering, The Australian National University, Canberra, ACT 2601, Australia

²King Abdullah University of Science and Technology (KAUST), KAUST Solar Center (KSC), Physical Sciences and Engineering Division (PSE), Thuwal 23955-6900, Kingdom of Saudi Arabia

³State Key Laboratory of Optoelectronic Materials and Technologies, School of Physics, Sun Yat-sen University, Guangzhou 510275, China

⁴Australian National Fabrication Facility, Department of Electronic Materials Engineering, Research School of Physics & Engineering, The Australian National University, Canberra, ACT, 2601, Australia

⁵Centre for Advanced Microscopy, The Australian National University, Canberra, ACT, 2601, Australia

E-mail: jun.peng@anu.edu.au or pengjun.88.81@gmail.com;
stefaan.dewolf@kaust.edu.sa;
thomas.white@anu.edu.au

Experiment Section

ZnO nanoparticle synthesis. The ZnO nanoparticles were synthesized according to the Ref [1]. In a typical preparation: (1) Weigh and prepare 30 mL of 0.552 M N(Me)₄OH·5H₂O (tetramethylammonium hydroxide) in EtOH (noted as Solution A). (2) Weigh

and prepare 90 mL solution of 0.101 M $\text{Zn}(\text{CH}_3\text{COO})_2 \cdot 2\text{H}_2\text{O}$ in DMSO (noted as Solution B). (3) Add solution A dropwise at approximately 3 mL/min to Solution B under constant stirring (noted as Solution C). (4) After 2 hours, add ethyl acetate (1:1 v/v) into the Solution C to wash the zinc oxide nanoparticle; and then use centrifuge to separate the zinc oxide nanoparticle from the solution; and then repeat the washing step one more time; after that, collect the ZnO particle and dry under vacuum at room temperature. (6) Then, the final products suspend in IPA (3~5 mg/ml).

Device fabrication. First, around 60-nm-thick PEDOT:PSS films were deposited on the pre-cleaned ITO substrates via spin coating the PEDOT:PSS (PVP Al 4083) solution at 4500 rpm/s with a ramp of 4500 rpm/s for 40 s. These samples were immediately annealed at 125 °C for 20 min, and then transferred into nitrogen-filled glovebox for the next deposition. Second, the MAPbI_3 films were deposited on the ITO/PEDOT:PSS substrates by spin coating the MAPbI_3 precursor solution at 3500 rpm with a ramp of 3500 rpm/s for 60 s, where the MAPbI_3 precursor was prepared by dissolving 1 mol methylamine iodine (MAI) and 1 mol PbI_2 in 1 mL anhydrous dimethyl sulphoxide (DMSO) and N,N-dimethylformamide (DMF) (2:8, v/v). During the spin coating process, around 200 μL Chlorobenzene was poured on the spinning substrates after 10 s. Substrates were then annealed at 100 °C for 10 min. Third, for the PCBM ETL, it was deposited on MAPbI_3 via spin coating the PCBM solution (20 mg/ml, in chlorobenzene) at 1000 rpm/s with a ramp of 1000 rpm/s for 40 s; while for the ZnO ETL, it was deposited on MAPbI_3 via spin coating the ZnO solution at 5000 rpm/s with a ramp of 5000 rpm/s for 10 s, and then repeated this process for three times. In addition, for the ultrathin PMMA:PCBM passivation layer, it was deposited on MAPbI_3 via spin coating the PMMA:PCBM^[2] blend solution (4 mg/ml (1:3, w/w), in chlorobenzene) at 5000 rpm/s with a ramp of 5000 rpm/s for 30 s. Finally, around 100 nm gold was deposited through by a mask (cell's effective area, 0.16 cm²).

J-V measurements. All devices were tested under 1 sun conditions (100 mW/cm², AM 1.5G, 25 °C) in a solar simulator system (model #SS150 from Photo Emission Tech Inc) equipped with a Xenon lamp. The light intensity was calibrated using a certified Fraunhofer CalLab reference cell. For the perovskite solar cells, all cells' J-V curves were tested at a 50 mV/s scan rate in a custom-built vacuum measurement jig without aperture mask. Note that reverse scan is from V_{oc} to J_{sc} (forward bias \rightarrow short circuit,

1.1 V \rightarrow -0.1V), and forward scan is from J_{sc} to V_{oc} (short circuit \rightarrow forward bias, -0.1 V \rightarrow 1.1 V). No preconditioning protocol has been used before the characterization.

EQE measurements. The external quantum efficiency (EQE) spectra of our perovskite cells were measured with a commercial EQE system (Newport).

Characterization—TEM. A JEOL 2100F FEGTEM system was used to investigate the ZnO nanoparticle.

Characterization—XPS and UPS. X-ray photoelectron spectroscopy (XPS) and ultraviolet photoelectron spectroscopy (UPS) measurements were carried out on an XPS machine (Escalab 250 Xi, Thermo Fisher), with a monochromatic Al K α (1486.7 eV) X-ray source for XPS and a He I (21.2 eV) gas discharge lamp for UPS.

Characterization—SEM. A tapping mode atomic force microscope (Multimode, Bruker) and a FEI Verios scanning electron microscope (SEM) were used to investigate the surface morphology of samples.

Characterization—XRD. X-ray diffraction analysis was performed with a Bruker D2 Phaser diffractometer operated at 30 kV, 10 mA at 2θ (Cu K α) 10–80°, step 0.02° and scan speed 2.3° min⁻¹.

Characterization—Transmittance. A PerkinElmer Lambda 1050 UV/Vis/NIR spectrophotometer was used to investigate the transmittance of samples.

Characterization—TRPL. Time-resolved photoluminescence (TRPL) decay measurements were performed using LabRAM HR Evolution system with a time-correlated single photon counting (TCSPC) system (DeltaPro-DD, Horiba). A 508nm diode laser (DD-510L, Horiba) with pulse duration of 110ps, fluence of \sim 10 μ J/cm²/pulse, and a repetition rate of 312.5 kHz was used for excitation. The PL signal was extracted at 770 nm. Both the incident light and the reflected light went through a 50x objective lens (LEICA PL FLUOTAR L 50x/0.55), which resulted in a spot size of \sim 2 μ m. The samples were kept in N₂ environment during the measurements. For the analysis of the time-resolved PL decay, a bi-exponential model in the Decay Analysis software was used to fit the experimental result and extract the lifetime.

Characterization—SCLC. Space charge limited current (SCLC) measurements were performed on electron-dominated devices with a structure of ITO/In-TiO_x (\sim 50 nm) /MAPbI₃/(w/wo) PMMA:PCBM (less than 5 nm)/ZnO (\sim 70 nm)/MgF₂ (\sim 1.5 nm) Al

(~100 nm), where the device without PMMA:PCBM layer is the control device (non-passivated cell), Note that the In-TiO_x films were prepared according to the Ref[3]; the electron-dominated devices were prepared by the same procedures as described in the aforementioned device fabrication; then, ~50 nm PCBM was deposited by spin-coating 20 mg/mL PCBM in CB at 1000 rpm/s for 40 s; and then, ~100 nm Al was deposited by thermal evaporation at a deposition rate of 1 Å/s. All SCLC tests were carried out at room temperature and under dark.

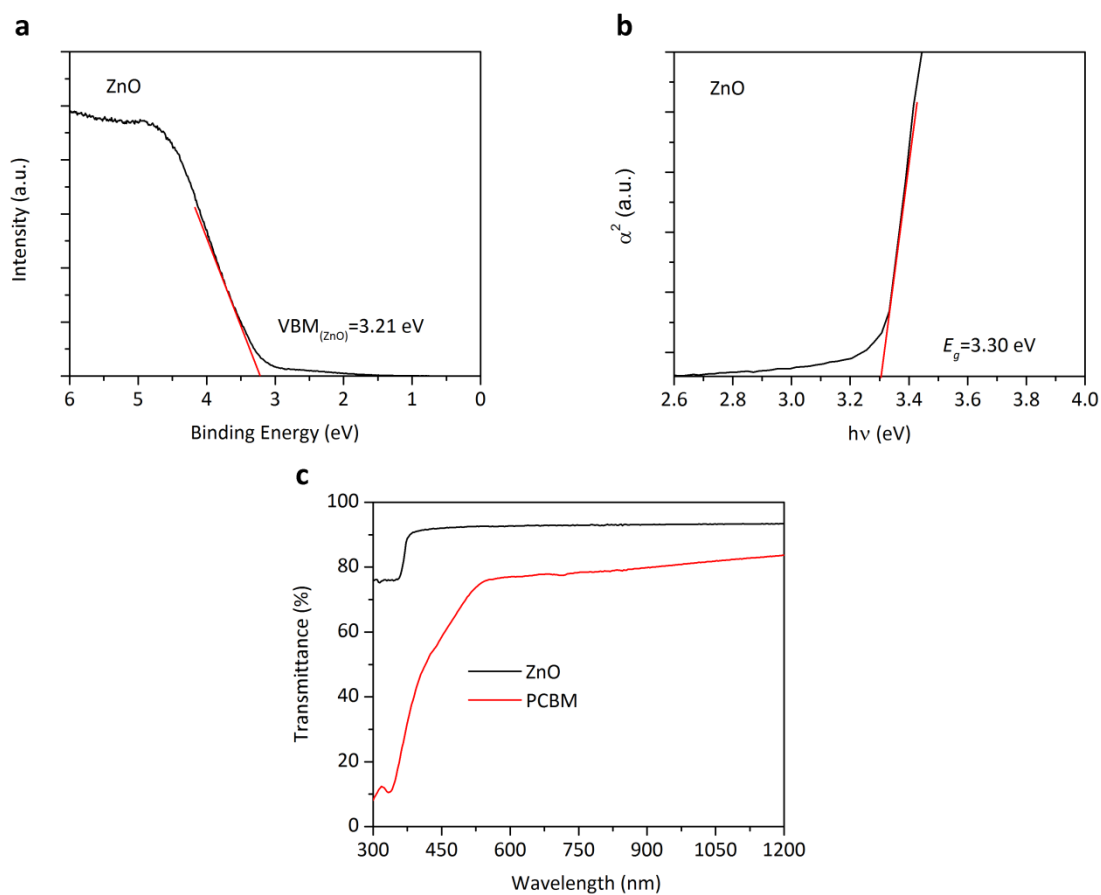


Figure S1. a) Valance band maximum (UPS) spectra of a ZnO nanoparticle thin film deposited on a Glass/ITO substrate. b) Optical bandgap of a ZnO nanoparticle (~70 nm) thin film deposited on a quartz substrate. c) Transmittance spectra of ZnO nanoparticle (~70 nm) and PCBM (~50 nm) thin films deposited on quartz substrates. Note that the ZnO and PCBM films deposited on quartz substrates were prepared by the same procedures as described in the aforementioned device fabrication.

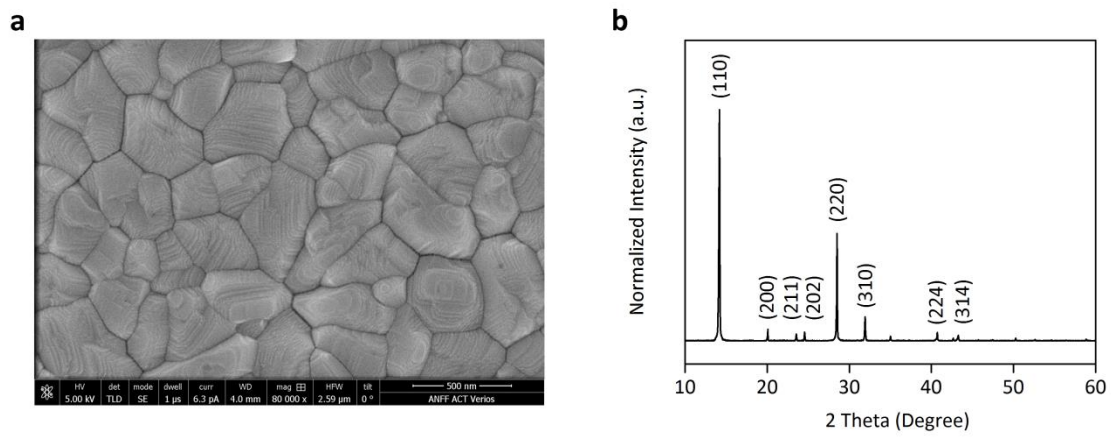


Figure S2. a) Scanning electron microscopy (SEM) image of a Glass/ITO/PEDOT:PSS/MAPbI₃ sample. b) XRD spectra of a MAPbI₃ perovskite thin film deposited on Glass/ITO/PEDOT:PSS substrate.

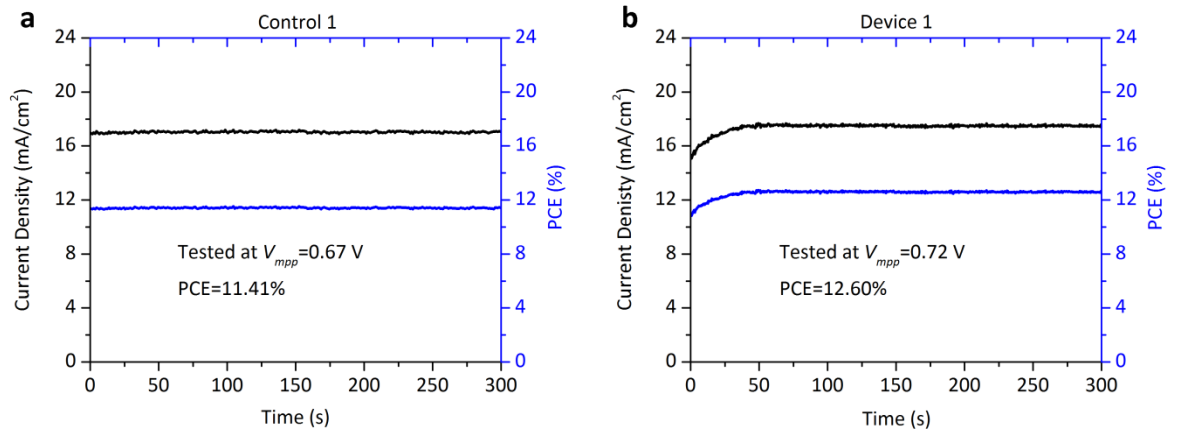


Figure S3. a) Steady-state current density and efficiency of the Control 1 (ITO/PEDOT:PSS/MAPbI₃/PCBM/Al) cell tested at $V_{mpp} = 0.67$ V. b) Steady-state current density and efficiency of the Device 1 cell (ITO/PEDOT:PSS/MAPbI₃/ZnO/Al) tested at $V_{mpp} = 0.72$ V.

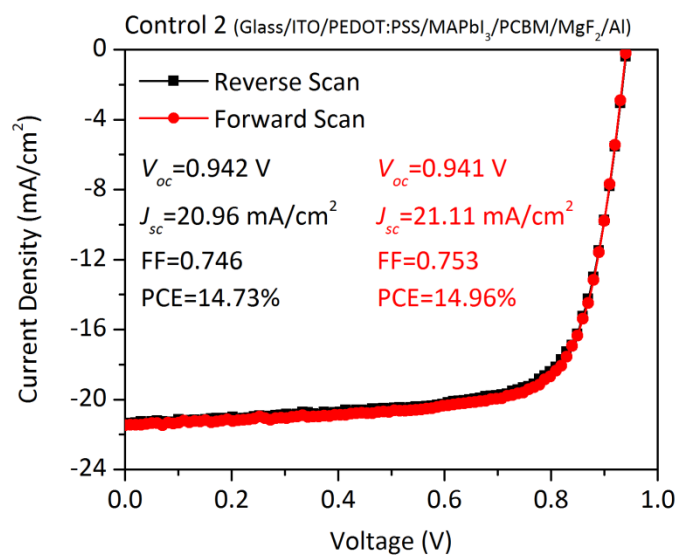


Figure S4. Current density-voltage curves of a Control 2 cell with a structure ITO/PEDOT:PSS/MAPbI₃/PCBM/MgF₂/Al. Note that the Control 2 was tested at a 50 mV/s scan rate.

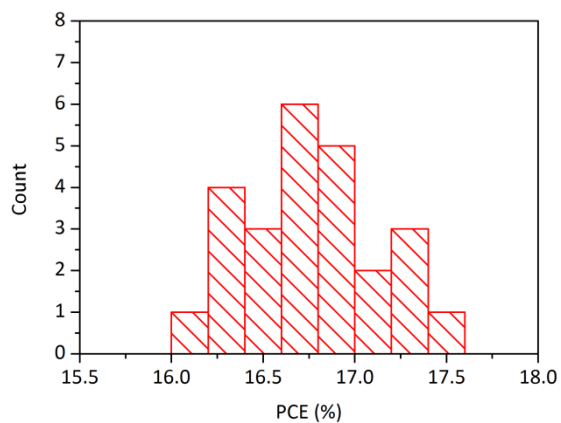


Figure S5. The PCE distribution of Device 3 cells with a structure of ITO/PEDOT:PSS/MAPbI₃/PMMA:PCBM/ZnO/MgF₂/Al. Note the PMMA:PCBM film is ultrathin (less than 5 nm). All PCEs were collected from reverse scans (tested at a 50 mV/s scan rate).

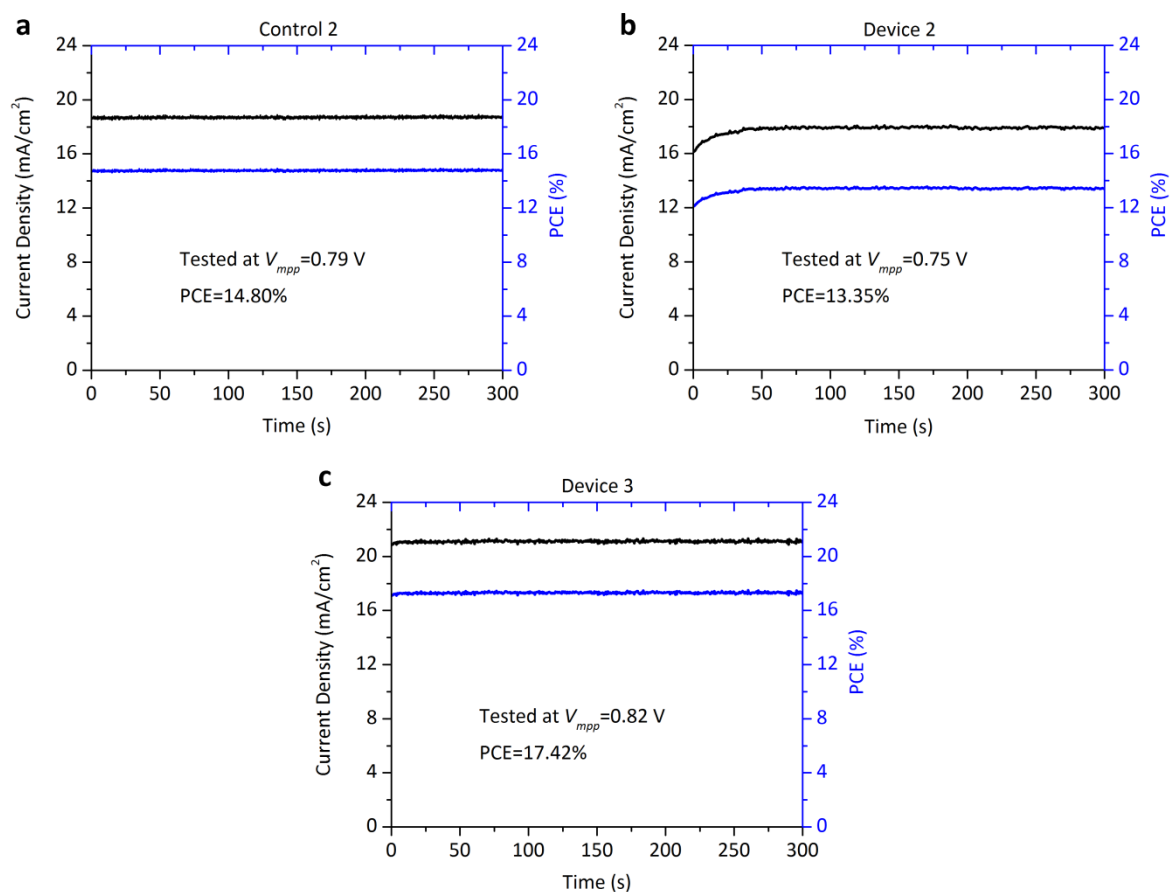


Figure S6. Steady-state current density and efficiency of the different structured inverted perovskite cells. a) Control 2 (ITO/PEDOT:PSS/MAPbI₃/PCBM/MgF₂/Al) tested at 0.79 V. b) Device 2 (ITO/PEDOT:PSS/MAPbI₃/ZnO/MgF₂/Al) tested at 0.75 V. c) Device 3 (ITO/PEDOT:PSS/MAPbI₃/PMMA:PCBM/ZnO/MgF₂/Al) tested at 0.82 V. Note the PMMA:PCBM film is ultrathin (less than 5 nm)

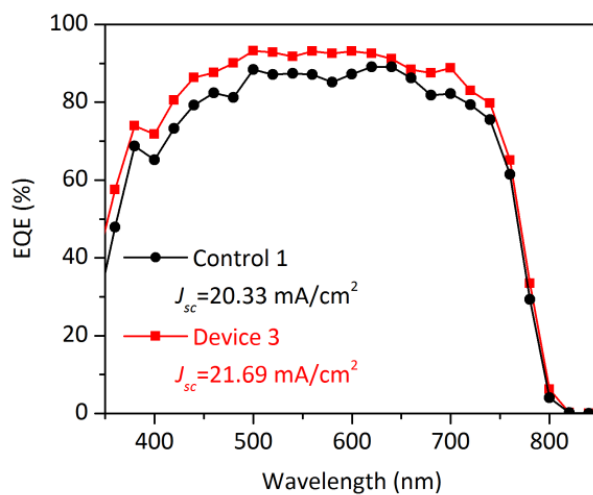


Figure S7. a) EQE spectra of Control 1 (ITO/PEDOT:PSS/MAPbI₃/PCBM/Al) and Device 3 (ITO/PEDOT:PSS/MAPbI₃/PMMA:PCBM/ZnO/ MgF₂/Al) cells.

Table S1. The detailed parameters of lifetimes (τ_1 , τ_2) and weight (A1, A2) extracted from the measured PL transient decay curves.

Sample	τ_1 (ns)	A1 (%)	τ_2 (ns)	A2 (%)
Perovskite	1.8	41.57	87.6	58.43
control 1	3.8	27.46	11.0	72.54
device 1	2.0	35.24	6.8	64.76
device 2	2.0	33.87	7.1	66.13
device 3	5.3	34.45	19.4	65.55

References

- [1] D. A. Schwartz, N. S. Norberg, Q. P. Nguyen, J. M. Parker, D. R. Gamelin, *J. Am. Chem. Soc.* **2003**, *125*, 13205.
- [2] J. Peng, Y. Wu, W. Ye, D. A. Jacobs, H. Shen, X. Fu, Y. Wan, N. Wu, C. Barugkin, H. T. Nguyen, D. Zhong, J. Li, T. Lu, Y. Liu, M. N. Lockrey, K. J. Weber, K. R. Catchpole, T. P. White, *Energy Environ. Sci.* **2017**, *10*, 1792.
- [3] J. Peng, T. Duong, X. Zhou, H. Shen, Y. Wu, H. K. Mulmudi, Y. Wan, D. Zhong, J. Li, T. Tsuzuki, K. J. Weber, K. R. Catchpole, T. P. White, *Adv. Energy Mater.* **2017**, *7*, 1601768.